Application of Constrained Optimisation Techniques in Electrical Impedance Tomography

A thesis submitted in partial fulfilment of the requirements of the Middlesex University for the degree of Doctor of Philosophy

by

R.H.F.W. BAYFORD

March 1994

School of Electronic Engineering

I may have all knowledge and understand all secrets

I may have the faith needed to move mountain

but, if I have not love, I am nothing.

ABSTRACT

A Constrained Optimisation technique is described for the reconstruction of temporal resistivity images. The approach solves the Inverse problem by optimising a cost function under constraints, in the form of normalised boundary potentials.

Mathematical models have been developed for two different data collection methods for the chosen criterion. Both of these models express the reconstructed image in terms of one dimensional (**1-D**) Lagrange multiplier functions. The reconstruction problem becomes one of estimating these **1-D** functions from the normalised boundary potentials. These models are based on a cost criterion of the minimisation of the variance between the reconstructed resistivity distribution and the true resistivity distribution.

The methods presented in this research extend the algorithms previously developed for X-ray systems. Computational efficiency is enhanced by exploiting the structure of the associated system matrices. The structure of the system matrices was preserved in the Electrical Impedance Tomography (EIT) implementations by applying a weighting due to non-linear current distribution during the backprojection of the Lagrange multiplier functions.

In order to obtain the best possible reconstruction it is important to consider the effects of noise in the boundary data. This is achieved by using a fast algorithm which matches the statistics of the error in the approximate inverse of the associated system matrix with the statistics of the noise error in the boundary data. This yields the optimum solution with the available boundary data. Novel approaches have been developed to produce the Lagrange multiplier functions.

Two alternative methods are given for the design of VLSI implementations of hardware accelerators to improve computational efficiencies. These accelerators are designed to implement parallel geometries and are modelled using a verification description language to assess their performance capabilities.

ACKNOWLEDGEMENTS

I would like to express my most sincere appreciation to the following people.

Professor George Goldspink, my director of studies, for his valuable guidance and support.

Dr Terry Fountain of the Physics and Image processing Group, University College London, for his much needed comments, constructive criticism and valuable input to this research.

Dr Ramon Prasad for his help and advice on the mathematical aspects of this research.

Dr Dave Holder of the Physiology department of University Collage London for providing me with measurement data and his valuable discussions.

Dr Stavros Drossos for his advice and comments.

Professor John Butcher and Dr Ebrahim Bushehri for their proof reading.

Bob and Audrey Gair for their proof reading and use of their Laser print.

CONTENTS

APPENDIX

LIST OF SYMBOLS

This is a list of symbols used in this thesis:

1-D	One dimensional
2-D	Two dimensional
D	Domain of image definition
FT	Fourier transform
θ_k	Sampled projection angle
$f(x,y)$	Two dimensional image cross section attenuation function (Cartesian co-ordinates)
$f(t,\theta)$	Two dimensional image (Polar co-ordinates)
$F(u,v)$	Two dimensional Fourier transform of $f(x,y)$ (Cartesian co-ordinates)
$F(\omega,\theta)$	Two dimensional Fourier transform of $f(t,\theta)$ (polar co-ordinates)
$\bar{f}(x,y)$	Estimate of the two-dimensional image
$\rho(x,y)$	Two dimensional resistivity image
$\mu(x,y)$	Two dimensional attenuation distribution
$C(.)$	Image functional or objective function
$p(t,\theta)$	One dimensional projection at angle θ
$p_k(x_k)$	Projection at angle θ_k
$P(\omega,\theta)$	Fourier transform of $p(t,\theta)$
$\hat{p}$	Calculated projections
$\bar{p}$	Estimated projections
σ	Conductivity
ρ	Resistivity
E	Electric field
J	Current field

$\lambda_k(x_k)$	Lagrange multiplier at angle θ_k
$B_\lambda(r,\phi)$	Backprojection operator
N	Number of available projections
S	Number of samples per projection
i,j,k,m	Integers
n	Iteration parameter
*	One dimensional circular (periodic) convolution
**	Two dimensional circular (periodic) convolution
DFT	Discrete Fourier transform
FT	Fourier transform
FFT	Fast Fourier transform
∇	Poisson operator $\frac{\mathbf{i}\partial}{\partial \mathbf{x}}+\frac{\mathbf{j}\partial}{\partial \mathbf{y}}+\frac{\mathbf{k}\partial}{\partial \mathbf{z}}$
Δ	Laplacian operator $\nabla^2=\frac{\partial^2}{\partial \mathbf{x}^2}+\frac{\partial^2}{\partial \mathbf{y}^2}$
γ	Relaxation factor
$\delta(.)$	Delta function
RT	Radon Transform
ln	Logarithm to base **e**
$\forall$	For all
$\wedge$	Logical AND
e	**2.71828**
E	Exchange matrix
σ_ε^2	Variance of vector ε
$\sum$	Summation
$\|.\|$	Euclidean norm

EIT	Electrical Impedance Tomography

APT	Applied Potential Tomography
CORT	Constrained Optimisation Reconstruction Technique
SNR	Signal-to-Noise Ratio
BPE	Backprojection Engine
PE	Processor Engine
PET	Positron Emission Tomography
TCT	Transmission Computerised Tomography
SPECT	Single Positron Emission Tomography
NRI	Nuclear Resonance Imaging
2DE	Two-dimensional Echocardiogram
IC	Integrated Circuit
PRF	Point Response Function
FWHM	Full-Width-at-Half-Maximum

inf	The greatest lower bound or infimum.

A normed linear space is a vector space f on which there is defined a real-valued function which maps each element $\mathbf{x},\mathbf{y}$ in f into a real number $\|\mathbf{x},\mathbf{y}\|$ called the norm of $\mathbf{x},\mathbf{y}$.

If $\mathbf{Z}$ is a normed linear vector space, the space of all bounded linear functionals on $\mathbf{Z}$ is called the normed dual of $\mathbf{Z}$ and is denoted by $\mathbf{Z}^*$ [4.5, pp. 106].

The notation $<\mathbf{x},\mathbf{x}^*>$ is used to define a functional $\mathbf{x}^*$ at a point $\mathbf{x}\in\mathbf{X}$. Hence given $\mathbf{x}\in\mathbf{X}$ the equation defines a functional on the space $\mathbf{X}^*$ [4.5, pp. 115].

LIST OF FIGURES

LIST OF TABLES

1 INTRODUCTION

1.1 Introduction

Obtaining information concerning the internal structure of an object, without affecting its original nature, is of great interest in non-invasive medical diagnosis and remote sensing. The information desired is the distribution of some physical property like density, absorption coefficient, resistivity or brightness. This information can be determined using strip integrals deduced from appropriate physical measurements. A set of such integrals measured over strips within a plane through the object, corresponding to one particular angle of view, is known as a **1-D** projection, as illustrated in Figure 1.1.

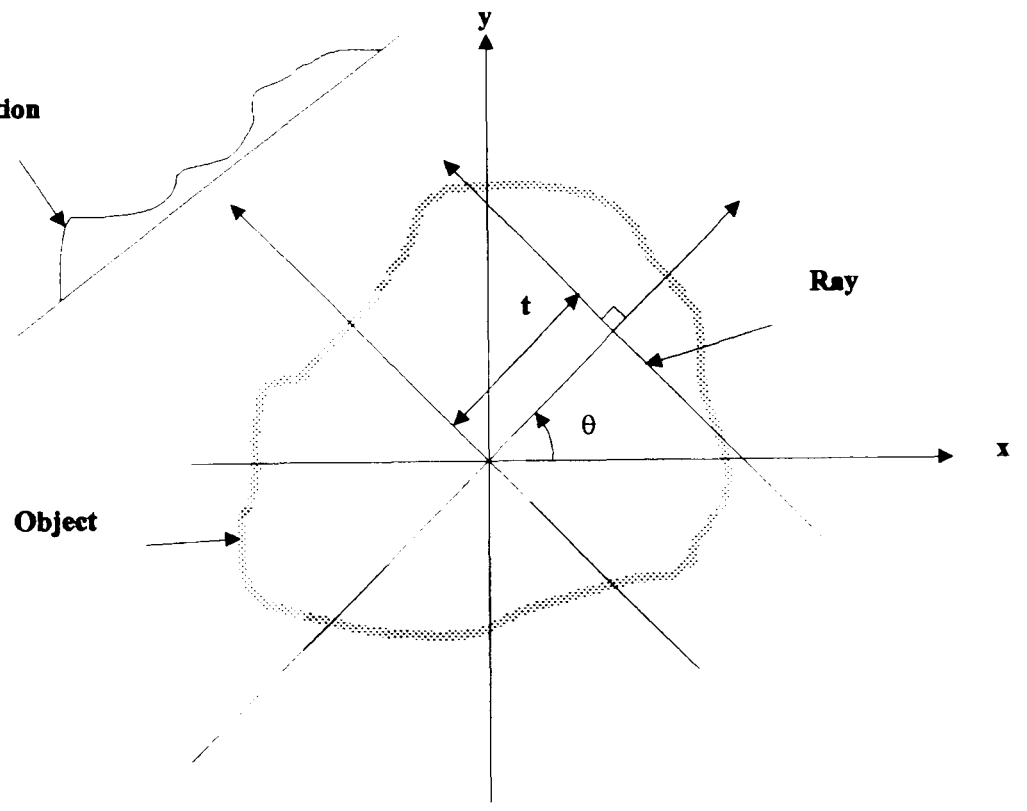

Figure 1.1 An object $f(x,y)$, and its projection

To obtain an estimate of the corresponding two-dimensional image, a set of **1-D** projection data corresponding to several strip integral measurements of an object at different angles of view is required. This technique is known as image reconstruction

from projections, or Tomography (from the Greek, Tomos (**tomos**) = slice).

Applications for this range from electron microscopy used to reconstruct the two-dimensional (**2-D**) Impurity Profiling [1.1] to radio astronomy reconstruction of X-ray structures of supernova remnants. One of the largest and most important applications is in the area of diagnostic medicine [1.2].

1.1.1 Medical Imaging

Tomography (Medical Imaging) allows the examination of a patient with no invasive action. In 1979, Allan N. Cormack and Godfrey N. Hounsfield jointly received the Nobel prize in medicine for their pioneering work in this field. In medical imaging a number of different camera systems have been developed. No one system is suited for all applications, all having advantages and disadvantages pertaining to their radiation source. The first tomography camera utilised X-rays, allowing the production of images of brain slices from multiple X-ray projections. In this technique, known as X-ray Transmission Computerised Tomography (TCT) [1.3][1.4], the radiation source is external to the object under examination. Attenuated distribution is determined by various slices of the human body from X-ray projections taken at several orientations. This gives the ability to separate structures and distinguishes between regions with very similar transmittance properties. If the radiation source is placed internally, information can be obtained concerning in vivo biochemical processes, e.g., the accumulation of a radiopharmaceutical substance within the body. This field is known as nuclear medicine.

1.1.2 Nuclear Medicine

The aim of nuclear medicine is to make quantitative measurements of the dynamic chemistry and flow physiology. This involves the detection of radiation emitted by a pharmaceutical substance labelled with a specific radionuclide, such as Tc-99m, I-123, C-11, O-15, or F-18. The radiopharmaceutical substance is generally

injected into the patient and localises within one or more organs depending on its biochemical properties. Hence, particular radiopharmaceuticals are used to evaluate specific organs, physiologic functions, or pathologic processes. This technique is known as emission computer tomography (ECT) [1.5]. Two alternative camera systems can be used. The first is known as Positron Emission Tomography (PET) [1.6], which uses radioisotopes that decay by emitting a positron. This travels a short distance (a few millimetres) before colliding with and annihilating an electron to produce two photons that travel in opposite directions from the point of annihilation. Two detectors, positioned on opposite sides of the patient, determine where the annihilation took place. To reduce the noise within larger source distributions, systems are under development using the Time-Of-Flight (TOF) methodology [1.7].

The second is called Single Photon Emission Tomography (SPECT), and differs from PET in the radioisotope used. Only a single photon is emitted. The direction of the ray can be determined only by using collimators. ECT systems all suffer from the problem of obtaining sufficient samples due to the lead collimators used to separate the detectors. The new systems use diatomic motions [1.8] to increase the number of samples. The gamma ray emission from the annihilation is attenuated by the tissue density, which requires compensation. Both of these instruments are known as gamma cameras.

1.1.3 Magnetic Resonance Imaging

Magnetic Resonance Imaging (MRI), [1.9][1.10] is one of the later additions to the reconstruction methods. The MRI scanner surrounds the body with powerful electromagnets, supercooled by liquid helium, which create a magnetic field 60,000 times as strong as that of the earth, (in the range of 0.3 to about 2.0T). At every point in the object this field causes a preference for the intrinsic spin angular momenta of the protons to be aligned parallel to the magnetic field, rather than the antiparallel direction. The energy difference between these two states corresponds to

electromagnetic radiation at the so-called "Larmor" frequency. For a magnetic field of 1.5T the Larmor frequency for protons is 63 MHz, a frequency that changes proportionately with the magnetic field strength. This net preference for spins to be parallel to the field in turn causes every point in the object to have a net magnetisation vector aligned in the same direction. When radio-frequency radiation is applied at the Larmor frequency in a direction perpendicular to the principal magnetic field, the magnetisation vector at each point tends to rotate away from the parallel direction. The actual nutation angle varies linearly with the amplitude and direction of the RF pulse. These pulse characteristics can be adjusted by the operator to obtain the desired nutation angle. Upon termination of the pulse the magnetisation then recovers back toward the parallel direction with a time constant of t_1 (the longitudinal relaxation time). Simultaneously, the component of magnetisation in the transverse plane tends to decrease with a time constant of t_2 (the transverse relaxation time). Any magnetisation tilted from the parallel direction rotates about the parallel axis at the Larmor frequency. This forms the basis for the measurement of the signal. The component of magnetisation rotating in the transverse plane at the Larmor frequency induces an EMF in a receiver coil. It is only the transverse magnetisation that is the measurable quantity in magnetic resonance. The magnetisation at each location in the object is determined by spatially encoding the received signal in such a way that its spatial dependence can be decoded. In MRI the magnetic gradients are used.

The techniques for obtaining images are classified into reconstructive and non reconstructive. The first method obtains images by taking projections of a particular slice of the body from the Fourier transforms of the MRI signals recorded in gradients directed at different orientations around the body. The two dimensional nuclear spin distribution of the slice is obtained by standard reconstruction algorithms. The second method is to obtain the images directly from the Fourier transforms of the appropriately recorded MRI signals that give the spin density along lines or alternatively at the single points of the image.

1.1.4 Ultrasonic Imaging

The next method for obtaining data for reconstruction is the use of ultrasonic techniques [1.11]. The generation of images from acoustic structures of the body tissue relies on the use of short acoustic pulses generated by a transducer, and on the measurement of the returning acoustic waves, echoes from the irradiated tissue. Typically the carrier-wave frequencies are in the range 2.5 to 10 MHz. The waves are progressive compressional waves that are transmitted by particle displacements with their associated variations in local pressure and density. [1.12]. Commercial systems for adults have wavelengths of about 0.7 mm, and transducer dimensions of about 12mm. The sound velocity varies according to the density and elasticity of the medium, varying from 1540 m/s in human soft tissue to over 4100 m/s in bone. Substantial noise can be encountered which is related to the scanning system. A conventional real-time two-dimensional echocardiogram (2DE) uses data from a single section (slice) through the heart, and displays grey scale images at the rate of 30 frames/s. Some systems use a single transducer or a dynamically focused annular array that is mechanically swept through a sector. Other systems adopt a phased linear array which electronically dynamically focuses within a sector from a fixed transducer position. Each system produces an image representing ultrasonic backscatter within a plane [1.13]. Three types of signal processing are used. Reflected signals produce backscatter images, transmitted signals produce attenuation and time-of-flight images [1.14][1.15].

1.1.5 Silicon Imaging

The tomography field is not confined to medical imaging. In the processing of integrated circuits (IC) the need for information regarding the diffusion phenomena in two dimensions has often been stated [1.16]. The fabrication process has seen a drive towards smaller geometries in the submicron region which has made it necessary to extend accurate modelling of both fabrication processes and devices to two and three dimensions.

This requires reliable device simulators. The common approach in simulation is to extract the results from the **1-D** process simulation and extend these to two dimensions. This approach is not satisfactory because the **2-D** shapes of the impurity profiles of the source and drain of a MOSFET strongly influence various effects like punchthrough, hot electron effects and the effective channel length of the device. A new technique has been developed [1.16] which reconstruct the **2-D** diffusion profile in silicon from a series of **1-D** measurements, using algorithms developed in estimation theory and previously applied to ECT. The problem of measuring the **2-D** distribution of dopants in silicon is very similar to the problem of image reconstruction in medical diagnostics, as both problems involve the estimation of the distribution of some quantity within a certain area.

1.1.6 Radioastronomy

Reconstruction methodologies have also been applied by Bracewell [1.17] in radioastronomy. **2-D** brightness distribution of a radio emitting body is useful to ascertain the nature of extra-territorial matter. Radio telescopes with narrow viewing aperture are used to receive radiation from a narrow strip of the sky. This corresponds to a strip integral of the two dimensional brightness distribution. As the earth rotates a set of strip scans in the same direction is obtained, corresponding to one projection. The scans are arranged at successive progressively advancing orientations. Projections at different views are accumulated from which the two dimensional bright image is reconstructed.

1.1.7 Electrical Impedance Tomography

The last method considered in this section is known as electrical imaging. It is a recent addition to the data collection methods used in tomography. Brown and Seagar [1.18] developed a system that uses the electrical impedance of various tissues within the human body to produce tomographic image maps of the resistivity distribution.

Applied Potential Tomography (APT) is the common name for this technique but other phrases are also used including electrical impedance imaging, conductivity imaging, impedance computed tomography and Electrical Impedance Tomography (EIT). The methods for obtaining tissue resistivity using two or four-electrode systems [1.19] are based on assumptions concerning the distribution of potential within a conductor volume when a constant current is applied to the electrodes. They require solutions of Laplace's and Poisson's equations, and are often referred to as the forward problem as opposed to the inverse problem of determining the spatial distribution of resistivity from measurements of surface potentials. The reconstruction problem is one of obtaining a solution to the inverse problem. This method will be considered in greater detail in later Chapters, as it is the objective of this research to develop reconstruction algorithms for the EIT system.

1.2 Mathematical Background

The earliest known mathematical work in image reconstruction from **1-D** projection data was established by Radon [1.20]. He determined that the cross sectional function of an object can be reconstructed exactly by an inversion formula using the measurement of line integrals of the cross section function. The function defined by the line integrals is known as the Radon transform of the cross section function. Thus, the transform which produces the projection from the image is called the Radon transform. A solution to this problem, developed in the early 1920's, is the summation method shown in the Chapter two. This method is simple but inaccurate and is implemented by simply backprojecting the projection data. Since then the 70's and 80's have seen a great deal of progress, but the most popular of these methods is still based on this early method. Although Radon is commonly acknowledged as the first to develop the mathematical foundation of tomography techniques, the measurement of distribution of resistivity developed by Frank Wenner [1.21] has origins dating to 1915. The early history of tomography can be found in Klotz [1.22]

and Littleton [1.23] who give examples that employ coded apertures for simple focusing techniques for singling out a specific layer. This technique was used before the advent of computer tomography (CT) and is sometimes called reconstructive tomography to distinguish it from other kinds of tomography.

Historically the reconstruction problem has been divided into two distinct and mathematical dissimilar classes of algorithms. Recently a third class has appeared, which is defined as optimisation. Its development can be closely linked with that of the Algebraic Reconstruction Technique (ART) algorithms [1.24].

The first approach is defined as the Transform method [1.25]. These reconstructions are based on analytic inversion formulae. The most common of all the Transform methods is the convolution back-projection algorithm. The map of the linear attenuation coefficients is reconstructed by backprojecting transmission projection data convolved with a spatial frequency filter [1.26]. The same reconstruction can be obtained by a **2-D** Fourier transform of the function that is made up of the **1-D** Fourier transforms of the projections, arranged along appropriate diagonals in the frequency space [1.27].

The second approach begins with an arbitrarily chosen sectional distribution that is then adjusted iteratively until the projections of the adjusted picture match the measured projections, subject to a specific criterion defining the acceptability of the reconstructed image [1.28]. The selection of the picture matching criterion is of key concern, as there is an infinite number of pictures having the same finite projection data, and the theorem defined by Herman [1.28] states that when the projection data set is noisy, there is no picture whose projections exactly match the measured projections. The iterative solutions require theoretical approximations for convergence to take place. These iterative techniques also require solutions to systems which yield large matrices, as a result the Convolution method [2.9] is favoured in many systems used today.

The third approach is based on the formulation of the reconstruction problem,

using constrained optimisation with the available projections used as constraints. This approach was first introduced as a Lagrange multiplier method by Goutis and Durrani [1.29], and has the advantage of combining the accuracy of ART with the speed of the convolution algorithm. A similar approach was also taken by Wood and Morf [1.30]. Their development of a fast implementation of a Minimum Variance Estimator yields a similar solution to that of Goutis and Durrani [1.29]. The main research presented in this thesis is an extension of the constrained optimisation approach for EIT.

1.3 Geometries and Governing Equations for Measurement Acquisition

In image reconstruction, the term geometry is generally used to define the properties of the radiation distribution through the medium under examination. To define a measurement geometry, and hence obtain a set of data for the reconstruction of an image, a solution to the Forward problem is required. The term Forward problem is used to described the general problem of finding the boundary values of an object, given the internal parameters. The solution to the Forward problem will depend on the radiation source used to illuminate the object under investigation, and is defined by governing equations. This radiation source need not be X-rays, as in the case of EIT. The solution to the Forward problem in X-ray systems is well known, but this is not the case in EIT, and various methods are used to obtain it. These are detailed in later Chapters. In this section, the measurement geometries applicable to the algorithms examined in this thesis are considered.

1.3.1 Parallel and Fan Beam

In TCT, two geometries for data collection have been adopted. These are known as parallel and fan beam as indicated in Figures 1.2 and 1.3 respectively. The data collection for fan beam is faster than parallel, as it involves less mechanical moving parts.

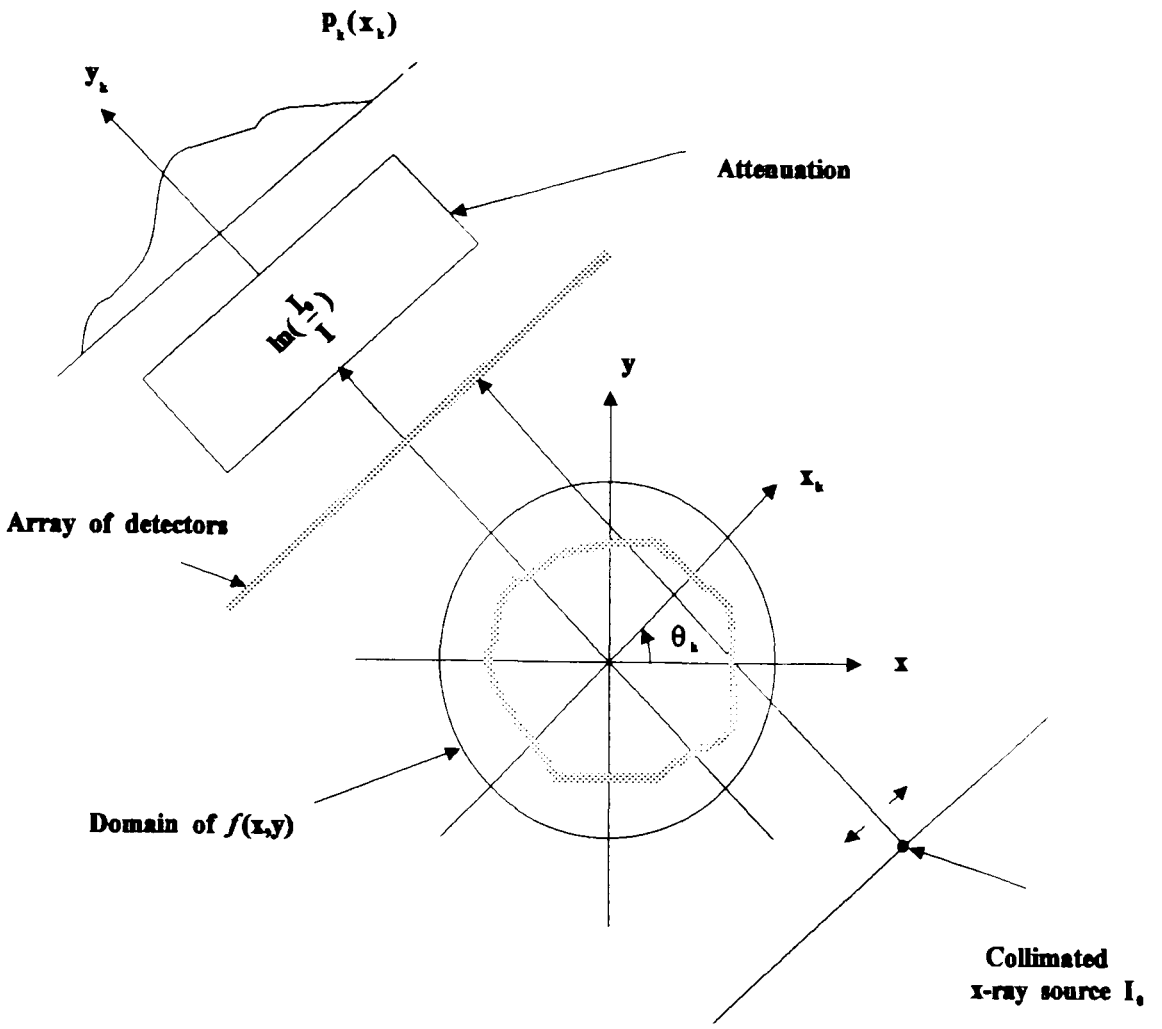

Figure 1.2 Parallel beam co-ordinate system where θ_k is the angle of rotation

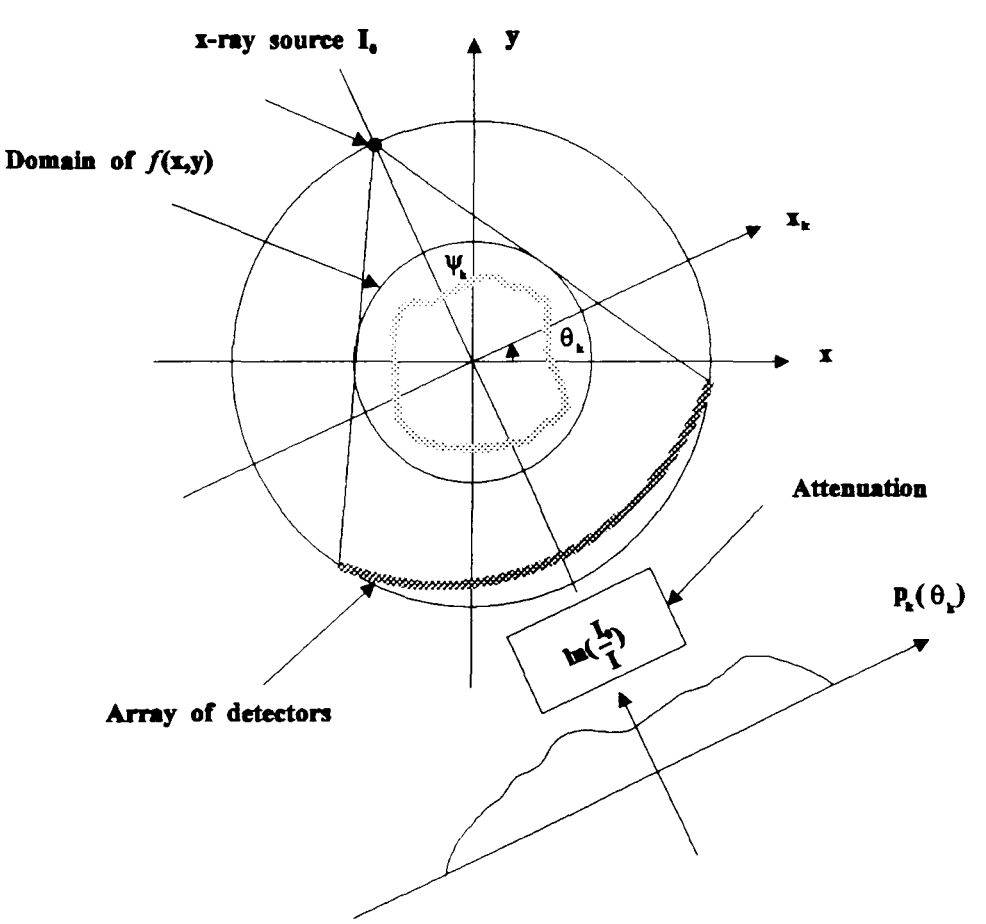

Figure 1.3 Fan beam system where θ_k is the angle of rotation

For the parallel beam co-ordinates the attenuation of an X-ray along a line is given by the general formula:

$$\mathbf{I = I_0 \exp(-\int_{l(x_k)} f(x,y)dy)} \qquad \mathbf{(1.1)}$$

Where $\boldsymbol{f(x,y)}$ is the cross section attenuation function, $\mathbf{I_0}$ is the intensity of the transmitted X-ray, $\boldsymbol{l(x_k)}$ is the integration length, and $\mathbf{x_k, y_k}$ are the rotated Cartesian co-ordinates defined as:

$$\begin{bmatrix} \mathbf{x_k} \\ \mathbf{y_k} \end{bmatrix} = \begin{bmatrix} \mathbf{\cos\theta_k} & \mathbf{\sin\theta_k} \\ \mathbf{-\sin\theta_k} & \mathbf{\cos\theta_k} \end{bmatrix} \begin{bmatrix} \mathbf{x} \\ \mathbf{y} \end{bmatrix} \qquad \mathbf{(1.2)}$$

Rearranging the equation (1.1) we can define the line integral of $\boldsymbol{f(x,y)}$ as:

$$\mathbf{p_k(x_k) = \ln \frac{I_0}{I} = \int_{l(x_k)} f(x,y)dy_k} \qquad \mathbf{(1.3)}$$

The estimation of $\boldsymbol{f(x,y)}$ from the projection measurements $\mathbf{p_k(x_k)}$ constitutes the reconstruction problem. The above definition is suitable for most reconstruction problems and forms the basis for most of the past reconstruction techniques. The work presented in this thesis is concerned with the application of specific algorithms to measurement systems that require models different from the one presented above. Their geometries do however have similarities to the X-ray parallel and fan beam geometries.

1.3.2 PET

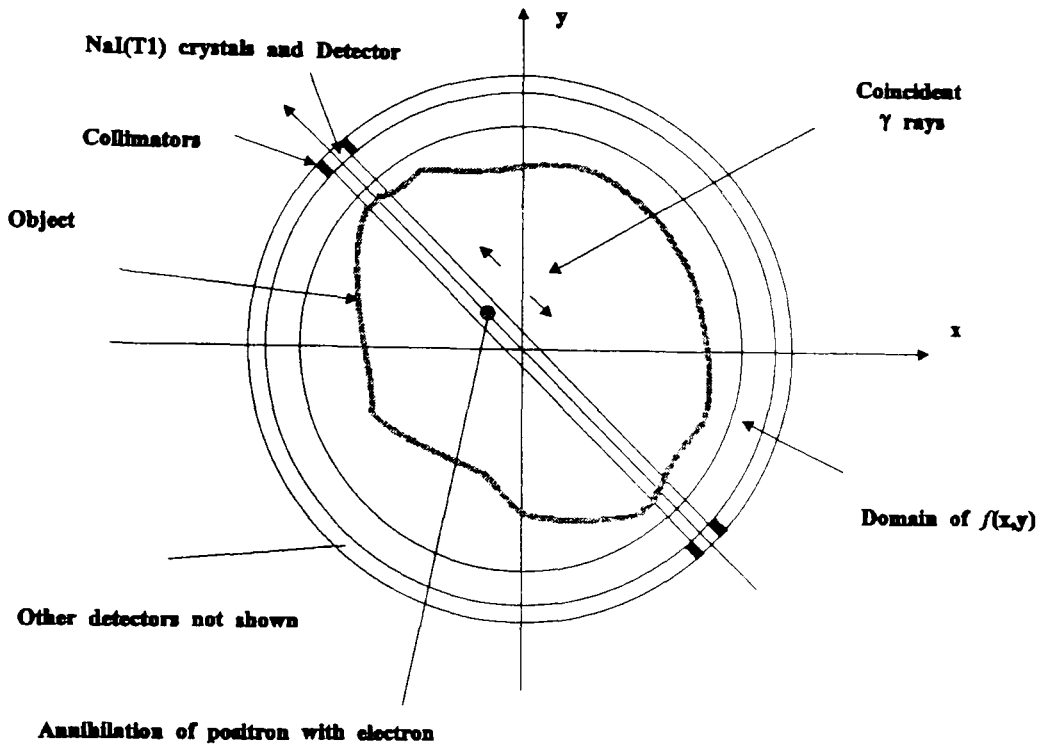

Figure 1.4 PET Geometry

The PET geometry illustrated in Figure 1.4 differs from the X-ray systems. The source of emission is derived from the internals of the object by means of positron radioisotopes. A major goal of both PET and SPECT, is to extract from the image data accurate measurements of source concentrations within regions as small as possible. The problems associated with absolute quantification are difficult to solve completely. However, within limits, a reasonable quantification is possible. The radiation emitted from within the object is attenuated giving a measurement model [2.35]:

$$\mathbf{p_k(x_k) = \int_{l(x_k)} f(x,y) e^{\left(-\int_{l(x_k)} \mu(x,y)\,dy_k\right)}\, dx_k} \qquad \mathbf{(1.4)}$$

1.3.3 EIT

The geometries defined in the previous section are related to the original research associated with Constrained Optimisation. These systems have well defined governing equations and the behaviour of the radiation as it passes through the

medium is well understood. In this research the objective is to apply the Constrained Optimisation approach which is detailed in Chapter four, to EIT. In EIT (illustrated in Figure 1.5) the image is a map of the resistivity, or conductance distribution, within a **2-D** circular region, surrounded by a medium of effectively infinite resistivity.

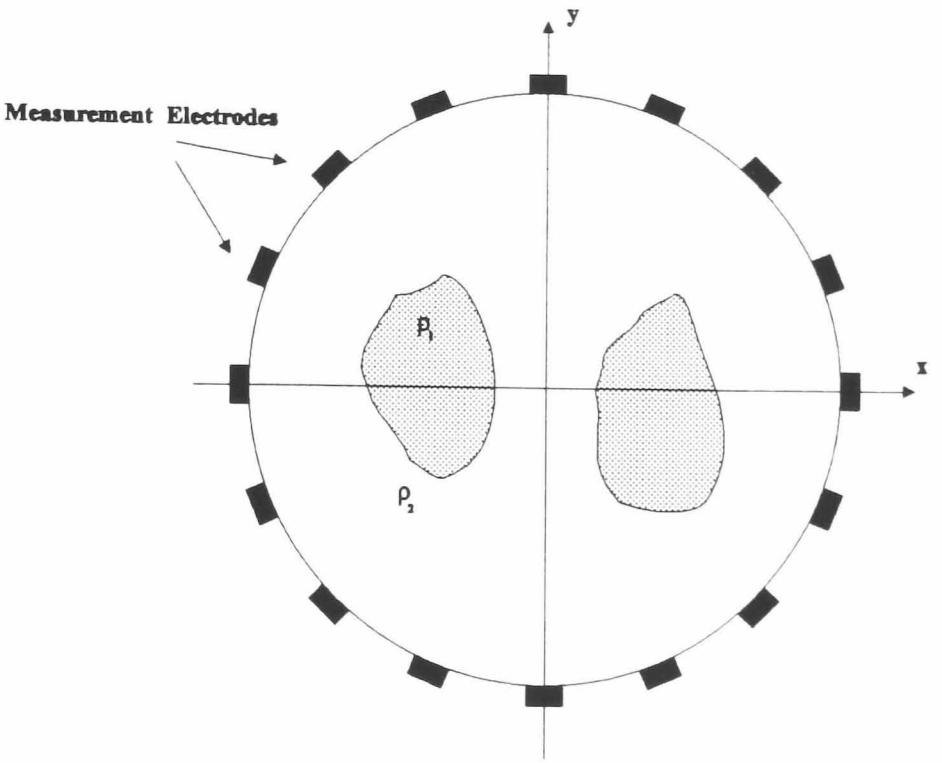

Figure 1.5 EIT system with idealised measurement configuration

If the medium is assumed to have an isotropic resistivity and is of known overall shape **D**, then the requirement is to obtain a theoretical model for resistance distribution within a **2-D** circular region surrounded by a medium of effectively infinite resistivity. Figure 1.5 shows the idealised measurement configuration with equally spaced electrodes. If a current is passed between an electrode pair it causes a current to flow within the region, in the low-frequency limit. The current field **J** and the electric field **E** are constrained by Kirchhoff's laws:

$$\underline{\nabla}.\mathbf{J} = 0 \qquad \text{and} \qquad \underline{\nabla}.\mathbf{E} = 0 \tag{1.5}$$

and by Ohm's law:

$$\mathbf{J} = \sigma \mathbf{E} \tag{1.6}$$

in which σ is the conductivity and:

$$\underline{\nabla} \equiv \hat{\mathbf{i}} \frac{\partial}{\partial x} + \hat{\mathbf{j}} \frac{\partial}{\partial y} + \hat{\mathbf{k}} \frac{\partial}{\partial z} \tag{1.7}$$

which is known as the Poisson operator. If it is assumed that the body is locally isotropic, then σ is a positive real number. Since $\underline{\nabla}.\mathbf{E} = 0$ has the form:

$$\mathbf{E} = -\underline{\nabla} V \tag{1.8}$$

where V is the voltage, equations (1.5) to (1.8) can be defined as a single elliptic equation for the distribution of the electric field within the region. This is known as Poisson's equation :

$$\underline{\nabla}.(\sigma \underline{\nabla} V) = 0 \tag{1.9}$$

When σ is known, V, $\mathbf{E}$, and $\mathbf{J}$ are completely determined by either the boundary voltage $V|_{\partial D}$, or the boundary current:

$$\sigma \frac{\partial V}{\partial n} = \mathbf{J}_n \Big|_{\partial D} \tag{1.10}$$

where $\mathbf{n}$ is the outward unit normal to $\partial \mathbf{D}$. For the analysis presented above, the complexity of equation (1.9) was reduced by the assumption that there are no current sources within the body, hence it can be set to zero. This is reasonable as the injected currents are applied at a frequency of **50kHz**, and there are no intrinsic current sources that have been observed at this frequency. For a homogeneous medium, σ is a constant and the governing equation can be further reduced to Laplace's equation:

$$\Delta V = 0 \tag{1.11}$$

where

$$\Delta = \underline{\nabla}.\underline{\nabla} = \frac{\partial^2}{\partial x^2} + \frac{\partial^2}{\partial y^2} + \frac{\partial^2}{\partial z^2} \tag{1.12}$$

is the Laplace operator.

If the current is passed between a particular pair of electrodes, a potential is developed along the boundary. The voltage will depend on the resistance within the region. For a unique reconstruction of the resistance distribution, all the boundary profiles are required. Other boundary profiles are obtained by passing current between other pairs of electrodes. Unlike the geometries of the X-ray systems, in EIT the solution to the Forward problem or geometry has to be found before the reconstruction of the resistivity of the region can be attempted. Another problem with EIT is that the assumption that the resistivity of the medium is homogenous does not hold true. A more detail analysis of the EIT system is given in Chapter three.

1.4 Computer System and Dedicated Hardware for Reconstruction

The systems for data acquisition for tomographic reconstruction algorithms typically take from several seconds to several minutes for each slice volume. The reconstruction times also vary greatly, typically in the range of seconds to minutes. Some advanced systems allow data to be acquired rapidly, in some cases at video frame rates. This allows the visualisation of moving structures such as the beating heart. Images are reconstructed after data acquisition, and displayed sequentially in a continuous loop to provide a dynamic display of time varying events. This has been termed "cine" tomography because, similar to a movie, dynamic events are recorded and visualised retrospectively. To view dynamic events as they occur and create "videographic" tomography reconstruction, reconstruction must be performed in real time. One of the main advantages of viewing the tomographic image in real time is the ability to use the systems interactively. There are two main parts of the reconstruction

system that must be considered for the goal of real time reconstruction. First, the acquisition of the data by the collection system, and second, the reconstruction procedure adopted. The CT projection data can take **30-50ms** to obtain, which would allow continuous data acquisition of **30** frames per second. The reconstruction procedure requires a large amount of computation. Reconstruction of **30** frames per second is extremely demanding and beyond the capability of present day serial computer systems, and requires parallel computer systems to achieve the desired performance.

The reconstruction requirements are limited by the current state of computer systems and technology development. The majority of computer systems and VLSI devices populating medical imaging systems [1.31], perform general computational tasks. These systems allow vector operations of real and complex dot product, real or complex addition, and other complex arithmetic operations to be invoked by a single instruction. There is a need for special purpose hardware to allow real-time operation of the reconstruction algorithms. The convolution back-projection technique for image reconstruction that is described in Chapter two is an ideal candidate for hardware implementation. Authur *et al.* [1.32] describe a system that uses digital signal processing chips to implement a digital convolver as a basic building block. The chip implements a Finite Impulse Response (FIR) filter with **8** taps and **4** bit precision in both the data and kernel. Each chip has **8**(**4**-bit x **4**-bit) multipliers and **8**(**13**-bit) accumulators with delay elements between the accumulators. The chips can be cascaded to implement longer kernels. The results obtained by Authur *et al.* [1.32] demonstrate that video-rate image reconstruction using filtered back-projection algorithm is feasible. The back-projection operation is computationally the most costly part of the operation. In the solution described above, back-projection is implemented using an analogue optical system consisting of a display, an anamorphic optical system, and a video camera. The disadvantage with the system is that the contrast and resolution is limited.

1.5 Scope of Thesis

This Chapter has summarised the diversity of methods for obtaining data to reconstruct images from their projections. No one system can offer a complete solution. Some techniques are better suited to dynamic visualisation of processes, and others provide highly accurate images of static data. In recent years the new technique of EIT has offered the possibility of obtaining information about dynamic physiological processes without the use of destructive radiation. The technique is still in its infancy, as the way of relating the changes in resistivity to the physiological process is not fully understood. To assist in the development of this technique, sophisticated reconstruction algorithms are required.

EIT algorithms have been developed independently of other techniques due to the nature of the reconstruction problem associated with EIT. Where appropriate, developments in traditional tomography have been used in EIT. Not all approaches developed for traditional tomography have been applied to EIT. One such method is the Constrained Optimisation Reconstruction Technique (CORT).

1.5.1 Aims and Objectives of the Research

The aim of the research reported in this thesis is to apply the constrained optimisation technique to the EIT system, with the objective of improving the reconstruction quality of the measured resistive distribution. The selection of the reconstruction approach also requires consideration of performance in terms of computation efficiency. As EIT systems are designed to be low cost, most are implemented on PC's. To improve the performance of a system developed for this application, research was carried out on developing hardware for accurate reconstruction procedures.

Two problems exist in EIT: First the solution to the Forward problem and second, the inverse problem or reconstruction problem. In this research, the Forward problem is solved analytically using existing methods. The inverse problem is then

solved using the Lagrange multiplier method. As the finite number of boundary potential data points available do not fully specify the image, it is necessary to form a model to select the reconstruction. The advantage of the Lagrange multiplier method is that it is derived from constrained optimisation approach, which uses the projections as constraints. The reconstruction models can be chosen such that they optimise some property of the solution, rather than arising from assumptions made for computational simplicity. It will be shown that a number of assumptions can be made in EIT regarding the nature of the geometry to obtain images at real-time rates, and that these assumptions, which could reduce the quality of the reconstructed image, have a minimal effect.

1.5.2 Structure of Thesis

This thesis is presented in the following order. An initial overview is presented in the first Chapter, including defining the aims and objectives of the research. The next Chapter then reviews existing methods for reconstructions, defining a taxonomy of methods. Due to the large diversity of approaches, only the important methods are considered. The EIT methods are considered separately in Chapter three and comparisons between them and other methods are given where appropriate. The EIT problem differs in some respects from those tackled by traditional approaches, so the taxonomy defined in the second Chapter is not used to classify the different approach taken in the EIT case.

In Chapter four, a description of the constrained optimisation approach for the solution of the reconstruction problem is given, concentrating on the parallel X-ray system. Parallel geometry is used to clarify the concept behind the methodologies. Both primal and dual methods are considered. The approach to image reconstruction, in which the reconstruction problem is embedded into a constrained optimisation problem, is explored in detail.

The fifth Chapter develops the optimisation approach and examines the

algorithms previously developed for both parallel and fan beam systems in X-ray tomography. This allows identification of useful properties in the associated system matrices that can be exploited for the EIT system.

In Chapter six an exposition of EIT geometries is given. Two data collection methods are examined and new reconstruction procedures are defined.

The results are analysed in Chapter seven for both modelled data and data obtained from a hardware phantom. This Chapter demonstrates the effectiveness of the new EIT algorithms with ideal, noisy and undersampled data. Consideration is also given to the problems of current distribution within the medium under examination.

In Chapter eight the hardware aspects for the solution of the reconstruction problem are examined. Only the parallel geometry is considered, and it is demonstrated that there are feasible hardware possibilities for accelerating the computation of the reconstruction problem for EIT systems.

Finally, the overall objectives and the new contributions of this research are summarised in Chapter nine. This includes the outcomes, together with the conclusions drawn from the research and proposals for future developments.

2 RECONSTRUCTION METHODS

2.1 Introduction

Reconstruction techniques are generally classified into two main categories, dependent on the approach and starting constraints. These are transform methods and series expansion methods. A third category has recently been introduced called Constrained Optimisation. The selection of a category for a particular technique is not always clear, but the use of a classification scheme is useful and popular, as it allows a measure between methods in terms of quality and speed. This Chapter reviews the mathematical methods used to reconstruct the images and classifies them into the categories defined above. The EIT methods do not fit easily into either of these categories and are considered separately in Chapter three.

Before proceeding with a survey of reconstruction methods, it is convenient to define some of the terminology used in this section. The object to be reconstructed is represented by f. A path of integration (specified by $l(t,\theta)$) is referred to as a ray. The scanning geometry will be confined to a parallel system as shown in the previous chapter unless otherwise stated. The problem of reconstruction can then be defined as: given $\mathbf{p(t,\theta)}$, find $f(x,y)$ or $f(\omega,\theta)$ (polar co-ordinates).

2.2 Taxonomy

The following is a list of known methods of reconstruction which fall within the first two categories, defined above:

	METHOD	CATEGORY
i)	Radon	Transform
ii)	Backprojection (Summation)	Transform
iii)	Fourier	Transform

iv)	Convolution backprojection	Transform
v)	ART	Series Expansion
vi)	SIRT	Series Expansion
vii)	ILST	Series Expansion
viii)	CORT	Optimisation

2.2.1 Radon

In 1917, J. Radon [1.17] established the mathematical foundations of the reconstruction problem from projections, and hence the transform which produces the projection from the image is called the Radon transform. Radon determined that the cross-section of an object can be reconstructed exactly by an inversion formula, in terms of measurements that are the line integrals of the cross section function. The function defined by a complete set of line integral measurements is known as the Radon transform. To define this mathematically let $f(\mathbf{x},\mathbf{y})$ denote the function that represents the spatial distribution of some physical quantity in two dimensions. Although f is unknown, a priori, in most cases it is known that the distribution is spatially bounded, so that it vanishes outside a finite region of the **2-D** plane, which is denoted by **D**. Figure 2.1 shows the basic geometry of the reconstruction system used in the analysis.

It is sometimes more convenient to express f in terms of polar co-ordinates $(\mathbf{t},\theta)$, rather than Cartesian co-ordinates $(\mathbf{x},\mathbf{y})$ Let $\mathbf{p}(\mathbf{t},\theta)$ denote the integral of f along the line $l(\mathbf{t},\theta)$. Hence:

$$\mathbf{p}(\mathbf{t},\theta) = \int_{l(\mathbf{t},\theta)} f\mathbf{ds} \qquad \textbf{(2.1)}$$

where $l(\mathbf{t},\theta)$ is the line whose normal through the origin makes an angle θ with the

positive **x**-axis, and has length **t**, where $-\infty < t < \infty$. Hence $l(t,\theta)$ is the line

$$x\cos\theta + y\sin\theta = t \tag{2.2}$$

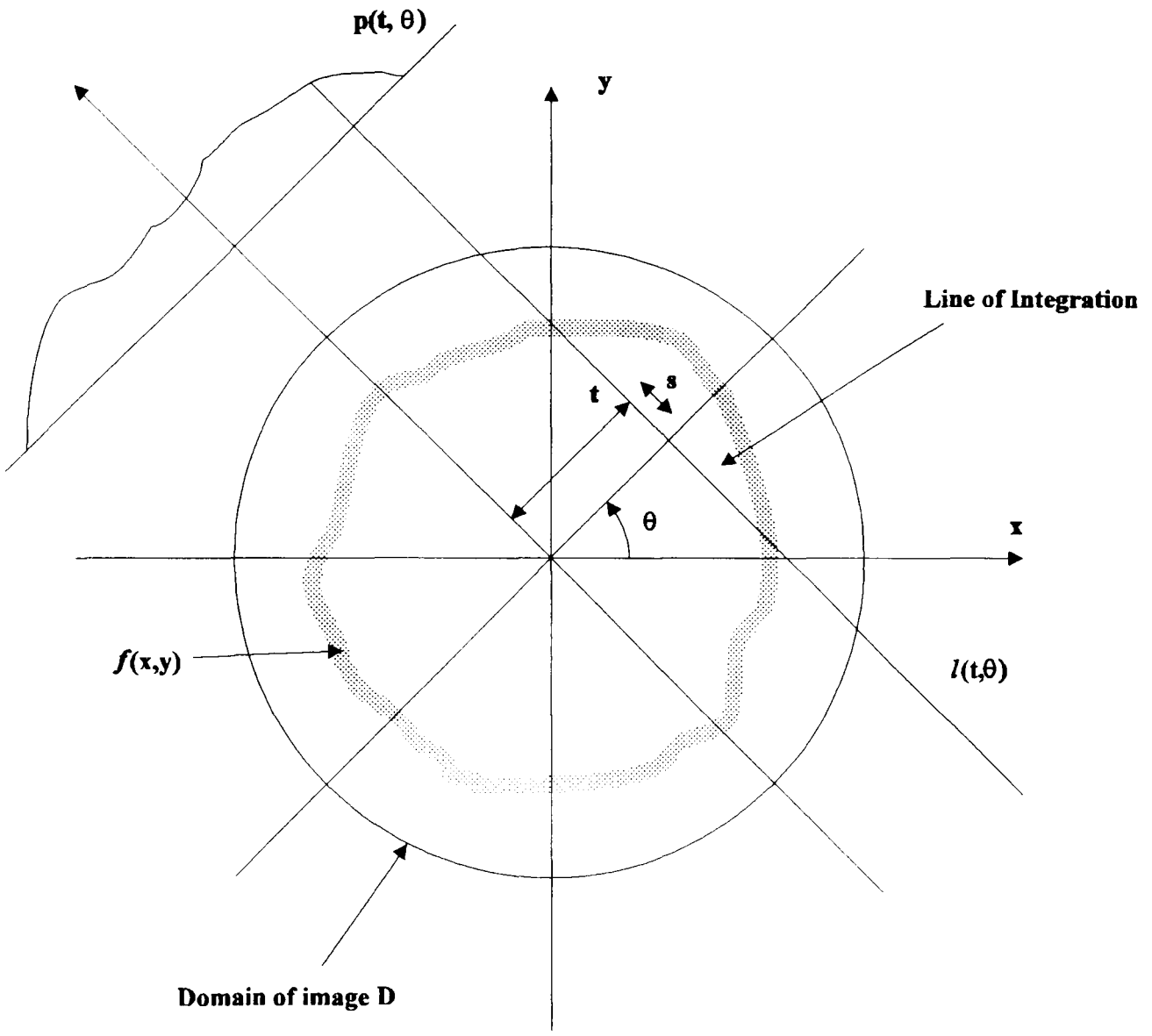

Figure 2.1 Projection Geometry

Using a delta function equation (2.1) can be rewritten as:

$$p(t,\theta) = \int_{-\infty}^{\infty}\int_{-\infty}^{\infty} f(x,y)\delta(x\cos\theta + y\sin\theta - t)dxdy \tag{2.3}$$

The function $\mathbf{p(t,\theta)}$ is known as the Radon transform of the function $f(t,\phi)$. Knowing the latter, the image $f(t,\phi)$ can be evaluated from the inversion formula:

$$f(t,\phi) = \frac{1}{2\pi^2}\int_0^{\pi}\int_{-\infty}^{\infty}\frac{\partial p(t,\theta)}{\partial t}\frac{1}{r\cos(\theta-\phi)-t}dtd\theta \qquad (2.4)$$

It would appear that Radon [1.17] had solved the reconstruction problem in 1917. However, there are practical problems in evaluating this integral. Radon's formula determines a picture from all its line integrals. In CT there is only a finite set of measurements. The measurement in CT can be used only to estimate the line integrals. Radon gave a mathematical formula, an efficient algorithm is required to evaluate it.

One of the first solutions to this problem appeared in the early 1920's is called the summation or backprojection method.

2.2.2 Backprojection (Summation) method

This simple method is implemented by summation of the intersection of the lines defined by the projections across a **2-D** surface. However, this method is inaccurate causing a blurred image. Despite the poor quality of the reconstructed image, the backprojection method is important, and most of the techniques used at present are based on improvements to this basic approach.

A brief analysis of this method is given in this section, as it forms the basis for the majority of the reconstruction algorithms in present use.

If **N** projections $\mathbf{p(t,\theta)}$ are available, then it is possible to obtain a reconstruction by the summation method [2.1] given by the formula:

$$\bar{f}(x,y) = \sum_{k=1}^{N} p(t,\theta_k) \qquad (2.5)$$

where $\bar{f}$ is the estimated image. This is represented diagrammatically in Figure 2.2 For each projection $\mathbf{p(t,\theta)}$, a **2-D** function is created by backprojecting (shifting the **1-D** function along the y_k axis). The summation of all the generated **2-D** functions

gives the estimated image.

The backprojection methods in various analogue and digital implementations have been proposed by a number of authors. A history of these methods can be found in Gordon and Herman [2.2]. The numerical evaluation of the integrals, and in particular the Riemann sums, are discussed in detail by Davis and Rabinowitz [2.3].

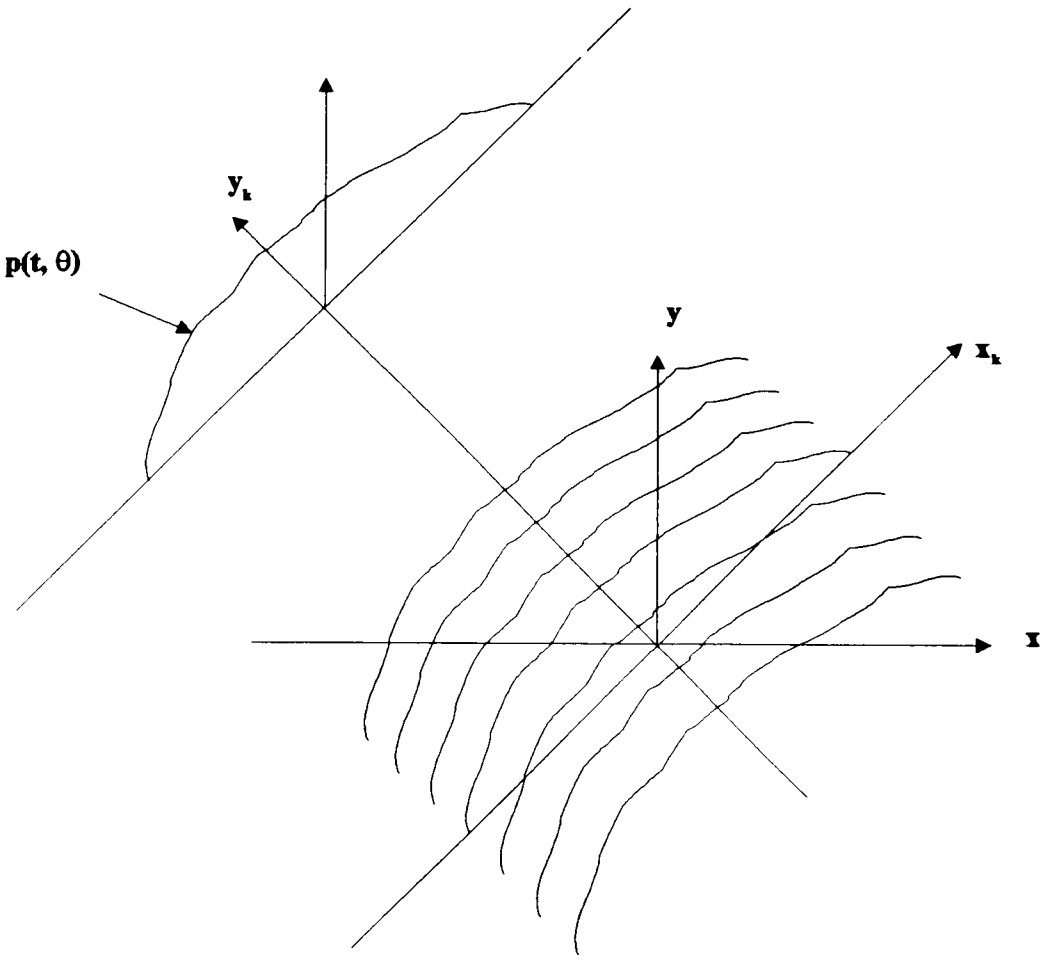

Figure 2.2 A 2-D function $f(x,y)$ produced by backprojecting the 1-D function $p(t,\theta)$ along y_k

2.2.3 Fourier

In 1956, Bracewell [2.4] discovered the projection (or central) Slice Theorem for bounded objects, which gives an exact solution using Fourier transforms. It was used to reconstruct the image of the sun in microwave radiation, from strip measurement by microwave antennas. Independently, DeRosier and Klug [2.5]

developed the same theorem for reconstruction of helical viruses from electromicrographs.

The Fourier method is based on the Projection Slice Theorem which is derived from the fundamental observation that the Fourier transform of a projection is a slice of the Fourier transform of its image. This is illustrated in Figure 2.3. and is derived mathematically as follows.

Consider the $(\mathbf{t},\mathbf{s})$ co-ordinate system illustrated in Figure 2.1 to be a rotated version of the original $(\mathbf{x},\mathbf{y})$ system expressed by:

$$\begin{bmatrix} \mathbf{t} \\ \mathbf{s} \end{bmatrix} = \begin{bmatrix} \cos\theta + \sin\theta \\ -\sin\theta + \cos\theta \end{bmatrix} \begin{bmatrix} \mathbf{x} \\ \mathbf{y} \end{bmatrix} \tag{2.6}$$

In the (t,s) co-ordinate system a projection along lines of constant $\mathbf{t}$ is written

$$\mathbf{p(t,\theta)} = \int_{-\infty}^{\infty} f(\mathbf{x},\mathbf{y})\mathbf{ds} \tag{2.7}$$

Its Fourier transform is given by:

$$\mathbf{P(\omega,\theta)} = \int_{-\infty}^{\infty} \mathbf{p(t,\theta)e^{-j2\pi\omega t}dt} \tag{2.8}$$

Substituting the definition of a projection into the above equation 2.8 gives:

$$\mathbf{P(\omega,\theta)} = \int_{-\infty}^{\infty} [\int_{-\infty}^{\infty} f(\mathbf{t},\mathbf{s})\mathbf{ds}]\mathbf{e^{-j2\pi\omega t}dt} \tag{2.9}$$

This result can be transformed into the $(\mathbf{x},\mathbf{y})$ co-ordinate system by using the relationship given in equation (2.6). Hence:

$$\mathbf{P(\omega,\theta)} = \int_{-\infty}^{\infty}\int_{-\infty}^{\infty} f(\mathbf{x},\mathbf{y})\mathbf{e^{-j2\pi\omega(x\cos\theta+y\sin\theta)}dxdy} \tag{2.10}$$

The right side of the equation (2.10) represents the **2-D** Fourier transform of a spatial frequency of $(\mathbf{u} = \omega\cos\theta, \mathbf{v} = \omega\sin\theta)$. Hence:

$$\mathbf{P(\omega,\theta)} \Leftrightarrow \mathbf{F(\omega,\theta)} \Leftrightarrow \mathbf{F(\omega\cos\theta,\omega\sin\theta)} \tag{2.11}$$

which is known as the Fourier Slice Theorem. The above result indicates that by taking the projections of an object function at angles $\theta_1, \theta_2, .., \theta_k$ and Fourier transforming each of these, it is possible to determine the values of $\mathbf{F(u,v)}$ on radial lines as shown in Figure 2.3.

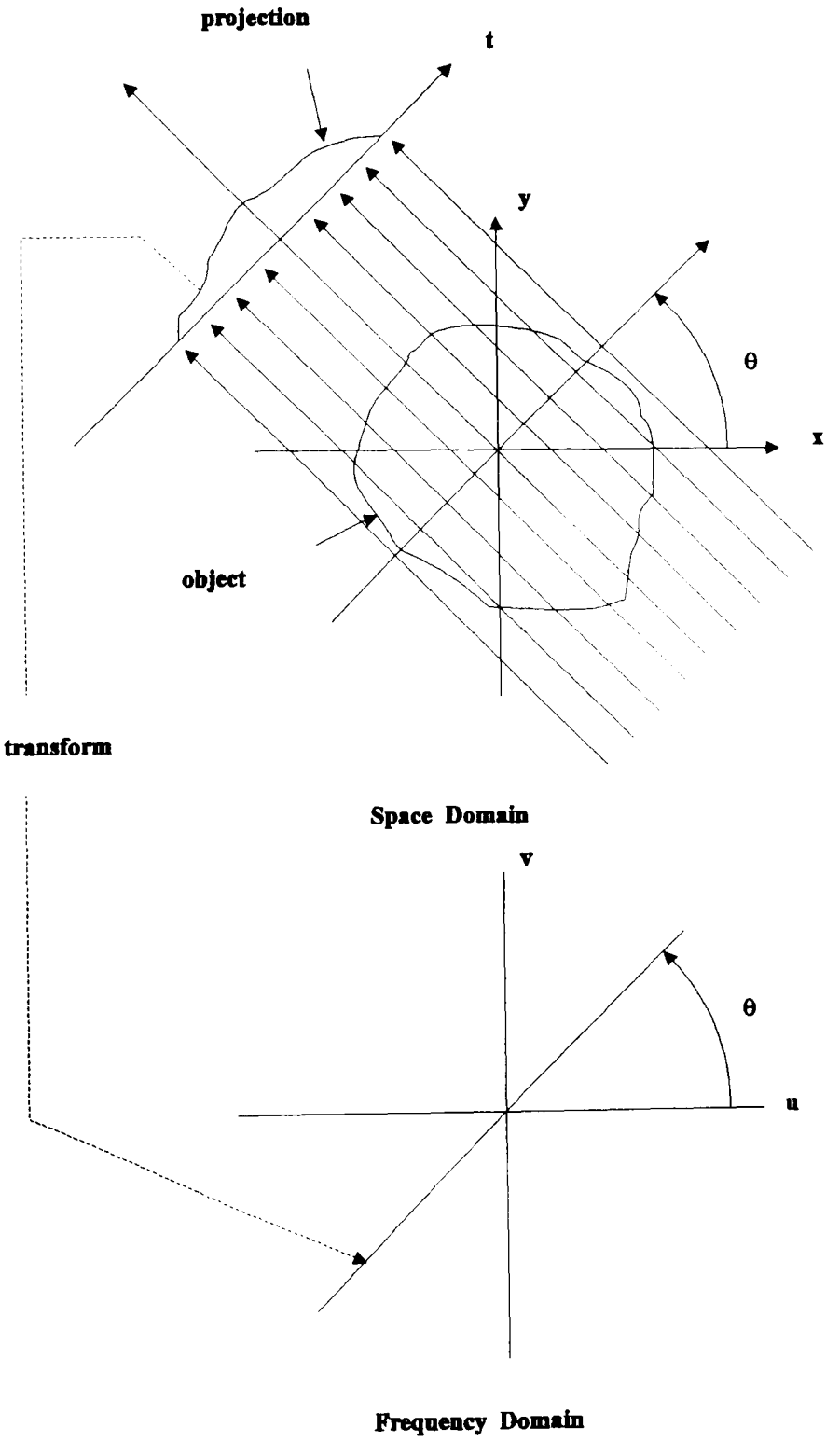

Figure 2.3 Illustration of the Fourier Slice Theorem

If an infinite number of projections is taken, then $\mathbf{F(u,v)}$ would be known for all points in the **u,v**-plane. The object function $\mathbf{F(u,v)}$ can be recovered by using the

Inverse Fourier transform:

$$f(x,y) = \int_{-\infty}^{\infty}\int_{-\infty}^{\infty} F(u,v)e^{j2\pi(ux+vy)}dudv \qquad (2.12)$$

If the function is bounded by $-\frac{D}{2} < x < \frac{D}{2}$ and $-\frac{D}{2} < y < \frac{D}{2}$, then the above can be defined as:

$$f(x,y) = \frac{1}{D^2}\sum_{m=-\frac{N}{2}}^{\frac{N}{2}}\sum_{n=-\frac{N}{2}}^{\frac{N}{2}} F(\frac{m}{D},\frac{n}{D})e^{j2\pi((\frac{m}{D})x+(\frac{n}{D})y)} \qquad (2.13)$$

for

$$-\frac{D}{2} < x < \frac{D}{2} \quad \text{and} \quad -\frac{D}{2} < y < \frac{D}{2} \qquad (2.14)$$

All the Fourier-based methods are related to the above theorem. The reconstruction problem can be defined as approximating the **2-D** image Fourier transform, from the available discrete set of points on the polar raster, then performing an inverse **2-D** Fourier transform to find the unknown $f(x,y)$. The Discrete Fourier Transform (DFT), is used to obtain the inverse transformation samples of the image Fourier transform on a Cartesian raster. These are obtained by interpolating the known polar raster samples.

The limitation of samples available, due to factors of scanning geometry and computation time, can cause aliasing artefacts to be present in the reconstructed image. It is possible to determine the N^2 coefficients required in equation (2.13), provided as many values of the function $F(u,v)$ are known on some radial lines [2.6]. The calculation involves solving a large set of simultaneous equations. This often leads to unstable solutions, due to small errors introduced when solving these large systems.

As there are a finite number of projections obtained from the scanning geometry, the function $F(u,v)$ is known only along a finite number of radial lines as shown in Figure 2.4. To implement equation (2.13) the radial points must be interpolated to points on a square grid. Since the density of the radial points becomes

sparser further away from the centre, the interpolation error also becomes larger. This implies that there is greater error in the calculation of the high frequency components in an image, than in the low frequency ones, which results in some degradation of the image.

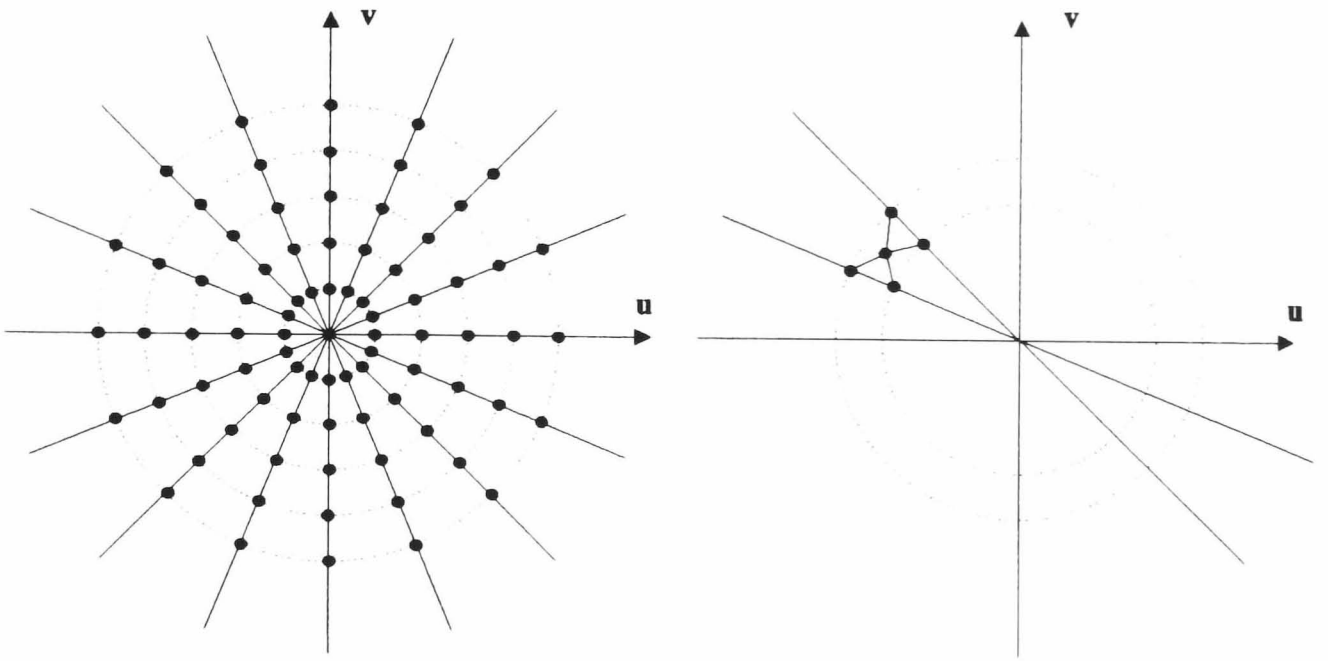

Figure 2.4(a) The polar raster of points in the Fourier space produced by computing the DFT of 8 projections with 11 samples per projection, (b) Nearest neighbour interpolation used to estimate Cartesian raster samples from the polar raster samples.

Another cause of artefacts in the reconstructions is known as Gibb's phenomenon, which is due to truncation of the Fourier domain. If the truncation is too abrupt, high-contrast features in the original object will be reconstructed with considerable overshoot and ripple. This implies aliasing in the spatial domain and presents itself within the image as noise. It is not possible to remove this effect completely, due to the limitation of the number of samples available, but improved reconstructions can be obtained by multiplying the projections by a window function. Window functions will be discussed in the Section 2.2.4.

An extension to the above methods is the 'rho filtered layergram' approach introduced by Smith [2.8]. It is an important method in the context of this research, as the main EIT reconstruction approach currently used is based on a variation of it. The rho-filtered layergram method attempts to deblur the picture that is obtained by backprojection alone. The method of debluring is based on the relationship between the **2-D** Fourier transform of a picture and the **2-D** Fourier transform of the backprojected Radon transform of the picture. The relationship is given by:

$$\mathbf{F}(\omega,\theta) = |\omega|[\mathbf{FT}[\mathbf{B}[\mathbf{R}f]]](\omega,\theta) \qquad \textbf{(2.15)}$$

For any point (ω,θ) with $\omega \neq 0$, where **B** denotes backprojection and **R** the Radon Transform, equation (2.15) gives rise to a four stage process for estimating f from the projection data $\mathbf{p}$. This process is detailed as follws:

a) Backproject $\mathbf{p}$, to obtain $\mathbf{Bp}$.

b) Calculate the **2-D** Fourier transform **FT[Bp]**.

c) Obtain a new function **F** of two polar variables by:

$$\mathbf{F}(\omega,\theta) = |\omega|[\mathbf{FT}[\mathbf{Bp}]](\omega,\theta) \qquad \textbf{(2.16)}$$

d) Estimate f by taking the inverse Fourier transform of **F**

$$\bar{f} = \mathbf{IFT}[\mathbf{F}] \qquad \textbf{(2.17)}$$

The result of the process of backprojection is sometimes known as a layergram. The concept of the rho-filtered layergram was introduced where the first polar variable of the **2-D** Fourier transform was denoted by the Greek letter ρ, and hence the operations described above are given this name. One of the main reconstruction algorithms developed for EIT is an adaptation of the rho-filtered layergram.

The relationship between the Image Radon and Fourier space is illustrated in Figure 2.5.

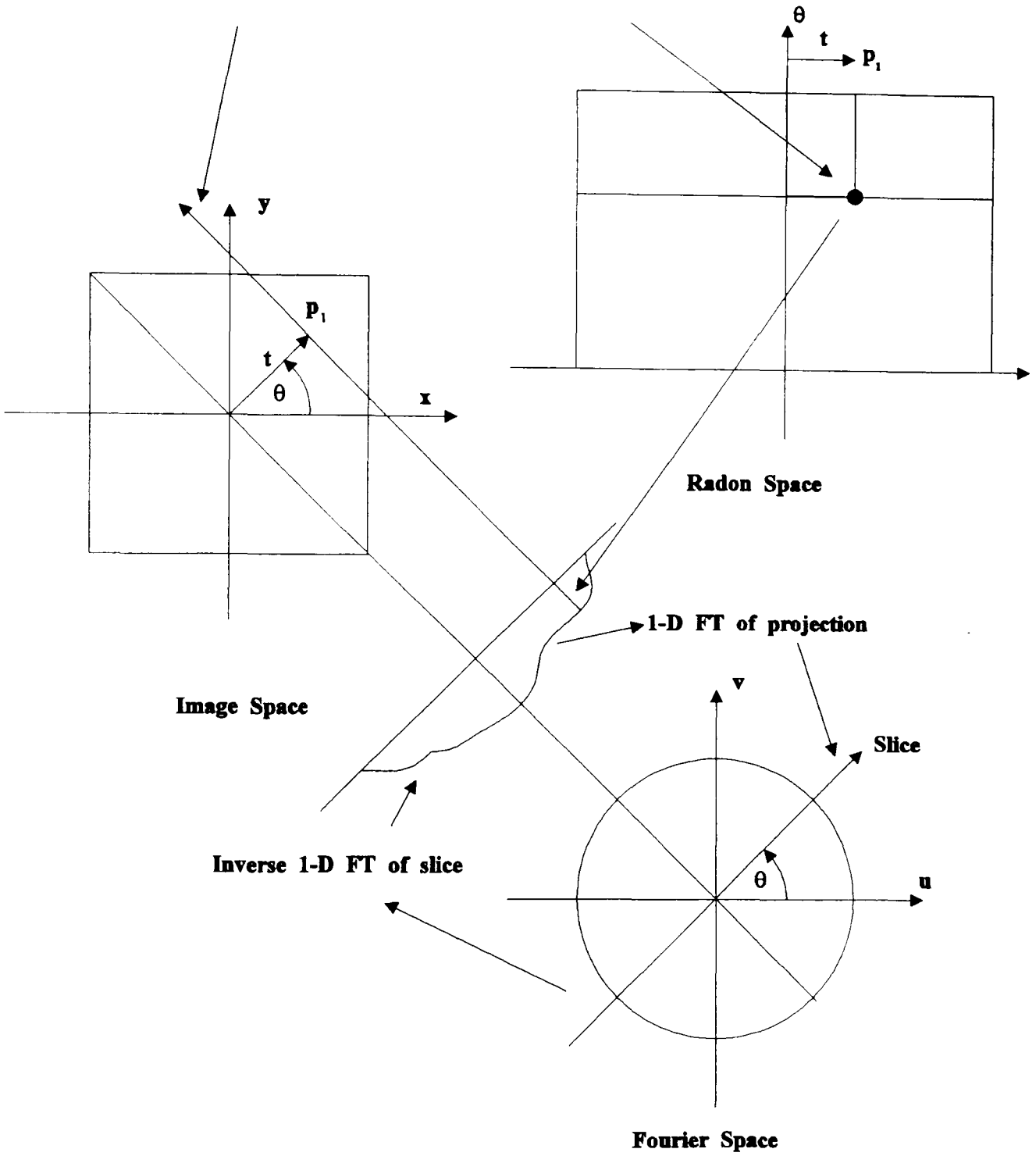

Figure 2.5 Image, Radon and Fourier space

2.2.4 Convolution

The convolution methods first developed by Ramachandran and Lakshminaryanan [1.24], and popularised by Shepp and Logan [2.9], are similar to the Fourier methods. The convolution method multiplies the **1-D** Fourier transform of each projection by the $|\omega|$ filter, and backprojects its inverse Fourier transform to produce

the reconstruction. This method is derived from the projection Slice theorem and can be viewed in the spatial domain as follows:

To reconstruct $f(x,y)$ at a point $Q(t,\theta)$ each $p(t,\theta)$ is multiplied, or weighted, by $2\pi|\omega|/N$. Therefore, $|\omega|$ represents the Jacobian for a change in variable between polar co-ordinates and the rectangular co-ordinates used in the Fourier transform.

A back projection algorithm can be derived from the projection slice theorem given in the previous section as follows:

If $p(t,\theta)$ is known for all the lines $l(t,\theta)$, then the inverse Fourier transform of the object function $f(x,y)$ can be expressed as:

$$f(x,y) = \int_{-\infty}^{\infty}\int_{-\infty}^{\infty} F(u,v)e^{j2\pi(ux+vy)}dudv \qquad (2.18)$$

Change the rectangular co-ordinate system for the polar co-ordinate system by using:

$$\begin{aligned} u &= \omega\cos\theta \\ v &= \omega\sin\theta \end{aligned} \qquad (2.19)$$

The differentials are replaced by:

$$dudv = |\omega|d\omega d\theta \qquad (2.20)$$

Equation (2.17) is rewritten as:

$$f(x,y) = \int_{0}^{2\pi}\int_{0}^{\infty} F(\omega,\theta)e^{j2\pi\omega(x\cos\theta+y\sin\theta)}\omega d\omega d\theta \qquad (2.21)$$

Splitting the integral into two by considering θ from 0 to π and π to 2π,

$$f(x,y) = \int_{0}^{\pi}\int_{0}^{\infty}\left\{F(\omega,\theta)e^{j2\pi\omega(x\cos\theta+y\sin\theta)} + F(\omega,\theta+\pi)e^{j2\pi\omega(x\cos(\theta+\pi)+y\sin(\theta+\pi))}\right\}\omega d\omega d\theta \qquad (2.22)$$

Using the property:

$$\mathbf{F(\omega,\theta+\pi)=F(-\omega,\theta)} \tag{2.23}$$

and:

$$\mathbf{t=x\cos\theta+y\sin\theta} \tag{2.24}$$

equation (2.21) can be written as:

$$\boldsymbol{f}\mathbf{(x,y)}=\int_0^{\pi}\left\{\int_{-\infty}^{\infty}\mathbf{F(\omega,\theta)}|\omega|\mathbf{e}^{j2\pi\omega t}\mathbf{d\omega}\right\}\mathbf{d\theta} \tag{2.25}$$

Substituting the Fourier transform of the projection at angle θ, for the **2-D** Fourier transform $\mathbf{F(\omega,\theta)}$, gives:

$$\boldsymbol{f}\mathbf{(x,y)}=\int_0^{\pi}\int_{-\infty}^{\infty}\mathbf{P(\omega,\theta)e}^{j2\pi\omega t}|\omega|\mathbf{d\omega d\theta} \tag{2.26}$$

Let the inner integral be denoted by $\mathbf{Q(t,\theta)}$, hence:

$$\mathbf{Q(t,\theta)}=\int_{-\infty}^{\infty}\mathbf{P(\omega,\theta)}|\omega|\mathbf{e}^{j2\pi t}\mathbf{d\omega} \tag{2.27}$$

and equation (2.26) can be rewritten as:

$$\boldsymbol{f}\mathbf{(x,y)}=\int_{-\infty}^{\infty}\mathbf{Q(x\cos\theta+y\sin\theta,\theta)d\theta} \tag{2.28}$$

Equation (2.27) is the Hilbert transform of the derivative of $\mathbf{p(t,\theta)}$, and is due to multiplying by $|\omega|=\mathbf{j\omega(-j}\,\boldsymbol{sgn}\,\omega\mathbf{)}$ in frequency. This corresponds to taking a derivative $\mathbf{(j\omega)}$ along with a Hilbert transform $\mathbf{(-j}\,\boldsymbol{sgn}\,\omega\mathbf{)}$. [2.9].

Equation (2.25) also represents a filtering operation when the frequency response of the filter is given by $|\omega|$. $\mathbf{Q(x\cos\theta+y\sin\theta,\theta)}$ is called the filtered projection. The resulting projections for different angles θ are added to form the estimate of $\boldsymbol{f}\mathbf{(x,y)}$. The operation, defined by equation (2.28), is known as

backprojection. Hence each filtered projection is smeared back, or backprojected over the image plane.

The function $|\omega|$ has the dimensions of spatial frequency. The integration should in principle be carried out over all spatial frequencies. This is not possible in practice, so the function is bandlimited. If **W** is defined as the highest frequency component in each projection, then from the sampling theorem the projections can be sampled at intervals of:

$$\mathbf{T} = \frac{1}{2}\mathbf{W} \tag{2.29}$$

Then a projection can be represented as:

$$\mathbf{p(mT,\theta)} \tag{2.30}$$

where

$$\mathbf{m} = \frac{-\mathbf{N}}{2},..,0,..,\frac{\mathbf{N}}{2}-1 \tag{2.31}$$

assuming $|\mathbf{t}|$ is bounded by **D**.

An algorithm can be defined using an FFT to approximate the Fourier transform $\mathbf{P(\omega,\theta)}$ of the projection by:

$$\mathbf{P(\omega,\theta)} \approx \mathbf{P(m2\frac{W}{N})} = \frac{\mathbf{1}}{\mathbf{2W}} \sum_{\mathbf{k}=-\frac{\mathbf{N}}{2}}^{\frac{\mathbf{N}}{2}-1} \mathbf{P(\frac{k}{2W},\theta)e}^{-\mathbf{j2\pi(\frac{mk}{N})}} \tag{2.32}$$

The modified projection $\mathbf{Q(t,\theta)}$ requires evaluation by discrete approximation.

If the Fourier transform $\mathbf{P(\omega,\theta)}$ is bandlimited, it is approximated by:

$$\mathbf{Q(t,\theta)} = \int_{-\mathbf{W}}^{\mathbf{W}} \mathbf{P(\omega,\theta)|\omega|e}^{\mathbf{j2\pi\omega t}}\mathbf{d\omega} \tag{2.33}$$

provided that **N** is large.

The projections $\mathbf{Q(t,\theta)}$ for **t**, at which the projections $\mathbf{p(t,\theta)}$ are sampled,

gives:

$$Q(\frac{k}{2W},\theta) \approx 2\frac{W}{N}\sum_{m=-\frac{N}{2}}^{\frac{N}{2}} P(m2\frac{W}{N},\theta)\left|m2\frac{W}{N}\right| e^{j2\pi(\frac{mk}{N})} \qquad (2.34)$$

where

$$k = -\frac{N}{2},..,-1,0,1,..,\frac{N}{2}$$

The function $Q(t,\theta)$, at the sampling points of the projection function, is approximately given by the inverse DFT of the product of $P(m2\frac{W}{N},\theta)$ and $\left|m2\frac{W}{N}\right|$.

Due to the truncation of the Fourier domain the filtered projection must be multiplied by a window function. This de-emphasises the high frequencies that may cause unwanted artefacts in the reconstructed image. A typical example of such a window is the Hamming window [2.7]. Hence equation (2.34) is given as:

$$Q(\frac{k}{2W},\theta) \approx (\frac{2W}{N}\sum_{m=-\frac{N}{2}}^{\frac{N}{2}} P(m\frac{2W}{N}).\left|m\frac{2W}{N}\right| H(m\frac{2W}{N}) e^{j2\pi(m\frac{k}{N})} \qquad (2.35)$$

where

$$H(m\frac{2W}{N}) \qquad (2.36)$$

represents the window function. From the convolution theorem equation (2.35) can be written as:

$$Q(\frac{k}{2N},\theta) \approx \frac{2W}{N} p(\frac{k}{2W},\theta) * \Phi(\frac{k}{2W}) \qquad (2.37)$$

where * denotes circular periodic convolution, and $\Phi(\frac{k}{2W})$ is the DFT of the discrete function

$$\left|m\frac{2W}{N}\right| H(m\frac{2W}{N}) \qquad (2.38)$$

The function $Q(t,\theta)$ can be obtained in the Fourier domain from equation (2.34), or in

the space domain by using equation (2.37). As interpolation in the space domain is simpler than in the frequency domain, the convolution method is preferred.

A number of observations can be made at this point about the analysis described above. Equation (2.27) can be expressed in the space domain as:

$$\mathbf{Q(t,\theta) = \int_{-\infty}^{\infty} P(\tau,\theta)\phi(t-\tau)d\tau} \qquad \textbf{(2.39)}$$

and may also be written as:

$$\mathbf{Q(t,\theta) = \int_{-\infty}^{\infty} j2\pi\omega P(\omega,\theta)[-\frac{j}{2\pi} sgn(\omega)]e^{j2\pi\omega t}d\omega} \qquad \textbf{(2.40)}$$

where

$$\mathbf{sgn(\omega) = \begin{bmatrix} 1\ for\ \omega > 0 \\ -1\ for\ \omega < 0 \end{bmatrix}} \qquad \textbf{(2.41)}$$

The convolution theorem for the discrete transform states that the convolution of two functions in the space domain is equivalent to multiplication in the Fourier domain. This can be written as:

$$\mathbf{Q(t,\theta) = [FT^{-1}\ of\ j2\pi\omega P(\omega,\theta)] * [FT^{-1}\ of\ -\frac{j}{2\pi} sgn(\omega)]} \qquad \textbf{(2.42)}$$

where * denotes circular (periodic) convolution. This result may also be rewritten as:

$$\mathbf{Q(t,\theta) = \frac{1}{2\pi^2 t} * \frac{dp(t,\theta)}{dt} = Hilbert\ Transform\ of\ \frac{dp(t,\theta)}{dt}} \qquad \textbf{(2.43)}$$

The reconstruction $\mathbf{f(x,y)}$ is obtained by the discrete approximation:

$$\mathbf{\bar{f}(x,y) = \frac{\pi}{K}\sum_{i=1}^{K} Q(x\cos\theta_i + y\sin\theta_i, \theta_i)} \qquad \textbf{(2.44)}$$

The convolution algorithm is demonstrated diagrammatically in Figure 2.6.

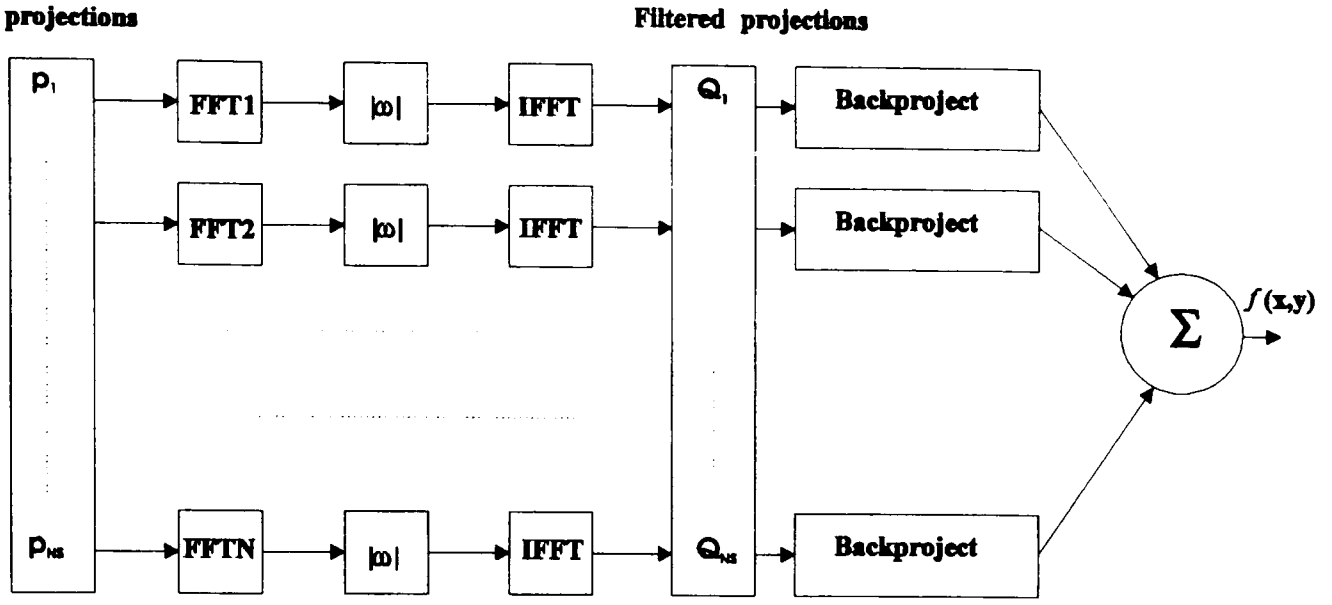

Figure 2.6 Block diagram of Convolution algorithm

A problem occurs with this formula due to the translation of polar to Cartesian co-ordinates, as positions in the polar space may not correspond exactly to positions in the Cartesian space. However it can be approximated with a suitable interpolation. Linear interpolation in often adequate. The effects of interpolation, when backprojecting using the convolution algorithms, were examined by Kwoh [2.10], Herman [2.11] and Peters [2.12].

The projection data are considered more reliable at low frequencies than high frequencies. The $|\omega|$ filter function (which has the highest value at the high frequencies), has the property of amplifying the noise at these frequencies. Rowland [2.13] made a detailed study of the effect on the reconstructed image of a number of alternative filter functions. Examples of these windows, including Hamming, are shown in Figure 2.7.

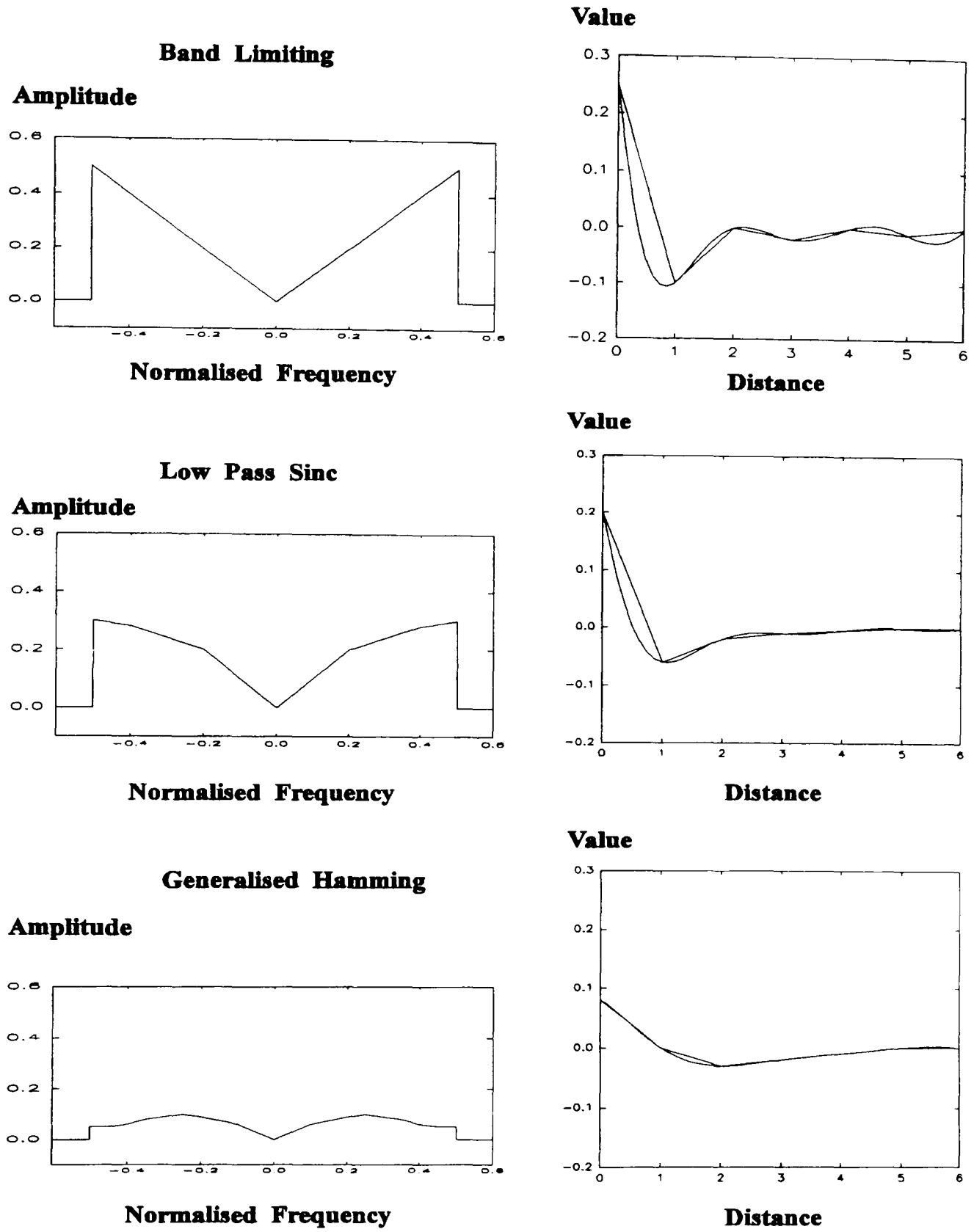

Figure 2.7 The frequency and spatial domain representations of the convolving functions. In the spatial domain, the smooth lines are the Fourier transforms of the bandlimiting, sinc, and Hamming ($\alpha = 0.54$) windows, the straight-line segments are the linear interpolation of the convolving discrete function.

The graphs show the standard convolving functions:

i) Bracewell [2.14] and Ramachandran [1.23] proposed the bandlimiting window, defined by:

$$\Phi(\omega) = \begin{bmatrix} 1 & |\omega| \leq \dfrac{1}{2\Delta x_k} \\ 0 & |\omega| > \dfrac{1}{2\Delta x_k} \end{bmatrix} \qquad (2.45)$$

ii) Shepp and Logan [2.9] proposed the low-pass, bandlimiting window Figure 2.7. defined by:

$$\Phi(\omega) = \begin{bmatrix} \omega \sin c(\pi\omega\Delta x_k) & |\omega| \leq \dfrac{1}{2\Delta x_k} \\ 0 & |\omega| > \dfrac{1}{2\Delta x_k} \end{bmatrix} \qquad (2.46)$$

This filter avoids the high frequency oscillations caused by the abrupt frequency cut-off of the filter in equation (2.45), and results in a smooth reconstruction.

iii) Hamming low-pass window proposed by Chesler and Riederer [2.15]. Defined as:

$$\Phi(\omega) = \begin{bmatrix} [\alpha + (1-\alpha)\cos(2\pi\omega\Delta x_k)] & |\omega| \leq \dfrac{1}{2\Delta x_k} \\ 0 & |\omega| > \dfrac{1}{2\Delta x_k} \end{bmatrix} \qquad (2.47)$$

is the most appropriate, if the reconstructed image in dominated by aliasing and noise. However, a reduction in aliasing and noise effects results in a loss of resolution in the reconstructed image, due to the attenuation of high frequency components.

Other window functions have been developed, but have not been included in this review. The selection of windows given in this review was based on those most commonly given in the literature. The filtered backprojection algorithms are the most commonly adopted techniques in image reconstruction, due to the low number of operations required for computation.

2.2.5 Algebraic Reconstruction Technique (ART)

The ART technique was developed by Gordon [2.16], and was extended by Hounsfield [2.17] in the first commercial X-ray CT scanner. It is based on the "method of projections" first proposed by Kaczmarz [2.18]. The Algebraic Reconstruction Technique (ART) formulates the reconstruction problem in a different manner from the cases described in the pervious sections. To describe the reconstruction problem for ART, a number of assumptions are made for simplicity and precision. ART assumes that the reconstructed image is enclosed in a square region. It is also assumed that the image is composed of **n** by **n** non-overlapping subregions, and in each of the subregions there is a uniform greyness. A ray is defined as a region of a picture that lies between two parallel lines shown in Figure 2.8. With this assumption, the system is defined in terms of a discrete set of data, unlike the previous case, which assumed the image is continuous.

The ART method operates iterativetly in the space (solution space) domain, and defines a great variety of algorithms. In the early 1970's, the integral equations that define the projections were formulated as a system of linear equations that could be solved by iterative methods. The fundamental concept behind ART is backprojection. The difference between a measured projection and the calculated projection from the current reconstruction is backprojected to produce the reconstruction of the next iteration.

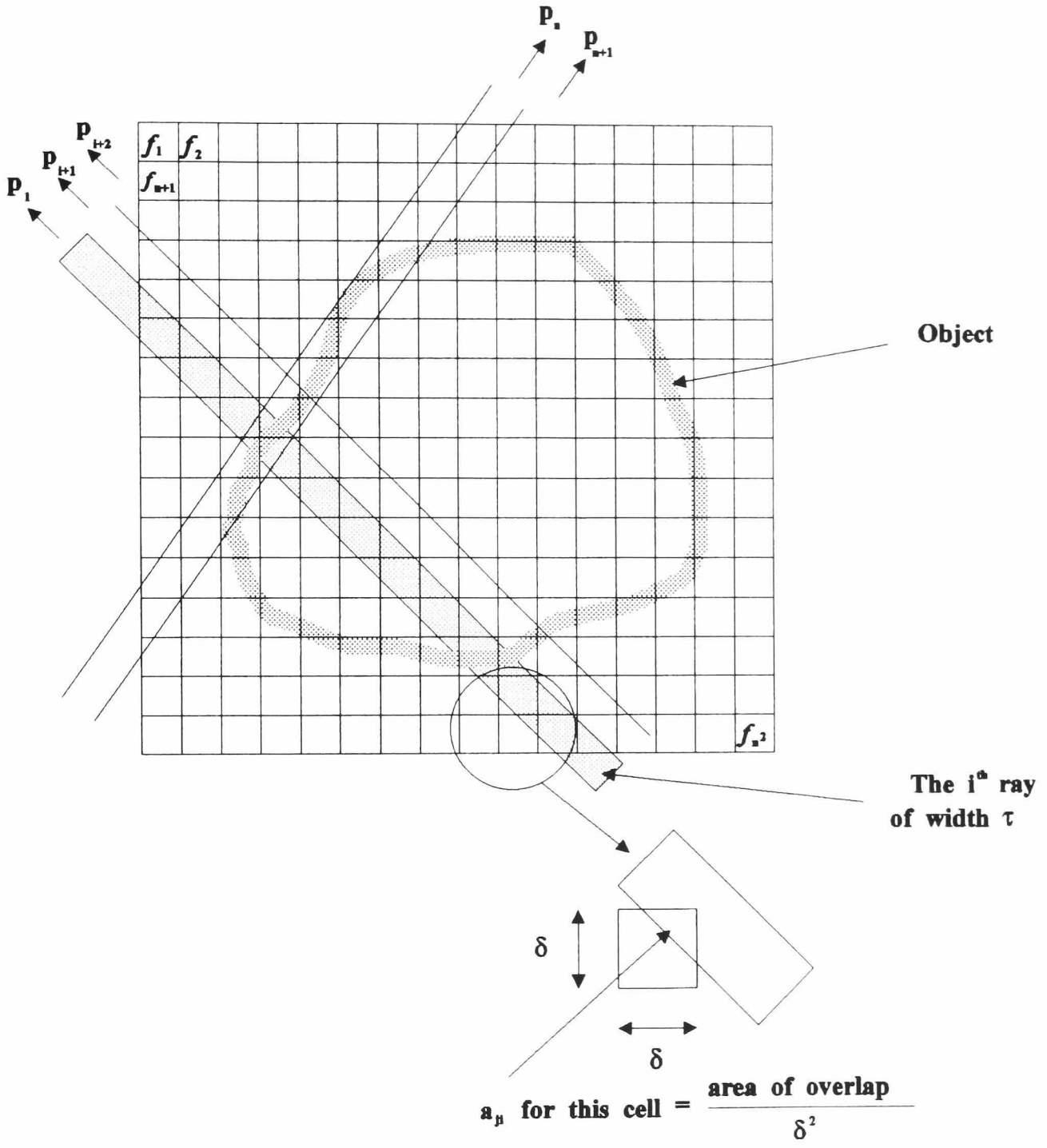

Figure 2.8 ART. A square grid is superimposed over the unknown image. Image values are assumed to be constant in each pixel region.

Later in this section it will be demonstrated that ART can be considered as a constrained optimisation method. Any prior knowledge (such as the image being reconstructed is non-negative), can be built into the algorithms. ART can be subdivided as follows:

2.2.5.1 Additive ART

The discrete model of the image reconstruction problem can be described by a system of linear equations as:

$$\bar{p}_k \approx \sum_{j=1}^{J} a_{kl}^{j} f_j \qquad (2.48)$$

or

$$\mathbf{p} = \mathbf{A}f + \mathbf{e} \qquad (2.49)$$

A is defined as the ART projection matrix, **e** is an error vector due to measurement noise. The assumption of uniform density within each pixel is used to calculate the **A** matrix elements.

The additive ART is an iterative method that aims at producing a solution to the system of equations defined in equation (2.48). Let

$$f_j^q (1 \le j \ge J) \qquad (2.50)$$

be the estimated value of f_j after **n** iterations, and defining

$$\bar{p}_{ki}^{q} = \sum_{j=1}^{J} a_{kl}^{j} f_j^q \qquad (2.51)$$

as the $\mathbf{ki}^{th}$ projection element calculated from the $\mathbf{q}^{th}$ picture estimate. This operation is sometime known as reprojection.

If:

$$S_{ki} = \sum_{j=1}^{J} (a_{kl}^{j})^2 \qquad (2.52)$$

then additive ART is defined by the algorithm:

$$f_j^{q+1} = f_j^q + (a_{ki}^j)\gamma_q \frac{p_{ki} - \bar{p}_{ki}^q}{S_{ki}} \qquad (2.53)$$

where

$$\mathbf{ki} = (\mathbf{q}\ \textit{mod}\ \mathbf{nm}) + \mathbf{1} \qquad (2.54)$$

The sequence of **ki**'s is **1,2,..,NS,1,2,..,NS,1,2,..**etc, and $0 < \gamma_q < 2$. This is set to a very small value [2.19][2.20]. Hence the ART algorithm is defined as the error between a projection measurement p_{ki} and the calculated p_{ki}^q, scaled by the quantity S_{ki}. Then the intensity of each image pixel f_j contributing to that projection measurement is increased by the product of the error and a_{ki}^j .

An initial approximation f^0 with similar characteristics to that of f is desirable to minimise the number of iterations required. As this is often unavailable, approximations such as the output of the summation method are employed.

There are three versions of additive ART that differ in the way f_j^q is obtained from $\bar{f}_j^q$:

i) Unconstrained ART (proposed by Kaczmarz [2.18] for the solution of systems of linear equations):

$$f_j^q = \bar{f}_j^q \qquad (2.55)$$

ii) Partially constrained ART:

$$f_j^q = \begin{bmatrix} 0, & if \bar{f}_j^q < 0 \\ \bar{f}_j^q, & otherwise \end{bmatrix} \qquad (2.56)$$

iii) Fully constrained ART:

$$f_j^q = \begin{bmatrix} 0, & if & \bar{f}_j^q < 0 \\ \bar{f}_j^q & if & 0 \le \bar{f}_j^q \le 1 \\ 1, & if & \bar{f}_j^q > 1 \end{bmatrix} \tag{2.57}$$

2.2.5.2 ART2

In 1973 Herman, Lent and Rowland [2.21] developed a variation on additive ART known as ART2. The only difference between ART and ART2 is that $\bar{f}_j^q$ is used instead of f_j^q in the formula for $\bar{f}_j^{q+1}$. Hence ART2 is formulated as:

$$\bar{f}_j^{q+1} = \bar{f}_j^q + (a_{ki}^j)\gamma_q \frac{p_{ki} - \bar{p}_{ki}^q}{S_{ki}} \tag{2.58}$$

$$f_j^0 = 0 \tag{2.59}$$

2.2.5.3 ART3

ART3 [2.22] aims at a solution within a pre-set error tolerance ε which may vary from one projection to another. Specifically, a solution is acceptable if:

$$p_i - \varepsilon_i \le \sum_{j=1}^{J} a_{ki}^j f_j \le p_i + \varepsilon_i \tag{2.60}$$

ART3 can be shown to converge to a solution in a finite number of iterations, provided a solution exists.

2.2.5.4 Multiplicative ART (MART)

Multiplicative ART [2.16] is specified by

$$f_j^{q+1} = \left(\frac{p_k}{\bar{p}_k^q}\right) f_j^q \tag{2.61}$$

where

$$f_i^0 > 0 \tag{2.62}$$

The choice between Additive ART and Multiplicative ART depends on the physics of

the radiation used to obtain the projections. MART has an advantage over additive ART in that once $f_j^q = 0$, then it remains so for all subsequent iterations.

All the ART methods use different approaches to improve the convergence properties. If the convergence to a solution can be improved, then the required number of iterations in finding the solution can be reduced. One of the problems associated with convergence is the constraints placed upon it. It is possible for a set of projections to have an infinite number of solutions or images that can be reconstructed from the same projection data. Gaarder and Herman [2.23] considered some of the statistical aspects of the convergence problem. They developed a principle of minimum variance (greatest uniformity) which can be explained as follows:

If it is assumed that there is available a solution such that $\mathbf{p} = \mathbf{A}\boldsymbol{f}$, then the unconstrained ART converges to a solution that minimise the image variances as:

$$\sigma^2 = \sum_{j=1}^{J} (f_j - \bar{f})^2 \qquad \textbf{(2.63)}$$

where

$$\bar{f} = \sum_{j=1}^{J} \frac{f_j}{J} \qquad \textbf{(2.64)}$$

is the mean density.

It is also useful to note that minimisation of the image variance is the same as minimisation of the image norm or energy. Hence if:

$$\|f\|^2 = \sum_{j=1}^{J} f_j^2 \qquad \textbf{(2.65)}$$

then

$$\sigma^2 = \sum_{j=1}^{J} (f_j^2 - 2f\bar{f} + \bar{f}^2) \qquad \textbf{(2.66)}$$

If the mean density $\bar{f}$ is assumed to be zero, equation (2.66) becomes the same as equation (2.63). This can be defined as selecting the smoothest of all pictures

consistent with the projection data. Such a smoothness criterion may not be the most appropriate in some applications. This criterion will be used later in the constrained optimisation methods.

The ART methods could also be classified as constrained optimisation methods, as ART iterativetly updates estimates of the image by backprojecting the errors between the measured projections and those corresponding to the current image estimate. This procedure converges to the image of minimum error energy that matches the measured projections exactly. This method is classified as a primal optimisation technique, since the iterations are performed directly in the solution space.

ART reconstructions usually suffer from "salt and pepper" noise, which is caused by the inconsistencies introduced in the set of equations by the approximations commonly introduced used for $\mathbf{a}_{ik}$'s. The result is that the computed ray-sums in equation (2.50), are usually poor approximations to the corresponding measured ray-sums. The effect of these inconsistencies is exacerbated by the fact that as each equation corresponding to the ray in a projection is taken up, it changes some of the pixels just altered by the preceding equation in the same projection. It is possible to reduce the effects of this noise in ART by adjusting the relaxation factor. The relaxation parameter γ is made a function of the iteration number. It becomes progressively smaller with increase in the number of iterations. The resulting improvements in the quality of reconstruction are usually at the expense of convergence.

2.2.6 Simultaneous Iterative Reconstruction Technique (SIRT)

The SIRT proposed by Gilbert [2.24] is an algebraic method modified from its forerunner, the Algebraic Reconstruction Technique. It usually leads to better images than those produced by ART at the expense of a slower convergence. SIRT is an iterative process and assigns a new density value to each pixel at each step of the iteration. If f_i^q is the estimated value of the density of the $\mathbf{i}^{th}$ pixel after $\mathbf{q}$ iterations,

and $\mathbf{L_j}$ the length of intersection of the centre line of the $\mathbf{j^{th}}$ ray and the reconstruction region, then the SIRT algorithm can be defined as follows.

The SIRT algorithm starts with a uniform picture:

$$f_i^0 = f_a \qquad \text{where } \mathbf{i=1,..,N} \tag{2.67}$$

f_a is an estimate of the average pixel density, which is based on the experimental projection data given by:

$$f_a \equiv \frac{1}{NN_\theta h^2} \sum_{j=1}^{M} R_j \tag{2.68}$$

where

$\mathbf{N_\theta}$ is the number of angles at which projection data is available,

$\mathbf{h}$ is the length of a side of a pixel,

$\mathbf{R_j}$ is the $\mathbf{j^{th}}$ measurement.

An auxiliary estimate of the pixel density $\bar{f}^{q+1}$ is made using the following formula:

$$f_i^{q+1} = \frac{\sum_{k=1}^{N} f_k^0}{\sum_{k=1}^{N} \bar{f}_k^{q+1}(max)} f_i^{q+1}(max) \tag{2.69}$$

where $\mathbf{i = 1,..,N}$. Similar to the ART methods, four classes of the additive SIRT algorithm can be defined, depending on the way the estimate of f_i^{q+1} from $\bar{f}_i^{q+1}$ is defined:

(1) Unnormalized, unconstrained SIRT:

$$f_i^{q+1} = \bar{f}_i^{q+1} \tag{2.70}$$

where $\mathbf{i = 1,..,N}$.

(2) Unnormalized, constrained SIRT:

$$f_i^{q+1} = \mathbf{max}(\bar{f}_i^{q+1}, 0) \tag{2.71}$$

where $\mathbf{i = 1,..,N}$.

(3) Normalised unconstrained SIRT:

$$f_i^{q+1} = \frac{\sum_{k=1}^{N} f_k^0}{\sum_{k=1}^{N} \bar{f}_k^{q+1}} \bar{f}_k^{q+1} \qquad (2.72)$$

where $\mathbf{i = 1,..,N}$.

(4) Normalised, constrained SIRT:

$$\bar{f}_i^{q+1}(\mathbf{max}) = \mathbf{max}(\bar{f}_i^{q+1}, 0) \qquad (2.73)$$

and

$$f_i^{q+1} = \frac{\sum_{k=1}^{N} f_k^0}{\sum_{k=1}^{N} \bar{f}_k^{q+1}(max)} \bar{f}_i^{q+1}(max) \qquad (2.74)$$

where $\mathbf{i = 1,..,N}$. Algorithms are called constrained if they always produce non-negative reconstruction, and normalised if they always produce reconstructions with an average density equal to f_a.

The SIRT algorithm also suffers from the inconsistencies in the forward process as ART, but by eliminating the continual and competing pixel update as each new equation is taken up, it results in smoother reconstructions.

2.2.7 Iterative Least Squares Technique (ILST)

This method is not detailed in full as it is similar to the methods described above. In the ILST [2.26], reprojections for all angles are calculated first. Each reconstruction point is considered in turn, and contributes to a point in each reprojection and projection for each angle. A correction that minimises the sum of the squares of the discrepancies between those values can be simply calculated and applied. When all reconstruction points have been corrected, the whole process has to be repeated because the modification of one point will invalidate the least squares estimate at all others.

2.3 Constrained Optimisation

This technique defines the reconstruction by embedding it into a constrained-optimisation problem, with the aim of obtaining the 'best' reconstruction by optimising a performance criterion. This category of reconstruction has been shown by Goutis, Leahy and Drossos [2.27] to give the highest quality image consistent with the available data.

There are two categories of constrained optimisation techniques. The first defines the problem in the solution space and is known as the primal method, the second is the dual approach which solves the problem in dual space. This will be defined in Chapter four. The dual approach has advantages over the primal method in two areas.

i) The dual optimisation exploits the natural geometry of the problem.

ii) If the available data are limited, the dual approach is still capable of producing a reasonable reconstruction.

In the previous section the ART algorithms were classified in the space domain. It is equally valid to define these algorithms as examples of constrained optimisation. ART iteratively updates estimates of the image by backprojecting the errors between the measured projections and those corresponding to the current image estimate. This procedure converges to the image of minimum error energy that matches the measured projections exactly. The method can be classified as a primal optimisation technique since the iterations are performed directly in the solution space. A detailed analysis of this method will be given in Chapter four.

2.4 Summary of Reconstruction Methods

Each method requires following the listed sequential operations.

Fourier Transform Technique - FTT

Transform each **1-D** projection into the Fourier domain.

Interpolate in the Fourier domain.

Multiply by appropriate window function.

Inverse Fourier Transform to obtain image estimate.

Rho-Filtered Layergram Technique - ρFLT

Backproject the projections.

Calculate the **2-D** Fourier transform of the backprojected projections.

Obtain a new function by multiplication by a filter function.

Estimate image by inverse Fourier transform of above function.

Convolution Backprojection Technique - CBT

For each projection angle:

Multiply the **1-D** Fourier transform of each projection by the $|\omega|$ - filter.

Backproject its inverse Fourier transform.

Algebraic Reconstruction Technique - ART

For each projection angle:

Take the reprojection.

Difference with the corresponding projection.

Backproject and add in the correction to the trial image.

Multiplicative Algebraic Reconstruction Technique - MART

For each projection angle:

Take the reprojection.

Divide the corresponding projection by the reprojection.

Backproject and multiply in the correction to the trial image.

Iterative Least Squares Technique - ILST

Calculate all reprojections.

For each point in the trial image:

Get the contributing projection and reprojection ray sums.

Compare them.

Calculate a new point value that minimises the disagreement.

Simultaneous Iterative Reconstruction Technique - SIRT

For each point in the trail image:

Calculate the reprojection ray sums.

Compare with the corresponding projection ray sums.

Calculate a new point value that minimises the disagreement.

Constrained Optimisation Reconstruction Technique - CORT

For the defined system geometry (assuming minimum variance model) calculate the pseudo inverse of the system matrix.

Multiply by the projection data to obtain the Lagrange multipliers

Backproject.

2.5 Discussion

The objective of this Chapter was to review the reconstruction procedures that have been previously developed, and to classify them into three categories. These were: transform, series expansion and constrained optimisation methods, (which are discussed in more detail in Chapter four). The classification scheme is based on the procedure used to obtain the solution to the reconstruction problem. A summary of these procedures is given below:

2.5.1 Transform Methods

1) Formulate a mathematical model of the problem, in which the known and unknown quantities are functions whose arguments come from a continuum of real numbers.

2) Solve for the unknown function by an inversion formula.

3) Adapt the inversion formula for application to discrete and noisy data.

In the last step, the algorithms that result do not perform identically on real data, since different approximations have been introduced.

2.5.2 Series Expansion Methods

1) Formulate a mathematical model of the problem which relates a finite set of known numbers, (i.e., the projection) data to a finite set of unknown numbers representing the image.

2) Solve numerically the system of equations obtained from step 1 .

2.5.3 Constrained Optimisation Methods

1) Select an error criterion (cost function) based on the difference between the true and the reconstructed image.

2) Formulate a model based on the optimisation of the above cost function.

2.5.4 Errors

All the algorithms detailed in this review have a number of potential sources of error. These can be summarised as:

a) undersampling of the projections, (all methods),

b) error in evaluation of $\mathbf{p}$, (all methods),

c) error due to truncation of the Fourier domain,

f) interpolation error in the Fourier domain,

g) undersampling of the Fourier domain,

h) error in evaluation of f (all methods).

2.5.5 Observations

The convolution backprojection method has dominated all other methods due to the straightforward implementation in software or hardware. It produces sharp, accurate images from good quality data. Fourier methods are not straightforward to implement due to the inelegant **2-D** interpolation required. There are two advantages to the filtered backprojection algorithm over a frequency domain interpolation scheme. The most important is the reconstruction procedure, which can be started as soon as the first projection has been measured. This reduces the required data storage at any one time. It is also usually more accurate to carry out interpolation in the space domain. A simple linear interpolation is often adequate for the backprojection algorithm, while more complicated approaches are needed for direct Fourier domain interpolation.

The backprojection operation is the most expensive part of the convolution algorithm, and hence a number of different schemes have appeared in the literature to improve the speed of backprojection. A zero order interpolation proposed by Kwoh *et al.* [2.28], increases the speed by a factor of two. Their results show reconstructions of similar quality to those obtained with linear interpolation if there are sufficient numbers of projections and a high signal-to-noise ratio. A two stage operation proposed by Peters [2.12], consisted of pre-interpolating the filtered projections to produce additional samples, and then using a zero order interpolation during backprojection. It is estimated that a reduction of one third in computation time is saved compared with linear interpolation. Herman [2.11] also investigated interpolation using linear and modified cubic spline methods, and concluded that both gave similar results, but the linear method was preferred due to its lower computational cost.

Some researchers have attempted to reduce the reconstruction computation time in the convolution algorithm by using hardware solutions. Kelieff and Durrani [2.29] use a Fast Hartley Transform (FHT) to improve performance. Their system was based around **16** transputers each with **256** Kbytes of external memory, which gives

reported times of **50** secs. for **195** projections, and image resolutions of **256** by **256** pixels. An alternative hardware solution is given in Chapter eight.

ART and Constrained Optimisation have two important advantages over the Fourier domain based methods:

i) explicit assumptions need not be made about the unknown projections.

ii) the statistics of the noise can be considered.

The choice between additive ART and Multiplicative ART depends on the physics of the radiation used. Although the ART methods produce superior images to those of the transform methods, they are computationally inconvenient, requiring manipulation of large data sets.

To keep this review of reconstruction methods brief, only the parallel geometries have been considered. Examples on fan beam can be found in Lakshminarayanan [2.30] and Herman [2.31]. A complete review of the transform methods is given by Lewitt [2.32]. Other reviews of reconstruction methods included Natterer [2.33], which gives a highly mathematical approach to the reconstruction problem, or Kak and Slaney [2.34] who provided a tutorial survey. Herman [2.19] also provided a good survey of the fundamentals of computerised tomography. For a medical and applications approach, Webb [2.35] provides a useful insight to the fundamentals.

3 REVIEW OF EIT RECONSTRUCTION METHODS

3.1 Introduction

In Electrical Impedance Tomography (EIT), there is a requirement to find a solution for both the Forward and Inverse problems, unlike the methods described in Chapter two, which have well defined Forward solutions. As the EIT methods do not fall easily into the categories defined in the Taxonomy presented in the previous Chapter, they are reviewed separately in this Chapter, making comparisons where appropriate and useful. This Chapter also identifies the problems associated with EIT that are not encountered with the systems described in pervious Chapters. These problems need to be addressed when the algorithms that are specifically developed for X-ray and PET system are adapted for EIT.

There are a number of key methods that have been developed for EIT. Most have only been validated with modelled data, with the exception of the filter backprojection algorithm used by Barber and Brown [1.18], which has been used in clinical evaluation. The solution of the Forward problem derived by Barber and Brown [1.18] is also exploited in the Constrained Optimisation Reconstruction Techniques (CORT), developed in Chapter five. Two main approaches for obtaining the reconstructions of the resistivity distribution have previously been developed.

The first uses a Finite Element Model (FEM), to obtain an estimate of the Forward problem. The FEM boundary potential is then compared with the measured data from the collection system. The difference information is then used to update the FEM model to obtain an improved estimate of the resistivity distribution. To improve the convergence of the solution, a method based on Newton-Raphson [3.1] is adopted. This approach is described in some detail later in this Chapter.

The second approach requires finding a solution for the Forward problem

analytically, to find the equipotential paths, then to use a filter backprojection method to reconstruct the resistivity distribution. A great deal of investigation has been undertaken by many researchers on the FEM algorithms and Newton-Raphson [3.5] methods, as they produce more accurate reconstructions than the filtered backprojection method, but at present have not been evaluated in the clinical environment. Another important point to note is that the filtered backprojection technique is used for dynamic imaging, whereas the FEM technique in mainly used for static images.

3.2 Forward, Inverse and Boundary Problems

In EIT the image reconstruction problem is defined in a number of ways.

i) The Forward problem is defined as:
Given ρ with boundary conditions $\mathbf{V_0}$ and $\mathbf{I_0}$. Find the internal voltages and current densities.

ii) The Inverse problem is defined as:
Given $\mathbf{V}$ and $\mathbf{I}$ on the boundary or internally. Find $\rho(\mathbf{x},\mathbf{y})$ inside domain of interest.

iii) The Boundary value problem is defined as:
Given boundary conditions $\mathbf{V_0}$ and $\mathbf{I_0}$. Find the internal ρ, $\mathbf{I}$ and $\mathbf{V}$.

Where ρ, $\mathbf{V}$ and $\mathbf{I}$ are the resistivity, voltage and impressed current source distribution within the region being examined, $\mathbf{V_0}$ and $\mathbf{I_0}$ are the voltage and current density at the boundary.

3.3 Potential Distribution within an Isotropic Resistive Medium

Chapter one briefly described the governing equations in terms of conductivity. In EIT, the theoretical problem to be dealt with is the reconstruction of resistivity distribution within a **2-D** circular region surrounded by a medium of infinite resistivity.

If the distribution of voltage within the region is given by a solution to the equation:

$$\Delta V + \underline{\nabla}\sigma . \underline{\nabla} V = 0 \qquad (3.1)$$

consistent with the known current or voltage boundary conditions, where $\sigma = \sigma(x, y)$ is the distribution of the conductivity within the region [1.18]. If σ is replaced by $\ln(\rho)$ where $\ln(\rho) = -\ln(\sigma)$ for convenience, then equation (3.1) can be rewritten as:

$$\Delta V = \underline{\nabla} \ln(\rho) . \underline{\nabla} V \qquad (3.2)$$

This suggested that the image of natural log of resistivity, rather than resistivity, should be reconstructed.

A general analytic solution to this complicated differential equation has not yet been reported in the literature. Numerical methods such as FEM are usually employed to derive the solution.

3.4 Data Collection Methods

There are a number of ways to obtain data in EIT. The two-electrode approach uses the same electrodes for the voltage or current application and for the measuring electrodes. Alternately the four-electrode system separates the measurement electrodes from the injection electrodes. The systems presented here are based on the four-electrode data collection method. The CORT algorithm developed in this research uses the four-electrode method with two data collection configurations known as the opposite [3.2], and neighbouring methods [3.3][3.4]. In the first method the current is applied through two neighbouring electrodes. Measurements are made from all other successive pairs of adjacent electrodes as illustrated in Figure 3.1(a). The neighbouring method of data collection has a very nonuniform current distribution. Most of the current travels near the peripheral electrodes for each boundary measurement, giving the highest current density at the boundary. This does not yield good sensitivity at the centre because the current density is low in this region, and hence good sensitivity is obtained only at the periphery.

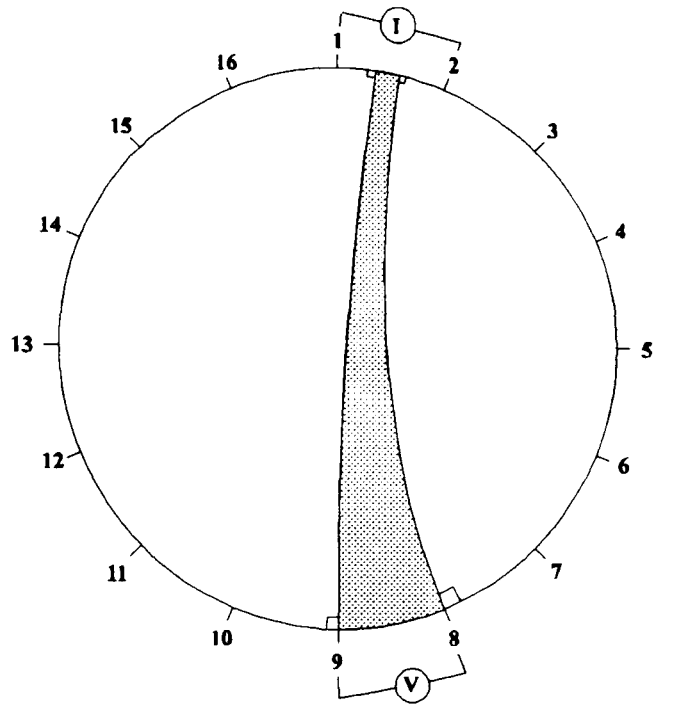

Figure 3.1(a) Neighbouring Method of Data Collection. Equipotential lines are formed in a homogenous medium by current injected through neighbouring electrodes, the voltage is measured between adjacent electrodes.

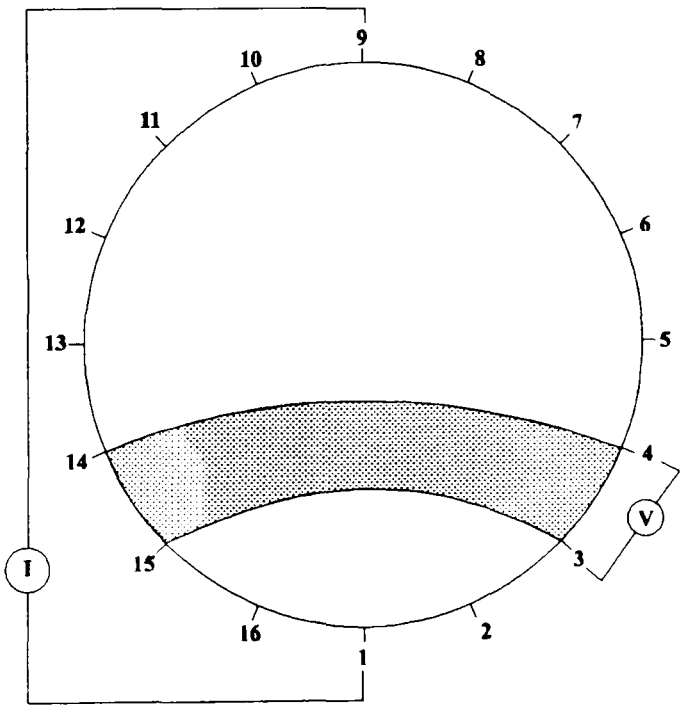

Figure 3.1(b) Opposite Method of Data Collection. Current is injected through diametrically opposed electrodes.

The opposite electrode data collection method used by Hue [3.2], is illustrated in Figure 3.1(b). The current is injected through diametrically opposed electrodes. The voltage reference electrode is adjacent to the current-injecting electrode. For a particular pair of current-injecting electrodes, the voltages are measured with respect to the reference at all electrodes, except the current-injecting electrodes. To obtain the next set of data, the current is switched to the next pair of opposite electrodes. The voltage reference is also changed accordingly, and the voltages are similarly measured with respect to the new reference. A complete set of data is obtained by switching the opposite placed electrodes through 180 degrees. As this method has a more uniform current density, it also has good sensitivity.

3.5 Finite Element Approximation

To solve the Forward problem a method has been derived known as the Finite Element Method (FEM). In FEM, the governing equation (3.2) is changed into the algebraic problem:

$$\mathbf{Y}\nu = \mathbf{c} \qquad \textbf{(3.3)}$$

Where $\mathbf{Y}$ is known as a master matrix, ν is the node voltage vector, and $\mathbf{c}$ is the node current vector. This is a linear system of equations that can be solved using various numerical techniques. Unlike the CORT method, introduced in Chapter four, the $\mathbf{Y}$ matrix in FEM is not well structured. The FEM method requires a number of stages. The physical domain is divided into a finite number of elements (mesh). These are usually triangular or quadrilateral elements. In EIT it is assumed that the resistivity in each element is homogeneous and isotropic. This process converts the continuous problem into a problem with a finite number of unknowns, by expressing the unknown field variables (voltages), in terms of certain interpolation functions within each element. These interpolation functions are defined in terms of values of the field variables at nodes of each element. Therefore, the nodal values of the field variables

become new unknowns, and the field variables inside the elements are determined from the nodal values by the interpolation functions. An example of this process is given in Webster [3.5].

3.5.1 Dirichlet Boundary Condition (Known Surface Voltages)

In most applications leading to Laplace's equation, it is required to solve a boundary value problem, that is, to determine the solution of Laplace's equation satisfying given boundary conditions, on the boundary **B** of the region **D** in which the equation is considered. This is known as the first boundary values problem, or Dirichlet problem. Hence, if some of the voltage values at the boundary are known, it is possible to find a solution for the corresponding node voltage to have those known boundary values.

3.5.2 Neumann Boundary Condition (Known Surface Currents)

If some of the current values at the surface i.e., the injected currents, are known, the corresponding elements of the current vector can be set to those known values. This gives a uniquely solvable linear system equation with all boundary data in it as:

$$\mathbf{Y}^{*}\mathbf{v} = \mathbf{c}^{*} \qquad \textbf{(3.4)}$$

where $\mathbf{Y}^{*}$ is the modified master matrix, $\mathbf{v}$ is the node voltage vector, and $\mathbf{c}^{*}$ is the modified current vector satisfying all constraints. The master matrix , **Y,** is an **N** by **N** matrix, where **N** is the number of nodes in the finite element mesh. **Y** also has the property of being symmetric. Hence to construct the **Y** matrix only the lower triangular portion, including the diagonal, is required.

3.5.3 Solution of System Equations

Usually the associated system matrix is symmetric, positive definite, and very sparse. There are a number of methods to obtain a solution to the system of equations. The first approach is a direct method that uses Gaussian elimination, or some variation of it. If the system matrix is positive definite, then Cholesky factorisation with forward and back substitution is a possible method, since it is numerically stable [3.6]. A second approach is an iterative method such as Gauss-Seidel, or Successive Over-relaxation (SOR) [3.7].

3.6 Backprojection Between Equipotential Lines

This method was developed by Barber and Brown [3.8], and is based upon backprojection between the equipotential lines. They use an approximation known as the dipole approach (appendix E), to find the equipotential lines (Forward problem) which assumes initially that the medium is circular and homogeneous. This same approximation is used for developing the CORT for EIT as detailed in Chapter six. The approximation results in significant error close to the electrodes, when the gap between the drive electrodes is not sufficiently small, due to the deviation of the true equipotential paths from the approximation.

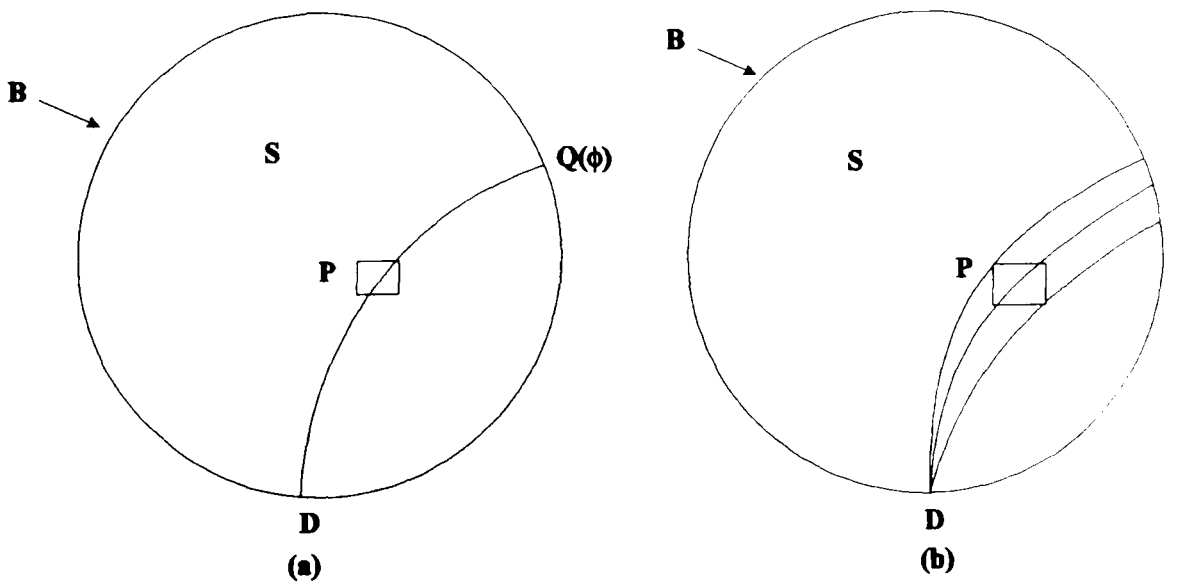

Figure 3.2 Backprojection of boundary voltages measurements

This approximation does however produce an improved spatial resolution, as compared with other solutions, such as the Bipolar system used in the opposite electrode data collection method (appendix F).

The Inverse problem is derived as follows.

Consider the single equipotential line shown in Figure 3.2(a). Let $\mathbf{V_r}$ be the potential measured at a point $\mathbf{Q(\phi)}$ on the boundary **B,** in a medium **S** of homogeneous resistivity ρ_r. Let $\mathbf{V_p}$ be the potential at the same point after the resistivity of the medium has changed from ρ_r to $\rho_r + \rho_p$. A linear approximation can then be obtained for the system in Figure 3.2(a), if it is assumed that the solution of:

$$\Delta \mathbf{V} = \underline{\nabla} \ln(\rho_r).\underline{\nabla}\mathbf{V} \qquad \textbf{(3.5)}$$

is $\mathbf{V_r}$, and the solution of the equation (3.6):

$$\Delta \mathbf{V} = (\underline{\nabla} \ln(\rho_r) + \underline{\nabla} \ln(\rho_p)).\underline{\nabla}\mathbf{V} \qquad \textbf{(3.6)}$$

is $\mathbf{V} = \mathbf{V_r} + \mathbf{V_p}$, then:

$$\Delta \mathbf{V_p} + \Delta \mathbf{V_r} = \underline{\nabla} \ln(\rho_r).\underline{\nabla}\mathbf{V_p} + \underline{\nabla} \ln(\rho_r).\underline{\nabla}\mathbf{V_r} + \underline{\nabla} \ln(\rho_p).\underline{\nabla}\mathbf{V_p} + \underline{\nabla} \ln(\rho_p).\underline{\nabla}\mathbf{V_r} \qquad \textbf{(3.7)}$$

If the terms in $\underline{\nabla}\mathbf{V_p}$ are eliminated as being small compared with the terms in $\underline{\nabla}\mathbf{V_r}$, then equation (3.7) can be rewritten as:

$$\Delta \mathbf{V_p} + \Delta \mathbf{V_r} = ((\underline{\nabla} \ln(\rho_p) + \underline{\nabla} \ln(\rho_r)).\underline{\nabla}\mathbf{V_r} \qquad \textbf{(3.8)}$$

If $\underline{\nabla} \ln(\rho_p)$ is small, then it can be assumed that $\underline{\nabla}\mathbf{V_p} << \underline{\nabla}\mathbf{V_r}$, and using equation (3.5), equation (3.8) can be rewritten as:

$$\Delta \mathbf{V_p} = \underline{\nabla} \ln(\rho_p).\underline{\nabla}\mathbf{V_r} \qquad \textbf{(3.9)}$$

This represents a linear relationship between $\ln(\rho)$ and V_p, assuming V_r is a fixed reference. It is assumed that the shapes of the equipotential lines are not changed significantly from the uniform case, illustrated in Figure 3.2(b). This is reasonable if the resistivity changes are small.

To obtain a reconstruction, the boundary voltage is measured before and after a change in resistivity. Then the natural logarithm of the normalised boundary voltage change is backprojected onto the image value of the pixel **P**, lying on the equipotential line at the point $Q(\phi)$. Hence if:

$$\frac{V}{V_r} \approx \ln(\rho_r + \rho_p) - \ln(\rho_r) \qquad (3.10)$$

then

$$\frac{V_r + V_p}{V_r} \approx \ln\left[1 + \frac{\rho_p}{\rho_r}\right] \qquad (3.11)$$

For small changes in resistivity, equation (3.11) can be approximated to:

$$\ln\left[1 + \frac{V_p}{V_r}\right] \approx \ln\left[1 + \frac{\rho_p}{\rho_r}\right] \qquad (3.12)$$

or

$$\frac{V_p}{V_r} \approx \frac{\rho_p}{\rho_r} \qquad (3.12)$$

Define $g(D)$ as a vector of the normalised boundary voltage change for drive pair **D**, and **p** as the image value of the pixel **P**. Then:

$$p = w(PD)g(D) \qquad (3.13)$$

where $w(PD) = [0,0,..,wj,0,..,0]$ is the backprojection vector for the pixel **P**, the drive pair **D**, and the j^{th} voltage measuring electrode pair. **wj** is a weighting factor for

angular uniformity. Since the above equation holds for all pixels, then:

$$\mathbf{p(D) = W(D)g(D)} \qquad \textbf{(3.14)}$$

where **p(D)** is a vector of image values of all pixels, and **W(D)** is a matrix whose rows are **w(PD)**. The final reconstructed image is obtained from:

$$\mathbf{p} = \sum_{D=1}^{n} \mathbf{p(D)} = \mathbf{Wg} \qquad \textbf{(3.15)}$$

where **n** is the number of drive electrode pairs used.

A number of filtering operations are required for complete reconstruction. First is a weighting factor required for angular uniformity. Assuming the electrodes are equally spaced, the equipotential lines are not circularly symmetric for all pixels except at the centre. This is due to the current distribution within the medium being nonuniform. The weighting factor is different for all pixels. Based on a conformal transform [3.9], between a central point and an offset point, the weight **wj** is computed from:

$$\mathbf{wj} = \frac{l - \mathbf{r}^2}{l^2} \qquad \textbf{(3.16)}$$

where l and **r** are shown in Figure 3.3.

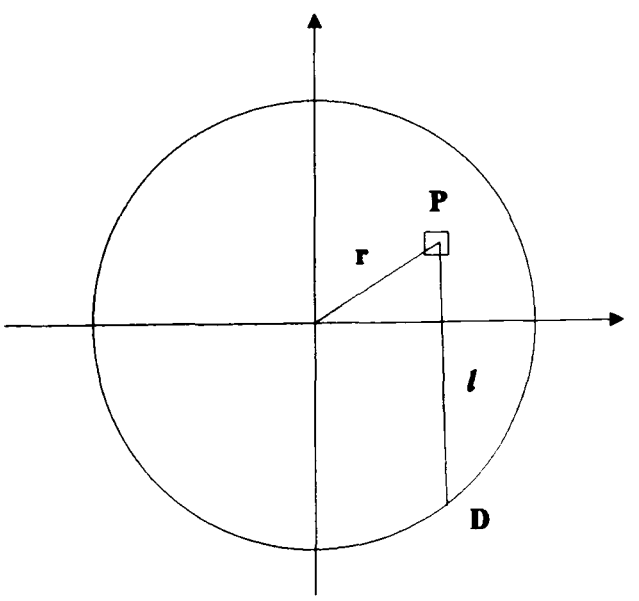

Figure 3.3 Computation of weighting

The second operation is filtering, to reduce the blurring inherent in backprojection. Seager [3.9] has shown that the spatial resolution depends on the location of the object in the circular medium.

One of the problems associated with the above method, is that only the diagonal elements of the matrix are used. Breckon and Pidcock [3.10] suggested that the backprojection method could be improved by utilising other sensitivity coefficients. These coefficients relate the magnitude of the change in voltage, measured between electrodes at the boundary of the object, to the change in resistivity that gives rise to it. The value of the sensitivity coefficient for a particular element (pixel) is affected by both the position of the pixel within the current density field and the position of the pixel with respect to the voltage sensing electrodes. Its value for an element at **x,y** can be calculated as the inner product of the field produced by a unit current flowing in the current drive electrodes, (the $\mathbf{m}^{th}$ pair of electrodes), and the field produced by a unit current flowing in the voltage sensing electrodes, (the $\mathbf{n}^{th}$ pair). On the basis of this idea, Kotre [3.11] developed a backprojection algorithm that used all the sensitivity coefficients as weights. Figure 3.4(a) illustrates a bounded volume of uniform resistivity ρ, which is carrying a constant current $\mathbf{I}$, supplied by the $\mathbf{m}^{th}$ pair of adjacent electrodes. A voltage, $\mathbf{V(m,n)}$, is developed between the $\mathbf{n}^{th}$ pair of surface electrodes. Figure 3.4(b) shows the same situation as Figure 3.4(a), except for the introduction, at a point denoted by $\mathbf{(x,y)}$, of a small volume element with the resistivity $\rho(\mathbf{x,y})+\delta\rho(\mathbf{x,y})$. The voltage sensed by the electrodes at the object boundary is now $\mathbf{V(m,n)}+\delta\mathbf{V(m,n)}$. Assuming that $\delta\rho(\mathbf{x,y})$ is small, it is reasonable to assume that the current density field is the same as for the case of uniform resistivity, and that:

$$\delta\mathbf{V(m,n)} \propto \delta\rho(\mathbf{x,y}) \qquad \textbf{(3.17)}$$

If the constant of proportionality is defined by a sensitivity coefficent $S_{m,n,x,y}$, then:

$$\mathbf{S_{m,n,x,y}} = \frac{\delta \mathbf{V(m,n)}}{\delta \rho \mathbf{(x,y)}} \tag{3.18}$$

If ϕ_m and ϕ_n are the potential fields, the sensitivity coefficient for an element centred at (x,y), can be defined as:

$$\mathbf{S_{m,n,x,y}} = \frac{\delta \mathbf{V(m,n)}}{\delta \rho \mathbf{(x,y)}} = \int_e \nabla \phi_m \nabla \phi_n \mathbf{ds} \tag{3.19}$$

where e denotes the area of integration over the element, as presented in Figure 3.4. The sensitivity matrix is computed in the same way as the Jacobian matrix in the modified Newton-Raphson method, using FEM. It can also be computed from the analytic solution of Laplace's equation for a homogeneous resistivity distribution. If the sets of boundary voltages $\mathbf{V(m,n)}$ and $\mathbf{V'(m,n)}$ are measured before, and after, a change in resistivity (due to a change in the body's physiological processes), an image of the temporal change in natural log resistivity can be produced from:

$$\mathbf{P(x,y)} = \sum_{m=1}^{M} \sum_{n=1}^{N} \mathbf{S_{m,n,x,y}} \ln[\frac{\mathbf{V'(m,n)}}{\mathbf{V(m,n)}}] \tag{3.20}$$

where $\mathbf{P(x,y)}$ denotes the pixel value.

This approach yields reasonable results, and Kotre [3.11] claims it improves the basic backprojection method. However, no quantitative analysis appears to have been published to compare this method with others. Also, Kotre [3.11] makes no attempt to pre-calculate a pseudo-inverse of the sensitivity matrix to improve computational efficiency. The reconstruction algorithm is known as a single pass reconstruction algorithm.

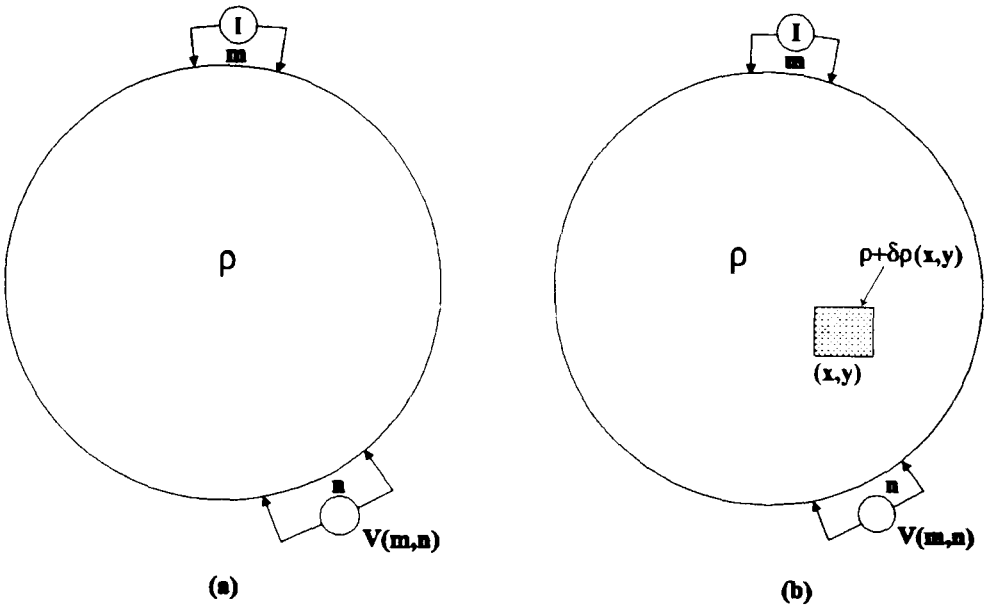

Figure 3.4 (a) A bounded volume of uniform resistivity, (b) A bounded volume where one element has changed resistivity.

3.7 Newton-Raphson Method

The Newton-Raphson (N-R) or Gauss-Newton method [3.1][3.7] is an iterative reconstruction algorithm developed for non-linear problems. In this method, an error function called the objective function is minimised. The error is a measure of the voltage responses of the assumed resistivity distribution, matched to those of the real distribution. As in the CORT case, the objective function is not unique. Yorkey [3.1] defines it as the equally weighted mean square difference between the measured and estimated voltage responses:

$$\phi(\rho) = \frac{1}{2}(\overline{\mathbf{V}}(\rho) - \mathbf{V}_0)^T(\overline{\mathbf{V}}(\rho) - \mathbf{V}_0) \qquad (3.21)$$

where $\mathbf{V}_0$ is the measured voltage on the boundary, and $\overline{\mathbf{V}}(\rho)$ the estimated voltage for a resistivity distribution ρ.

The problem is defined as finding a value of ρ that minimises ϕ. The derivative is set to zero:

$$\phi'(\rho) = (\overline{\mathbf{V}}'(\rho))^T(\overline{\mathbf{V}}(\rho) - \mathbf{V}_0) = 0 \qquad (3.22)$$

where $(\overline{\mathbf{V}}'(\rho))^{T} = \dfrac{\partial \overline{\mathbf{V}}_i}{\partial \rho_i}$. This known as a Jacobian matrix. Taking the Taylor series expansion of $\phi'(\rho)$, and keeping only the linear terms:

$$\phi'(\rho^{k+1}) \approx \phi'(\rho^{k}) + \phi''(\rho^{k})\Delta\rho^{k} = 0 \qquad \textbf{(3.23)}$$

where

$$\rho^{k+1} = \rho^{k} + \Delta\rho^{k} \qquad \textbf{(3.24)}$$

The term ϕ'' is a Hessian matrix [3.16], which can be expressed as:

$$\phi'' = (\overline{\mathbf{V}}')^{T}\overline{\mathbf{V}}' + (\overline{\mathbf{V}}'')^{T}(\mathbf{I} \otimes (\overline{\mathbf{V}} - \mathbf{V}_0)) \qquad \textbf{(3.25)}$$

where $\otimes$ is the Kronecker matrix product, and $\mathbf{I}$ is an identity matrix As the second term $\overline{\mathbf{V}}''$ in equation (3.25) is relatively small, it can be omitted. Therefore:

$$\phi'' = (\overline{\mathbf{V}}')^{T}\overline{\mathbf{V}}' \qquad \textbf{(3.26)}$$

Substituting equation (3.26) and (3.22) into equation (3.23), to find a new estimate of the resistivity:

$$\Delta\rho^{k} = -[\overline{\mathbf{V}}'(\rho^{k})^{T}\overline{\mathbf{V}}'(\rho^{k})]^{-1}[\overline{\mathbf{V}}'(\rho^{k})]^{T}[\overline{\mathbf{V}}'(\rho^{k}) - \mathbf{V}_0] \qquad \textbf{(3.27)}$$

The flow chart given below demonstrates the full procedure. The calculation of $\overline{\mathbf{V}}$ and $\overline{\mathbf{V}}'$ requires the use of the FEM.

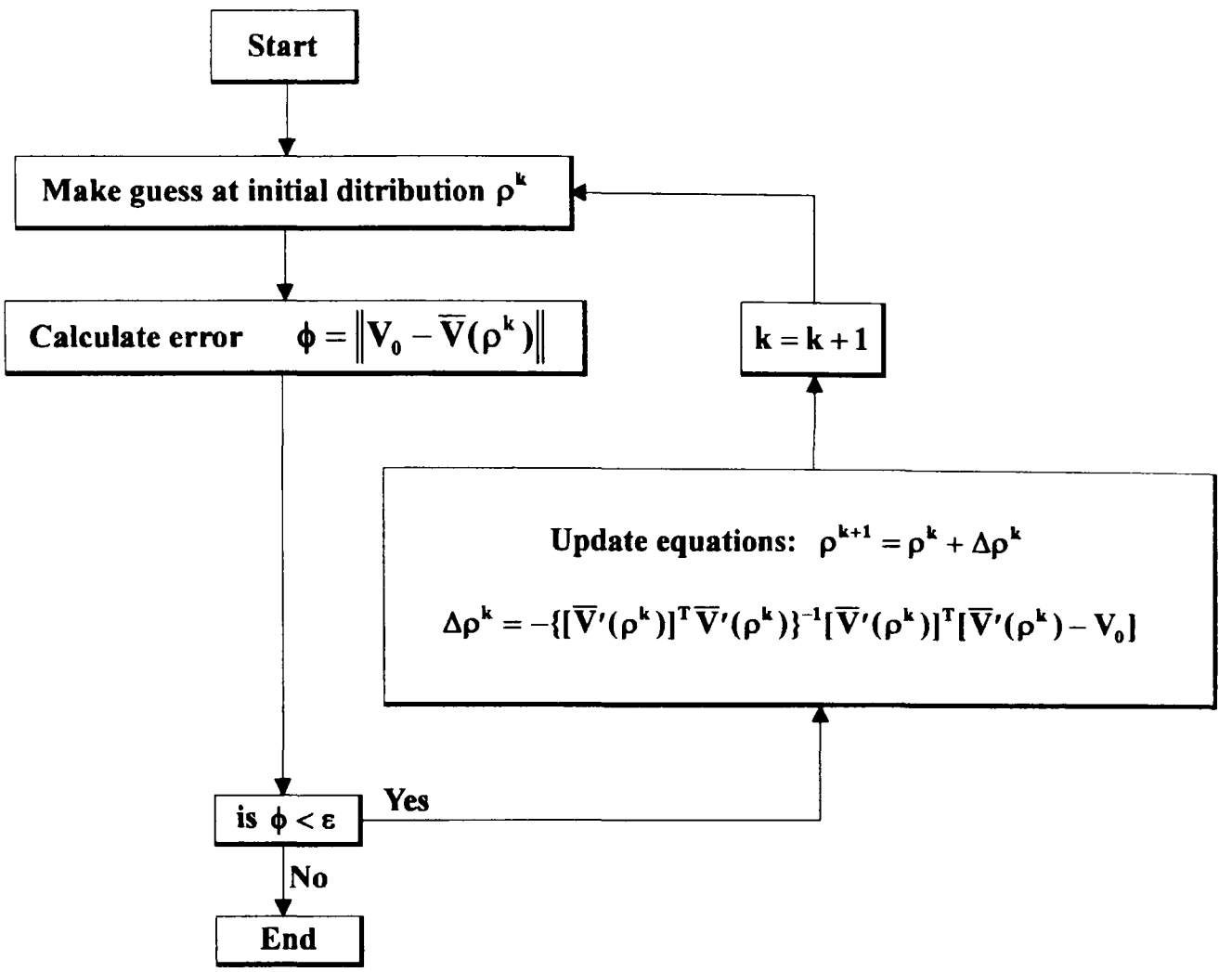

Figure 3.5 Flow chart of Newton-Raphson Algorithm

As illustrated in the flow chart (Figure 3.5), an initial guess of the distribution is made. The theoretical voltage response for the given current distributions is calculated using a finite element method. The calculated voltages are subtracted from the measured voltages to obtain the objective function. If it is less than the error criterion, the guessed distribution is considered to be the desired distribution. If it is not, the distribution is updated using equation (3.25). This procedure is repeated until the error criterion is met. The step size of the updating depends on the application, and is usually less than the initial distribution ρ^k to achieve a guaranteed convergence. If the step size is too big, even though it may converge fast during the first few iterations, it causes oscillation in the neighbourhood of the solution. The Newton-Raphson's performance is well known to be a quadratic function of ρ. In EIT, the voltages are nonlinear

functions of the resistivity distribution, instead of quadratic functions. Therefore the search may result in a local minimum, depending upon the initial guess. In applications to biomedicine, there is sufficient prior knowledge to provide a good initial guess. A more detailed analysis of this method can be found in Yorkey [3.1], who produced a modified version of the algorithm with improved convergence properties.

3.8 Perturbation Method

In this method developed by Kim [3.12], a circular computer model of a **2-D** transverse plane is simulated. A perturbation matrix is then calculated by changing the resistivity of one element, and then calculating the changes in currents at current measuring electrodes, using FEM. From the resulting perturbation matrix and Laplace's equation, the differences between the true and computed current densities are backprojected, according to each element's sensitivity. Yorkey *et al.* [3.13] developed an improved perturbation technique, with better reconstructions, using fewer restrictions on the prior knowledge of the resistivity distribution. They used a reconstruction similar to Gilberts [2.24] SIRT, described in Chapter two. Kim *et al.* [3.14] also improved the technique by calculating the perturbation matrix once only. This method is not favoured, as it is generally agreed that the current injection method of data collection is better than voltage application in obtaining accurate resistivity distributions. This is due to difficulties in measuring the current accurately.

3.9 Double Constraint Method

The double constraint method developed by Wexler [3.15] solves Poisson's equation by the FEM, using Neumann and Dirichlet boundary conditions successively in each iteration. Initially a homogenous resistivity distribution is assumed. The resistivity distribution is updated at each iteration, by using the difference between the two boundary conditions for a given resistivity distribution.

3.10 Summary of EIT Methods:

Finite Element Method (Newton-Raphson)

Make initial guess of resistivity distribution and create FEM model.

Calculate error between the measured boundary voltages and FEM model.

Update until error criterion is met.

Backprojection between Equipotential lines

Approximate the forward solution analytically.

Backproject between the equipotential lines.

Filter to compensate for current distribution and blurring, using a ramp function.

Sensitivity Coefficient Method

Approximate the Forward problem analytically.

Backproject between equipotential lines.

Weight using sensitivity coefficients.

Perturbation Method

For a constant input voltage, change the resistivity of each pixel.

Measure the resulting current change in all electrodes.

Create a perturbation matrix from the above.

From the perturbation matrix and Laplace's equation, backproject the difference between the true and computed current densities.

Double Constraint Method

Calculate the voltage and current density with Neumann boundary conditions.

Calculate the voltages inside, with both Neumann and Dirichlet boundary conditions.

Calculate the new resistivity distribution, from the minimisation of the squared error, between the electric current densities of the above operation.

3.11 Discussion

The objective of this review is to identify the difference between the EIT and X-ray reconstruction procedures. The main difference is indicated by the difficulty in categorising the EIT methods in the same way as those described in Chapter two, as EIT requires solutions to the Forward problem as well as the Inverse. There are some similarities between the two methods. The backprojection method in EIT could be considered as a Transform method, and the FEM algorithms as series expansions.

EIT methods tend to be defined in terms of the types of image they produce. These are defined as dynamic or static images. The backprojection methods produce difference (dynamic) images, showing the change in resistivity from one set of data to the next. The FEM creates static images and requires considerably more time to compute the reconstruction, but the accuracy is increased.

In the FEM approach a model of the resistive distribution is created using FEM. The boundary data obtained from this model are then compared with the measured boundary data. The objective of this method is to minimise the error between the calculated and measured boundary. The most common method for solving this problem is the modified Newton-Raphson algorithm, developed by Yorkey *et al.* [3.17], which gives good images for computer-simulated data. However, there are no reported results which give satisfactory images from measured data, when a physical

phantom is used. This is due to three main reasons:

1) Yorkey *et al.* [3.17] used a FEM model which did not include the electrode-electrolyte contact impedance. Thus it has a large modelling error in $\overline{\mathbf{V}}(\rho)$.

2) The neighbouring method is used to inject current patterns. The resulting voltages $\mathbf{V_0}$ have a poor signal-to-noise (SNR). The FEM modelling error for the injection method is also large due to the non-smooth Neumann conditions, which leads to a poor convergence of the FEM.

3) The information matrix $\overline{\mathbf{V}}'(\rho^k)^T\overline{\mathbf{V}}'(\rho^k)$ is ill-conditioned. This results in an inaccurate inverse matrix and makes the resistivity update very sensitive to the modelling and measurement errors.

Various improvements have being made to the N-R algorithm. Hue *et al.* [3.18] developed a reconstruction method which minimises the effects of the ill-conditioning. They also incorporate a complete FEM model for both the internal and boundary domains, to minimise the modelling error in $\overline{\mathbf{V}}(\rho)$, and used an optimum current-injection and voltage measurement method to obtain the measured data $\mathbf{V_0}$ with maximal SNR. Further improvements were modelled by Woo *et al.* [3.19]. to produce more accurate images, by reducing the undesirable effects of the ill-conditioned Hessian matrix. The results obtained by Woo *et al.* [3.19] do not show any significant improvement in quality.

It can be seen from this review that although there are many approaches to reconstructing images in EIT, no one method produces the definitive solution. The main aim of the research defined in Chapter one is to adapt to EIT the CORT originally developed for X-ray and PET systems, with the objective of obtaining the speed and quality advantages of CORT. It will be seen in later Chapters that the adaptation of CORT lends itself best to dynamic imaging, using the solution of the Forward problem obtained in the backprojection methods described in this Chapter.

4 CONSTRAINED OPTIMISATION

4.1 Introduction

In this Chapter, the third category of reconstruction techniques, known as constrained optimisation, is analysed. The objective of the analysis presented in this Chapter is to embed the reconstruction problem into the framework of a constrained optimisation problem, by the application of variational principles. The methods examined in this section were introduced by Goutis and Durrani [1.29], and extended to define a unified theory by Leahy and Goutis [4.1]. Wood and Morf [1.30], also developed a similar approach based on a general minimum variance estimator. Their algorithms yield reasonable results in the case of low measurement noise and regular measurement geometry. The methods developed by Goutis and Durrani [1.29], were further enhanced by Leahy and Goutis [4.1], to introduce a new technique for image reconstruction from a set of data corrupted by additive noise. The new approach detailed in this Chapter uses a vector space setting and the concept of duality, to optimise a convex or concave cost function, subject to a set of constraints.

The constrained optimisation approach to image reconstruction will form the bases of the algorithms developed for EIT in Chapter six, and the architectures in Chapter eight.

4.2 The Primal Method

The first approach to be considered in developing the constrained optimisation problem is termed the Primal method. This defines the reconstruction problem in the solution space by the application of the Euler-Lagrange method. For a given finite set of projection data with a finite set of samples, the reconstruction problem has an infinite number of solutions. This was indicated in Chapter two by the different choice of convergence criterion, which produced different images. This problem can be

overcome by using constrained optimisation techniques to define a desirable class of images, from which the reconstruction can be selected, or even a unique image by optimising a cost criterion or error function using the projection data as constraints.

The objective of the constrained optimisation approach is to find a suitable cost function that reflects a desirable property of the solution This approach is based on a branch of mathematics called the calculus of variations. The advantage with this approach is that the model used to find the reconstruction of the image is dimensionally reduced, compared with those used in the ART methods described in Chapter two. Estimates of the **1-D** Lagrange multipliers are required rather than the image itself, as in the ART models. The reconstruction problem is formulated as follows.

A general functional $\mathbf{C(.)}$ for a **2-D** image can be expressed in terms of

i) The image $f(\mathbf{x},\mathbf{y})$,

ii) its partial derivatives,

iii) the locations of the continuous image points $\mathbf{x}$ and $\mathbf{y}$.

The reconstruction problem is then stated as follows.

There is a requirement to obtain a function $f(\mathbf{x},\mathbf{y})$ that minimises the functional $\mathbf{C(.)}$ defined as:

$$\mathbf{C(.)} \equiv \mathbf{C}(\mathbf{x},\mathbf{y},f,f_{\mathbf{x}},f_{\mathbf{y}}) \tag{4.1}$$

subject to a set of constraints, where the subscripts are employed to indicate partial differentiation to avoid cumbersome notation. Hence:

$$f_{\mathbf{x}} = \frac{\partial f}{\partial \mathbf{x}} \qquad f_{\mathbf{xy}} = \frac{\partial^2 f}{\partial \mathbf{y}\partial \mathbf{x}} \quad \text{etc.}$$

The proofs developed by Durrani and Goutis [1.29] use the $\mathbf{n^{th}}$ partial derivatives. This was omitted in this analysis to simplify the notation, and will affect the proof only if higher order interpolation is required.

4.2.1 Constraints

In this analysis, the constraints are first assumed to come from a collection system that has a parallel geometry. Other geometries will be considered later. Consider Figure 4.1, in which the parallel geometry is redefined to have a finite width Δt. Then a single strip of integration for the ki^{th} projection at angle θ_k (assuming that any noise is ignored at present), can be defined as:

$$p(t_i,\theta_k) = \int_{t_i}^{t_{i+1}} \int_{A(x_k)}^{B(x_k)} f\,ds\,dt \tag{4.2}$$

where $t_{i+1} - t_i = \Delta t$, or:

$$p(t_i,\theta_k) = \int_{t_i}^{t_{i+1}} \int_{A(x_k)}^{B(x_k)} f(x,y)\,dx_k\,dy_k \tag{4.3}$$

where

$i = 1,2,..,M$ M is the number of samples per projection,

$k = 1,2,..,N$ N is the number of projections,

and

$$\begin{bmatrix} x_k \\ y_k \end{bmatrix} = \begin{bmatrix} +\cos\theta_k & +\sin\theta_k \\ -\sin\theta_k & +\cos\theta_k \end{bmatrix} \begin{bmatrix} x \\ y \end{bmatrix} \tag{4.4}$$

where the Jacobian of the above transformation is unity.

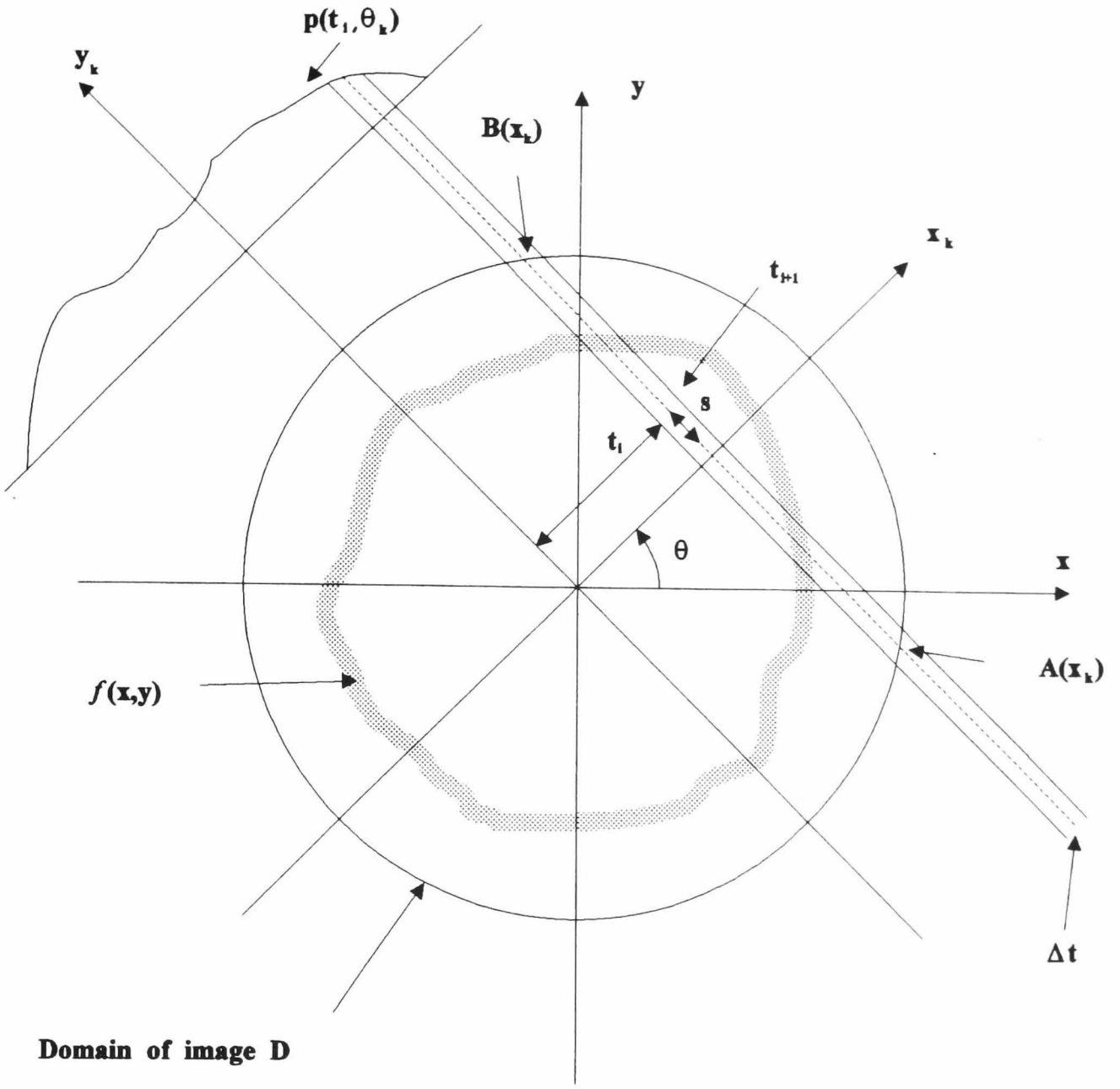

Figure 4.1 Parallel Geometry

To simplify the equation (4.3), let the path defined by the limits **A** and **B** be defined as **s**, and also let the limits of the ray width defined by β_1 and β_2 be defined as **s′**. The ray width is assumed to be a single line for the primal method. Hence equation (4.3), using Cartesian co-ordinates on both sides, can be rewritten as:

$$\mathbf{p_k(x_k) = \int_s f(x,y)dy_k} \qquad \textbf{(4.5)}$$

Using the constraints, the reconstruction problem can be defined as finding a function $f(\mathbf{x},\mathbf{y})$ such that the integral:

$$\mathbf{I} = \int\int_{\mathbf{D}} \mathbf{C}(.)\mathbf{dxdy} \tag{4.6}$$

is a minimum, subject to the constraints:

$$\sum_{\mathbf{k=1}}^{\mathbf{N}} \mathbf{p_k}(\mathbf{x_k}) = \sum_{\mathbf{k=1}}^{\mathbf{N}} \int_{\mathbf{s}} f(\mathbf{x},\mathbf{y})\mathbf{dy_k} \tag{4.7}$$

where **N** is the number of projections, and **D** represents the domain of the image. This can be written as:

$$\sum_{\mathbf{k=1}}^{\mathbf{N}} (\mathbf{p_k}(\mathbf{x_k}) - \int_{\mathbf{s}} f(\mathbf{x},\mathbf{y})\mathbf{dy_k}) = \mathbf{0} \tag{4.8}$$

Using the Euler-Lagrange method [4.2][4.3], a continuous Lagrange multiplier is introduced for every projection, and the Euler-Lagrange equation can be defined as:

$$\mathbf{I} = \int\int_{\mathbf{D}} \mathbf{C}(.)\mathbf{dxdy} + \sum_{\mathbf{k=1}}^{\mathbf{N}} \int_{\mathbf{s'}} \lambda_{\kappa}(\mathbf{x_k})[\mathbf{p_k}(\mathbf{x_k}) - \int_{\mathbf{s}} f(\mathbf{x},\mathbf{y})\mathbf{dx_k}]\mathbf{dy_k} \tag{4.9}$$

Introducing a delta function, and performing co-ordinate transformation whose Jacobians are unity, the above equation can be rewritten as:

$$\mathbf{I} = \int\int_{\mathbf{D}} [\mathbf{C}(.) + \sum_{\mathbf{k=1}}^{\mathbf{N}} \lambda(\mathbf{x}\cos\theta_{\mathbf{k}} + \mathbf{y}\sin\theta_{\mathbf{k}} - \mathbf{t})[\mathbf{p}(\mathbf{x}\cos\theta_{\mathbf{k}} + \mathbf{y}\sin\theta_{\mathbf{k}} - \mathbf{t})\delta(-\mathbf{x}\sin\theta_{\mathbf{k}} + \mathbf{y}\cos\theta_{\mathbf{k}} - \mathbf{t}) - f(\mathbf{x},\mathbf{y})]]\mathbf{dxdy} \tag{4.10}$$

The first term in equation (4.10) represents the criterion to be optimised (or the functional whose cost is to be minimised) by maximising or minimising the area under **C(.)**. The second term does not contribute to the cost criterion as long as the

projections of the reconstructed image, f, equal the available data.

Applying a first order variation to f (appendix A), and using Green's theorem [1.29], a solution for a general optimum is obtained. The condition for which an optimum of $\mathbf{I}$ occurs is satisfied when the following (modified Euler) differential equation holds:

$$\frac{\partial \mathbf{C}}{\partial f} - \frac{\partial}{\partial \mathbf{x}}\left(\frac{\partial \mathbf{C}}{\partial f_{\mathbf{x}}}\right) - \frac{\partial}{\partial \mathbf{y}}\left(\frac{\partial \mathbf{C}}{\partial f_{\mathbf{y}}}\right) - \sum_{\mathbf{k}=1}^{\mathbf{N}} \lambda_{\mathbf{k}}(\mathbf{x}_{\mathbf{k}}) = 0 \qquad \textbf{(4.11)}$$

$\frac{\partial \mathbf{C}}{\partial f}$ represents the variation of the functional form with values of the reconstructed image f.

For a specific cost criterion, a relationship between the desired image $f(\mathbf{x},\mathbf{y})$ and the associated Lagrange multiplier $\lambda_{\mathbf{k}}(\mathbf{x}_{\mathbf{k}})$ can be obtained from the above equation. This relationship is referred to as the model of the image, corresponding to the specific cost function.

4.2.2 Models

The choice of the cost function is very important as it defines the quality of the final reconstructed image and the computational requirements of the system used to evaluate the model. A table of suitable functions and models is given in Table 4.1, which was obtained from Leahy and Goutis [4.1]. This is an updated version of the table Durrani and Goutis [1.29] produced, and includes the dual methods. The cost function restricts the infinite number of functions to a limited subset that satisfy the constraints. A selection of cost criteria are examined in this section.

Table 4.1 **Table of Models**

Cost Criterion	Minimum Energy	Maximum Entropy	Minimum Cross Entropy
	Primal Functionals		
Constraint Sets	$\int_D \frac{f(r)^2}{2} dr$	$\int_D \ln[f(r)]dr$	$\int_D f(r)\ln[\frac{f(r)}{f'(r)}]dr$
Solution	Models		
Unconstrained	$\bar{f}_1(r) = \lambda^T W(r)$	$\bar{f}_2(r) = \frac{1}{\lambda^T W(r)}$	$\bar{f}_3(r) = \frac{f'(r)}{e} \exp[\lambda^T W(r)]$
Bounded	$\bar{f}(r) = \max[\min[\bar{f}_1(r), \beta], \alpha]$	$\bar{f}(r) = \max[\min[\bar{f}_2(r), \beta], \alpha]$	$\bar{f}(r) = \max[\min[\bar{f}_3(r), \beta], \alpha]$
Intensity Constraints	$\bar{f}(r) = f_1(r) + \mu$	$\bar{f}(r) = \frac{1}{f_1(r)+\mu}$	$\bar{f}(r) = \frac{f'(r)}{e} \exp[\bar{f}_1(r) - \mu]$
Noise Constraints	Dual Functionals		
Exact data matching	$\phi_1(\lambda) = \lambda^T p^0 - \int_D \frac{\bar{f}(r)^2}{2} dr$	$\phi_2(\lambda) = \lambda^T p^0 + \int_D \ln[\bar{f}(r)]dr$	$\phi_3(\lambda) = \lambda^T p^0 + \int_D \bar{f}(r)dr$
Variance matching	$\phi(\lambda) = \phi_1(\lambda) - \sqrt{\delta\lambda^T C\lambda}$	$\phi(\lambda) = \phi_2(\lambda) - \sqrt{\delta\lambda^T C\lambda}$	$\phi(\phi) = \phi_3(\lambda) - \sqrt{\delta\lambda^T C\lambda}$
Covariance matching	$\phi(\lambda) = \phi_1(\lambda) - \sum_{i=1}^{N} \sqrt{\delta_i \lambda^T P_k \lambda}$	$\phi(\lambda) = \phi_2(\lambda) - \sum_{i=1}^{N} \sqrt{\delta_i \lambda^T P_k \lambda}$	$\phi(\lambda) = \phi_3(\lambda) - \sum_{i=1}^{N} \sqrt{\delta_i \lambda^T P_k \lambda}$

Summary of Models and Dual Functionals for Various Cost Criteria and Constraints. Note that the Models are affected only by Constraints on the Solution, and the Dual Functionals by Constraints on the error statistics.

$f(\mathbf{r})$ is the desired image defined in section 4.3, $\phi(\lambda)$ is the dual Lagrangian, μ is the intensity constraint (section 4.5), α is the upper bound (section 4.5), β is the lower bound (section 4.5), C denotes the noise covariances [2.16], P_k denotes the periodram matrixes [4.8], δ and δ_i are the confidence limits chosen from tables.

4.2.2.1 Least Squares or Backprojection Model

The Least Squares, or backprojection model, is obtained by using the same criterion for convergence as the unconstrained additive ART defined in the previous Chapter. This defines a model which converges to a solution that minimises the energy of the image. This is the same as minimising the image variance. Therefore, if the variance is substituted into the cost criterion and the mean density is set to zero: $[f^2/2 = \mathbf{C}]$, equation (4.11) can be rewritten as:

$$f(\mathbf{x},\mathbf{y}) - \sum_{k=1}^{N} \lambda_k(\mathbf{x}_k) = 0 \qquad \textbf{(4.12)}$$

This can be rearranged as:

$$f(\mathbf{x},\mathbf{y}) = \sum_{k=1}^{N} \lambda_k(\mathbf{x}_k) \qquad \textbf{(4.13)}$$

which defines the image f in terms of the undefined Lagrange multipliers. To determine the undetermined Lagrange multipliers, the model equation (4.13) is substituted back into equation (4.5) for the projections. Hence the projections are defined as:

$$\mathbf{p}_k(\mathbf{x}_k) = \sum_{k=1}^{N} \int_s \lambda_k(\mathbf{x}_k)\mathbf{dy}_k \qquad \textbf{(4.14)}$$

or in matrix form:

$$\mathbf{p} = \mathbf{G}\lambda \qquad \textbf{(4.15)}$$

where $\mathbf{p}$ and λ are now column vectors, and $\mathbf{G}$ is a system matrix defining the

proportions of λ that contribute to each projection point. Inverting equation (4.15) gives:

$$\mathbf{G^{+}p = \lambda} \qquad \textbf{(4.16)}$$

where $\mathbf{G^{+}}$ is the pseudo inverse of $\mathbf{G}$. The construction of the system matrix is considered in the next Chapter. Its properties are important in the formulation of computer algorithms. The system matrix and its inverse will be examined in more detail in Chapter five.

4.2.2.2 Entropy Based Cost Criteria

The significance of entropy, or uncertainty in image reconstruction, is not clearly defined in the literature. Entropy is considered as a measure of the degree of randomness of a set of random variables. For the image reconstruction problem, entropy is defined as the minimisation of spurious structures in the reconstructed image. The available literature suggests two different definitions of entropy.

The first is borrowed from information theory [4.5], which assumes that each image point emits random discrete particles (photons) with a probability proportional to intensity (brightness). The probability that a photon is emitted from the object situated at $\mathbf{(x,y)}$ is:

$$\mathbf{p(x,y)} = \frac{f(\mathbf{x,y})}{f_{\mathrm{T}}} \qquad \textbf{(4.17)}$$

where $\mathbf{p}$ is the intensity of emission from the $\mathbf{(x,y)}$ point and f_{T} is the total image intensity. If f_{T} is assumed to be unity, the entropy of the probability distribution is:

$$\mathbf{p_1} = -\iint_{\mathbf{D}} f(\mathbf{x,y}) \ln f(\mathbf{x,y}) \mathbf{dxdy} \qquad \textbf{(4.20)}$$

The second definition is taken from work on spectral analysis [4.6]. The problem in the spectrum analysis case is to estimate the power spectrum, which is the

Fourier transform of the auto-correlation function of a stationary random process. $f(x,y)$ is considered as a **2-D** spectrum, hence the second entropy measured is defined as:

$$p_2 = \iint_D \ln f(x,y)\,dx\,dy \tag{4.21}$$

If the first definition of entropy, equation (4.17), is substituted into equation (4.9), the result is:

$$\frac{d(f \ln f)}{df} - \sum_{k=1}^{N} \lambda(x_k) = 0 \tag{4.22}$$

This can be written as:

$$f(x,y) = e^{-1} \exp\left(\sum_{k=1}^{N} \lambda(x_k)\right) \quad x,y \in D \tag{4.23}$$

Employing the Entropy definition 1 model (Table 4.1), the projections can be expressed as:

$$\hat{p}(x_k) = \int_s \exp\left[\left(\sum_{m=1}^{N} \lambda(x_m)\right) - 1\right] dy_k \tag{4.24}$$

where

$$x_m = x\cos\theta_m + y\sin\theta_m \tag{4.25}$$

and

$$x_k = x\cos\theta_k + y\sin\theta_k \tag{4.26}$$

Multiplying equation (4.24) by $\lambda(x_k)$ and integrating over s', we obtain:

$$\sum_{k=1}^{N} \int_{s'} \hat{p}(x_k)\lambda(x_k)\,dx_k = \int_s \int_{s'} f \ln f\,dx\,dy + constant \tag{4.27}$$

which is the cost function. Durrani and Goutis [1.29] define a relationship that allows

an iterative procedure for evaluating the Lagrange function $\lambda(\mathbf{x}_k)$. Using equations (4.24) and (4.27), the cost functional reduces to:

$$\mathbf{I} = \sum_{k=1}^{N} \int_{s'} \lambda(\mathbf{x}_k)\mathbf{p}(\mathbf{x}_k)\mathbf{dx}_k - \int_{s'} \hat{\mathbf{p}}(\mathbf{x}_q)\mathbf{dx}_q \qquad \textbf{(4.28)}$$

where

$$\hat{\mathbf{p}}(\mathbf{x}_q) = \int_{s} \mathbf{exp}[(\sum_{q=1}^{N} \lambda(\mathbf{x}_q)) - \mathbf{1}]\mathbf{dy}_q \qquad \textbf{(4.29)}$$

and $\mathbf{p}(\mathbf{x}_k)$ is defined by equation (4.5).

The Lagrange multiplier may be computed by means of the hill-climbing relationship:

$$\lambda^{m+1}(\mathbf{x}_k) = \lambda^{m}(\mathbf{x}_k) + \gamma \frac{\partial \mathbf{I}}{\partial \lambda(\mathbf{x}_k)}\bigg|_{m} \qquad \textbf{(4.30)}$$

The initial estimate of $\lambda^{0}(\mathbf{x}_k) = \mathbf{p}(\mathbf{x}_k)$ or the normalised value $(\frac{\mathbf{p}(\mathbf{x}_k)}{\mathbf{length\ s}})$ where:

$$\frac{\partial \mathbf{I}}{\partial \lambda(\mathbf{x}_k)}\bigg|_{m} = \mathbf{p}(\mathbf{x}_k) - \hat{\mathbf{p}}(\mathbf{x}_k)$$

and γ is the step length, $\mathbf{m}$ represents the iteration number. The Lagrange functions obtained from equation (4.30) are backprojected, then each pixel is multiplied as indicated in equation (4.31), to give the reconstructed image:

$$f = \mathbf{exp}(-1 + f_1) \qquad \textbf{(4.31)}$$

where f_1 is the reconstructed image obtained from the Lagrange functions.

The main disadvantage of the entropy models is the fact of the non-linear estimation of the Lagrange multipliers being computationally intensive.

4.2.2.3 Minimum Gradient Norm

Durrani and Goutis [1.29] also proposed a minimum gradient norm cost function, which takes into account the effect of local intensity variations and includes a smoothness measure of the image. The cost function consists of a set of gradient terms:

$$\mathbf{I} = \frac{1}{2}\iint_{D} \left(\frac{\partial f}{\partial \mathbf{x}}\right)^2 + \left(\frac{\partial f}{\partial \mathbf{y}}\right)^2 \mathbf{dxdy} \qquad \textbf{(4.32)}$$

The solution of this equation for the parallel case is:

$$-\nabla^2 f(\mathbf{x},\mathbf{y}) = \sum_{\mathbf{k}=1}^{\mathbf{N}} \lambda(\mathbf{x_k}) \qquad \textbf{(4.33)}$$

where

$$\nabla^2 = \frac{\partial^2}{\partial \mathbf{x}^2} + \frac{\partial^2}{\partial \mathbf{y}^2} \qquad \textbf{(4.34)}$$

is known as the Laplacian operator.

The above equation is one form of a Poisson differential equation. This is difficult to solve analytically, though Durrani and Goutis [1.29] derived a solution by considering a frequency domain interpretation. A brief account of the approach is given here for comparison purposes. Let $\mathbf{F(u,v)}$ equal the **2-D** Fourier transform of $\boldsymbol{f(x,y)}$, then:

$$\mathbf{F(u,v)} = \frac{1}{(\mathbf{u}^2+\mathbf{v}^2)} \sum_{\mathbf{k}=1}^{\mathbf{N}} \{\mathbf{L_k(u_k)}\delta(\mathbf{v_k}) ** \mathbf{W(u,v)}\} \qquad \textbf{(4.35)}$$

where $\mathbf{u}$ and $\mathbf{v}$ are the spatial frequencies, and $\mathbf{L_k(.)}$ is the **1-D** Fourier transform of the Lagrange function, $\delta(.)$ is a Dirac delta function, and $**$ is used to denote **2-D** convolution. $\mathbf{w(x,y)}$ is the Fourier transform of the spatial window, defined as:

$$\mathbf{w(x,y)} = \begin{bmatrix} \mathbf{1} & \mathbf{x,y \in D} \\ \mathbf{0} & \mathbf{otherwise} \end{bmatrix} \tag{4.36}$$

The spatial frequencies, representing a rotation by angle θ_k, are defined by:

$$\begin{bmatrix} \mathbf{u_k} \\ \mathbf{v_k} \end{bmatrix} = \begin{bmatrix} \mathbf{\cos\theta_k + \sin\theta_k} \\ \mathbf{-\sin\theta_k + \cos\theta_k} \end{bmatrix} \begin{bmatrix} \mathbf{u} \\ \mathbf{v} \end{bmatrix} \tag{4.37}$$

Using the cost function as the criterion for reconstruction would require computing the Lagrange functions by an iterative procedure, evaluating the Fourier transform, and convolving it with $\mathbf{W(u,v)}$, scaling the **2-D** Fourier transform to obtain $\mathbf{F(u,v)}$, then performing a **2-D** inverse Fourier transform to obtain the reconstructed image.

A cost criterion based on an improvement to the minimising of the mean square deviation of the intensity, which incorporates the minimisation of a weighted sum of the image deviation and local discontinuity to achieve smoother reconstruction, is given by Durrani and Goutis [1.29] as:

$$\frac{\mathbf{1}}{\mathbf{2}}\left[\mathbf{(1-a)f^2 + a}\left\{\left(\frac{\partial \mathbf{f}}{\partial \mathbf{x}}\right)^2 + \left(\frac{\partial \mathbf{f}}{\partial \mathbf{y}}\right)^2\right\}\right] \tag{4.38}$$

where **a** is a weighting factor $\mathbf{0 \le a \le 1}$, which controls the cut-off and roll-off of a symmetric **2-D** filter. A model was obtained for this criterion as:

$$\mathbf{(1-a)f(x,y) - a\nabla^2 f(x,y)} = \sum_{k=1}^{n} \lambda_k(\mathbf{x}_k) \tag{4.39}$$

Applying a **2-D** Fourier transformation yields:

$$\mathbf{F(u,v)} = \frac{\dfrac{\mathbf{1}}{\mathbf{1-a}}}{\mathbf{1} - \left(\dfrac{\mathbf{a}}{\mathbf{1-a}}\right)\left(\mathbf{u^2 + v^2}\right)}\left[\sum_{k=1}^{N} \mathbf{L_k(u_k)\delta(v_k) ** W(u,v)}\right] \tag{4.40}$$

It is suggested by Durrani and Goutis [1.29] that this technique can handle noisy data and can be extended to include higher-order spatial filters. Drossos and Goutis [5.7] also developed other techniques based on the minimum variance model for handling noisy data, which is detailed in Chapter five.

This method was considered as computationally expensive and therefore not explored beyond this analysis for the EIT system, or used in the development of the machine architecture presented in Chapter eight.

4.3 Dual Method

The dual optimisation method is based on the Primal-Dual method given by Luenberger [4.4], (appendix B), whose approach to the optimisation problem uses vector space methods. Due to the choice of interpolation scheme in the Primal method, the solution yielded is the same for the minimum energy model. It is presented here as an example of an alternative approach to developing reconstruction models. This technique was first applied in signal processing by McClellan and Lang [4.7] for solving the multidimensional maximum entropy spectral estimation problem. Unlike the primal method described in the previous section, this approach treats the projection data as discrete from the start. A solution for the reconstruction problem is obtained by the application of the Lagrange multiplier theorem for linear vector spaces. This theorem states that the solution of the constrained primal problem is identical to that of an unconstrained dual problem in which the dual functional is expressed in terms of the Lagrange multiplier vector.

The theoretical formulation of the dual optimisation method was developed by Leahy *et al.* [4.8] for both tomography and spectral estimation. This was extended by Leahy and Goutis [4.1] to produce a general procedure for solving constrained reconstruction and restoration problems. The spectral estimate problem is not addressed in this research.

To demonstrate the dual method, a vector space setting is adopted and hence

vector space notation will be used. The problem can be generalised to include all geometries, but this analysis will be confined to the parallel system illustrated in Figure 4.2. Let the desired image $f(\mathbf{r})$ be an element of the normed linear space (or solution space) **C[D]** of continuous bounded functions, defined on the compact set **D** with norm:

$$\|f\| = \max|f(\mathbf{r})| \; \textit{for all} \; \mathbf{r} \in \mathbf{D} \qquad (4.41)$$

where **r** is a multidimensional co-ordinate vector.

The image is assumed to have non-negative quantities, which is generally the case in practice for X-ray and PET images. This allows the solution to be confined to a convex set. (A set is said to be convex if, given $f_1 \wedge f_2 \in \mathbf{C}$, all points of the form $\alpha f_1 + (1-\alpha) f_2$ with $0 < \alpha < 1$ are in **C**. [4.4]). Hence:

$$\Omega = \{f \in \mathbf{C}|\mathbf{D}|, f(\mathbf{r}) > 0 \forall \mathbf{r} \in \mathbf{D}\} \qquad (4.42)$$

This is an open set, hence all images for which $f(\mathbf{r}) = 0, \forall \mathbf{r} \in \mathbf{D}$ are excluded. Although this is a severe restriction, the image $f(\mathbf{r})$ can take on any value, provided there is an $\varepsilon > 0$ such that $f(\mathbf{r}) > \varepsilon, \forall \mathbf{r} \in \mathbf{D}$ and the value of ε can be arbitrarily small. Physically this means that the image $f(\mathbf{r})$ is never zero or less within the domain, but can be arbitrarily small.

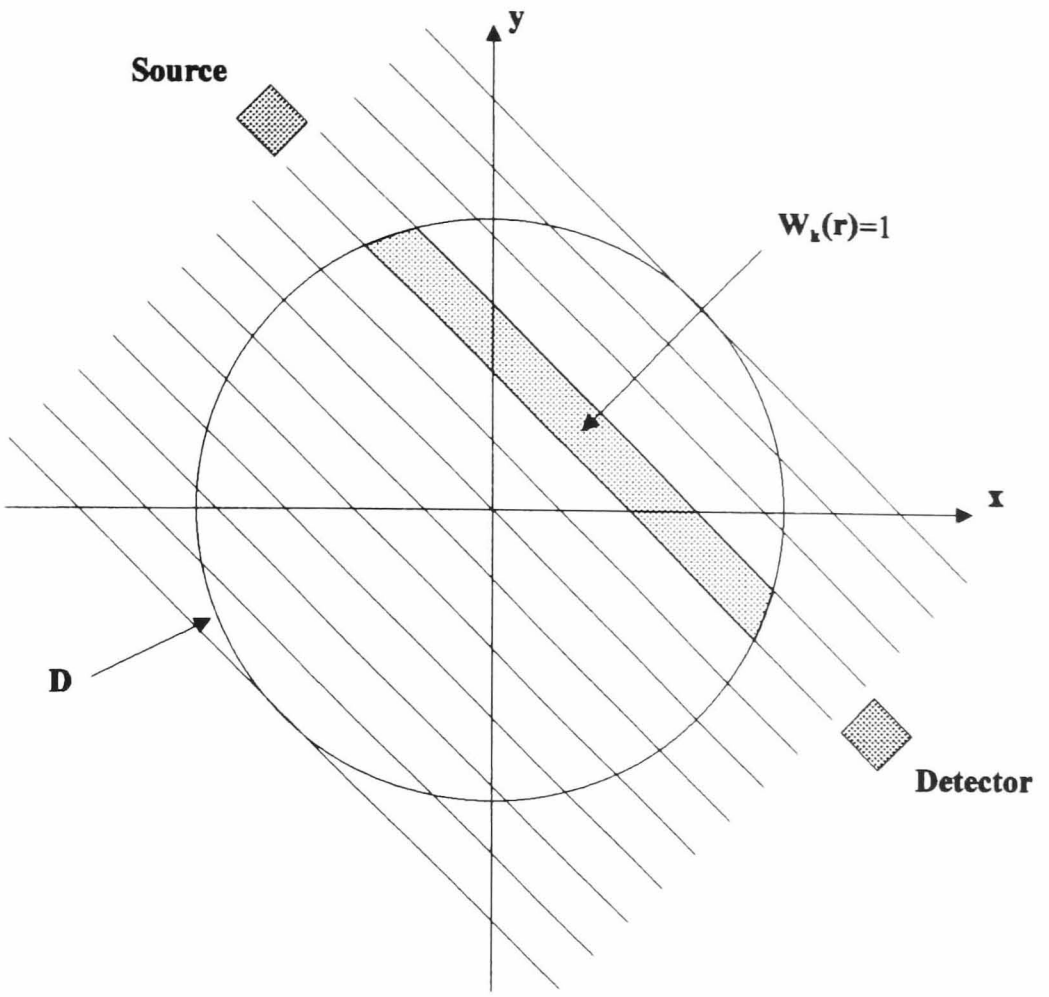

Figure 4.2 The geometry of a parallel beam tomography system illustrating the integral kernel $W_k(r)$, corresponding to the k^{th} projection sample.

Consider first the integral equation for the parallel geometry, shown in Figure 4.2, defined as:

$$\mathbf{p_k} = \int_D f(\mathbf{r})\mathbf{W_k}(\mathbf{r})d\mathbf{r} + \eta_k \qquad \textbf{(4.43)}$$

where $\mathbf{k} = 1, 2, .., N, .., SN$. $\mathbf{W_k(r)}$ defines the region through which the $\mathbf{k^{th}}$ beam passes with an appropriate weighting, and η_k is an additive noise process. The above equation can also be written for a discrete linear system in matrix notation as:

$$\mathbf{p} = \mathbf{Wf} + \eta_k \qquad \textbf{(4.44)}$$

where

$$\mathbf{p}^T = (p_1, p_2, .., p_N) \qquad \textbf{(4.45)}$$

and

$$\eta_k^T = (\eta_1, \eta_2, .., \eta_k) \qquad (4.46)$$

W denotes an **N** by **S** system matrix,

N denotes the number of projections, and

S denotes the number of samples.

4.3.1 Noiseless Solution

For most problems, the prior information available may be separated into two groups of constraints: First, those governing particular properties of the solution such as upper and lower bounds, and second, those based on the statistical properties of the noise. The simplest technique for solving the above equation is to ignore the presence of noise, and find a pseudoinverse of **W** denoted by $\mathbf{W}^+$. Hence the reconstructed image could be obtained from:

$$f = \mathbf{W}^+\mathbf{p} \qquad (4.47)$$

The results from this equation are generally very poor, since noise effects are often amplified in the matrix pseudo inversion, due to the presence of small eigenvalues in **W** [4.1].

4.3.2 Optimal Solution

To examine this method consider again the constraints in vector form. The vector space notation presented below will be used to denote the subvector of **p**, corresponding to the projection angle such that:

$$\mathbf{p}^T = (\mathbf{p}_1, \mathbf{p}_2, \ldots, \mathbf{p}_N) \qquad (4.48)$$

The notations $\mathbf{W}_k(\mathbf{r})$ and λ_k are similarly defined. As the parallel strip is a constant width throughout its length, its width will be defined as having a value of unity for the

strip, and zero outside the boundary of the particular strip. An assumption is made before proceeding with this explanation that each projection subvector is statistically independent, and the noise on each projection is drawn from a multivariate Gaussian process with **S** by **S** covariance matrix **C**. Each component of the subvector $\mathbf{p}_l$ is a scalar defined on the normed linear space denoted by **R** with norm:

$$\|\mathbf{p}\| = \left| \sum_{k=1}^{N} \mathbf{p}_k^2 \right|^{\frac{1}{2}} \qquad \textbf{(4.49)}$$

and **R** is defined as $\mathbf{E}^N$. **R** is assumed to be a convex set containing all functions consistent with the prior knowledge of the system. It is useful to note that the constraints can be considered as priors, as they are normally obtained from the system geometry before the reconstruction problem is solved. Using the above notation, the constraint integral equation (4.43) becomes the linear transformation $\mathbf{G}(f) = \mathbf{p}$ from Ω onto **R**

The aim here is to select a single $f \in \Omega$ that matches the constraints. Hence the dual functional must have the property of being convex to yield a single optimum in Ω. The desire is to find $f \in \Omega$, which minimises $\mathbf{h}(f)$, such that $\mathbf{G}(f) = \mathbf{p}^0$, where $\mathbf{G}(f) = \mathbf{p}^0$ denotes the constraints of the solution that match the given data $\mathbf{p}^0$. This representation combines all the projection samples for each projection into a single vector.

A functional representing a desired feature of the solution can be defined as:

$$\mathbf{h}(f) = \int_{\mathbf{D}} \mathbf{H}(f(\mathbf{r}))\mathbf{dr} \qquad \textbf{(4.50)}$$

where $\mathbf{H}(f(\mathbf{r}))$ denotes the cost function. This functional is assumed to be convex.

The constrained primal problem can be stated using the above vector space notation as: A function $f \in \Omega$ is required which will minimise $\mathbf{h}(f)$, such that $\mathbf{G}(f) = \mathbf{p}^0$.

The solution to the primal problem is identical to that of an unconstrained dual problem, which is obtained by application of a Lagrange multiplier theorem for linear equality constraints. The Lagrange multiplier λ required for optimising the dual problem belongs to the dual space of the constrained space $\mathbf{Z}$. The dual of $\mathbf{E}^N$ is itself $\mathbf{E}^N$, and hence $\lambda \in \mathbf{Z}^*$ where $\mathbf{Z}^*$ denotes the dual space.

From the theorems developed by Leahy *et al.* [4.8], the minimum of the primal problem is defined as:

$$\mu_0 = \inf_{f \in \Omega} \left\{ \mathbf{h}(f) + < \mathbf{p}^0 - \mathbf{G}(f), \mathbf{r}_0^* > \right\} \tag{4.51}$$

where $< \mathbf{p}^0 - \mathbf{G}(f), \mathbf{r}_0^* >$ represents the functional $\mathbf{r}_0^* \in \mathbf{R}^*$ on $\mathbf{p}^0 - \mathbf{G}(f)$.

Two conditions are placed on the above result:

1) μ_0 is finite, this insured by the openness of Ω.

2) There is an $f \in \Omega$ with $\mathbf{p}^0 - \mathbf{G}(\mathbf{f}) = \mathbf{R}$

This follows from the openness of Ω. Equation (4.51) states that there is a $\mathbf{r}_0^* \in \mathbf{R}^*$ which on substitution in equation (4.51) reduces the problem to an unconstrained one. The $\mathbf{r}_0^*$ is unknown, and hence can be found by applying a second theorem to obtain the dual problem as:

$$\mu_0 = \max_{\mathbf{r}^* \in \mathbf{R}^* \ \wedge \ f \in \Omega} \left\{ \inf [\mathbf{h}(f) + < \mathbf{p}^0 - \mathbf{G}(f), \mathbf{r}^* >] \right\} \tag{4.52}$$

The term in the outer brackets is defined as the dual Lagrangian $\phi(\mathbf{r}^*)$. The dual of $\mathbf{R}$ is itself $\mathbf{E}^N$, therefore the Lagrange multiplier $\mathbf{r}^*$ may be written as the vector:

$$\lambda^T = (\lambda_1, \lambda_2, .., \lambda_N) \tag{4.53}$$

where λ_i is a scalar. If μ_0 denotes the minimum of $\mathbf{h}(f)$ at the solution of the primal problem, the identical solution of the unconstrained dual problem is given as:

$$\phi(\lambda) = \inf_{f \in \Omega}[\mathbf{h}'(f)] = \inf_{f \in \Omega}[\mathbf{h}(f) + \sum_{k=1}^{N} \lambda_k (\mathbf{p}_k^0 - \mathbf{p}_k)] \qquad (4.54)$$

The infimum (greatest lower bound) in equation (4.54), is obtained at a stationary point in Ω, at which the Fre´chet derivative [4.4, p.172] of the term in the outer brackets in equation (4.54) is equal to zero. The Fre'chet derivative of the open set Ω is:

$$\delta\mathbf{h}'(f;\mathbf{k}) = \int_D [\frac{\mathbf{dH}(f(\mathbf{r}))}{\mathbf{d}f(\mathbf{r})}\mathbf{k}(\mathbf{r}) - \sum_{k=1}^{N} \lambda_k \mathbf{W}_k(\mathbf{r})]\mathbf{dr} \;\forall f;\mathbf{k} \in \Omega \qquad (4.55)$$

where

$$\delta\mathbf{h}(f;\mathbf{k}) = \lim_{\alpha \to 0} \frac{1}{\alpha}[\mathbf{h}(f + \alpha\mathbf{k}) - \mathbf{h}(f)] \qquad (4.56)$$

Setting the derivative to zero gives:

$$\frac{\mathbf{dH}(f(\mathbf{r}))}{\mathbf{d}f(\mathbf{r})} = \sum_{k=1}^{N} \lambda_k \mathbf{W}_k(\mathbf{r}) \qquad (4.57)$$

If a specific cost function is substituted into equation (4.57), a model for f is obtained in terms of the Lagrange Multiplier vector and the $\mathbf{W}_k(\mathbf{r})$ functions. This optimisation procedure follows the primal-dual method of Luenberger (appendix C), and yields the unconstrained dual functional.

The above procedure can be summarised as follows:

1) Choose the cost functional and define the model using equation (4.57).
2) Substitute this model in $\mathbf{h}'(f)$, equation (4.54), and find the optimum Lagrange multiplier vector λ.

3) Substitute λ back into the model to obtain the final image.

This procedure will yield a single optimum in Ω for any convex cost functional, provided there is at least one $f \in \Omega$ such that $\mathbf{G}(f) = \mathbf{p}^0$, due to the convex nature of the problem.

4.4.3 Image Reconstruction in the Presence of Noise

The models developed in the analysis for the dual optimisation presented in the above sections do not account for measurement noise because they match the projections constraints exactly. These models were extended by Leahy *et al.* [4.8] to express functions $f \in \Omega$ such that the statistics of the error $\varepsilon = \mathbf{G}(f) - \mathbf{p}^0$ comply with those of the measurement noise. It was shown that statistical constraints such as variance, covariance and probability density function (pdf) can be incorporated into a single penalty function $\mathbf{P}(\varepsilon)$. The penalty function should be chosen so that the optimal solution of the constrained problem, subject to one or more constraints, is close to the optimal solution of the unconstrained problem. The cost function $\mathbf{h}(f)$ was used to select a single $f \in \Omega$ complying with the constraints which was shown to be approximately equal to the unconstrained minimisation:

$$\min_{f \in \Omega} \mathbf{h}(f) + \mu \mathbf{P}(\varepsilon) \qquad \textbf{(4.58)}$$

where μ is a positive constant. As μ approaches infinity, the solution of this unconstrained minimisation approaches the constrained minimisation of $\mathbf{h}(f)$. Techniques for solving equation (4.58) and details of the penalty function $\mathbf{P}$ are given in [4.1]. Note that the 'penalty' for violating a constraint is a high value of equation (4.58), the modified objective function.

4.3.4 Minimum Variance and Maximum Entropy Models

The comments made for the primal method described in section 4.22 are also valid for the dual. Hence the same cost criterion can be used to choose the cost functional with this optimisation approach. Therefore, substitution of the convex energy functional in equation (4.56) yields the model:

$$f(\mathbf{r}) = \sum_{k=1}^{N} \lambda_k \mathbf{W}_k(\mathbf{r}) \tag{4.59}$$

Each element λ_k of the Lagrange multiplier vector is backprojected over the region defined by $\mathbf{W}_k(\mathbf{r})$, with appropriate weighting to generate the reconstructed image.

Replacing the model for $f(\mathbf{r})$ in the dual functional equation (4.54) gives:

$$\phi(\lambda) = -\frac{1}{2}\int_D f^2(\mathbf{r})\mathbf{dr} + \mathbf{p}^{0T}\lambda \tag{4.60}$$

and maximising by setting $\nabla\phi(\lambda) = (\mathbf{p} - \mathbf{p}^0)$ produces the linear system:

$$\mathbf{p} = \mathbf{G}\lambda \tag{4.61}$$

where

$$\mathbf{G}(\mathbf{k},\mathbf{l}) = \int_D \mathbf{W}_k(\mathbf{r})\mathbf{W}_l(\mathbf{r})\mathbf{dr} \tag{4.62}$$

The maximum entropy method, as shown in the primal case, can be derived from two definitions:

$$\mathbf{h}_{1e} = \int_D \ln(f(\mathbf{r}))\mathbf{dr} \tag{4.63}$$

or

$$\mathbf{h}_{2e} = -\int_D f(\mathbf{r})\ln(f(\mathbf{r}))\mathbf{dr} \tag{4.64}$$

The latter is used by Minerbo [4.9] to produce a multiplicative model for Tomography, and the former yields the model [4.8]:

$$f(\mathbf{r}) = \frac{1}{\sum_{k=1}^{N} \lambda_k W_k(\mathbf{r})} \tag{4.65}$$

with the dual functional:

$$\phi(\lambda) = \int_D \ln(f(\mathbf{r}))d\mathbf{r} + \mathbf{p}^{0T}\lambda \tag{4.66}$$

4.4 Geometries

The theory in the preceding sections dealt with reconstruction of images from their parallel projections. In generating these parallel data, a source and detector combination has to scan linearly over the length of a projection, then rotate through a certain angular interval, and scan linearly over the length of the next projection, etc. A complete set of projection data can require a few minutes to collect. A much faster way to generate the line integrals is to use the fan beam geometry described in Chapter one. A complete projection can be obtained in the same time period as a single line integral measurement of the parallel geometry. There are two types of fan projection geometry, depending upon whether the projections are sampled at equiangular or equispaced intervals. Only the equiangular systems are reviewed in this research, as no investigation at present has taken place using CORT for equispaced intervals. This Chapter only reviewed the parallel geometry. In the next Chapter the Divergent ray geometry is reviewed in association with the system matrix produced by the data collection structure. New geometries associated with the EIT data collection system are then introduced in Chapter six.

4.5 Priors

In many systems, the properties of the solution may be known in the form of the upper and lower bounds on the image, the overall intensity, or regions of zero intensity. For most problems, the prior information, assuming it is available, can be

separated into two groups of constraints: first those governing particular properties of the solution such as upper and lower bounds, and second, priors based on the statistical properties of the noise.

The properties can be utilised in the formation of a solution as follows.

Let $\mathbf{R}_i$ denote constraints sets based on the solution properties, and $\mathbf{S}_i$ denote constraints based on noise statistics. Hence the Upper and Lower bounds can be defined by two constants α and β, then $f(\mathbf{r})$ must belong to the following set:

$$\mathbf{R}_1 = \{f \in \Omega : \alpha \le f(\mathbf{r}) \le \beta \forall \mathbf{r} \in \mathbf{D}\} \qquad \textbf{(4.67)}$$

For intensity constraints, if an overall upper intensity bound $\mathbf{I}_0$ is known, the constraint set may be defined as:

$$\mathbf{R}_2 = \left\{ f \in \Omega : \int_{\mathbf{D}} f(\mathbf{r}) d\mathbf{r} \le \mathbf{I}_0 \right\} \qquad \textbf{(4.68)}$$

In most reconstruction problems, certain properties of the noise process are known or may be measured. Background noise, for example, may be measured without a signal and its statistics obtained empirically. Alternatively, the noise process may be characterised by using known physical models.

If the use of priors such as the noise statistics is to be exploited in EIT, further investigations into the nature and properties of the noise are required. In the EIT system the noise statistics are not easily obtained. For example, the capacitance of the electrode leads collecting the measurement data will vary as their position changes. As yet, there has been no reported studies on characterisation of the background noise.

Normally the noise constraints can be introduced as constraint sets defined in the solution space. Leahy and Goutis [4.1] introduced the notation Γ_i to define the image of the set $\mathbf{S}_i \subset \Omega$ in $\mathbf{R}^N$, under the linear transformation $\mathbf{G}$, as:

$$\Gamma_i = \{\mathbf{p} \in \mathbf{R}^N : \mathbf{G}(f) = \mathbf{p} \text{ for some } f \in S_i\} \qquad (4.69)$$

The usual method for defining constraint sets is to construct confidence regions about the expected values of the statistics such that the estimate has a 95 per cent likelihood of lying within this region if it is drawn from the correct distribution. Although such a choice is intuitively appealing and has been widely used [4.10], there are problems associated with it. Since the set boundary forms an upper bound on the statistic (lower bounds are not used in general, since they result in non-convex sets), the nature of the constrained optimisation method is such that the solution will usually lie on the boundary of the set, and hence the choice of the confidence region will affect the final solution.

A suggestion for applying the above to EIT is given in Chapter nine. More details of the different constraints, such as variance matching constraints and covariance matching constraints, can be found in Leahy and Goutis [4.1]

4.6 Discussion

Leahy and Goutis [4.1] demonstrated that dual methods are better suited to CT problems, where constraints are imposed only on the error statistics. The advantage arises from the differing structure of the primal and dual models. In the primal model, the algorithm requires the calculation or storage of the intersection of the beam paths with the square pixels. This is computationally expensive and there is little common geometric structure between different projection angles. In the dual case, the model is a function of the beam paths, and the algorithm requires only the calculation of the intersections of overlapping beam paths. This gives regions of more regular structure than the path/pixel intersections and is exploited to reduce significantly computational requirements. When the solution itself is constrained, however, the relative merits of the two methods are not so clear.

It should be noted that the interpolation scheme used to generate the **1-D**

Lagrange multipliers primal model from their discrete values, is the same as the one adopted for the backprojection functions $\mathbf{W_k(r)}$ dual model. This gives minimum energy models which are identical. The interpolation scheme is required as only a finite number of data points per projection are available to estimate the continuous Lagrange multipliers.

5 COMPUTER ALGORITHMS

5.1 Introduction

The structure of the system matrix, which depends upon the collection geometry, is critical in the formulation of various algorithms for reconstruction. Over the next two Chapters, four system matrices are presented, relating to specific collection geometries. The parallel and fan beam geometries associated with X-ray and PET systems are analysed in this Chapter as necessary precursors to the more complex curvilinear geometries. Also given is the selection of specific algorithms used to compute the Lagrange multipliers.

The reconstruction algorithms examined in this Chapter were developed by Durrani and Goutis [1.28], and extended by Goutis and Drossos [5.7]. Two main algorithms, including their variations, are presented. These are known as the Recursive and Direct algorithms. Although other algorithms exist, these were selected for their suitability for adaptation to new EIT geometries introduced in Chapter six.

In the previous Chapter, the minimum variance model was formulated for parallel geometry by choosing as the cost function the variance between the reconstructed image and the original. This yields a backprojection model in terms of the Lagrange multipliers. The choice of a suitable cost function reflects the desirable properties of the solution, these properties being determined by the nature of the image produced by the reconstruction. The minimum variance model was selected for the EIT implementation presented in the next Chapter because it produces smooth reconstruction which is ideal for resistivity images. This model is linear, which has proved to be very popular, due to its relative simplicity for computation. All the algorithms presented in this Chapter are based on the minimum variance model.

5.2 Parallel System Matrix Structure

Both Goutis [1.29] and Drossos [5.7] utilise the structure of the system matrix

to accelerate the reconstruction algorithm. This minimises the number of operations required to compute the Lagrange multipliers. The reconstruction of the associated system matrix and the iterative algorithm are given below:

Consider the minimum variance parallel model, derived in the previous Chapter (eqn. 4.13), which expressed the image $f(x,y)$ in terms of the **1-D** continuous Lagrange multiplier functions $\lambda_k(x_k)$ as:

$$f(x,y) = \sum_{n=1}^{N} \lambda_n(x_n) \qquad (5.1)$$

The Lagrange multiplier functions can be estimated from the measured projections using:

$$p_k(x_k) = \sum_{n=1}^{N} \int_{-\sqrt{r^2-x_k^2}}^{\sqrt{r^2-x_k^2}} \lambda_n(x_n)\,dy_k \qquad (5.2)$$

where

$$\begin{aligned} x_k &= \quad x\cos\theta_k + y\sin\theta_k \\ y_k &= -x\sin\theta_k + y\cos\theta_k \end{aligned} \qquad (5.3)$$

and r denotes the radius of the domain **D**, as illustrated in the previous Chapter in Figure 4.1. The strip width is assumed to be constant.

Determining the Lagrange multipliers from equation (5.2) will allow the evaluation of the Lagrange multipliers as defined in equation (5.1). For discrete data, the projections are assumed to have S samples per projection. The matrix version of equation (5.2) leads to:

$$p_k = \sum_{z=1}^{N} G_{kz}\lambda_z \quad , k = 1,2,\ldots,N \qquad (5.4)$$

where

$$\mathbf{p}_k^T = [\mathbf{p}_k(\mathbf{x}_1), \mathbf{p}_k(\mathbf{x}_2), .., \mathbf{p}_k(\mathbf{x}_k), .., \mathbf{p}_k(\mathbf{x}_S)] \quad = \mathbf{SN} \text{ row vector}$$

$$\lambda_z^T = [\lambda_z(\mathbf{x}_1), \lambda_z(\mathbf{x}_2), .., \lambda_z(\mathbf{x}_q), .., \lambda_z(\mathbf{x}_s)] \quad = \mathbf{SN} \text{ row vector}$$

and

$$\mathbf{x}_q = -\mathbf{r} + (2\mathbf{q} - 1)\frac{\mathbf{r}}{\mathbf{S}} \quad , \mathbf{q} = 1, 2, \ldots, \mathbf{S}$$

$\mathbf{T}$ denotes the transposition,

$\mathbf{G}_{kz}$ is an $\mathbf{S}$ by $\mathbf{S}$ matrix.

If the projections are taken at equi-spaced angles, then each matrix $\mathbf{G}_{kz}$ depends only on the angle:

$$|\theta_n - \theta_k| = \left|\frac{\pi}{\mathbf{N}}(\mathbf{n} - \mathbf{k})\right| \qquad \textbf{(5.5)}$$

The blocks $\mathbf{G}_{kk}$ are diagonal for all $\mathbf{k}$. Equation (5.4) may be rewritten as:

$$\mathbf{p} = \mathbf{G}\lambda \qquad \textbf{(5.6)}$$

$\mathbf{G}$ in equation (5.6) is a system matrix which defines the proportions of λ's that contribute to each projection point. The system matrix, in effect, can be seen as representing the weighting on $\mathbf{G}$ due to the intersections of the parallel rays.

In practice, a finite number of data points per projection are available. An interpolation scheme is employed to estimate the continuous Lagrange multipliers from their values at a finite number of points. If the Lagrange multipliers are considered to be constant, then the elements of the $\mathbf{G}$ matrix will be dependent only on the limits of integration defined in equation (5.2). Hence, whatever the formulation of a solution to equation (5.3), to find the unknown Lagrange multipliers λ, the construction of the $\mathbf{G}$ matrix can be considered as independent of the projection data, and defined only by the physical geometry of the reconstruction data collection system. This allows the inverse

of the matrix to be computed in non-real time.

The **G** matrix is well structured and is known as a block circulant matrix. It consists of $\mathbf{N^2}$ submatrices, each **S** by **S** in size. The elements of the matrix **G** will depend only on the interpolation scheme used to estimate their values. If the radiation source used to obtain the projection data has a definable width, then the line integral that defines the element value within the projection subvector can also be assumed to have width. This leads to the assumption that the projections are formed from strips, and the values within the strips are taken to be constant (i.e., zero order interpolation). If λ_n is taken to be a constant, the elements in the submatrix depend only on the area of the intersection of the strips. If the path formed by a strip of width **d** at angle θ_n is defined as $|\mathbf{A}|$ and the path formed by a strip of the same width at angle θ_k is defined as $|\mathbf{B}|$, then the value of the element will be the area of a parallelogram formed by the intersection of the strips, as shown in Figure 5.1. If $\pi - |\theta_n - \theta_k|$ is equal to θ, then the area of the parallelogram is given by:

$$|\underline{\mathbf{A}} \times \underline{\mathbf{B}}| = |\mathbf{A}||\mathbf{B}| \sin\theta = \frac{\mathbf{d}}{\sin\theta}\frac{\mathbf{d}}{\sin\theta}\sin\theta = \frac{\mathbf{d}^2}{\sin\theta} \qquad (5.7)$$

where $\mathbf{0} \le \theta_n, \theta_k < \pi$ and **d** is the width of the strip. This produces constant values in the submatrix.

The intersection of strips outside the domain of **D** is not considered, and the matrix element values associated with them are set to zero. This limitation on the circular domain **D** gives a block circulant structure to the system matrix which can also be seen in the other geometries considered later in this section. The edge elements are estimated separately and produce variable values in an elliptic boundary of the submatrices.

It can be observed from Figure 5.1 that each submatrix $\mathbf{G}_{kz}$ is symmetric with respect to the first and second diagonals. This is termed 'radial symmetric', as indicated by the shaped areas in Figure 5.1(a).

Equal intersection areas

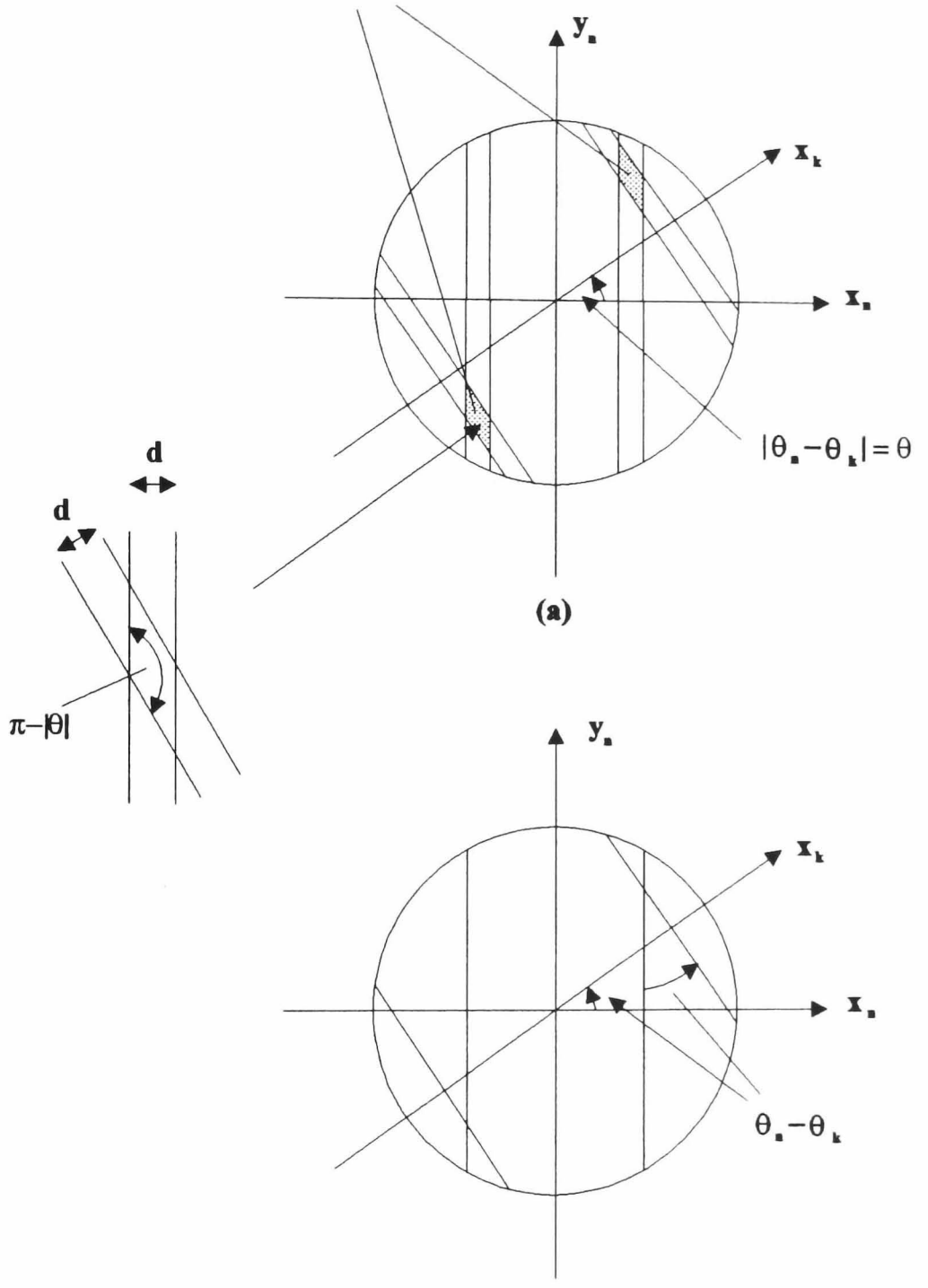

Figure 5.1 Intersecting strips in parallel geometry

The structure of the **G** matrix is fully contained within the first half block row shown in equation (5.8):

$$\begin{bmatrix} \mathbf{G}_0 & \mathbf{G}_1 & \mathbf{G}_2 & .. & \mathbf{G}_{\frac{N-1}{2}} & \tilde{\mathbf{G}}_{\frac{N-1}{2}} & .. & \tilde{\mathbf{G}}_1 \\ \mathbf{G}_1 & \mathbf{G}_0 & \mathbf{G}_1 & .. & \mathbf{G}_{\frac{N-3}{2}} & .. & .. & \tilde{\mathbf{G}}_2 \\ \mathbf{G}_2 & \mathbf{G}_1 & \mathbf{G}_0 & .. & .. & .. & .. & .. \\ .. & .. & .. & .. & .. & .. & .. & .. \\ \tilde{\mathbf{G}}_1 & \tilde{\mathbf{G}}_2 & .. & \tilde{\mathbf{G}}_{\frac{N-1}{2}} & \mathbf{G}_{\frac{N-1}{2}} & .. & .. & \mathbf{G}_0 \end{bmatrix} \qquad (5.8)$$

where

$$\mathbf{G}_{kz} = \mathbf{G}_{|k-z|} = \mathbf{E}\tilde{\mathbf{G}}_{|k-z|} \qquad (5.9)$$

and

$$\mathbf{E} = \begin{bmatrix} 0 & .. & 1 \\ .. & 1 & .. \\ 1 & .. & 0 \end{bmatrix} \qquad (5.10)$$

E is called an exchange matrix, and the **G** matrix is known as a permuted block circulant matrix. The tilde (~) denotes the permutation effect. Each non-diagonal submatrix consists of three regions (Figure 5.3): zero, variable values in the transition band, and constants. A plot of the matrix for $\mathbf{S} = 5$ and $\mathbf{N} = 5$ is presented in Figure 5.2 which demonstrates the structure of the **G** matrix with pseudo colour.

The structure of the submatrices can be utilised to reduce the storage requirements and to assist in formulation of the algorithm to compute the unknown Lagrange multipliers.

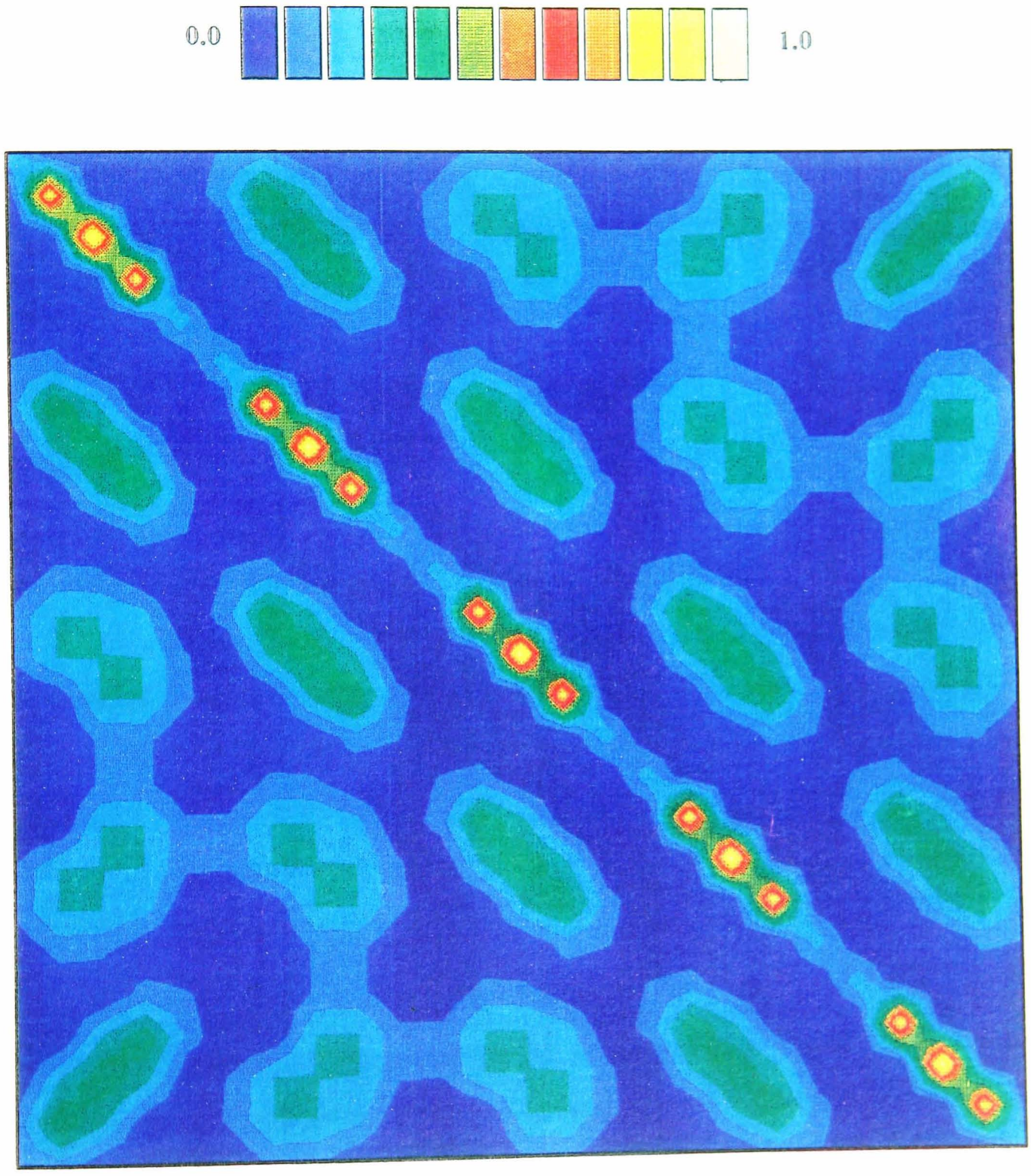

Figure 5.2 Plot of the system matrix (eqn. 5.8) for parallel system S = 5 N = 5

5.3 Recursive Algorithms

There are a number of ways to formulate a solution to find the Lagrange multipliers. To reduce the computation time, a number of assumptions are made which assist in the construction of the system matrix and processing of the inverse. These assumptions are based on the physical constraints of the collection system.

A block successive relation method was used by Goutis and Drossos [5.1] for the solution of the system given in equation (5.4) and this is presented below. The properties of the **G** matrix are utilised to reduce the computational requirements. The solution to the system in equation (5.4) is given by:

$$\lambda_{kd}^{n+1} = \lambda_{kd}^{n} + \frac{\gamma}{G_0(i,i)}\varepsilon_{kd} \qquad (5.11)$$

where

$$\varepsilon_{kd} = p_{kd} - \hat{p}_{kd}^{n} \qquad (5.12)$$

n is the number of iterations, and γ is the relaxation parameter.

This is similar to the recursive algorithm given for ART methods, except the structure of the system matrix used is well defined, and can be used to reduce the number of operations. ε_{kd} is the error between the estimated and measured projections and is used to define the number of iterations. **n** is defined to match the statistics of the noise in the true projections to the error ε_{kd}. The initial estimate of the Lagrange multiplier is obtained using:

$$\lambda_{kd}^{0} = \frac{p_{kd}}{G_0(i,i)} \;\forall\; ki \qquad (5.13)$$

The structure of the associated system matrix is used to obtain fast implementation by making use of areas of equal elements in the submatrices. Every submatrix is symmetric with respect to the first and second diagonal.

The algorithm is based on the observation that the product of the i^{th} subrow and a subvector is equal to the product of the previous $(i-1)^{th}$ subrow and the subvector plus the product of the difference subrow and the subvector. The i^{th}

difference subrow is generated by subtracting each element of the $(\mathbf{i}-\mathbf{1})^{\text{th}}$ subrow from the corresponding element of the $\mathbf{i}^{\text{th}}$ subrow. The number of nonzero elements in the difference subrow is very small as the submatrix differs in a few elements only. This is illustrated in Figure 5.3.

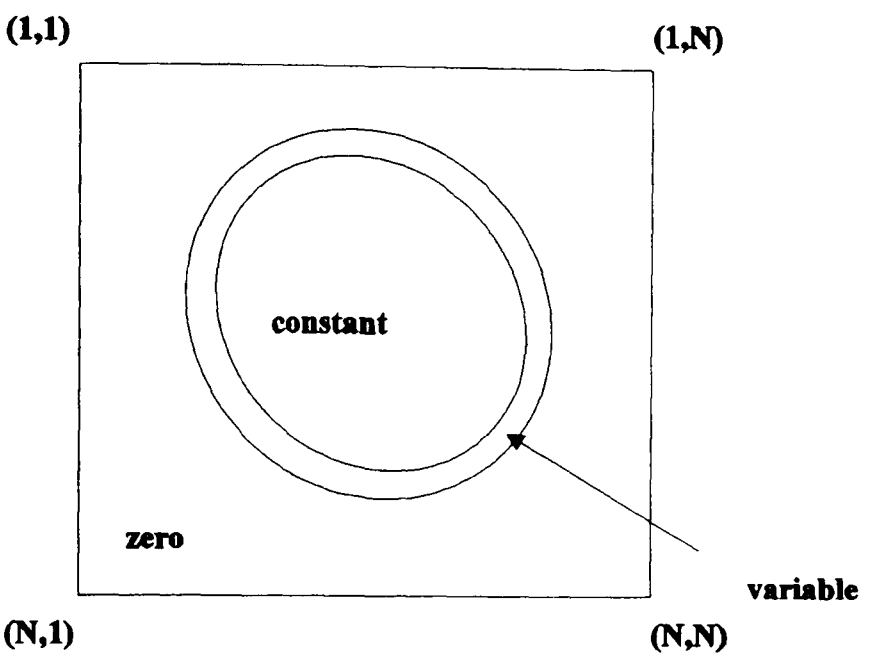

Figure 5.3 Submatrix structure

The average variable number of non-zero elements in the difference submatrix is defined by $\beta = \mathbf{3}$. Hence the product of the $\mathbf{i}^{\text{th}}$ subrow and subvector require β instead of $\mathbf{S}$ arithmetic operations. This reduces the storage requirements. A summary of the basic algorithm is given below:

Step 1: Calculate $\mathbf{G_k}$ for $\mathbf{k} = \mathbf{0,1,2,..,}\frac{\mathbf{N}}{\mathbf{2}}$

Step 2: Derive the difference submatrices $\Delta\mathbf{G_k}$ for $\mathbf{k} = \mathbf{0,1,2,..,}\frac{\mathbf{N}}{\mathbf{2}}$,

i.e. in each $\mathbf{G_k}$ replace the $\mathbf{i}^{\text{th}}$ subrow by the difference of the $(\mathbf{i}-\mathbf{1})^{\text{th}}$ subrow, for $\mathbf{i} = \mathbf{2,3,..,S}$.

Step 3: Store every nonzero element of $\Delta\mathbf{G_k}$, also store the necessary indices to identify the elements.

Step 4: Compute the initial estimate of the Lagrange multipliers using:

$$\lambda_{ki}^{0} = \frac{p_{ki}}{G_0(i,i)} \forall ki$$

Step 5: Estimate $\hat{p}_{ki}^{n}$, $i = 1, 2, .., S$, from λ^n and the difference matrix.

Note that the product of a subvector and the i^{th} subrow is equal to the sum of its products, with the $(i-1)^{th}$ subrow and the i^{th} difference subrow respectively.

Step 6: Update λ^{th}. Hence:

$$\lambda_{ki}^{n+1} = \lambda_{ki}^{n} + \frac{\gamma}{G_0(i,i)}(p_{ki} - \hat{p}_{ki}^{n})$$

where $i = 1, 2, .., S$ and γ is the relaxation factor.

Steps 5 and 6 are repeated for all projections, until the statistics of the error

$$\varepsilon_{ki} = p_{ki} - \hat{p}_{ki}$$

between the estimated and measured projections become approximately equal to the statistics of the noise in the true projection data.

Step 7: Backproject the λ's to produce the reconstruction.

It should be noted that steps 1 to 3 are performed once only for the specific geometry of the collection system in order to pre-compute ΔG_k, which is stored for use in all future reconstructions.

If $\gamma = 1$, the successive relaxation procedure is the same as a Gauss-Seidel iteration method [5.4]. For Gaussian noise, the value of the relaxation parameter γ should be kept small to allow enough iterations to take place and hence make the error as Gaussian as possible.

As there has been no approximation in the solution of the system given in equation (5.3), the algorithm converges. In contrast, the ART methods oscillate due to

the effect of the approximation on critical eigenvalues. Examples of the results obtained for the parallel case are shown by Durrani and Goutis [1.28]. For the parallel beam case with a limited number of projections (41) and (80) points per projection, the reconstruction is of reasonable quality. The fan beam image gives a poorer reconstruction, particularly on the periphery. The results do not demonstrate the effect of noise added to the projection data. The quality of the fan beam was improved by Drossos [5.4].

5.4 Direct Algorithms

The iterative method detailed in section 5.2.2 used the structure of the matrix to reduce the computation required. To obtain the Lagrange multipliers, a number of iterations **n** are required. **n** is dependent on the match of the statistics of the measurement noise to the statistics of the projection error:

$$\boldsymbol{\varepsilon} = (\mathbf{p} - \hat{\mathbf{p}}^{\mathbf{n}}) \qquad \textbf{(5.14)}$$

There are a number of ways by which the system matrix can be directly inverted. Two methods have been developed and are presented in the following sections. The first method was developed originally by Durrani and Goutis [1.28] and is known as the DFT inverse or nonrecursive algorithm. This technique is presented to demonstrate the evolution of the algorithm chosen for the new geometries. The second method was developed by Drossos [5.4] and is based on the Jacobi iteration method.

5.4.1 DFT Inverse Algorithm (Nonrecursive Algorithm)

As the associated system matrices are circulant, they can be diagonalised using block DFT techniques and the inverted block eigenvalues can be stored for future use. This block diagonalised form of the inverse matrix can be utilised to produce fast direct algorithms. The diagonalisation of a circulant matrix is given by Hunt [5.2] and was

extended for block and permuted block circulant matrices by Durrani and Goutis [1.28] to produce a fast algorithm. First a brief account of the diagonalisation process is given.

5.4.2 Diagonalisation of Block and Permuted Block Circulant Matrices

The submatrices of **G** are known as circulant matrices, consisting of **S** by **S** different elements. The rows of the **G** submatrices are related by a circular shift to the right That is, the last element in one row is equal to the first element in the row immediately below. This is illustrated in the following equation:

$$\mathbf{G}_{\text{Circulant}} = \begin{bmatrix} \mathbf{g}_0 & \mathbf{g}_1 & \mathbf{g}_2 & .. & \mathbf{g}_{N-1} \\ \mathbf{g}_{N-1} & \mathbf{g}_0 & \mathbf{g}_1 & .. & \mathbf{g}_{N-2} \\ .. & .. & .. & .. & .. \\ \mathbf{g}_1 & \mathbf{g}_2 & \mathbf{g}_3 & .. & \mathbf{g}_0 \end{bmatrix} \qquad (5.15)$$

A block circulant matrix has a similar structure to the circulant matrix, except that the element of the matrix are themselves circulant matrices. The block circulant matrix has the form:

$$\mathbf{G}_{\text{Block circulant}} = \begin{bmatrix} \mathbf{G}_0 & \mathbf{G}_1 & \mathbf{G}_2 & .. & \mathbf{G}_{N-1} \\ \mathbf{G}_{N-1} & \mathbf{G}_0 & \mathbf{G}_1 & .. & \mathbf{G}_{N-2} \\ .. & .. & .. & .. & .. \\ \mathbf{G}_1 & \mathbf{G}_2 & \mathbf{G}_3 & .. & \mathbf{G}_0 \end{bmatrix} \qquad (5.16)$$

The permuted block circulant matrices were described briefly in section 5.2.1. This type of matrix was introduced by Goutis [5.3]. Each block row is generated from the preceding one by post-, or pre-, multiplication of the last submatrix by an exchange matrix, illustrated in equation (5.10).

The diagonalisation of a circulant matrix is given by Hunt [5.2] as:

$$\mathbf{G}_{\text{Circulant}} = \mathbf{W}\mathbf{D}\mathbf{W}^{-1} \qquad (5.17)$$

where $\mathbf{D}$ is an $\mathbf{N}$ by $\mathbf{N}$ diagonal matrix, whose elements are the eigenvalues of $\mathbf{G}_{\mathbf{Circulant}}$, and $\mathbf{W}$ is an $\mathbf{N}$ by $\mathbf{N}$ matrix with columns of $\mathbf{N}$ linearly independent eigenvectors of $\mathbf{G}_{\mathbf{Circulant}}$. Hunt [5.2] demonstrated that the $\mathbf{k}^{\mathbf{th}}$ eigenvalue of $\mathbf{G}_{\mathbf{Circulant}}$, denoted by $\mathbf{y(k)}$, is equal to the $\mathbf{k}^{\mathbf{th}}$ harmonic of the DFT of the first row of $\mathbf{G}_{\mathbf{Circulant}}$:

$$\mathbf{y(k)} = \sum_{\mathbf{i=0}}^{\mathbf{N-1}} \mathbf{g(i)} \exp\left(\mathbf{j}\frac{2\pi}{\mathbf{N}}\mathbf{ki}\right) \tag{5.18}$$

where $\mathbf{k} = \mathbf{0,1,2,..,N-1}$ and the eigenvectors are given as:

$$\mathbf{w(k)} = \begin{bmatrix} \mathbf{1} \\ \exp\left(\mathbf{j}\frac{2\pi}{\mathbf{N}}\mathbf{k}\right) \\ \exp\left(\mathbf{j}\frac{2\pi}{\mathbf{N}}\mathbf{2k}\right) \\ \mathbf{..} \\ \exp\left(\mathbf{j}\frac{2\pi}{\mathbf{N}}\mathbf{(N-1)k}\right) \end{bmatrix} \tag{5.19}$$

for $\mathbf{k} = \mathbf{0,1,2,..,N-1}$. The collection of the column vectors $\mathbf{w(k)}$ into a matrix is denoted by $\mathbf{W}$:

$$\mathbf{W} = [\mathbf{w(0), w(1), w(2),.., w(N-1)}] \tag{5.20}$$

The $\mathbf{ki}^{\mathbf{th}}$ element of $\mathbf{W}$ is:

$$\mathbf{W(k,i)} = \exp\left(\mathbf{j}\frac{2\pi}{\mathbf{N}}\mathbf{ki}\right) \tag{5.21}$$

and the inverse has the form:

$$\mathbf{W^{-1}(k,i)} = \frac{\mathbf{1}}{\mathbf{N}}\exp\left(-\mathbf{j}\frac{2\pi}{\mathbf{N}}\mathbf{ki}\right) \tag{5.22}$$

Hence $\mathbf{W^{-1}}$ is the DFT matrix, and the element circulant matrix $\mathbf{G}_{\mathbf{Circulant}}$ can be diagonalised using the DFT. This can be extended to include block circulant and permuted block circulant matrices, to produce block and permuted block diagonal matrices. The diagonalisation of the latter was examined in detail by Durrani and

Goutis [1.28].

The transform matrix for diagonalising block circulants is constructed as follows. Let:

$$\mathbf{w_S(i,m) = exp(j\frac{2\pi}{S}im)} \qquad \textbf{(5.23)}$$

and

$$\mathbf{w_N(k,n) = exp(j\frac{2\pi}{N}kn)} \qquad \textbf{(5.24)}$$

Based on this notation, a matrix **W** is defined as having elements **SN** by **SN**, and containing $\mathbf{S^2}$ partitions of size **N** by **N**. The $\mathbf{im^{th}}$ partition of **W** is:

$$\mathbf{W(i,m) = w_S(i,m)W_N} \qquad \textbf{(5.25)}$$

for **i, m = 0,1,2,..,S-1**. Then $\mathbf{W_N}$ is an **N** by **N** matrix with elements:

$$\mathbf{W_N(k,n) = w_N(k,n)} \qquad \textbf{(5.26)}$$

for **k,n = 0,1,2,..,N-1**

The inverse matrix $\mathbf{W^{-1}}$ is also of size **SN** by **SN**, with $\mathbf{S^2}$ partitions of size **N** by **N**. The $\mathbf{im^{th}}$ partition of $\mathbf{W^{-1}}$, symbolised as $\mathbf{W^{-1}(i,m)}$, is:

$$\mathbf{W^{-1}(i,m) = \frac{1}{S}w_N^{-1}(i,m)W_N^{-1}} \qquad \textbf{(5.27)}$$

where $\mathbf{w_S^{-1}(i,m)}$ is:

$$\mathbf{w_S^{-1}(i,m) = exp(-j\frac{2\pi}{S}im)} \qquad \textbf{(5.28)}$$

for **i,m = 0,1,2,..,S-1**. The matrix $\mathbf{W_N^{-1}}$ has elements:

$$\mathbf{W_N^{-1}(k,n) = \frac{1}{N}w_N^{-1}(k,n)} \qquad \textbf{(5.29)}$$

where

$$w_N^{-1}(k,n) = \exp(-j\frac{2\pi}{N}kn) \qquad (5.30)$$

for **k,n =0,1,2,..,N-1**. It can be verified, by direct substitution of the elements of **W** and $\mathbf{W}^{-1}$, that:

$$\mathbf{WW}^{-1} = \mathbf{W}^{-1}\mathbf{W} = \mathbf{I} \qquad (5.31)$$

where **I** is the **SN** by **SN** identity matrix.

From the results for the circulant matrix, and if G is a block circulant matrix, it can be shown that:

$$\mathbf{G} = \mathbf{WDW}^{-1} \qquad (5.32)$$

or

$$\mathbf{D} = \mathbf{W}^{-1}\mathbf{GW} \qquad (5.33)$$

5.4.3 Nonrecursive Reconstruction Algorithm

The ability to diagonalise the permuted block circulant matrix can be utilised in establishing an algorithm. A brief account of the procedure is presented. $\mathbf{G}_{\text{Blockcirculant}}$ may be expressed as:

$$\mathbf{G}_{\text{Blockcirculant}} = [\mathbf{W} \otimes \mathbf{I}] \begin{bmatrix} \mathbf{Y}(0) & & & \\ & \mathbf{Y}(1) & & \\ & & \ddots & \\ & & & \mathbf{Y}(N-1) \end{bmatrix} [\mathbf{W}^{-1} \otimes \mathbf{I}] \qquad (5.34)$$

where **W** is the DFT matrix, $\otimes$ denotes the Kronecker product, and the block **S** by **S** element eigenvalues $\mathbf{Y(k)}$ are given by extending equation (5.18) as:

$$\mathbf{Y(k)} = \sum_{i=0}^{N-1} \mathbf{G(k)} \exp(j\frac{2\pi}{\mathbf{N}}\mathbf{ki}) \qquad (5.35)$$

Similarly the block diagonal form of the permuted block circulant matrix **G** is given by:

$$\mathbf{G} = \mathbf{R}[\mathbf{W} \otimes \mathbf{I}] \begin{bmatrix} \mathbf{Y(0)} & & & \\ & \mathbf{Y(1)} & & \\ & & \ddots & \\ & & & \mathbf{Y(N-1)} \end{bmatrix} [\mathbf{W}^{-1} \otimes \mathbf{I}]\mathbf{R} \qquad \textbf{(5.36)}$$

where **R**, which is also equal to $\mathbf{R}^{-1}$, is illustrated in equation (5.37) as an **NS** by **NS** block diagonal matrix with $\mathbf{N(S \times S)}$ diagonal blocks $\mathbf{R(i)}$. For **i** even, $\mathbf{R(i)} = \mathbf{I}$ and for **i** odd, $\mathbf{R(i)} = \mathbf{E}$, which is the exchange matrix:

$$\mathbf{R} = \begin{bmatrix} \mathbf{I} & \mathbf{E} & \mathbf{I} & \mathbf{E} & \mathbf{I} \\ \mathbf{E} & \mathbf{I} & \mathbf{E} & \mathbf{I} & \mathbf{E} \\ \mathbf{I} & \mathbf{E} & \mathbf{I} & \mathbf{E} & \mathbf{I} \\ \mathbf{E} & \mathbf{I} & \mathbf{E} & \mathbf{I} & \mathbf{E} \\ \mathbf{I} & \mathbf{E} & \mathbf{I} & \mathbf{E} & \mathbf{I} \end{bmatrix} \qquad \textbf{(5.37)}$$

The **S** by **S** block eigenvalues of **G** are given by:

$$\mathbf{Y(k)} = \sum_{i=0}^{N-1} \mathbf{G(i)R(i)} \exp(-\mathbf{j}\frac{2\pi}{\mathbf{N}}\mathbf{ik}) \qquad \textbf{(5.38)}$$

Recalling from the previous section that:

$$\mathbf{p} = \mathbf{G}\lambda \qquad \textbf{(5.39)}$$

or

$$\mathbf{p} = \mathbf{R}[\mathbf{W} \otimes \mathbf{I}]\Lambda[\mathbf{W}^{-1} \otimes \mathbf{I}]\mathbf{R}\lambda \qquad \textbf{(5.40)}$$

where Λ is a $\mathbf{NS \times NS}$ block diagonal matrix $\Lambda(\mathbf{k},\mathbf{k}) = \mathbf{Y(k-1)}$. The block diagonal matrix Λ has singular submatrices. Taking the pseudo inverse of Λ, the solution to the system given in equation (5.40) is:

$$\lambda = \mathbf{R}[\mathbf{W} \otimes \mathbf{I}]\Lambda^{+}[\mathbf{W}^{-1} \otimes \mathbf{I}]\mathbf{Rp} \qquad \textbf{(5.41)}$$

where + denotes the pseudo inverse. The Λ^+ is obtained by substituting every radially symmetric block eigenvector by its pseudo inverse.

Utilising the above equation, a nonrecursive algorithm can be formulated to compute λ from the projections $\mathbf{p}$. FFT's can also be used to compute the DFT parts. The steps of the nonrecursive algorithm are detailed below:

Step 1: Compute the vector $\mathbf{Rp}$. This is obtained by reordering $\mathbf{p}$ such that

$$\mathbf{p_{kl}(new) = p_{k(N+l-1)}(old)}$$

for

$$\mathbf{i = 1, 2, .., S \ \wedge \ k \ odd \ only}$$

Step 2: Perform $\mathbf{S}$ number of FFT's, each of length $\mathbf{N}$ on the $\mathbf{N}$-length series

$$\mathbf{p_{1q}, p_{2q}, \cdots, p_{Nq}}$$

where $\mathbf{q = 1, 2, .., S}$ and assign the $\mathbf{k^{th}}$ DFT coefficient corresponding to any $\mathbf{q^{th}}$ element of the vector $\mathbf{W_k^* p}$.

Step 3: Compute Λ. The procedure is essentially the same as Steps 1 and 2 with the difference that the operations are performed on known submatrices, rather than vectors.

Step 4: Invert Λ to obtain Λ^+. For a specified geometry with $\mathbf{N}$ and $\mathbf{S}$ fixed, steps 3 and 4 need to be performed only once, and Λ^+ is stored for future use.

Step 5: Compute $\mathbf{W_k}$. Perform FFT's and finally reorder the DFT coefficients to obtain the λ subvectors.

Step 6: Backproject the λ to produce the final reconstruction.

A diagram of the algorithm steps is presented in Figure 5.4. Although this algorithm looks promising for adoption for the EIT system, the pseudo inverse does not match the noise statistics and hence produces inferior quality reconstructions as compared with other methods presented in later sections.

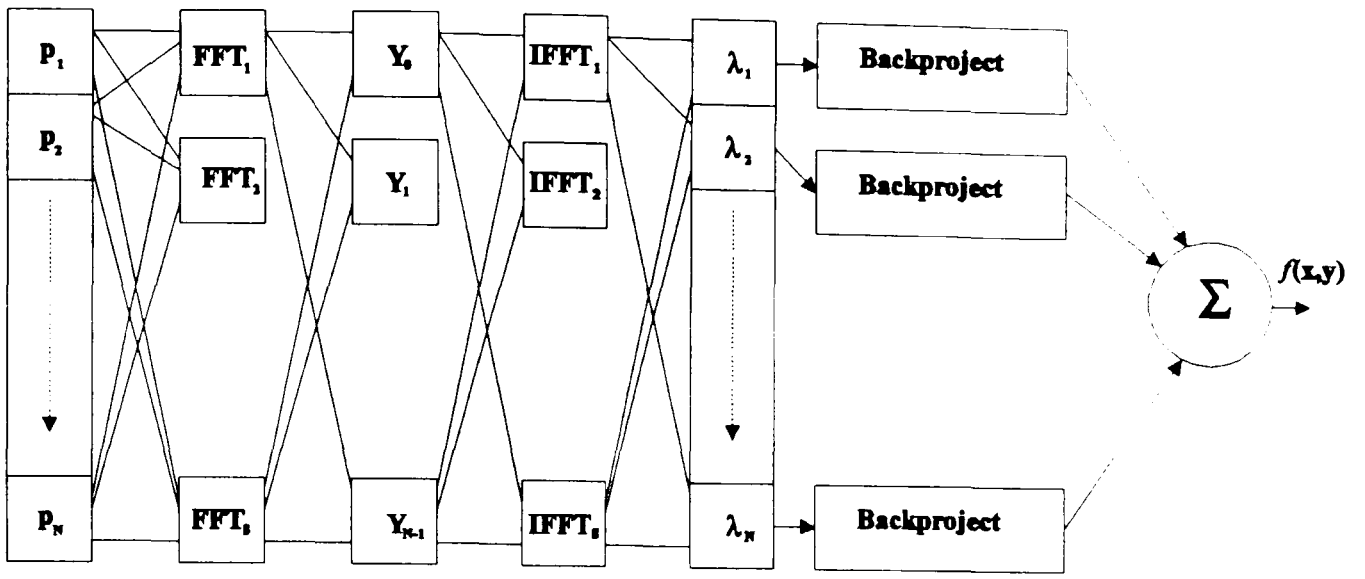

Figure 5.4 Block Diagram of the Nonrecursive Algorithm

5.4.4 Jacobi Method

This direct algorithm was introduced by Drossos [5.4] and is based on the Jacobi method for the solution of linear systems. The method has a distinct advantage over the recursive algorithm as the inverse can be precalculated and stored for future use. The diagonalisation presented by Durrani and Goutis [1.28], and given in the previous section, is used to reduce the required storage. The iterative method (which is also known as the successive corrections or relaxation method) replaces approximations by corresponding new ones as soon as the latter have been computed. An alternative method is known as Jacobi iteration. It is similar to the Gauss-Seidel iteration, but differs in not using improved values until a step has been completed, and then replacing λ^n by λ^{n+1} entirely for the next cycle. The Jacobi iteration can be adapted to form a direct algorithm as follows.

If we rewrite equation (5.4), it can be expressed as the matrix multiplication:

$$\hat{\lambda}^n = \mathbf{M}^n \hat{\mathbf{p}} \qquad \textbf{(5.42)}$$

$\mathbf{M}^n$ denotes the specific approximation of the pseudo inverse of $\mathbf{G}$ associated with the $\mathbf{n}^{th}$ iteration. Writing equation (5.42) using equation (5.43):

$$\mathbf{M}^n = \mathbf{M}^{n+1} + \gamma \mathbf{M}^0 (\mathbf{I} - \gamma \mathbf{M}^{n-1}) \tag{5.43}$$

where

$$\mathbf{M}^0(\mathbf{i},\mathbf{i}) = \frac{\mathbf{1}}{\mathbf{G}_0(\mathbf{i},\mathbf{i})} \tag{5.44}$$

and

$$\mathbf{M}^0(\mathbf{i},\mathbf{j}) = \mathbf{0} \;\forall\; \mathbf{i} = \mathbf{j} \tag{5.45}$$

is identical to the Jacobi closed form solution:

$$\mathbf{M}^n = \sum_{i=0} [\mathbf{I} - \mathbf{sG}]^i \mathbf{s} \tag{5.46}$$

where

$$\mathbf{s} = \gamma \mathbf{M}^0 \text{ and } 0 < \gamma < 2 \tag{5.47}$$

If $\mathbf{G}$ is permuted block circulant, then $\mathbf{M}^n$ will also be permuted block circulant. $\mathbf{M}^n$ can be pre-calculated, hence λ^n is obtained by simply multiplying $\mathbf{M}^n$ by the projection data. λ^n is then backprojected to obtain the desired reconstructed image $f(\mathbf{x},\mathbf{y})$. The iteration number $\mathbf{n}$ and γ are predetermined from external measurements of the collection geometry. They are chosen so that the noise statistics of the measurement system match the noise statistics of the calculated projection data.

The number of operations can be further reduced by block diagonalising the $\mathbf{M}^n$ matrix to obtain the block eigenvalues. In addition, the symmetry of the matrix can be used to reduce the storage requirement. The algorithm for computing the reconstruction consisted of two parts, first the stages to find the inverse of $\mathbf{M}^n$, which

is computed in non-real time, and second, the real time segments. The second part computes the Lagrange multipliers for backprojection. A summary of the complete process is given below.

Step 1: Evaluate $\mathbf{M}^0$ to obtain a good initial estimate of $\mathbf{M}^n$. Hence:

$$\mathbf{M}^0 = \frac{1}{\mathbf{G(i,i)}} \quad \mathbf{for\ i = 1, 2, .., (SN)}$$

and

$$\mathbf{M}^0(\mathbf{i,j}) = 0 \quad \mathbf{i \neq j}$$

This choice for initial estimate corresponds to

$$\hat{\boldsymbol{\lambda}}^0 = \mathbf{M}^0\hat{\mathbf{p}}$$

which is the projection vector $\hat{\mathbf{p}}$ with each of its elements scaled by their associated strip area.

Step 2: Input the noise energy σ_η^2 and the relaxation factor γ. A low value is preferable.

Step 3: Evaluate

$$\mathbf{M}^n = \mathbf{M}^{n-1} + \frac{\gamma}{\mathbf{G(i,i)}}[\mathbf{I} - \mathbf{GM}^{n-1}]$$

Only the first half block row of $\mathbf{M}^n$ needs to be calculated

Step 4: If

$$\sigma_{[\hat{\mathbf{p}}-\hat{\mathbf{p}}^n]} \geq \sigma_\eta^2$$

then increment n by one and repeat step 3, else step 5

Step 5: Store

$$\mathbf{M}_\mathbf{k}^\mathbf{n}$$

where $\mathbf{k = 1, 2, .., (\frac{N}{2} + 1)}$

or alternatively diagonalise and store the block eigenvalues:

$$\mathbf{Y}_\mathbf{k}^\mathbf{n}$$

where $\mathbf{k = 1, 2, .., (\frac{N}{2} + 1)}$

The $\mathbf{M}^n$ is diagonalised as:

$$\mathbf{M}^n = \mathbf{R}[\mathbf{W} \otimes \mathbf{I}]\mathbf{D}^n[\mathbf{W}^{-1} \otimes \mathbf{I}]\mathbf{R}$$

where $\mathbf{D}^n$ is an **NS** by **NS** block diagonal matrix, with each block eigenvalue of $\mathbf{M}^n$, hence:

$$\mathbf{D}^n(\mathbf{k},\mathbf{k}) = (\mathbf{Y}(\mathbf{k}-\mathbf{1}))^n$$

and **R** is an **NS** by **NS** block diagonal matrix with $\mathbf{N}(\mathbf{S} \times \mathbf{S})$ diagonal blocks.

At this point the algorithm has two options, depending on whether matrix diagonalisation is used or not.

Option A: Using $\mathbf{M}_k^n$

Step 1: Estimate the Lagrange multipliers using:

$$\lambda^n = \mathbf{M}^n\hat{\mathbf{p}}$$

Step 2: Backproject the Lagrange multipliers to produce the reconstructed image.

Option B: Using $\mathbf{D}^n$

Step 1: Compute the block diagonal matrix $\mathbf{D}^n$ using equation 5.43 and:

$$\mathbf{M}^n = \mathbf{R}[\mathbf{U} \otimes \mathbf{I}]\mathbf{D}^n[\mathbf{U} \otimes \mathbf{I}]\mathbf{R}$$

where **n** corresponds to the specific SNR adopted. Store the blocks for future uses with fixed **N,S** and approximately equal SNR.

Step 2: Take the block DFT of **p** to obtain **G** and compute the product $\mathbf{D}^n\mathbf{G}$. Then use the inverse block DFT to find the Lagrange multiplier vector λ^n.

Step 3: Backproject λ^n to obtain the reconstructed image.

The matrix $\mathbf{M}^n$ or $\mathbf{D}^n$ need be calculated only once, as its values depend on the structure of the data collection system.

5.5 Divergent Ray Geometry

Consider the divergent ray geometry presented in Figure 5.5

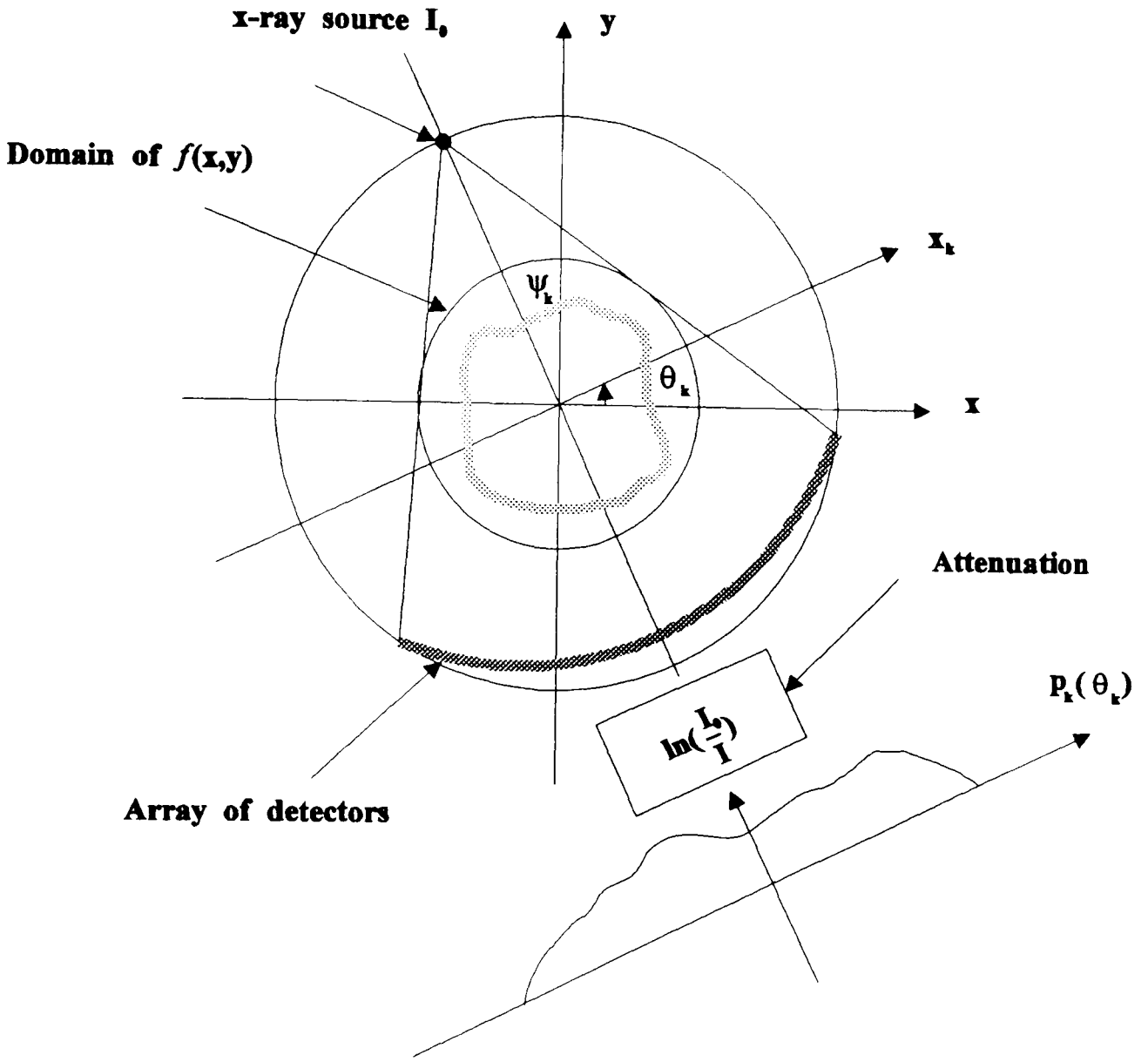

Figure 5.5 Divergent ray geometry

The $\mathbf{i}^{th}$ measurement of the $\mathbf{k}^{th}$ fan beam projection of a **2-D** image $f(\mathbf{x},\mathbf{y})$, defined in the region **D**, at angle ψ_k is:

$$\mathbf{p_{ki}} = \int_{Q_i}^{Q_i+\Delta\theta} \int_{A(\theta_k)}^{B(\theta_k)} f(\mathbf{x},\mathbf{y})\mathbf{dr_k}\mathbf{d\theta_k} \qquad \textbf{(5.48)}$$

where

$$\theta_k = \tan^{-1} \frac{-x\cos\psi_k - y\sin\psi_k + R}{-x\sin\psi_k + y\cos\psi_k} \tag{5.49}$$

and

$$r_k = [R_D^2 + r^2 - 2R_D r\cos(\psi_k - \phi)]^{\frac{1}{2}} \tag{5.50}$$

R is the distance of the source **S** from the origin **O**, and the angular strip is defined by $\Delta\theta = \theta_{k(i-1)} - \theta_{ki}$. Note, for convenience, polar co-ordinates have been adopted. The angular strips $\Delta\theta$ are assumed to be constant in this analysis.

The above is based on the analysis by Durrani and Goutis [5.6]. Kak and Slaney [2.34] present a similar analysis, but for consistency the notation of Durrani and Goutis [5.6] is adopted.

For continuous projections, the **ki**th strip can be considered as a line and equation (5.48) can be simplified to:

$$p_k(\theta_k) = \int_s f(x,y)dr_k \tag{5.51}$$

where $A(\theta_k) \Rightarrow B(\theta_k) \equiv s$, and $k = 1, 2, .., N$.

Following the procedure defined in the previous section for the parallel geometry, a general cost criterion is considered initially. Then the minimum variance cost criterion is introduced to form a model, hence restating the reconstruction problem for the fan beam geometry. A function $f(x,y)$ is required such that the integral:

$$I = \int\int_D C(.)dxdy \tag{5.52}$$

is a minimum subject to the constraints:

$$\sum_{k=1}^{N} p_k(\theta_k) = \sum_{k=1}^{N} \int_s f(x,y)dy_k \tag{5.53}$$

Rewritten as:

$$\sum_{k=1}^{N} [p_k(\theta_k) - \int_s f(x,y)dy_k] = 0 \tag{5.54}$$

using the Euler-Lagrange method as before, a continuous Lagrange multiplier is introduced for every projection, and the Euler-Lagrange equation can be defined as:

$$\mathbf{I} = \int\int_{\mathbf{D}} \mathbf{C}(.)\mathbf{dxdy} + \sum_{\mathbf{k=1}}^{\mathbf{N}} \int_{\mathbf{s'}} \lambda_{\mathbf{k}}(\theta_{\mathbf{k}})[\mathbf{p}_{\mathbf{k}}(\theta_{\mathbf{k}}) - \int_{\mathbf{s}} f(\mathbf{x},\mathbf{y})\mathbf{dr}_{\mathbf{k}}]\mathbf{d}\theta_{\mathbf{k}} \qquad \textbf{(5.55)}$$

where $\mathbf{s'} = \mathbf{0} \Rightarrow \pi$ and $\lambda_{\mathbf{k}}(\theta_{\mathbf{k}})$ are the **1-D** Lagrange multiplier functions.

If the integral over $\mathbf{r}_{\mathbf{k}}$ in the above equation is taken outside, and using the change of elements from Cartesian to polar variables:

$$\mathbf{dxdy} = \mathbf{r}_{\mathbf{k}}\mathbf{dr}_{\mathbf{k}}\mathbf{d}\theta_{\mathbf{k}} \qquad \textbf{(5.56)}$$

then equation (5.55) can be rewritten as:

$$\mathbf{I} = \int\int_{\mathbf{D}} [\mathbf{C}(.) + \sum_{\mathbf{k=1}}^{\mathbf{N}} \lambda_{\mathbf{k}}(\theta_{\mathbf{k}})[\mathbf{p}_{\mathbf{k}}(\theta_{\mathbf{k}})\delta(\mathbf{r}_{\mathbf{k}} - \frac{\mathbf{A}+\mathbf{B}}{\mathbf{2}}) - \frac{f(\mathbf{x},\mathbf{y})}{\mathbf{r}_{\mathbf{k}}}]]\mathbf{dxdy} \qquad \textbf{(5.57)}$$

where $\delta(.)$ is a delta function. This is the form given in Durrani and Goutis [5.6].

The first variation of $\mathbf{I}$ is obtained as in the previous Chapter. Hence, from appendix A, the first variation is given as:

$$\frac{\partial \mathbf{C}}{\partial f} - \frac{\partial}{\partial \mathbf{x}}\left(\frac{\partial \mathbf{C}}{\partial f_{\mathbf{x}}}\right) - \frac{\partial}{\partial \mathbf{y}}\left(\frac{\partial}{\partial f_{\mathbf{y}}}\right) - \sum_{\mathbf{k=1}}^{\mathbf{N}} \frac{\lambda_{\mathbf{k}}(\theta_{\mathbf{k}})}{\mathbf{r}_{\mathbf{k}}} = \mathbf{0} \qquad \textbf{(5.58)}$$

Minimising the image variance by substituting $\frac{1}{2}f^2$ for $\mathbf{C}(.)$ gives:

$$f(\mathbf{x},\mathbf{y}) = \sum_{\mathbf{k=1}}^{\mathbf{N}} \frac{\lambda_{\mathbf{k}}(\theta_{\mathbf{k}})}{\mathbf{r}_{\mathbf{k}}} \qquad \textbf{(5.59)}$$

This is the minimum variance model or backprojection model for the fan beam geometry.

Assuming the projections are at equiangles then:

$$\psi_{k+1} - \psi_k = \frac{2\pi}{N} \forall k \tag{5.60}$$

where ψ_k denotes the projection angle. Adopting the minimum variance model gives the i^{th} measurement of the k^{th} projection as:

$$p_{ki} = \int_{Q_i}^{Q_i+\Delta\theta} \int_{A}^{B} \sum_{k=1}^{N} \frac{\lambda_k(\theta_k)}{r_k} dr_k d\theta_k \tag{5.61}$$

where

$$i = 1, 2, .., S$$
$$k = 1, 2, .., S$$

and

$$Q_i = (i-1)\Delta\theta$$
$$\Delta\theta = \frac{\pi}{S}$$

$\Delta\theta$ is the angular width between projection and is assumed to be constant.

5.5.1 Matrix Structure

Discretising each $\lambda_k(\theta_k)$ into S values, gives λ as a row vector:

$$\lambda_k'^T = [\lambda'_{1k}, \lambda'_{2k}, .., \lambda'_{kS}] \tag{5.62}$$

where λ_{ki} corresponds to the ki^{th} strip with the origin at O_k, and the index i is specified in Figure 5.4. Angle θ_k is measured in a clockwise direction. If the projection measurements are indexed in the same way, equation (5.61) is rewritten as a matrix equation in the form of a linear system:

$$p' = B'\lambda' \tag{5.63}$$

where

$$\lambda'^T = [\lambda_1'^T, \lambda_2'^T, .., \lambda_N'^T] \tag{5.64}$$

$$\mathbf{p}'^{T} = [\mathbf{p}_1'^{T}, \mathbf{p}_2'^{T}, .., \mathbf{p}_N'^{T}] \tag{5.65}$$

$\mathbf{B}'$ is used in this case to define the associated system matrix for a fan beam system The primes are used to denote the indexing used in Figure 5.4. Goutis and Drossos [5.7] used this index to utilise the special properties of the system matrix. The elements of matrix $\mathbf{B}'$ are rearranged to obtain $\mathbf{B}$. This is achieved by introducing a new numbering scheme, as defined by Goutis and Drossos [5.7], for the divergent-ray strips which in effect rearranges the elements of λ' and $\mathbf{p}'$.

$\mathbf{B}$ is block circulant, unlike the parallel case where $\mathbf{G}$ was permuted block circulant. The rearrangement scheme [5.7] allows the linear system of equation (5.53) to be rewritten as:

$$\mathbf{p} = \mathbf{B}\lambda \tag{5.66}$$

or

$$\begin{bmatrix} \mathbf{p}_1 \\ \mathbf{p}_2 \\ .. \\ \mathbf{p}_{\frac{N}{2}} \\ .. \\ \mathbf{p}_N \end{bmatrix} = \begin{bmatrix} \mathbf{B}_0 & \mathbf{B}_1 & .. & \mathbf{B}_{\frac{N}{2}-1} & \mathbf{B}_{\frac{N}{2}} & \mathbf{B}_{\frac{N}{2}-1}^{T} & .. & \mathbf{B}_2^{T} & \mathbf{B}_1^{T} \\ \mathbf{B}_1^{T} & \mathbf{B}_0^{T} & .. & \mathbf{B}_{\frac{N}{2}-2} & \mathbf{B}_{\frac{N}{2}-1} & \mathbf{B}_{\frac{N}{2}} & .. & \mathbf{B}_3^{T} & \mathbf{B}_2^{T} \\ .. & .. & .. & .. & .. & .. & .. & .. & .. \\ \mathbf{B}_{\frac{N}{2}-1}^{T} & .. & .. & .. & \mathbf{B}_0 & .. & .. & .. & \mathbf{B}_{\frac{N}{2}} \\ .. & .. & .. & .. & .. & .. & .. & .. & .. \\ \mathbf{B}_1 & \mathbf{B}_2 & .. & .. & \mathbf{B}_{\frac{N}{2}-1}^{T} & .. & .. & \mathbf{B}_1^{T} & \mathbf{B}_0 \end{bmatrix} \begin{bmatrix} \lambda_1 \\ \lambda_2 \\ .. \\ \lambda_{\frac{N}{2}} \\ .. \\ \lambda_N \end{bmatrix} \tag{5.67}$$

where $\mathbf{p}$ and λ are column vectors:

$$\mathbf{p}^{T} = [\mathbf{p}_1^{T}, \mathbf{p}_2^{T}, .., \mathbf{p}_N^{T}] \tag{5.68}$$

$$\lambda^{T} = [\lambda_1^{T}, \lambda_2^{T}, .., \lambda_N^{T}] \tag{5.69}$$

and $\mathbf{B}$ satisfies the symmetry condition:

$$\mathbf{B}_i = \mathbf{B}_{N-i}^{T} \tag{5.70}$$

An example of the submatrix structure is shown in Figure 5.6.

The elements of the system matrix are obtained by evaluating equation (5.63). If assumption is again made that the value of $\lambda_k(\theta_k)$ is constant within each strip, then the contribution of λ_{nj} into $\mathbf{p}_{ki}$ is specified by:

$$\mathbf{h}_{nj,ki} = \int\int_{s} \frac{1}{\mathbf{r}_k \mathbf{r}_n} d\mathbf{r}_k d\theta_k \qquad (5.71)$$

where **s** in this case denotes the intersection area of the **ki** and **nj** strip, lying within the region (appendix D). To maintain the block circulant nature of the system matrix, the elements of λ and **p** require rearranging.

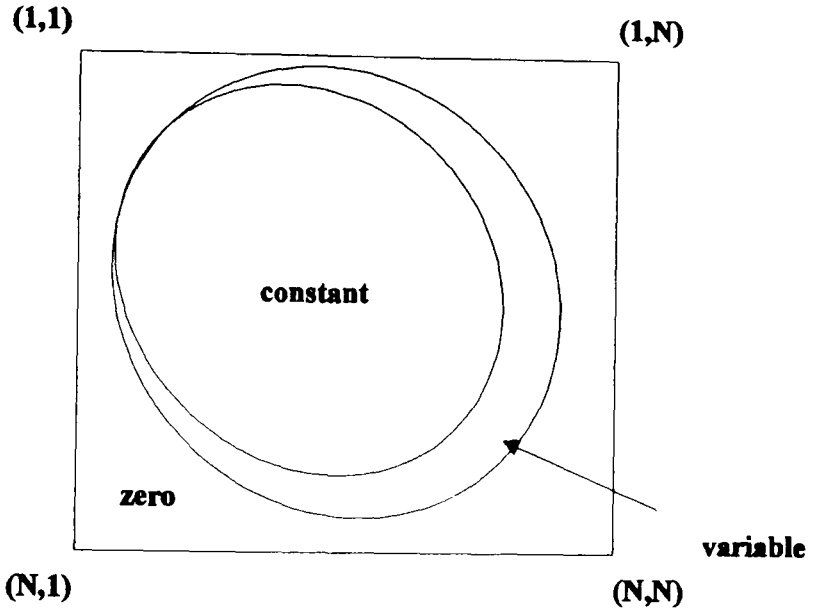

Figure 5.6 Diagram of submatrix structure for fan beam geometry

5.5.2 Recursive Algorithm

The block successive relaxation method can be employed for the solution of the system, and due to the element rearrangement, the properties of the system matrix **B** can be utilised to reduce the computational requirements. The algorithm for the fan beam system is similar to that of the parallel system. It is observed that the product of the $\mathbf{i}^{th}$ subrow and a subvector, is equal to the product of the previous $(\mathbf{i}-\mathbf{1})^{th}$ subrow and the subvector, plus the product of the difference subrow and the subvector. The $\mathbf{i}^{th}$ difference subrow is generated by subtracting each element of the $(\mathbf{i}-\mathbf{1})^{th}$ subrow

from the corresponding element of the $\mathbf{i}^{th}$ subrow. The number of nonzero elements in the difference subrow is very small, as the subrow differs in only a few elements. The average number is defined by $\beta = 3$, hence the product of the $\mathbf{i}^{th}$ subrow and subvector require β instead of $\mathbf{S}$ arithmetic operations. This reduces the storage requirements. A summary of the basic algorithm is given below.

Step 1: Calculate $\mathbf{B_k}$ for $\mathbf{k = 0,1,2,..,\frac{N}{2}}$. The $\mathbf{(mj)}$ element is given by equation (5.60), where the integral is taken and the intersection area of $\mathbf{(l,m)}$ and $\mathbf{(k+1,j)}$ strips lies within the domain $\mathbf{D}$.

Step 2: Derive the difference submatrices $\Delta\mathbf{B_k}$ for $\mathbf{k = 0,1,2,..,\frac{N}{2}}$, i.e. in each $\mathbf{B_k}$ replace the $\mathbf{i}^{th}$ subrow by the difference of the $\mathbf{(i-1)}^{th}$ subrow, for $\mathbf{i = 2,3,..,S}$.

Step 3: Store every non-zero element of $\Delta\mathbf{B_k}$, and also store the necessary indices to identify the elements.

Step 4: Compute the initial estimate of the Lagrange multipliers using:

$$\lambda_{kl}^{0} = \frac{\mathbf{p_{kl}}}{\mathbf{B_0(i,i)}} \forall \mathbf{ki}$$

Step 5: Estimate $\hat{\mathbf{p}}_{kl}^{n}$ where $\mathbf{i = 1,2,..,S}$ from λ^n and the difference matrix.

Note that the product of a subvector and the $\mathbf{i}^{th}$ subrow is equal to the sum of its products with the $\mathbf{(i-1)}^{th}$ subrow and the $\mathbf{i}^{th}$ difference subrow, respectively.

Step 6: Update λ_k. Hence:

$$\lambda_{kl}^{n+1} = \lambda_{kl}^{n} + \frac{\gamma}{\mathbf{B_0(i,i)}}(\mathbf{p_{kl}} - \hat{\mathbf{p}}_{kl}^{n})$$

where $\mathbf{i = 0,1,2,..,S}$ and γ is the relaxation factor.

Steps (5) and (6) are repeated for all projections, until the statistics of the error between the estimated and measured projections

$$\varepsilon_{kl} = \mathbf{p_{kl}} - \hat{\mathbf{p}}_{kl}$$

becomes approximately equal to the statistics of the noise in the true projection data.

Step 7: Rearrange λ to obtain λ'. using Table 1 given by Goutis and Drossos [5.7], and backproject to produce the reconstruction.

It should be noted that steps (1) to (3) are performed once only for the specific geometry of the collection system, in order to pre-compute $\Delta \mathbf{B}_k$ which is stored for use in all future reconstructions. Also if $\gamma = 1$, the successive relation procedure is the same as the Gauss-Seidel iteration method.

5.5.3 Direct Algorithms

The Jacobi algorithm detailed for the parallel case is the only noise matching direct algorithm developed so far. It is similar to the parallel geometry and hence the diagonalising procedure described in section 5.4.1 is also similar. The only difference is that $\mathbf{B}$ is a block circulant matrix. The details are not given here, but can be found in [5.7] and section 5.4.

5.6 Discussion

The review in this Chapter, of available algorithms to compute the unknown Lagrange multiplier functions has enabled the appropriate selection of a compute-efficient method for use with the EIT system. The aim of all the approaches is to use the structure of the associated system matrix to reduce the number of operations required. In the fan beam case, further rearrangement of the elements was required to obtain areas of equal elements in the system matrix. Also in the fan case, the rearrangement of elements produces a block circulant matrix, unlike the parallel case which has a permuted block circulant structure.

It should be noted that an exact pseudo inverse of the system matrix, as indicated in Chapter four, is not desired. These inverses are known as pseudo inverse

because the associated matrices are singular. Shim [5.8] verified that the exact pseudo inverse produces severely distorted images.

Goutis [5.1] developed the iterative algorithm, based on the backprojection model, which estimated the discrete **1-D** Lagrange multipliers by making use of the special structure of the associated system matrix, relating the Lagrange multipliers to the projections using areas of equal elements within the system matrix. The iterative algorithm terminates when the error between the measured projection and the projection corresponding to the solution is small enough, the size of the error being obtained by observation of the quality of the reconstructed image.

A non-iterative algorithm was also suggested by Durrani and Goutis [1.28] for both parallel and fan beam geometries using the FFT algorithm to compute the diagonalised matrix. This is known as the nonrecursive method. Although it produced good results for ideal projection data, the solutions for noisy projection data were of poor quality.

The drawback with both of these algorithms is that the noise in the projection data was not considered. The final algorithm (Jacobi) presented in this Chapter uses the constraints of matching the statistics of the measurement noise to the statistics of the error between the measured projections and the reconstruction projections. It was developed primarily for the fan beam system by Drossos [5.7] and was considered as the most suitable for adaption for the EIT system.

The requirement for diagonalisation will depend on the number of samples obtained from the data collection system. With X-ray systems these data sets are large, and reduction in storage requirement is highly desirable. The EIT systems given in the next Chapter use considerably smaller collection geometries and the algorithm based on the Jacobi method was used to obtain results without use of diagonalisation. As collection systems improve by the use of more electrodes, diagonalisation of the associated system matrices may be required.

A comparison of the algorithms including convolution is presented in table 5.1.

The values given for storage can be considered only as approximations, as data compression techniques have not been exploited. The convolution measure is based upon Shepp's [2.9] and Herman's [2.31] values. **N** is the number of projections, **S** is the number of samples per projection, **n** defines the number of iterations and β gives the average number of non-zero elements per row in the difference submatrix.

Table 5.1 **Comparison of Algorithms**

Algorithms	**Total number of real Multiplications**	**Typical number of real Multiplications for N=16, S=16, $\beta = 3$ and n=50**	**Storage (word size)**
Nonrecursive Parallel	$2SN\log_2 N + 5NS^2$	21900	$\frac{(N+1)S^2}{8}$
Jacobi Direct Parallel	$2SN\log_2 N + 6NS^2$	25996	$2NS^2 + 2NS$
Iterative Parallel	$n\beta N^2S + 4NS^2$	630784	$\frac{\beta NS}{4} + 2NS$
Convolution Parallel	$NS^2 + 4NS^2$	20480	$S + 2NS$
Backprojection Parallel	$4NS^2$	16384	$S + 2NS$
Jacobi Direct fan	$2NS\log_2 N + 8NS^2$	34188	$2NS^2 + 2NS$
Iterative fan	$n\beta N^2S + 6NS^2$	638976	$\frac{\beta NS}{2} + 2NS$
Convolution fan	$NS^2 + 6NS^2$	26112	$S + 2NS$
Backprojection fan	$6NS^2$	24576	$S + 2NS$

It can be seen from table 5.1 that a large proportion of the computation is spent on backprojection. This justifies the need for hardware development to improve the speed of this part of the operation.

It is worth restating the objectives of this Chapter. To exploit the CORT in EIT, a detailed analysis of the algorithms developed for X-ray systems has been undertaken. This analysis had the objective of identifying which algorithms were the most suitable for EIT implementation. The geometries of X-ray systems give structures to the submatrices in the associated system matrices. These can be exploited to obtain the maximum computational efficiency. As the EIT geometries differ from the X-ray systems, it will be seen in Chapter six that these properties cannot be used. Most of the methods yield a permuted block circulant structure in their associated system matrices, allowing block DFT techniques to be used to reduce the storage requirements of the implemented algorithms. Another key feature is the use of the closed form Jacobi solution, in which the inverse maintains the block circulant structure, again allowing the use of block DFT techniques to reduce storage requirements. The EIT system developed in Chapter six uses significantly less data than X-ray systems due to the technical problems associated with the data collection. This means that the requirements for minimisation of the storage and improvement in computational efficiency are not as important as they are in the case of the larger data collection capacities of X-ray systems. A key feature of the algorithms given in this Chapter is that they can be optimised to match the error in the statistics of the inverses to that of the statistics of the additive noise in the collection system. This has great advantage in EIT, which uses noisier data than do X-ray systems.

6 EIT GEOMETRIES AND MODELS

6.1 Introduction

The objective of this Chapter is to develop the new models, and hence the algorithms, for the EIT system. These are based on two data collection methods which give rise to new geometries, termed the parallel orthogonal curvilinear and divergent orthogonal curvilinear.

The following analysis adapts the general formulation for the solution of **2-D** and **3-D** scanning systems, as defined by Goutis and Durrani [5.6], for the EIT geometries. New models are derived to obtain reconstructions of resistivity distribution. The geometries in EIT are given by an analytical solution to the Forward problem that defines the paths of the equipotential lines. This includes analysis of the structure of the associated system matrix and the development of algorithms to produce reconstructions. A number of reconstructions from simulated data of resistivity are given to demonstrate that the new algorithms produce reasonable results.

6.2 Geometries

The geometry of the systems previously described refers to the paths followed by the radiation. In EIT, the definition refers to the equipotential paths defined by the solution to the Forward problem for a homogenous medium. As detailed in Chapter three, there are two approaches to obtaining data in EIT for the production of difference images. Models are derived for both the opposite electrode method and the dipole method. The opposite method is considered first.

The analysis is approached by considering the potential distribution within an isotropic resistive medium. A brief analysis was given in Chapter one and is expanded in this Chapter to incorporate CORT. Passing a current between a pair of electrodes

(known as a drive pair) will cause a current to flow within the region, as shown in Figure 6.1, and discussed in Chapter one. The distribution of potential within the region is given by the solution of the equation:

$$\Delta\rho^{-1}\mathbf{V} = 0 \qquad \textbf{(6.1)}$$

If the resistivity were uniform within the region, then equation (6.1) would reduce to Laplace's equation. For current passing between a particular pair of electrodes, the potential at a point within the region depends on the distribution of the resistance within the region. Measurement of a single boundary potential profile for a current pair of current electrodes, does not provide sufficient information to reconstruct uniquely the required distribution of resistance. However, if other boundary profiles can be obtained, the resulting set of measurements may permit an approximate reconstruction of the required distribution. Equation 6.1 represents a non-linear relationship between $\mathbf{V}$ and ρ due to $\nabla\mathbf{V}$.

6.3 Parallel Orthogonal Curvilinear System

A new geometry is introduced, termed parallel orthogonal curvilinear, which takes its name from the path of the equipotential lines, defined by the conformal transform described in this section.

In this system, the data are obtained by injecting current into opposing electrodes around a circular medium. Other electrodes are equally spaced around the medium, in pairs, to measure potential difference as illustrated in Figure 6.1. These potential differences are translated into a measure of resistivity between the equipotential lines in the medium as described above. The nature of the data collection system limits the number of samples $\mathbf{S}$ to $\mathbf{n(n-4)/2}$ values in the range of $\mathbf{0}$ to π, where $\mathbf{n}$ is the number of electrodes. (The effects of this limitation are examined in the next Chapter.)

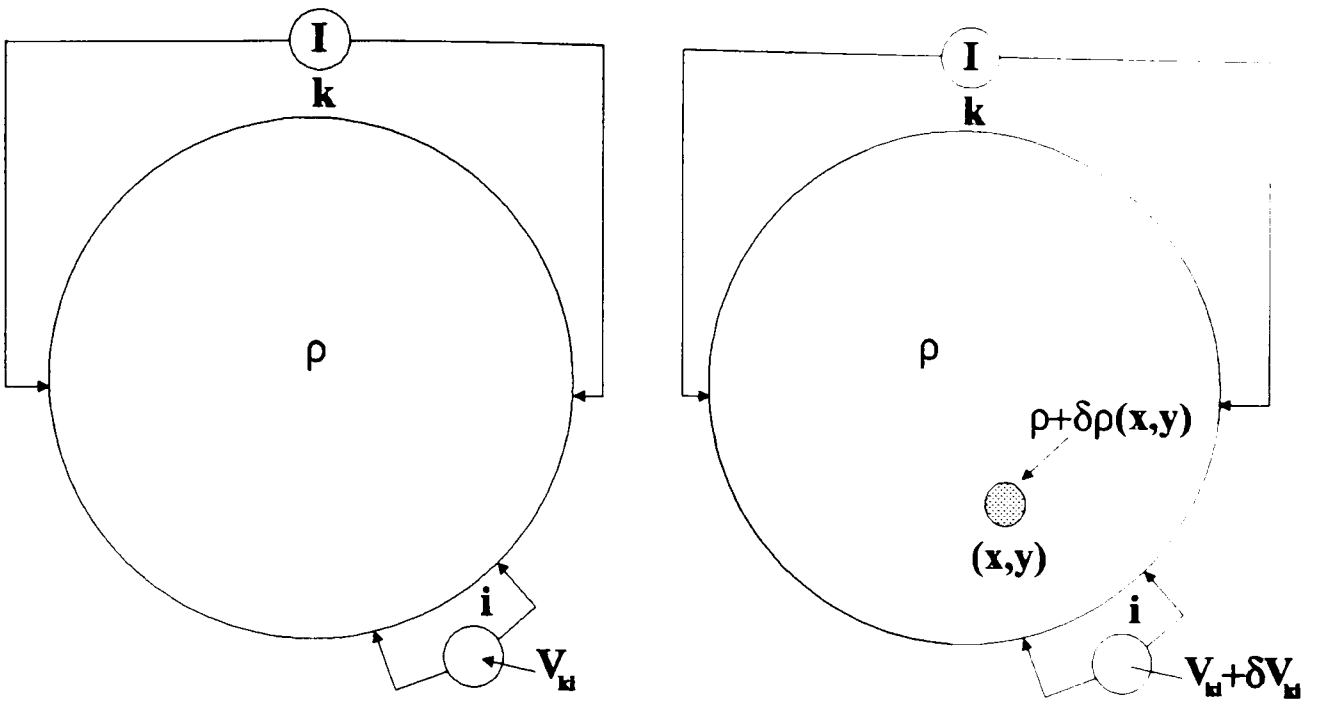

(a) **(b)**

Figure 6.1 Schematic diagram illustrating the four electrode method for collecting impedance tomography data in (a) a bounded volume of uniform resistivity, and (b) a bounded volume where one volume element has changed resistivity.

If it is assumed that a bounded volume of uniform resistivity, ρ, is carrying a constant current $\mathbf{I}$, supplied by the $\mathbf{k}^{th}$ pair of electrodes as illustrated in Figure 6.1, a voltage $\mathbf{V_{ki}}$ is developed between the $\mathbf{i}^{th}$ pair of boundary electrodes. If there is a change in the resistivity of the small volume element located at point $(\mathbf{x},\mathbf{y})$, the change can be represented as:

$$\rho + \delta\rho(\mathbf{x},\mathbf{y}) \tag{6.2}$$

The resistance value of the volume element is given by:

$$\mathbf{P(x,y)} = \mathbf{ln}(\rho + \delta\rho(\mathbf{x},\mathbf{y})) - \mathbf{ln}(\rho) \tag{6.3}$$

and

$$\mathbf{P(x,y)} = \mathbf{ln}[1 + \frac{\delta\rho(\mathbf{x},\mathbf{y})}{\rho}] \approx \frac{\delta\rho(\mathbf{x},\mathbf{y})}{\rho} \tag{6.4}$$

where $\delta\rho(\mathbf{x},\mathbf{y}) << \rho$. The voltage sensed by the electrodes at the boundary is now:

$$\mathbf{V}'_{kl} = \mathbf{V}_{kl} + \delta\mathbf{V}_{kl} \qquad \textbf{(6.5)}$$

where $\mathbf{V}_{kl}$ represents a potential boundary profile measurement, and $\delta\mathbf{V}_{kl}$ is a solution to Laplace's equation. Substituting equation (6.5) into (6.1) gives:

$$\Delta\mathbf{V}_{kl} = \underline{\nabla}\rho\underline{\nabla}\mathbf{V}_{kl} + \underline{\nabla}\rho\underline{\nabla}\delta\mathbf{V}_{kl} \qquad \textbf{(6.6)}$$

Since $\Delta\delta\mathbf{V}_{kl} = \mathbf{0}$ and if $\underline{\nabla}\rho$ is small, it can be assumed that $\underline{\nabla}\mathbf{V}_{kl} << \underline{\nabla}\delta\mathbf{V}_{kl}$, therefore equation (6.4) can be rewritten as:

$$\Delta\mathbf{V}_{kl} = \underline{\nabla}\rho\underline{\nabla}\delta\mathbf{V}_{kl} \qquad \textbf{(6.7)}$$

which is a linear relationship between ρ and $\mathbf{V}_{kl}$. If $\delta\rho(\mathbf{x},\mathbf{y})$ is small, it is reasonable to assume that the current density field is the same as for uniform resistivity, and hence:

$$\delta\mathbf{V}_{kl} \propto \delta\rho(\mathbf{x},\mathbf{y}) \qquad \textbf{(6.8)}$$

When the boundary voltages $\mathbf{V}'_{kl}$ and $\mathbf{V}_{kl}$ are measured before and after a change in resistivity has occurred, an image of the temporal change in (natural) log resistivity can be produced. The reconstruction of ρ requires the inversion of equation (6.7) for a set of boundary measurements. In this research it is achieved as follows.

The solution to the Forward problem can be found analytically by using a conformal transformation. The equipotential lines follow approximately the path defined by the conformal transformations, known as the bipolar co-ordinate system (appendix E). To analyse this transformation, let $\mathbf{w}$ denote a complex variable that is the complex potential of the bipolar system defined by:

$$\mathbf{w = u + jv = k \ln\left(\frac{r_1 e^{j\theta_1}}{r_2 e^{j\theta_2}}\right) = k \ln\left(\frac{z+a}{z-a}\right)} \qquad \textbf{(6.9)}$$

where

$$\mathbf{z = x + jy} \qquad \textbf{(6.10)}$$

hence

$$\mathbf{u + jv = k \ln\left(\frac{r_1}{r_2}\right) + jk(\theta_1 - \theta_2)} \qquad \textbf{(6.11)}$$

where

$$\mathbf{r_1 = \sqrt{(x+a)^2 + y^2}}$$
$$\mathbf{r_2 = \sqrt{(x-a)^2 + y^2}}$$

and θ_1, θ_2 are defined in appendix E. The real part of equation (6.11) gives the equipotential paths in the medium:

$$\mathbf{u_k = \ln\left(\frac{r_1}{r_2}\right)} \qquad \textbf{(6.12)}$$

and the imaginary part, the current paths:

$$\mathbf{v_k = \tan^{-1}\left(\frac{y_k}{y_k + a}\right) - \tan^{-1}\left(\frac{y_k}{y_k - a}\right)} \qquad \textbf{(6.13)}$$

$\mathbf{k = 1}$ in both cases. Also $\mathbf{x_k}$ and $\mathbf{y_k}$ can be defined by:

$$\mathbf{x_k = \frac{a \sinh u_k}{\cosh u_k - \cos v_k}} \qquad \textbf{(6.14)}$$

$$\mathbf{y_k = -\frac{\sin v_k}{\cosh u_k - \cos v_k}} \qquad \textbf{(6.15)}$$

and

$$\mathbf{x_k = x \cos\theta_k + y \sin\theta_k}$$
$$\mathbf{y_k = -x \sin\theta_k + y \cos\theta_k} \qquad \textbf{(6.16)}$$

The transformations in equations (6.12) and (6.13) map the current and equipotential

lines in the **x, y** plane to the **u, v** plane, and equations (6.14) and (6.15) map the values in the **u, v** plane to the **x, y** plane. This is demonstrated in Figure 6.2.

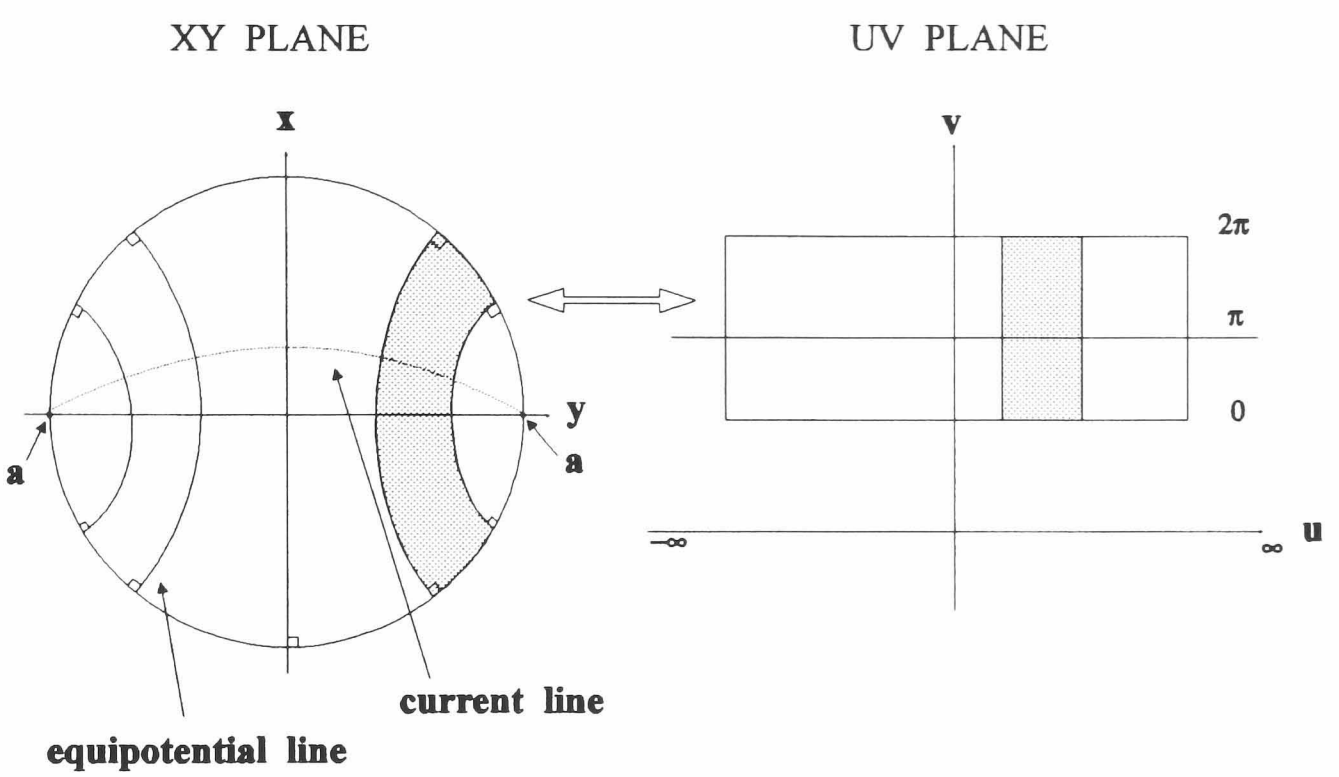

Figure 6.2 Bipolar Co-ordinate System

It was found that these transformations are not invariant to rotation. This limited the possibility of deriving a solution in the **u, v** space directly. The origin of these transforms and the data collection system will be explained in more detail in Chapter seven. To utilise the transformation of the bipolar system, the following approach is adopted.

Consider the curvilinear system shown in the Figure 6.3:

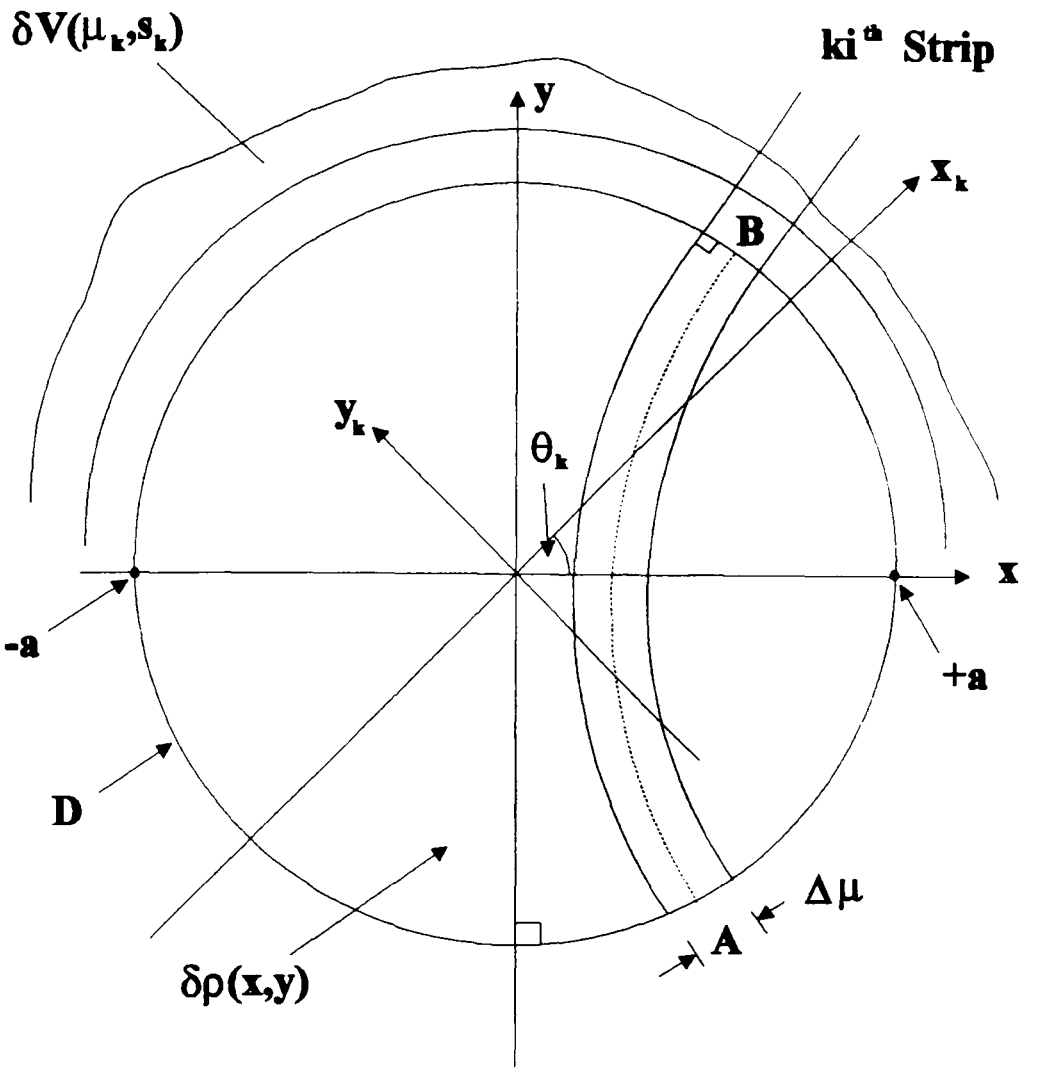

Figure 6.3 Parallel Orthogonal Curvilinear System

Let (μ_k, s_k) form a curvilinear co-ordinate system in the **2-D** plane, in which $\mu_k = x_k$ and $s_k = u_k$ are used to denote the curved paths. The k^{th} general projection of a **2-D** space limited object, represented by the function $\delta\rho(x,y)$, can be defined as:

$$\delta V_{kd} = \int_{\mu_l}^{\mu_{l+1}} \int_{A(s_k)}^{B(s_k)} \delta\rho(x,y) W_k' ds_k d\mu_k \qquad (6.17)$$

where $\Delta\mu = \mu_{l+1} - \mu_l$ and W_k' represents the current distribution along the strip defined by the path s_k. Using the principle of superposition, the normalised boundary potentials can be defined as:

$$\frac{\delta V_{kd}}{V_{kd}} = \frac{\delta\rho(x,y)}{\rho} \qquad (6.18)$$

:If V_{kl} and ρ are constants, and $\frac{W_k'}{W_k}$ is assumed to be constant for this part of the analysis, where W_k is the current density for the reference boundary potential. Then:

$$\frac{\delta V_{kl}}{V_{kl}} = \int_{\mu_1}^{\mu_{i+1}} \int_{A(s_k)}^{B(s_k)} \frac{\delta\rho(x,y)}{\rho} \frac{W_k'}{W_k} ds_k d\mu_k \qquad (6.19)$$

$A(s_k)$ and $B(s_k)$ are the limits of the integration along the curved path and $\Delta\mu$ is the width of the strip of integration. For this analysis, the width is assumed to be a constant. This assumption is an approximation which can be maintained only if the sample (number of electrodes) is large compared to the size of the domain of the image **D**. Equation (6.19) defines the projection data in terms of the natural log of the resistivity as a function of difference potential. From equation (6.12) the projection path can be defined by:

$$s_k = \frac{1}{2}[\ln((x_k + a)^2 + y_k^2) - \ln((x_k - a)^2 + y_k^2)] \qquad (6.20)$$

To simplify the notation, let the limits of the integration path $A \Rightarrow B$ be denoted by ω, and the width $\mu_i \Rightarrow \mu_{i+1}$ be denoted by ω', similar to those used in the previous Chapter for parallel and fan beam geometries. The path width of the projection is defined as a single line, indicated by the dotted line in Figure 6.3. The integrals along these paths form the projections at angle θ_k.

The projection can be defined as:

$$\frac{\delta V_k(\mu_k)}{V_k} = \int_w \frac{\delta\rho(x,y)}{\rho} \frac{W_k'}{W_k} ds_k \qquad (6.21)$$

where δV is the measured voltage at the boundary, and ρ represents the resistivity distribution of the medium. s_k in the path of the equipotential line. The associated normalised projection is given by:

$$\left(\frac{\delta V_k(\mu_k)}{V_k(\mu_k)}\right)' = \frac{\delta V_k(\mu_k)/V_k(\mu_k)}{\int_w J_k(\mu_k s_k)\,ds_k} \tag{6.22}$$

where the scaling Jacobian is:

$$J_k(\mu_k, s_k) = \begin{vmatrix} \frac{\partial \mu_k}{\partial x} & \frac{\partial s_k}{\partial x} \\ \frac{\partial \mu_k}{\partial y} & \frac{\partial s_k}{\partial y} \end{vmatrix} \tag{6.23}$$

which for the equipotential lines is obtained from equation (6.23), as follows:

$$\frac{\partial s_k}{\partial x} = \frac{1}{2}\frac{2(x+a)}{(x+a)^2+y^2} - \frac{1}{2}\frac{2(x-a)}{(x-a)^2+y^2} \tag{6.24}$$

$$\frac{\partial s_k}{\partial y} = \frac{1}{2}\frac{2y}{(x+a)^2+y^2} - \frac{1}{2}\frac{2y}{(x-a)^2+y^2} \tag{6.25}$$

Therefore:

$$\frac{dy}{dx} = \frac{\left(\frac{x+a}{(x+a)^2+y^2} - \frac{x-a}{(x-a)^2+y^2}\right)}{\left(\frac{y}{(x+a)^2+y^2} - \frac{y}{(x-a)^2+y^2}\right)} \tag{6.26}$$

$$\frac{dy}{dx} = -\left(\frac{r_2^2(x+a) - r_1^2(x-a)}{r_2^2 y - r_1^2 y}\right) \tag{6.27}$$

$$J_k(\mu_k s_k) = -\left(\frac{x(r_2^2 - r_1^2) + a(r_2^2 + r_1^2)}{y(r_2^2 - r_1^2)}\right) \tag{6.28}$$

The procedure for applying the optimisation for this geometry follows the same approach as the methods described earlier. For the primal method, the projections are considered as continuous and the conductance strips are approximated to single lines. Denoting $C(.)$ as a general cost function and using these constraints, the reconstruction problem can be defined as follows.

Find a function $\rho(x,y)$ such that the integral:

$$I = \int\int_{D} C(.)dxdy \tag{6.29}$$

is a minimum subject to the constraints:

$$\sum_{k=1}^{N} \frac{\delta V_k}{V_k} = \sum_{k=1}^{N} \int_{s} \frac{\delta \rho(x,y)}{\rho} S'_k ds_k \tag{6.30}$$

where

$$S'_k = \frac{W'_k}{W_k} \tag{6.31}$$

or rewritten as:

$$\sum_{k=1}^{N} \{ \frac{\delta V_k(\mu_k)}{V_k(\mu_k)} - \int_{s} \frac{\delta \rho(x,y)}{\rho} S'_k ds_k \} = 0 \tag{6.32}$$

The reconstruction is optimised for the general criterion:

$$I = \int\int_{D} C(.)dxdy + \sum_{k=1}^{N} \int_{s'} \lambda_k(\mu_k) [\frac{\delta V_k(\mu_k)}{V_k(\mu_k)} - \int_{s} \frac{\delta \rho(x,y)}{\rho} S'_k ds_k] d\mu_k \tag{6.33}$$

$\lambda(\mu_k)$ denotes the Lagrange multipliers, and (μ_k, s_k) is defined in Figure 6.3. **D** is the domain of definition of the resistivity object, and **A** and **B** are the limits of integration deduced from the boundaries of the object.

The functional **I** may be written as:

$$I = \int\int_{D} \{ C(.) + \sum_{k=1}^{N} \lambda_k(\mu_k) [\frac{\delta V_k(\mu_k)}{V_k(\mu_k)} \delta(s_k - \frac{A+B}{2}) - \frac{\delta \rho(x,y)}{\rho} S'_k J_k(\mu_k, s_k) \} dxdy \tag{6.34}$$

Following the procedure as defined for the parallel case in the preceding section, the solution to the optimisation is given by:

$$\frac{\partial C}{\partial \rho'} - \frac{\partial}{\partial x}\left(\frac{\partial C}{\partial \rho'_x}\right) - \frac{\partial}{\partial y}\left(\frac{\partial C}{\partial \rho'_y}\right) - \sum_{k=1}^{N} \lambda_k(\mu_k) S'_k J_k(\mu_k, s_k) = 0 \qquad \textbf{(6.35)}$$

where

$$\rho' = \frac{\delta\rho(x,y)}{\rho} \qquad \textbf{(6.36)}$$

and

$$\rho'_x = \frac{\partial \rho'}{\partial x} \qquad \rho'_{xy} = \frac{\partial^2 \rho'}{\partial y \partial x} \quad \text{etc.}$$

Then substituting the energy $\frac{1}{2}\rho'^2(x,y)$ for $C(.)$ in the above equation to obtain a specific model. Hence:

$$\rho' = \sum_{k=1}^{N} \lambda_k(\mu_k) S'_k J_k(\mu_k, s_k) \qquad \textbf{(6.37)}$$

This represents the minimum energy model (the variance between the estimated and reconstructed resistivity) with an attenuation correction due to the current distribution in the region. This weighting coefficient is discussed in more detail in Chapter seven. To determine the Lagrange multipliers, the model equation (6.37) is substituted back into equation (6.21) for the projections. Hence the projections are defined as:

$$\frac{\delta V_k(\mu_k)}{V_k(\mu_k)} = \sum_{n=1}^{N} \int_s \lambda_n(\mu_n) S'_k J_n(\mu_n, s_n) J_k(\mu_k, s_k) ds_k \qquad \textbf{(6.38)}$$

Redefining the projections as conductance strips:

$$\frac{\delta V_k(\mu_k)}{V_k(\mu_k)} = \sum_{n=1}^{N} \int_{\mu_1}^{\mu_{t+1}} \int_{A(x_k)}^{B(x_k)} \lambda_n(\mu_n) S'_k J_n(\mu_n, s_n) J_k(\mu_k, s_k) ds_k d\mu_k \qquad \textbf{(6.39)}$$

6.3.1 Matrix Structure

The evaluation of the Lagrange multipliers uses some of the assumptions defined for the previous geometries. The value of $\lambda_k(\mu_k)$ is assumed to be constant within each conductance strip. It is also assumed that the equipotential lines are normal to the boundary of the domain **D**. The error in this approximation will be reduced if the number of samples is increased. These small perturbations are considered later in Chapter seven.

The discrete version of equation (6.39) may be rewritten in matrix form as:

$$\mathbf{p_k} = \sum_{z=1}^{N} \mathbf{Y'_{kz} S'_k J_{kz}} \qquad \textbf{(6.40)}$$

where $\mathbf{k = 1, 2, .., N}$ and $\frac{\delta \mathbf{V_k}}{\mathbf{V_k}} = \mathbf{p_k}$ which, with λ_z is a column vector:

$$\mathbf{p_k^T} = [\mathbf{p_k(x_1), p_k(x_2), .., p_k(x_k), .., p_k(x_s)}] \qquad \textbf{(6.41)}$$

$$\lambda_z^T = [\lambda_z(x_1), \lambda_z(x_2), .., \lambda_z(x_q), .., \lambda_z(x_s)] \qquad \textbf{(6.42)}$$

where

T	denotes transposition,
$\mathbf{Y'_{kz}}$	is the unscaled associated system matrix,
$\mathbf{S'_k}$	is the normalised current distribution weighting,
$\mathbf{J_{kz}}$	is the scaling Jacobian.

The scaling Jacobian would normally be combined with $\mathbf{Y'_{kz}}$, and then equation (6.40) may be rewritten as:

$$\frac{\delta \mathbf{V}}{\mathbf{V}} = \mathbf{YS'}\lambda \qquad \textbf{(6.43)}$$

This is the discrete version of equation (6.40), where **Y** is a system matrix defining the proportions of λ that contribute to each projection point. If the weighting coefficient $\mathbf{S'}$ is taken to be unity, then the **Y** matrix is permuted block circulant. For this

geometry the current distribution is assumed to be approximately uniform. This assumption requires verification with an opposite data collection system (section 6.3), which was not available for this research. This is not the case for the second geometry described later. The weighing coefficient $\mathbf{S}'$ is incorporated into the backprojection operation to preserve the structure of the associated system matrix. This is not necessary for parallel orthogonal curvilinear geometry but is required for the system geometry detailed in the next section. An interpolation scheme to estimate the continuous Lagrange multipliers from their values at a finite number of points is developed as follows.

Assuming that the Lagrange multipliers are constant, then the elements of the $\mathbf{Y}$ matrix will be dependent only on the limits of integration defined in equation (6.40) and on the scaling Jacobian. Evaluation of the elements of the $\mathbf{Y}$ matrix can be achieved by approximation. From equation (6.40), the observation can be made that the element values are related to the areas of intersection of the strips whose boundaries are defined by the limits of the integrand. By assuming that the width of the curvilinear conductance strips is constant, the area is defined by the intersection of two curvilinear strips as demonstrated in Figure 6.4.

A further assumption is made to assist in the evaluation of the area ie., that the curvilinear strip areas can be approximated by an intersecting parallelogram, similar to the parallel case presented in Chapter four.

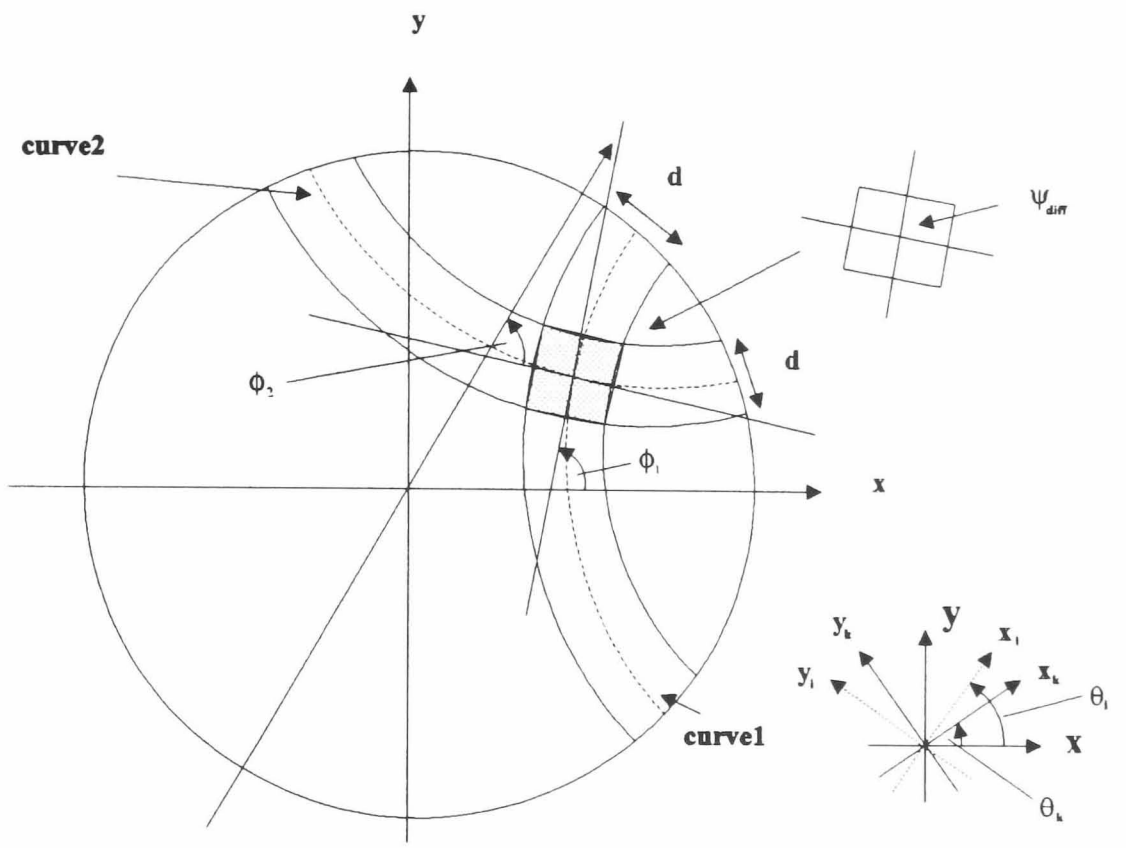

Figure 6.4 Intersection of curvilinear strips

Consider Figure 6.4 with a single intersection defined by the shaded region, also shown as an approximate parallelogram. The centres of the two strips are denoted by the dash lines curve 1 and curve 2. The unrotated slope of curve 1 is defined by:

$$\tan\phi_1 = \left.\frac{dy}{dx}\right|_{curve1} \tag{6.44}$$

and the unrotated slope of curve 2 is similarly defined by:

$$\tan\phi_2 = \left.\frac{dy}{dx}\right|_{curve2} \tag{6.45}$$

If the rotations of curves **1** and **2** from the horizontal ($\theta = 0$) are denoted by θ_k and θ_i respectively, the angle of rotation from the horizontal for the first curve is given by:

$$\theta_k + \phi_1 = \psi_1 \tag{6.46}$$

and the angle of rotation from the horizontal for the second curve :

$$\theta_i + \phi_2 = \psi_2 \tag{6.47}$$

Hence the angle between the curves is:

$$\psi_1 - \psi_2 = \psi_{diff} \tag{6.48}$$

Also the area of the parallelogram may be defined as:

$$|\underline{\mathbf{A}} \times \underline{\mathbf{B}}| = \frac{\mathbf{d}^2}{\sin(\psi_{diff})} \tag{6.49}$$

The edge elements are approximated to half the value of elements inside the domain. Hence the area of the edge elements is defined as:

$$\frac{1}{2}|\underline{\mathbf{A}} \times \underline{\mathbf{B}}| = \frac{\mathbf{d}^2}{2\sin(\psi_{diff})} \tag{6.50}$$

As with the parallel system, intersections outside the domain **D** are not considered, and the matrix elements associated with them are set to zero.

To demonstrate the construction of the submatrix structure, consider a simple system with $\mathbf{S} = \mathbf{5}$ and $\mathbf{N} = \mathbf{5}$, shown in Figure 6.5

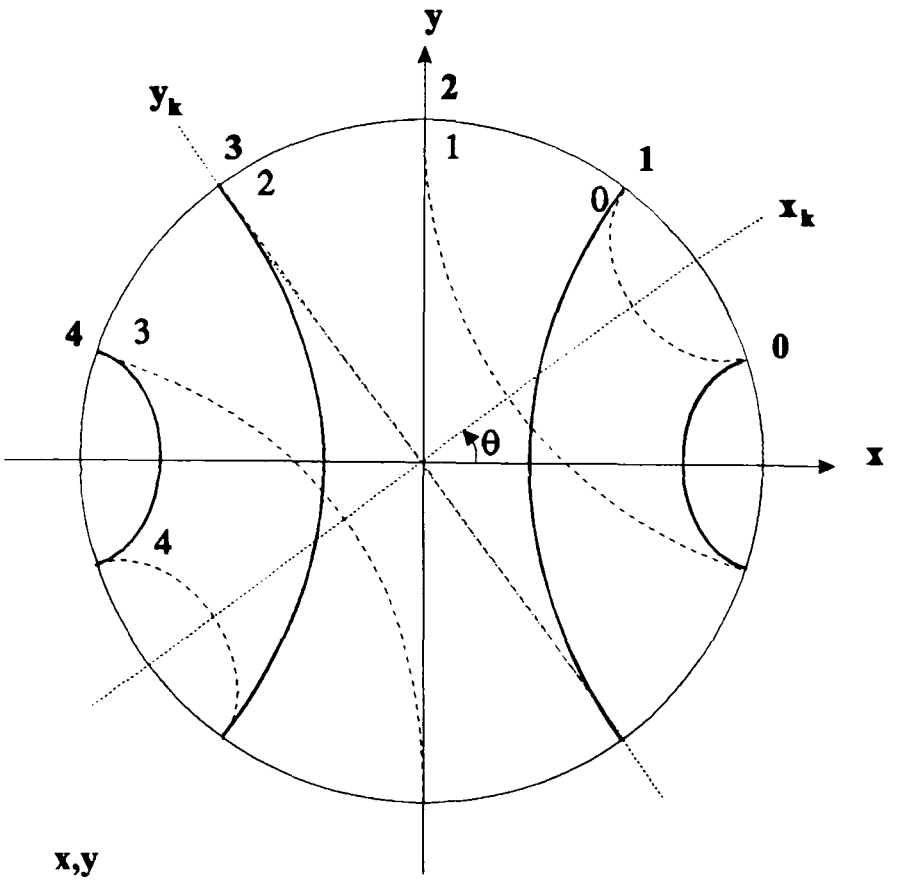

x_k, y_k \ x,y	0	1	2	3	4
0	$\frac{1}{2}$	$\frac{1}{2}$	0	0	0
1	$\frac{1}{2}$	1	$\frac{1}{2}$	0	0
2	0	$\frac{1}{2}$	1	$\frac{1}{2}$	0
3	0	0	$\frac{1}{2}$	1	$\frac{1}{2}$
4	0	0	0	$\frac{1}{2}$	$\frac{1}{2}$

Y Submatrix

Y Submatrix construction

"1" means 1 full parallelogram

"1/2 " means half parallelogram

"0" means no intersection

Figure 6.5 Example of submatrix structure and evaluation

The structure of the $\mathbf{Y}$ matrix is again fully contained within the first half block row as shown in equation (6.51), but the regions of equal elements within submatrices are not present, as was the case with the parallel and fan beam systems. The algorithms presented in Chapter five exploited this property to reduce storage requirements, unlike the algorithms given in this Chapter. This is not a significant problem in the EIT system, as the data set is greatly reduced compared to the X-ray system.

$$\mathbf{Y} = \begin{bmatrix} \mathbf{Y_0} & \mathbf{Y_1} & \mathbf{Y_2} & .. & \frac{\mathbf{Y_{N-1}}}{2} & \frac{\tilde{\mathbf{Y}}_{\mathbf{N-1}}}{2} & .. & \tilde{\mathbf{Y}}_{\mathbf{1}} \\ \mathbf{Y_1} & \mathbf{Y_0} & \mathbf{Y_1} & .. & \frac{\mathbf{Y_{N-3}}}{2} & .. & .. & \tilde{\mathbf{Y}}_{\mathbf{2}} \\ \mathbf{Y_2} & \mathbf{Y_1} & \mathbf{Y_0} & .. & .. & .. & .. & .. \\ .. & .. & .. & .. & .. & .. & .. & .. \\ \tilde{\mathbf{Y}}_{\mathbf{1}} & \tilde{\mathbf{Y}}_{\mathbf{2}} & .. & \frac{\tilde{\mathbf{Y}}_{\mathbf{N-1}}}{2} & \frac{\mathbf{Y_{N-1}}}{2} & .. & .. & \mathbf{Y_0} \end{bmatrix} \qquad \textbf{(6.51)}$$

A plot of the matrix for $\mathbf{S = 5}$ and $\mathbf{N = 5}$ is presented in Figure 6.6, which demonstrates the structure of the $\mathbf{Y}$ matrix by use of pseudo colour.

6.3.2 Recursive Algorithm

Again the block successive relaxation method can be employed for the solution of the system. The formulation of a solution uses the same approach as detailed in Chapter four. Hence the solution to the system in equation (6.51) is given by:

$$\lambda_{kl}^{n+1} = \lambda_{kl}^{n} + \frac{\gamma \varepsilon_{kl}}{\mathbf{Y_0(i,i)}} \qquad \textbf{(6.52)}$$

where

$$\varepsilon_{kl} = \left(\frac{\delta \mathbf{V}_{kl}}{\mathbf{V}_{kl}}\right) - \left(\frac{\delta \mathbf{V}_{kl}}{\mathbf{V}_{kl}}\right)^{n} \qquad \textbf{(6.53)}$$

and is the difference between the measured normalised boundary potential $(\delta \mathbf{V}_{kl}/\mathbf{V}_{kl})$, and the calculated normalised boundary potential $(\delta \mathbf{V}_{kl}/\mathbf{V}_{kl})^{n}$.

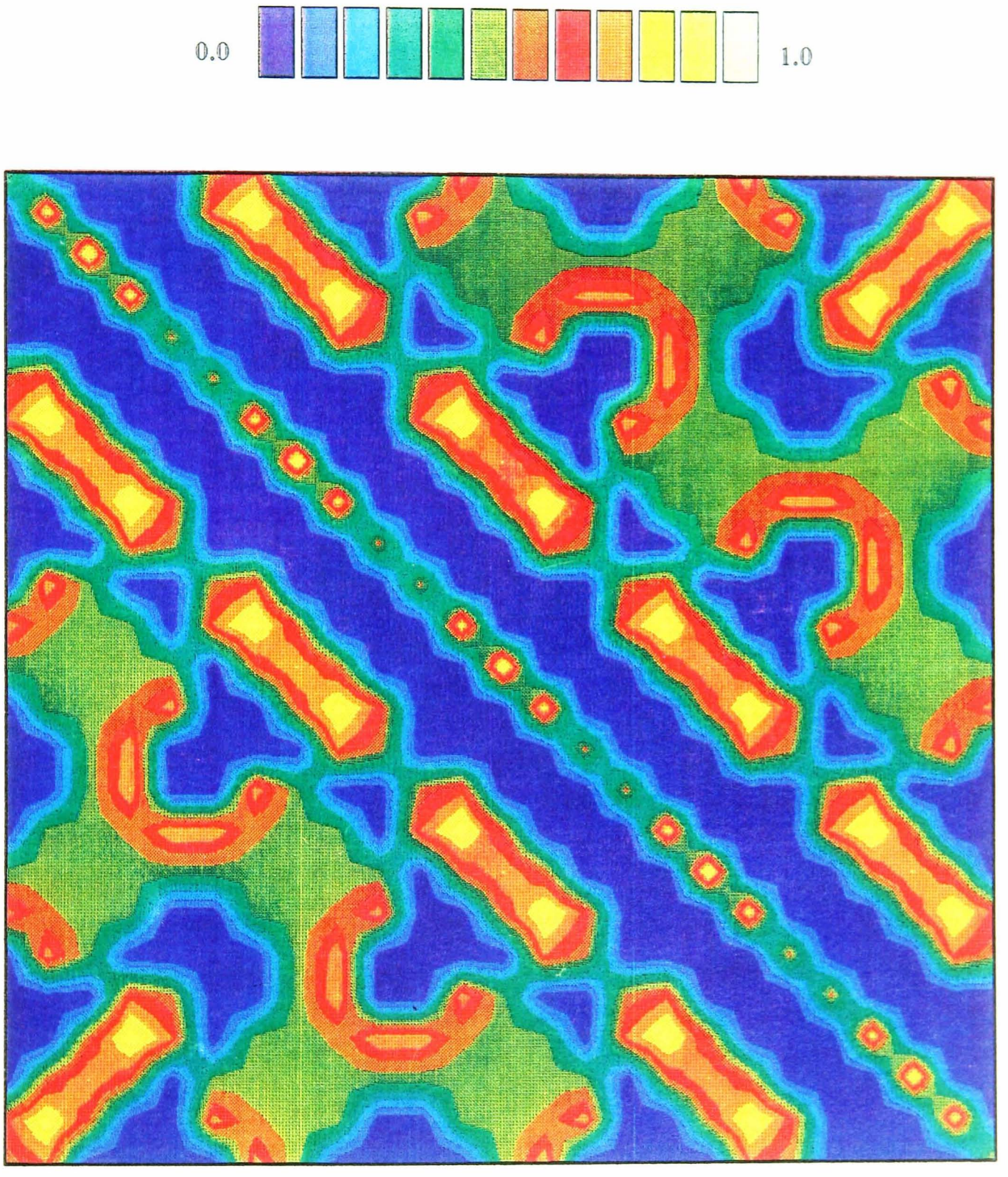

Figure 6.6 Plot of the matrix for S = 5 and N = 5 (eqn. 6.51)

To compute the initial estimate of the Lagrange multipliers:

$$\lambda_{ki}^{0} = \frac{1}{Y_0(i,i)} \forall ki \qquad (6.54)$$

Due to the different structure of the submatrix in the curvilinear system compared with that of the parallel case shown in Chapter four, the difference submatrices are not produced. Hence Step 2, as defined in Chapter four of section 4.22, is omitted. Otherwise the process for evaluating the Lagrange multipliers is the same. A relaxation factor of $\gamma = 0.001$ with $n = 50$ was found to yield the optimum results with simulated data (see Chapter seven). The effect on the relaxation parameter of the deviation of equipotential lines from their paths was considered by the addition of Gaussian noise to the associated system matrix. The deviation cannot be modelled simply as the addition of Gaussian noise to data. A fuller analysis would require lengthy investigation using hardware phantoms (section 7.2) and was not undertaken in this research.

6.3.3 Direct Algorithm

This approach is essentially the same as that used for the parallel and fan beam systems. Increased storage is required due to the structure of the associated system matrix. One half of a block row is required to reconstruct the complete matrix. As the permuted block circulant structure is maintained in the inverse, the same storage is required. The limitation of not producing a difference matrix for both recursive and direct algorithms in order to reduce the storage requirements is not a major problem as the number of data samples within the EIT data collection system is limited.

Improvement in the EIT system may require further investigation into enhancing the algorithm if video rate tomography is required. In this research, a hardware solution is proposed in Chapter eight as a means of improving reconstruction

speeds. At present the need for reconstructions at real time rate is being debated by researchers. Many applications require that data be collected in real time, with the reconstruction being produced at a later time for analysis.

The results shown in this Chapter were generated using the direct algorithm. The values of the relaxation parameter and the number of iterations were obtained empirically, as explained in Chapter seven.

6.4 Results

A simple phantom was developed to demonstrate the technique. The same test phantom was used for parallel and divergent curvilinear systems (Figure 6.7(a)).

A resolution of 65 by 65 was adopted to present the results. Both **2** and **3-D** noiseless plots (Figure 6.7(b)) are presented to demonstrate the reconstructions.

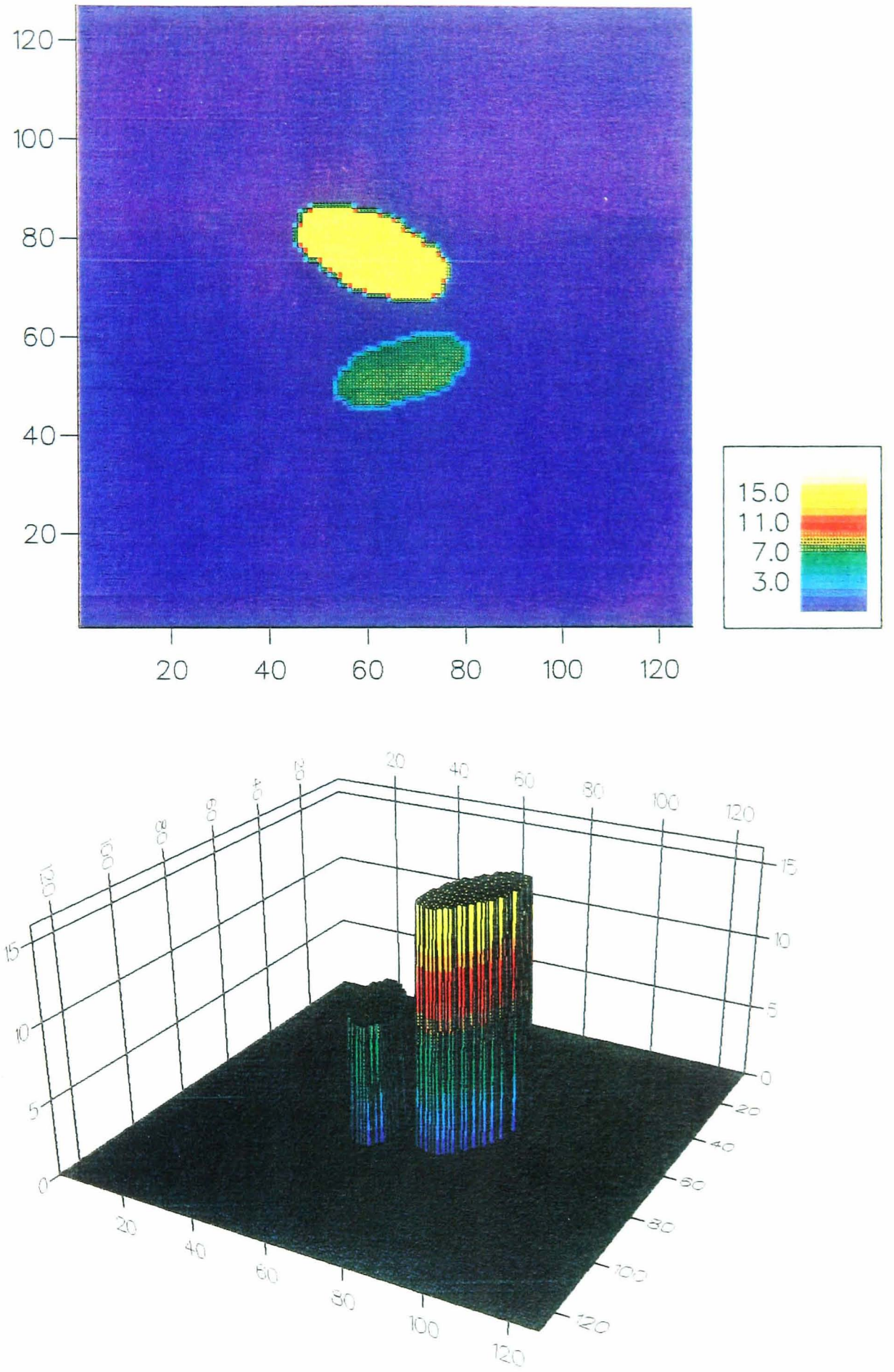

Figure 6.7(a) Original test Phantom

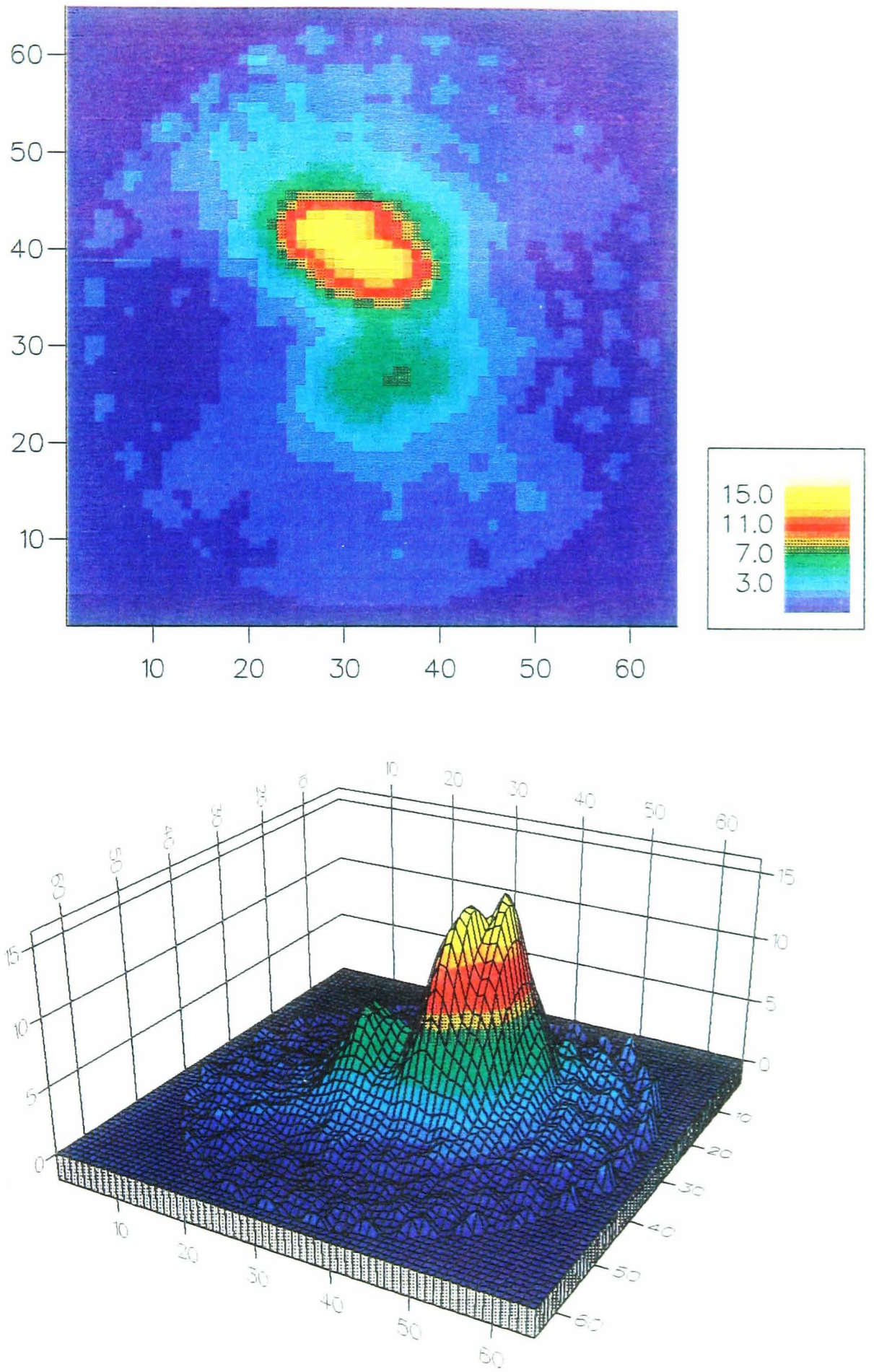

Figure 6.7(b) 2-D and 3-D plots of the reconstruction

(γ = 0.001 and n = 50)

6.5 Divergent Orthogonal Curvilinear System

A second approach to data collection in EIT is known as the dipole method and is illustrated in Figure 6.8

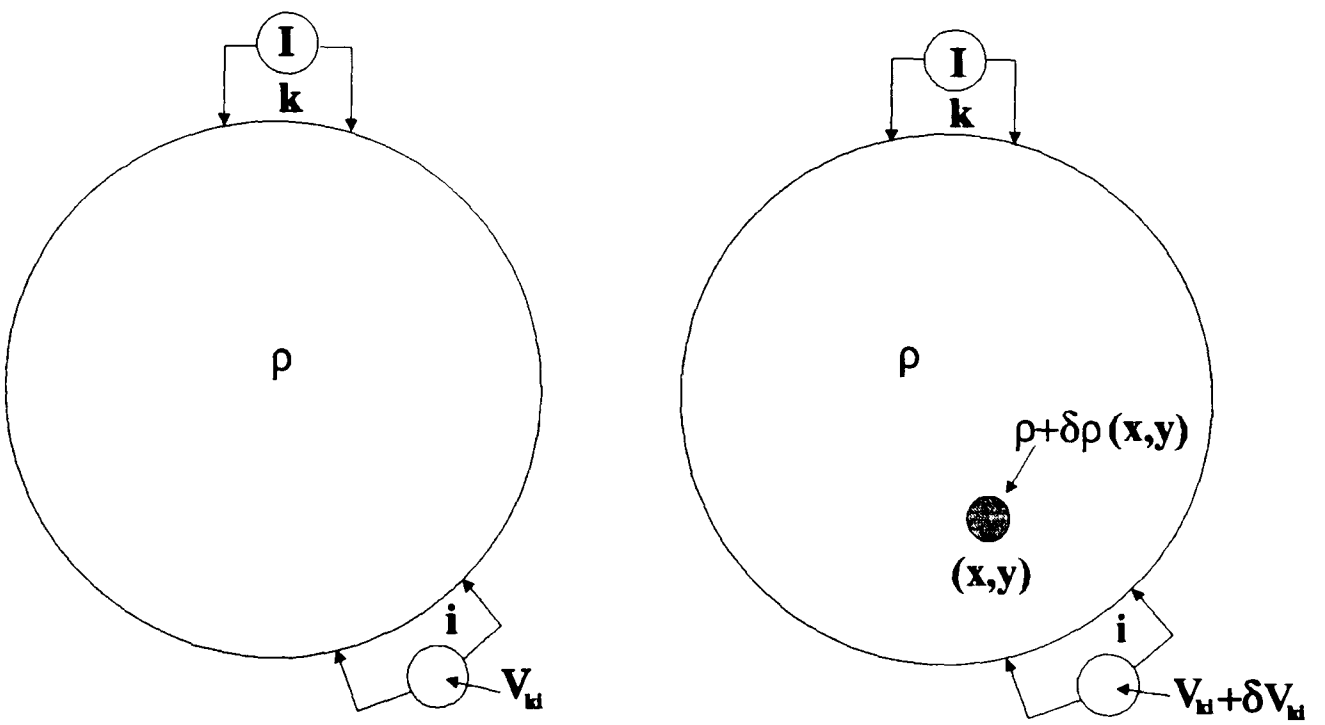

(a) **(b)**

Figure 6.8 Schematic diagram illustrating the four electrode method for collecting impedance tomography data in (a) a bounded volume of uniform resistivity, and (b) a bounded volume where one volume element has changed resistivity.

The current is injected by two adjacent electrodes, while pairs of electrodes placed around the object measure the potential differences for each pair. In this collection system the data collection is over a 2π range and the number of samples is given by $n(n-3)/2$, where n is the number of electrodes. As in the parallel orthogonal system, the data can be translated into a measure of difference resistivity for the strip lying within the equipotential lines in a homogeneous medium. The dipole method produces equipotential lines which follow the path defined by the conformal

transformation (appendix F):

$$\mathbf{w = u + jv = \frac{1}{x + jy}} \tag{6.55}$$

hence

$$\mathbf{u_k = \frac{x}{x^2 + y^2}} \qquad \mathbf{v_k = \frac{-y}{x^2 + y^2}} \tag{6.56}$$

$$\mathbf{x_k = \frac{u}{u^2 + v^2}} \qquad \mathbf{y_k = \frac{v}{u^2 + v^2}} \tag{6.57}$$

and

$$\begin{aligned} \mathbf{x_k} &= \mathbf{x\cos\theta_k + y\sin\theta_k} \\ \mathbf{y_k} &= \mathbf{-x\sin\theta_k + y\cos\theta_k} \end{aligned} \tag{6.58}$$

For constant values of **u** in the **u,v** space, the path of the equipotential lines can be mapped in the **x,y** space, and for constant **v** in the **u,v** space the current paths will map in the **x,y** space, as demonstrated in Figure 6.10. The transformation produces only an approximation to the actual equipotential paths. The errors resulting from this approximation will be considered in the next Chapter.

A collection geometry based on these transformations is presented in Figure 6.9. The variance model can be derived for the above transformations as follows.

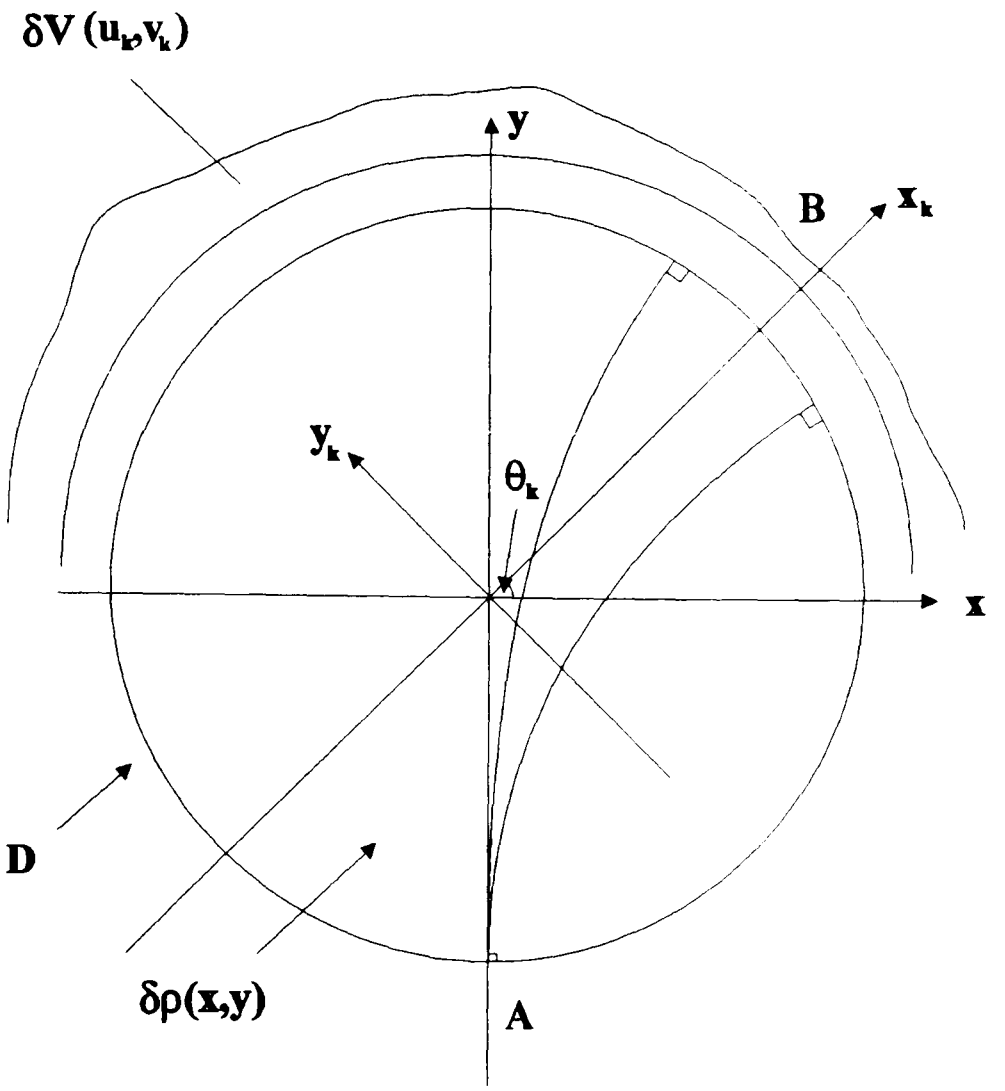

Figure 6.9 Divergent Orthogonal Curvilinear System

For the divergent system let $(\mathbf{u_k}, \mathbf{v_k})$ denote the co-ordinate system in the **2-D** plane. The $\mathbf{k^{th}}$ general projection of a **2-D** space limited object, represented by the function $\delta\rho(\mathbf{x},\mathbf{y})$, can be defined as:

$$\delta V_{kl} = \int_{\mu_l}^{\mu_{l+1}} \int_{A(v_k)}^{B(v_k)} \delta\rho(x,y) W_k' dv_k du_k \qquad (6.59)$$

where $\Delta\mu = \mu_{l+1} - \mu_l$, and $\mathbf{W_k'}$ represents the current distribution along the strip defined by the path $\mathbf{v_k}$. Using the principle of superposition, the normalised boundary potentials can be defined as:

$$\frac{\delta V_{kl}}{V_{kl}} = \frac{\delta\rho(x,y)}{\rho} \tag{6.60}$$

If V_{kl} and ρ are constants, and $\frac{W_k'}{W_k}$ is assumed to be constant for this part of the analysis, where W_k is the current density for the reference boundary potential. Then:

$$\frac{\delta V_{kl}}{V_{kl}} = \int_{\mu_l}^{\mu_{l+1}} \int_{A(v_k)}^{B(v_k)} \frac{\delta\rho(x,y)}{\rho} \frac{W_k'}{W_k} dv_k du_k \tag{6.61}$$

$A(v_k)$ and $B(v_k)$ are the limits of the integration along the curved path and $\Delta\mu$ is the width of the strip of integration that is not constant in the x,y plane for this system.

The associated normalised projection is given by:

$$\left(\frac{\delta V_k(u_k)}{V_k(u_k)}\right)' = \frac{\delta V_k(u_k)/V_k(u_k)}{\int_w J_k(u_k,v_k)dv_k} \tag{6.62}$$

where the scaling Jacobian is given by:

$$J_k\left(\frac{x,y}{u,v}\right) = \begin{vmatrix} \frac{\partial u_k}{\partial x} & \frac{\partial v_k}{\partial x} \\ \frac{\partial u_k}{\partial y} & \frac{\partial v_k}{\partial y} \end{vmatrix} \tag{6.63}$$

where

$$\frac{\partial u}{\partial x} = \frac{y^2 - x^2}{(x^2 - y^2)^2} \qquad \frac{\partial u}{\partial y} = \frac{-2xy}{(x^2 + y^2)^2}$$

$$\frac{\partial v}{\partial x} = \frac{2xy}{(x^2 + y^2)^2} \qquad \frac{\partial v}{\partial y} = \frac{y^2 x^2}{(x^2 + y^2)^2}$$

Hence:

$$J\left(\frac{u,v}{x,y}\right) = \frac{1}{(x^2 + y^2)^2} \tag{6.64}$$

The procedure for applying the optimisation approach for this geometry

follows the same form as before. If the projection is considered in the $\mathbf{u,v}$ space, then following the procedure defined for a general cost criterion, a function $\rho(\mathbf{x,y})$ is required such that the integral:

$$\mathbf{I} = \iint_{\mathbf{D}} \mathbf{C(.)dxdy} \tag{6.65}$$

is a minimum subject to the constraints:

$$\sum_{k=1}^{N} \frac{\delta \mathbf{V_k(v_k)}}{\mathbf{V_k}} = \sum_{k=1}^{N} \int_{w} \frac{\delta \rho(\mathbf{x,y})}{\rho} \mathbf{S'_k du_k} \tag{6.66}$$

where

$$\mathbf{S'_k} = \frac{\mathbf{W'_k}}{\mathbf{W_k}} \tag{6.67}$$

which can be rewritten as:

$$\sum_{k=1}^{N} \{ \frac{\delta \mathbf{V_k(v_k)}}{\mathbf{V_k}} - \int_{w} \frac{\delta \rho(\mathbf{x,y})}{\rho} \mathbf{S'_k du_k} \} = 0 \tag{6.68}$$

Using the Euler - Lagrange method:

$$\mathbf{I} = \iint_{\mathbf{D}} \mathbf{C(.)dxdy} + \sum_{k=1}^{N} \int_{w} \lambda_k(\mathbf{v_k}) [\frac{\delta \mathbf{V_k(u_k)}}{\mathbf{V_k(u_k)}} - \int_{w'} \frac{\delta \rho(\mathbf{x,y})}{\rho} \mathbf{S'_k J_k du_k}] \mathbf{dv_k} \tag{6.69}$$

where $\mathbf{w' = 0 \Rightarrow 2\pi}$, and $\lambda_k(\mathbf{v_k})$ are the **1-D** Lagrange multipliers functions. Transforming from **(u,v)** to **(x,y)** space, the equation (6.69) can be written as:

$$\mathbf{I} = \iint_{\mathbf{D}} \{ \mathbf{C(.)} + \sum_{k=1}^{N} \lambda_k(\mathbf{v_k}) [\frac{\delta \mathbf{V_k(u_k)}}{\mathbf{V_k}} \delta(\mathbf{J_k} - \frac{\mathbf{A+B}}{2}) - \frac{(\frac{\delta \rho(\mathbf{x,y})}{\rho})}{\mathbf{J_k}} \mathbf{S'_k}] \} \mathbf{dxdy} \tag{6.70}$$

where $\delta(.)$ is a delta function.

Minimising the variance by substituting:

$$\frac{1}{2}\left(\frac{\delta\rho(x,y)}{\rho}\right)^2 \tag{6.71}$$

for $\mathbf{C(.)}$ gives:

$$\frac{\delta\rho(x,y)}{\rho} = \sum_{k=1}^{N} \lambda_k(v_k) J_k S_k \tag{6.72}$$

This is the variance model for the divergent curvilinear geometry. The $\mathbf{i^{th}}$ measurement of the $\mathbf{k^{th}}$ projection is given by:

$$\frac{\delta V_{ki}}{V_{ki}} = \sum_{n=1}^{N} \int_{\mu_i}^{\mu_{i+1}} \int_{A(v_k)}^{B(v_k)} \lambda_k(v_k) S_k' J_n J_k \, du_k dv_k \tag{6.73}$$

Therefore rewriting equation (6.74) to include the scaling Jacobian gives:

$$\frac{\delta\rho(x,y)}{\rho} = \sum_{k=1}^{N} \frac{\lambda_k(v_k)}{(x_k^2 + y_k^2)^2} S_k' \, du_k dv_k \tag{6.74}$$

Hence the projections can be defined by:

$$\frac{\delta V_{ki}}{V_{ki}} = \sum_{n=1}^{N} \int_{\mu_i}^{\mu_{i+1}} \int_{A(v_k)}^{B(v_k)} \frac{\lambda_n(v_n)}{(x_n^2 + y_n^2)^2 (x_k^2 + y_k^2)^2} S_k' \, du_k dv_k \tag{6.75}$$

6.5.1 Matrix Structure

Two approaches can be taken to evaluate the elements of the associated system matrix. In both cases the values of $\lambda_k(v_k)$ are assumed to be constant. It is also assumed that the equipotential lines are normal to the boundary of the domain **D**. The implications of this assumption are considered later.

The discrete version of equation (6.75) may be written as:

$$\mathbf{p_k} = \sum_{k=1}^{N} \mathbf{A'_{kz} S'_z J_{kz}} \tag{6.76}$$

where $\mathbf{k = 1,2,..,N}$ and $\frac{\delta V_k}{V_k} = p_k$ also:

$$\mathbf{p_k^T = [p_k(x_1), p_k(x_2), .., p_k(x_k), .., p_k(x_s)]} \tag{6.77}$$

$$\boldsymbol{\lambda_z^T = [\lambda_z(x_1), \lambda_z(x_2), .., \lambda_z(x_q), .., \lambda_z(x_s)]} \tag{6.78}$$

T denotes transposition,

$\mathbf{A'_{kz}}$ is the unscaled associated system matrix,

$\mathbf{S'_k}$ is the normalised current distribution weighting,

$\mathbf{J_{kz}}$ is the scaling Jacobian.

The scaling Jacobian would normally be combined with $\mathbf{A'_{kz}}$, and equation (6.76) may then be rewritten as:

$$\frac{\delta \mathbf{V}}{\mathbf{V}} = \mathbf{AS'\lambda} \tag{6.79}$$

As with the previous cases, this is the discrete version of equation (6.75), where **A** is a system matrix that defines the proportions of λ which contribute to each projection point. The weighting function **S'**, which represents the current distribution, is introduced during backprojection to preserve the structure of the associated system matrix. From equation (6.75) the observation can be made that the element values are related to the areas of intersection of the divergent orthogonal curvilinear wedges. The boundaries of these wedges are the equipotential lines as demonstrated in Figure 6.10(b).

There are two approaches to evaluating the areas of the intersections. The first is an exact method that maps the curvilinear wedges into the $\mathbf{u,v}$ plane. Consider Figure 6.10(b). A curvilinear wedge shown by the shaded region is bounded by two adjacent values of α_1, e.g. α_1, α_2 .

Their value in the **u, v** plane is:

$$\mathbf{u_1} = \frac{\mathbf{1}}{\mathbf{2\alpha_1}} \text{ and } \mathbf{u_2} = \frac{\mathbf{1}}{\mathbf{2\alpha_2}} \tag{6.80}$$

The boundary of the medium **D** is defined by a **v** value limit in the **u, v** plane. This is specified by:

$$\mathbf{v} = -\frac{\mathbf{1}}{\mathbf{2r_0}} = -\frac{\mathbf{y}}{\mathbf{x^2 + y^2}} \tag{6.81}$$

where:

$$\mathbf{r_0} = \beta_0 \tag{6.82}$$

For the **abc** wedge, the **v** boundary values are specified by:

$$\mathbf{v = 0 \rightarrow v = -\frac{1}{2r_0}} \tag{6.83}$$

The **a'b'c'** wedge can also be specified in a similar way as:

$$\mathbf{u_1'} = \frac{\mathbf{1}}{\mathbf{2\alpha_1'}} \text{ and } \mathbf{u_2'} = \frac{\mathbf{1}}{\mathbf{2\alpha_2'}} \tag{6.84}$$

and

$$\mathbf{v' = 0 \rightarrow v' = -\frac{1}{2r_0}} \tag{6.85}$$

If a new set of co-ordinates is introduced, sitting on the centre of the medium:

$$\bar{\mathbf{y}} = \mathbf{y} - \beta_0 \tag{6.86}$$

$$\bar{\mathbf{x}} = \mathbf{x} \tag{6.87}$$

and

$$\bar{\mathbf{x}}\mathbf{r_i} = \mathbf{r_0 \cos\theta} \qquad \bar{\mathbf{y}}\mathbf{r_i} = \mathbf{r_0 \sin\theta} \tag{6.88}$$

using **i** to denote the initial and f the final values as indicated in Figure 6.10(b). Then after rotation by θ_k where:

$$\theta_k = \mathbf{k}\frac{2\pi}{\mathbf{N}} \qquad \text{where } \mathbf{k=1,2,..,N} \tag{6.89}$$

The final rotation can be defined as:

$$\bar{\mathbf{x}}\mathbf{r_f} = \mathbf{r_0 \cos(\theta + \theta_k)} \tag{6.90}$$

$$\bar{\mathbf{y}}\mathbf{r_f} = \mathbf{r_0 \sin(\theta + \theta_k)} \tag{6.91}$$

Initially:

$$\mathbf{u_i} = \frac{\bar{\mathbf{x}}}{\bar{\mathbf{x}}^2 + (\bar{\mathbf{y}} + \beta_0)^2} \tag{6.92}$$

This can be rewritten as:

$$\mathbf{u_i} = \frac{\cos\theta}{2\mathbf{r}_0(1+\cos\theta)} \tag{6.93}$$

or

$$\mathbf{u_i} = \frac{1 - \tan(\frac{\theta_k}{2})}{2\mathbf{r}_0(1+\tan(\frac{\theta_k}{2}))} \tag{6.94}$$

After rotation by θ_k , i.e. $\theta \rightarrow \theta + \theta_k$:

$$\mathbf{u}_f = \frac{1 - \tan(\frac{\theta+\theta_k}{2})}{2\mathbf{r}_0(1+\tan(\frac{\theta+\theta_k}{2}))} \tag{6.95}$$

Hence, as the circle wedge rotates (or co-ordinates rotate), the $\mathbf{u_i}$ is equal to a constant line moved to different positions in the **u,v** plane. To evaluate the intersection area of the curvilinear wedges in the **x,y** plane requires mapping the co-ordinates to the **u,v** plane, calculating the portion of overlay in the **u,v** plane (Figure 6.10(c)), and multiplying by the scaling Jacobian.

A second approach to evaluating the A matrix elements is to approximate the curvilinear wedges by triangles. The area of a curvilinear wedge can be approximated by:

$$\frac{2\pi\mathbf{R}_0}{\mathbf{N}\mathbf{R}_1} \tag{6.96}$$

where $\mathbf{R}_0$ is the maximum length of the wedges, and $\mathbf{R}_1$ is the length at intersection. If the width of the wedge is known at the point of intersection then the area estimate is approximated by the parallel case of intersecting parallelograms whose widths are defined by the width of the wedges. Hence intersection or element area is given by:

$$\textbf{element area} = \frac{\textit{wedge}_1 \times \textit{wedge}_2}{\sin\theta} \tag{6.97}$$

where θ is the angle of intersection. This is a reasonably good approximation if the

number of electrodes **N** is large.

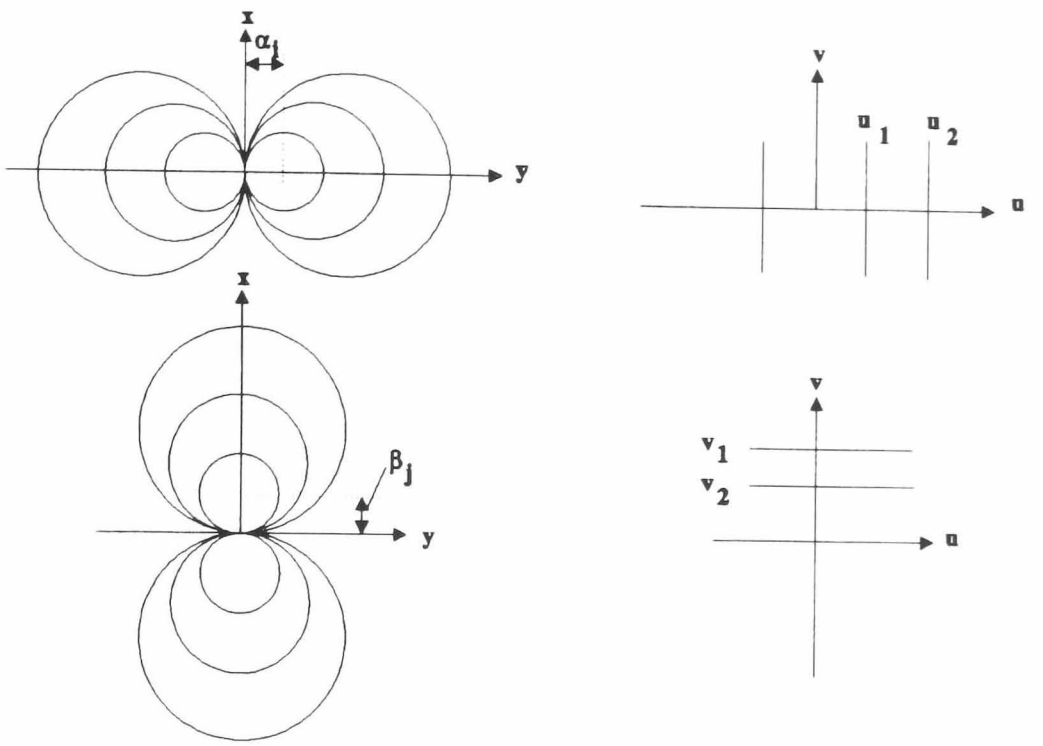

(a)

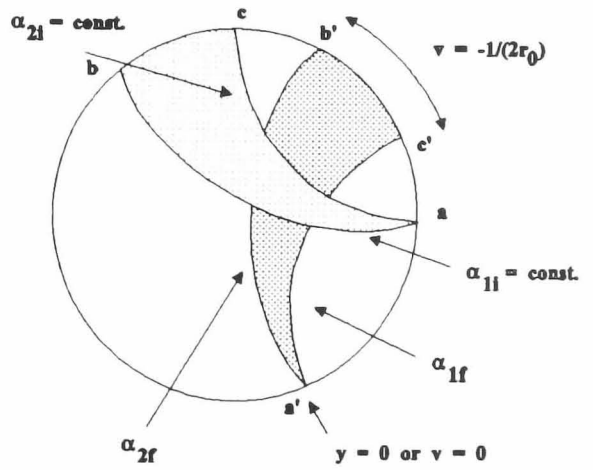

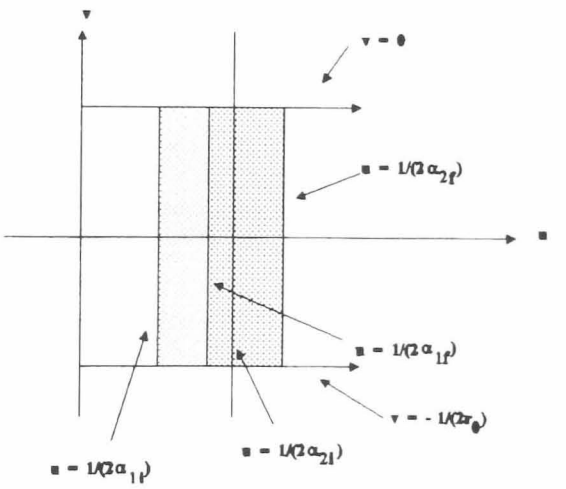

(b) **(c)**

Figure 6. 10(a) u,v plane, (b) overlap in the x,y plane (Intersection of Curvilinear wedges), (c) overlap in the u,v plane.

The structure of the system matrix is shown in Figure 6.11. The structure is similar to the system matrix for the parallel orthogonal curvilinear geometry in that it is permuted block circulant and has the general form given in equation (6.98):

$$\mathbf{A} = \begin{bmatrix} \mathbf{A}_0 & \mathbf{A}_1 & \mathbf{A}_2 & .. & \frac{\mathbf{A}_{N-1}}{2} & \frac{\tilde{\mathbf{A}}_{N-1}}{2} & .. & \tilde{\mathbf{A}}_1 \\ \mathbf{A}_1 & \mathbf{A}_0 & \mathbf{A}_1 & .. & \frac{\mathbf{A}_{N-3}}{2} & .. & .. & \tilde{\mathbf{A}}_2 \\ \mathbf{A}_2 & \mathbf{A}_1 & \mathbf{A}_0 & .. & .. & .. & .. & .. \\ .. & .. & .. & .. & .. & .. & .. & .. \\ \tilde{\mathbf{A}}_1 & \tilde{\mathbf{A}}_2 & .. & \frac{\tilde{\mathbf{A}}_{N-1}}{2} & \frac{\mathbf{A}_{N-1}}{2} & .. & .. & \mathbf{A}_0 \end{bmatrix} \qquad \textbf{(6.98)}$$

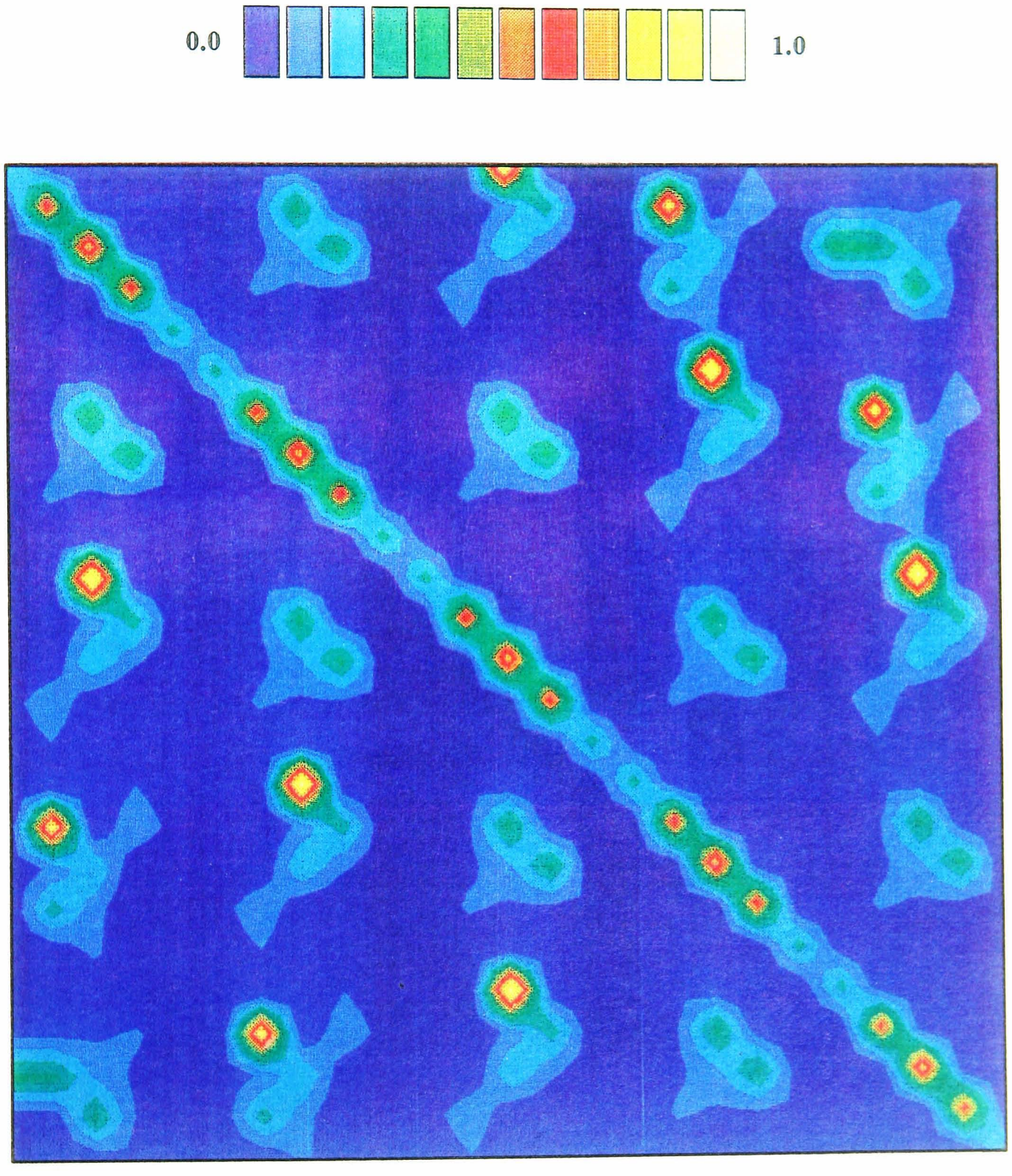

Figure 6.11 Plot of the matrix for S = 5 and N = 5 (eqn. 6.98)

6.5.2 Recursive Algorithms

The block successive relation method can also be employed to find a solution to the system of equations. The formulation of the solution uses the approach detailed in Chapter four. The solution to the system in equation (6.98) is given by:

$$\lambda_{kl}^{n+1} = \lambda_{kl}^{n} + \frac{\gamma \varepsilon_{kl}}{A_0(i,i)} \tag{6.99}$$

where

$$\varepsilon_{kl} = \left(\frac{\delta V_{kl}}{V_{kl}}\right) - \left(\frac{\delta V_{kl}}{V_{kl}}\right)^{n} \tag{6.100}$$

and is the difference between the measured normalised boundary potentials $(\delta V_{kl}/V_{kl})$ and the calculated normalised boundary potentials $(\delta V_{kl}/V_{kl})^{n}$. Step 2, as defined in Chapter five, is again omitted from the algorithm for evaluation of the Lagrange multipliers. This is due to the submatrices not having a structure that can be exploited to reduce storage.

6.5.3 Direct Algorithms

The approach is the same as the parallel curvilinear system, the details of which can be found in section 6.2. As the current distribution weighting is applied in the backprojection procedure, the structure of the associated system matrix is maintained and the matrix is permuted block circulant.

6.6 Results

The test phantom generated for the parallel curvilinear case was used for the divergent system. A resolution of 65 by 65 was adopted to present the results. The results presented in this section demonstrate that reconstructed images can be produced by the procedures described in this Chapter. A fuller analysis of the results is presented in Chapter seven, where data obtained from a hardware collection system are demonstrated.

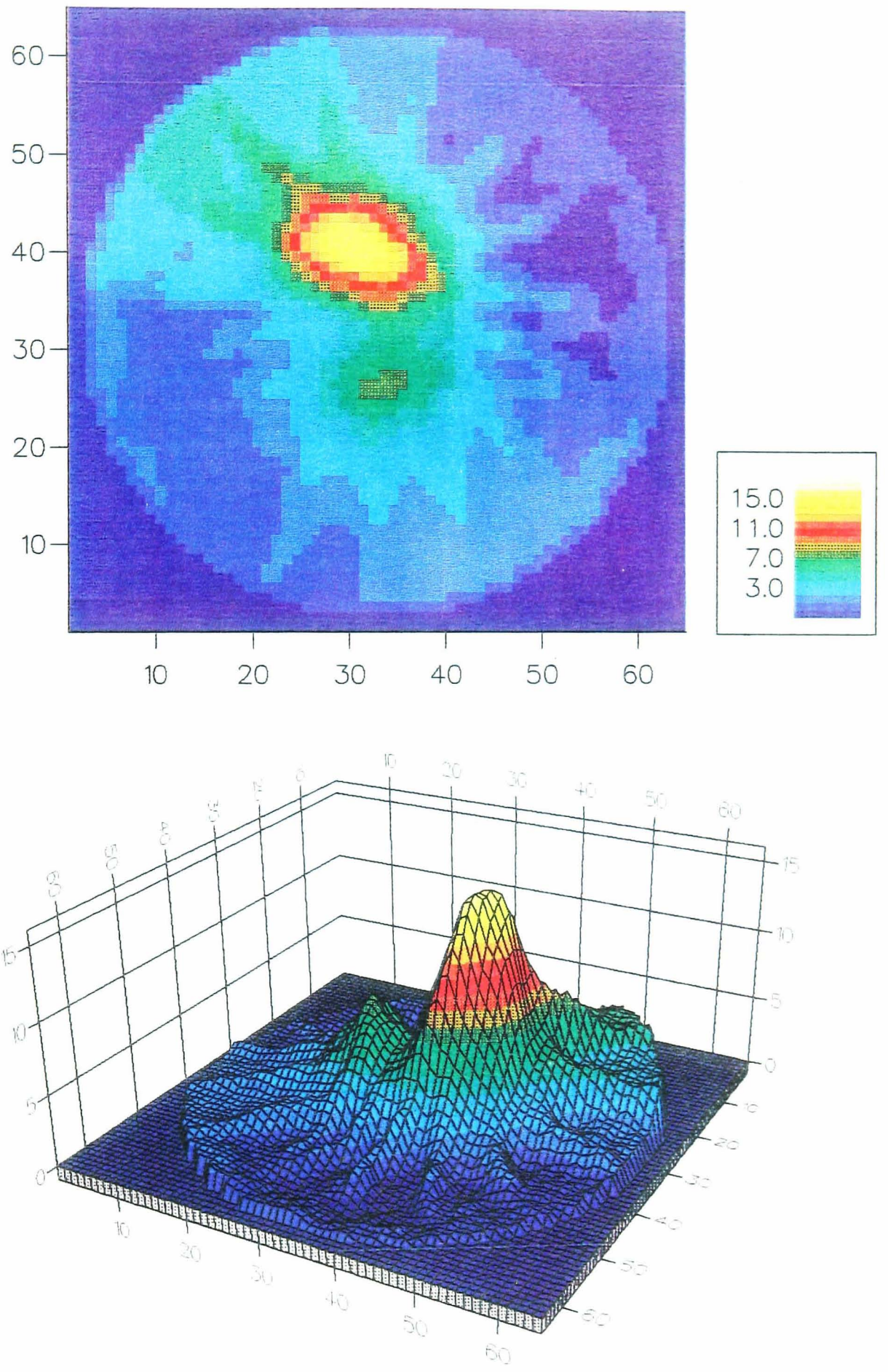

Figure 6.12 2-D and 3-D plots of reconstruction

(γ = 0.002 and n = 50)

6.7 Discussion

The objectives of this Chapter were to define new models specifically for the opposite and dipole method of data collection in EIT, and to obtain images of the changes in resistivity from different sets of boundary profiles. An initial set of results is given in Figures 6.7 and 6.12 . These show that a resistivity image can be produced using the proposed models. A key objective in the development of these models was to maintain the structure of the associated system matrix. This allows the use of the procedures discussed in Chapter five. The structures of the associated matrices were maintained by applying the weighting for the current distribution during the backprojection operation and not during the evaluation of their Lagrange multipliers.

The analysis presented in this Chapter clearly demonstrates that it is possible to adapt the constrained optimisation technique to the new geometries associated with the EIT system. A number of assumptions have been made in the analysis to assist in the development of the reconstruction procedure. The implication of these will be considered in Chapter seven. In the parallel and fan beam systems, the evaluation of the associated system matrix elements was made by precise estimates of the areas of intersections. These were reasonably straightforward for these cases due to the nature of the sources used to obtain the data. In the systems presented in this Chapter there is no guarantee that the equipotential lines follow the paths predicted by the transformations. The approximations used in the simulated results do not appear to degrade the reconstructed image. These estimates and their possible effects are considered in the next Chapter.

The use of variational principles in EIT to derive models for the reconstruction of resistive images is not unique to this research. Kohn and Vogelius [6.1] proposed a variational method which is demonstrated with software phantoms by Kohn and McKenney [6.2]. However, the method presented in this research differs in a number of important aspects. The models derived produce images of the natural log of the difference resistivity, unlike the images produced by Kohn and McKenny [6.2] which

are static images which rely on the use of FEM's. to model the resistivity distribution. The CORT methods maintain the structure of the associated system matrix, thus allowing the use of the efficient algorithm detailed in Chapter five. In addition, noise match techniques can be exploited as demonstrated in Chapter seven. As yet, no results have appeared which demonstrate that their algorithms produce reasonable results with boundary data obtained from hardware phantoms or clinical measurements. The following Chapter will present such results, based on the CORT methods.

7 PERFORMANCE EVALUATION OF RECONSTRUCTION ALGORITHMS

7.1 Introduction

The purpose of this Chapter is to evaluate the performance of the results obtained from the new algorithms. The algorithms are evaluated with boundary data modelled from both mathematical (software) and hardware phantoms. The data obtained from the hardware phantom were obtained using the Sheffield Mark I [7.15] data collection system, to illustrate the viability of the technique in a clinical environment.

To assist in the evaluation of the results, performance measurement parameters are defined as: a) spatial resolution, b) conductivity resolution and c) conductivity contrast [3.9]. These parameters are used by EIT researchers to determine measurement errors, movement artefacts and electrode location errors. Although the above parameters define the limits of the EIT data collection system, they do not included errors introduced by the reconstruction algorithms. Further parameters discussed below will be used to evaluate these properties.

7.2 Phantoms

To test the algorithms for EIT applications a controlled source was required which models the boundary data. This model is known as a phantom. Two types of phantom have been developed for evaluating reconstruction results. The first is a software phantom that attempts to model the boundary potentials of the medium under test using mathematical approximations, and the second, known as a hardware phantom, uses physical materials to model the boundary potential. The hardware phantom is a box or cylindrical shape filled with a material of homogenous resistivity

or with a collection of separate materials of different resistivity.

The development of physical hardware phantoms is a complex subject as the real objects in a system under clinical examination are non linear and usually do not have discontinuities. An example of the range of organ impedance at low frequencies is given in table 7.1. (Barber and Brown 1984) [3.5].

Tissue	**Resistivity**
Cerebrospinal fluid	65Ωcm
Plasma	66Ωcm
Blood	150Ωcm
Liver	350 to 550Ωcm
Neural tissue -grey matter -white matter	580Ωcm 284Ωcm 682Ωcm
Lung	727 to 2363Ωcm
Fat	2060 to 2720Ωcm
Bone	16600Ωcm

Table 7.1 The resistivity of organ tissue at low frequencies (20 to 100 kHz)

Several researchers have addressed the issue of hardware phantoms by constructing resistor networks [7.1] or using tanks filled with a saline solution [7.2]. As yet, no accurate solution has been devised. To indicate the problem of constructing a hardware phantom, several issues need to be addressed regarding the materials used.

i) What are the electrical properties at EIT frequencies and how freely can they be altered?

ii) What is the temperature stability of the material used to model the

medium under examination?

iii) How fast, if at all, do ionic species leach out of the material, especially if two samples are in contact?

Due to these drawbacks, both types of phantom were used to evaluate the algorithms. The mathematical phantom gives a controlled source where the effect of additive noise could be studied, and the hardware phantom illustrated the problem of resolution due to current sensitivity.

The hardware phantom constructed to model the boundary potentials is illustrated in Figure 7.1. It uses a clear perspex cylinder of 89mm internal diameter filled with a saline solution of 0.2% concentration. Glass and polyacrylamide rods were placed into the solution to model changes of resistivity at selected locations.

One example of clinical data is also given to illustrate the contrast between hardware modelled data and real clinical data. This is not intended to be a full evaluation with modelled clinical data, as a detailed study would require more research. To fully assess the algorithms used in a clinical environment is outside the scope of this research. It is suggested that this would be a good area for future investigation. Further details of work on hardware phantoms can be found in the E.C. workshop on Phantoms for EIT [7.1].

The normalised boundary data created from the mathematical phantom was modelled from an image consisting of 127 by 127 pixels. This produced a set of boundary data with 15 samples per boundary profile for both geometries. The parallel curvilinear geometry has 15 boundary profiles over a range of $\mathbf{0}$ to π, and the divergent curvilinear geometry uses 15 boundary profiles over the range of 0 to $\mathbf{2\pi}$. The use of sub-sampling to model the boundary profiles is intended to improve accuracy. The phantom used in this research, is more complex than the Brown and Seager's version [3.4] using two objects to demonstrate the interaction between objects.

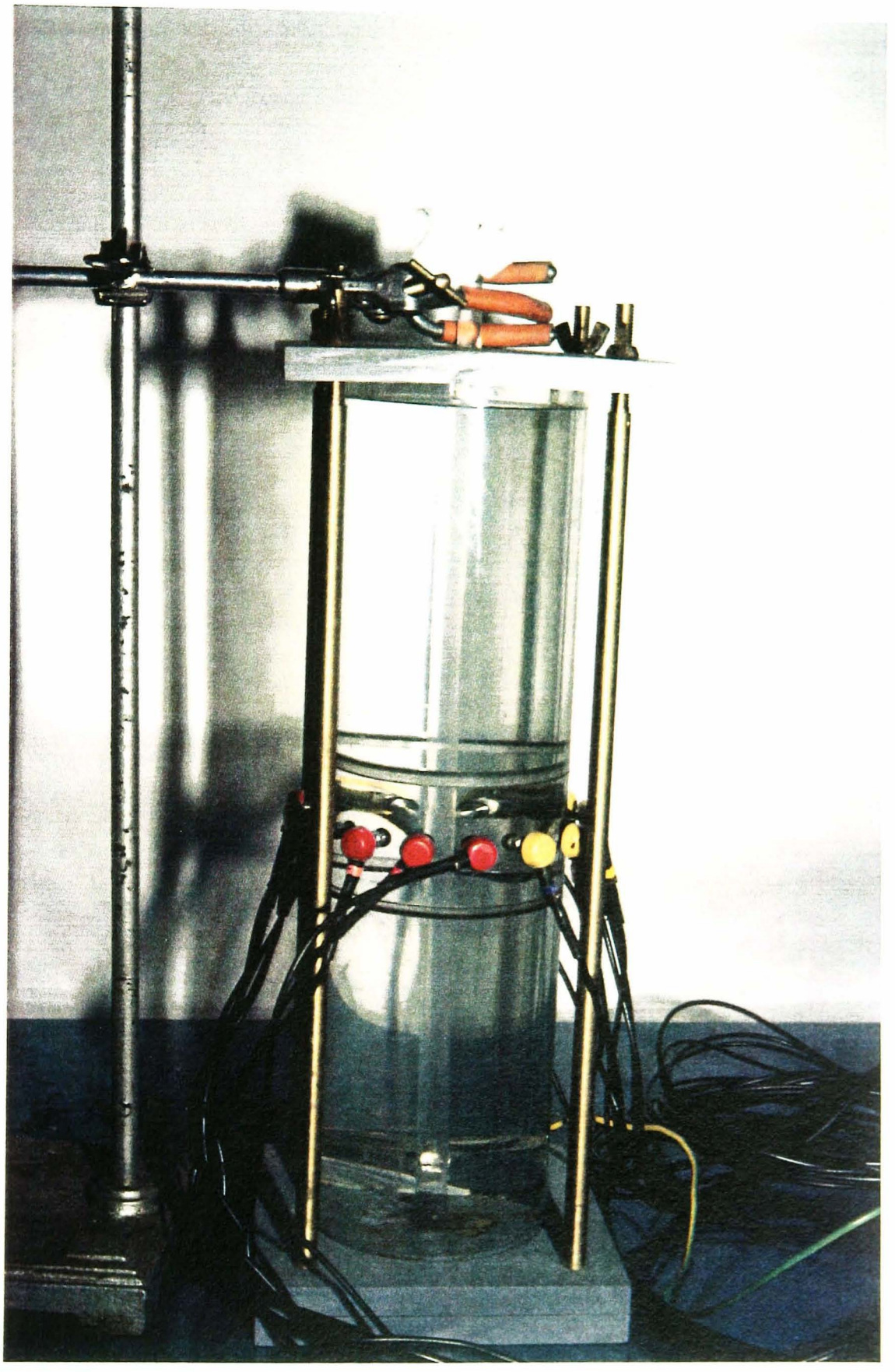

Figure 7.1 Hardware phantom

7.3 Reconstruction Performance Parameters

To evaluate the quality of reconstructions obtained from an impedance imaging system, two sets of parameters are required; those which measure the ability of an impedance imaging system to distinguish between different conductivity distributions, and a set which identifies the performance of the reconstruction algorithms. There are many different ways of measuring the performance of the impedance imaging system.

In EIT, the change in pixel density represents a change in the natural log (ln) of the resistivity corresponding to a physiological change [3.4]. In the system used in this research, the number of samples available for each boundary potential measurement, and hence the total number of boundary measurements, was limited. This limitation restricts the spatial resolution of the EIT system. It is suggested by Holder [7.3] that the spatial resolution (defined as the distance apart that two objects need to be separated to give an impedance value of 1/e of the peak changes), for a point impedance disturbance in a tank of saline might be expected to be roughly 20% of the tank diameter at the centre or 10 to 16% near the edge. This limit may change with improvement in data collection technology.

The following parameters are used in EIT to define performance limits. In the evaluation of reconstruction algorithms, it is important to separate the data collection limits from the limitations of the algorithms. Seager [3.9] defines three parameters for system performance.

a) The spatial resolution is the smallest region of a medium in which the conductivity can be independently determined. This is best illustrated with Figure 7.2. A small region of radius $\mathbf{r_a}$ and conductivity σ_a is shown within a larger circular region of radius $\mathbf{r_b}$ and conductivity σ_b. It is useful to think of the region σ_a as a particular picture element (pixel) within the overall image. The spatial resolution is used to define the smallest region (pixel) in which the conductivity can be independently determined.

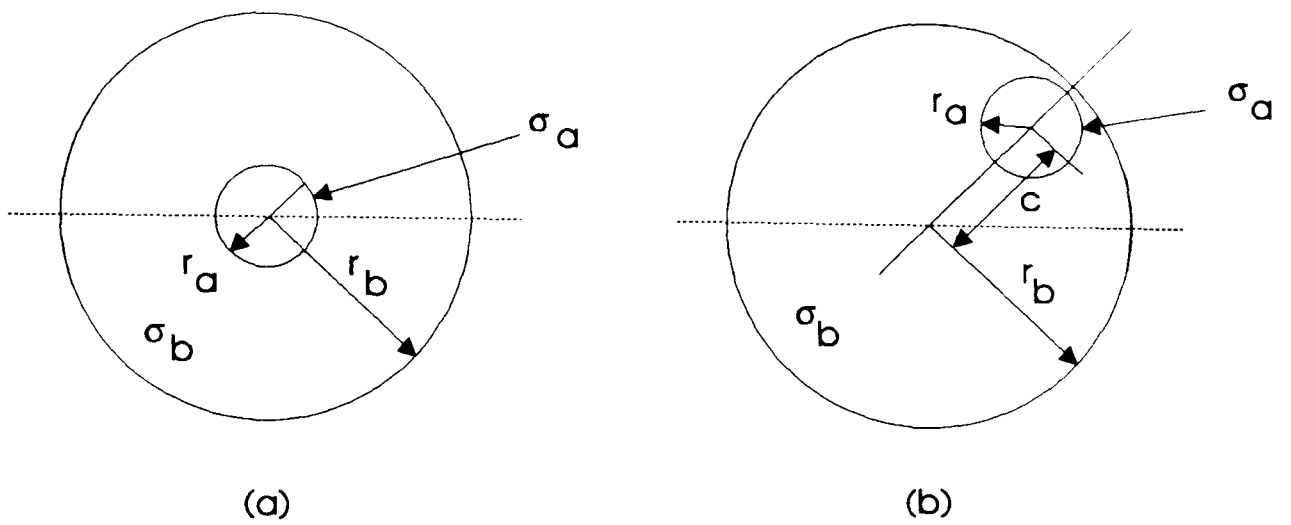

Figure 7.2 Circular objects with (a) centre anomaly and (b) an offset anomaly.

Seager [3.9] defines this as:

$$\textit{Spatial resolution} = \frac{r_a}{r_b} \qquad (7.1)$$

b) The conductivity resolution is the smallest range in which the conductivity of a region (pixel) can be isolated. It is described as the fractional change in conductivity contrast and is defined as:

$$\textit{Conductivity resolution} = \frac{\delta\alpha}{\alpha} \qquad (7.2)$$

c) α is the conductivity contrast, and is the ratio of the conductivity of an anomaly to that of its surrounding region. Therefore:

$$\textit{Conductivity contrast} = \frac{\sigma_a}{\sigma_b} \qquad (7.3)$$

To understand how these parameters relate to the performance of the data collection system, consider the situation depicted in Figure 7.3 [3.9] for the dipole data collection system.

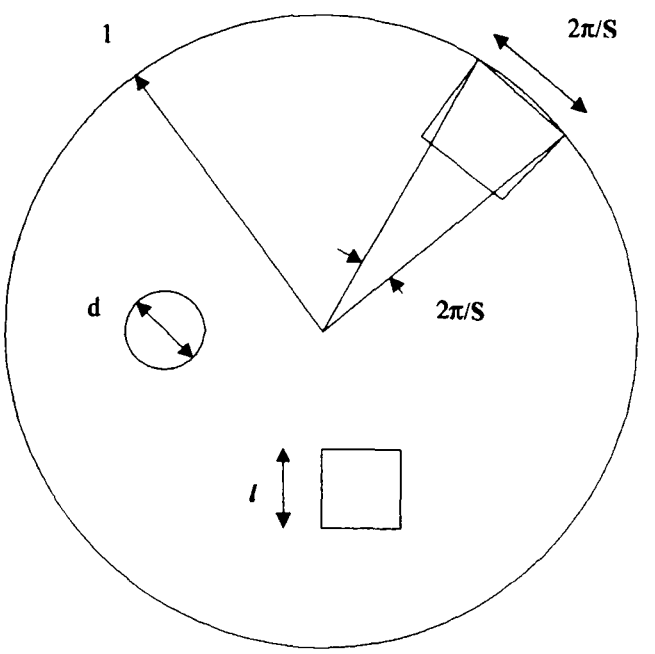

Figure 7.3 Resolution illustration

If a circular region of unit radius has **S** equispaced electrodes attached to its boundary, the angle between each electrode is $2\pi/S$. The best resolution it is reasonable to expect at the boundary is equal to the electrode spacing. Suppose this resolution is represented by a square pixel of side $2\pi/S$, centred π/S below the boundary, as shown in Figure 7.3.

The effective resolution at the centre of the region may be found from the relationship (appendix G):

$$\lim_{r_a \Rightarrow 0} \left(\frac{r}{r_a}\right) = \frac{1}{(1-c^2)} \qquad (7.4)$$

where **r** is the effective resolution, and both r_a and **c** are defined in Figure 7.2. Substituting $r_a = \pi/S$ and $c = 1 - \pi/S$ into equation 7.4 gives:

$$r = \frac{\pi S}{(2\pi S - \pi^2)} \qquad (7.5)$$

A plot of the resolution against the number of electrodes is presented below in Figure 7.4, and the pixel size against the number of electrodes is given in Figure 7.5

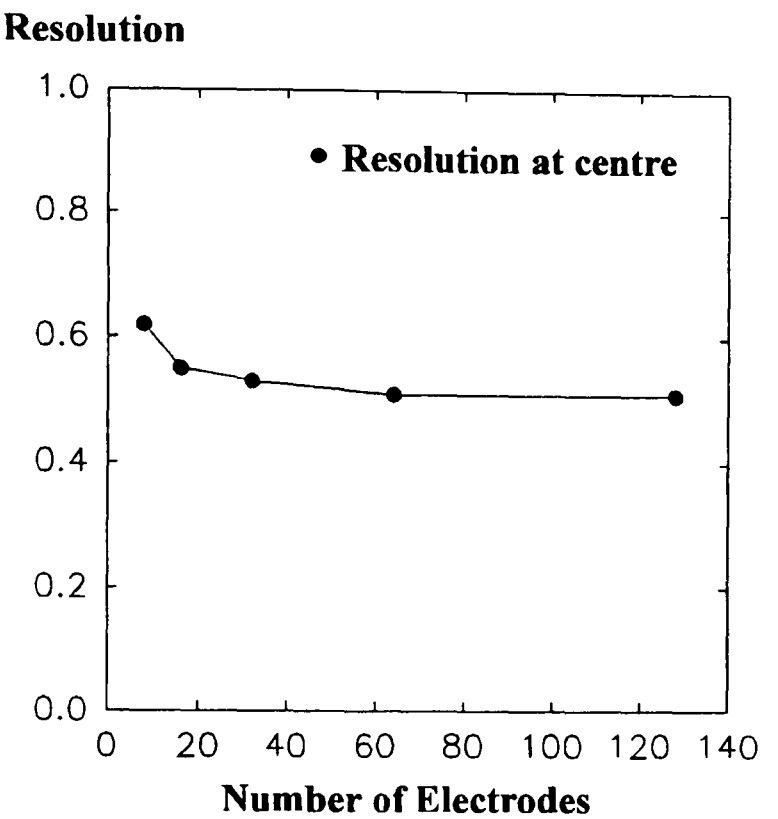

Figure 7.4 Effective resolution as a function of number of electrodes

The graph in Figure 7.4 appears to indicate that at the centre of the region the resolution does not increase with the increase of the number of electrodes. This can be explained as follows. The current density is very high near the edge and very low near the centre. The contribution to the voltage at the boundary from any point is proportional to the product of Green's function (log distance in **2-D**), the gradient of the log of conductivity and the gradient of the potential. Also, beyond some value of **S,** no more useful information about the central region can be obtained. As the information is limited, so is the resolution that can be achieved there.

From the reciprocity theorem [7.4], if there are **S** electrodes, then at most $\mathbf{S(S-1)/2}$ independent measurements can be obtained. If the independent measurements are used to create an image composed of equal size square pixels or round pixels, having length and diameter $\boldsymbol{l}$ and **d** respectively, then the smallest pixel

that can be resolved is shown in Figure 7.5.

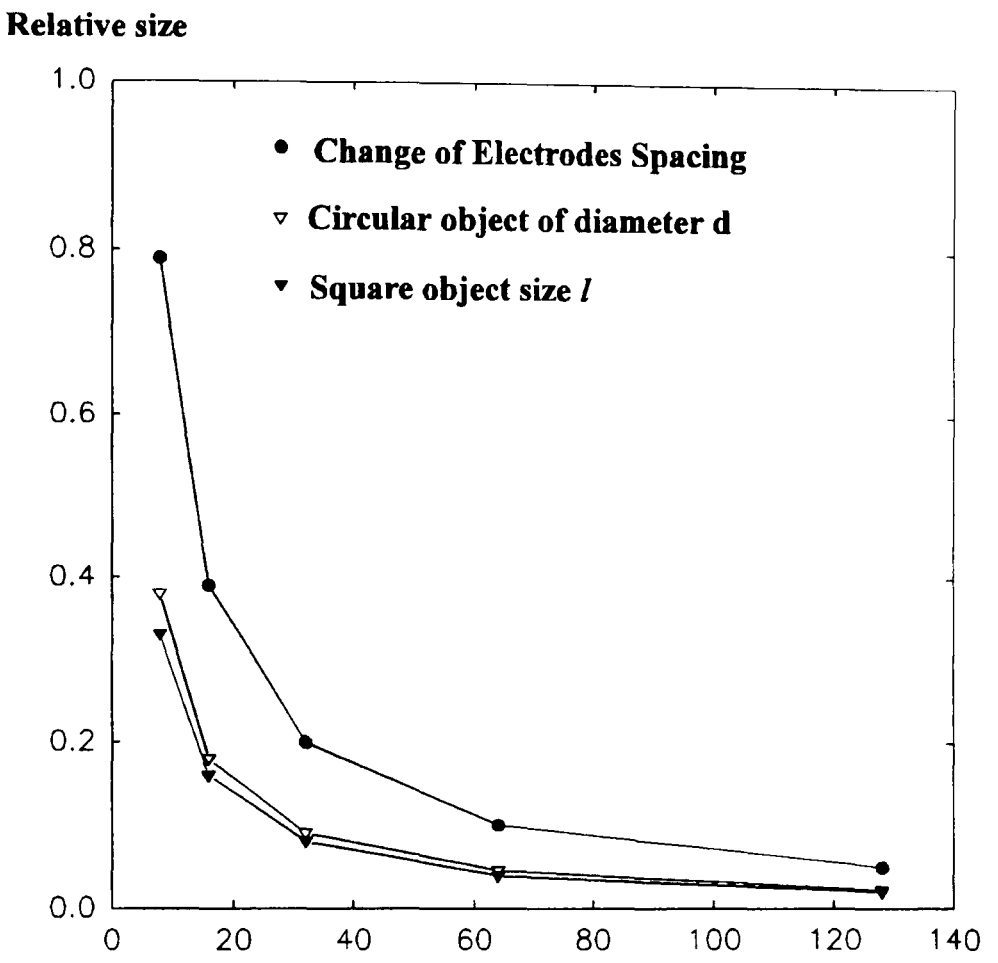

Figure 7.5 Pixel size against number of electrodes

The circular diameter **d** is defined by:

$$\mathbf{d} = 2\left[\frac{2}{(S(S-1))}\right]^{\frac{1}{2}} \tag{7.6}$$

and the length of the sides of the square is defined by:

$$l = \left[\frac{2\pi}{(S(S-1))}\right]^{\frac{1}{2}} \tag{7.7}$$

These parameters define performance limits for the EIT system. The reconstruction algorithm resolution is also limited by the distribution of the current density in the medium under examination.

The variation of resolution in different position in the medium was also investigated by Eyuboglu *et al.* [7.12], using experimental data obtained from the Sheffield Mark I system. Their definition of spatial resolution is based on the full-width-at-half-maximum (FWHM) of a point response function (PRF), where the PRF is modelled using a narrow conductor and an insulator placed in a tank filled with saline. For off-centre points, the PRF was found not to have the same FWHM in the radial direction and the tangential direction, i.e. perpendicular to the radial direction. The FWHM in both directions increases towards the centre. This increase in the tangential FWHM is less than the increase in the radial FWHM. The maximum FWHM at the centre was found to be 24% of the array diameter for both a conductor and an insulator using the Sheffield system.

Eyuboglu *et al.* [7.12] give the minimum FWHM for the conductor object as 12.7% of the array diameter in the radial direction, but the tangential FWHM at the same point is given as 21% of the array diameter. The minimum FWHM for the insulator object is given as 14.5% of the array diameter in the radial direction, but the tangential FWHM at the same point is 22% of the array diameter. The FWHM resolution is better for the conductor than the insulator, as expected, because of the different perturbation of current flow lines.

A number of other performance parameters have been suggested in the literature, but are not detailed here. These include distinguishability, [7.13] which is defined as the norm of the voltage differences divided by the norm of the current density and is a measure of the ability of a pattern of currents to distinguish between two conductivities. A detailed discussion of distinguishability is given by Cheney and Isaacson [7.14]. Visibility and sensitivity performance parameters are detailed in appendix G.

7.3.1 Current Density

The above analysis show that the spatial resolution for the dipole data collection method is not uniform due to the non-uniform distribution of current density

introducing a weighting factor. Barber and Brown [7.5] originally suggested that the weighting factor was required to compensate for the equipotential lines not being circularly symmetric for all pixels. This was redefined by Seager *et al.* [3.9] using a conformal transformation. Seager *et al.* [3.9] derive the weighting factor to compensate for the non-uniform current density (appendix G). The weighting is a compromise between resolution and accuracy of the reconstructed image. This is the same weighting factor for current density which Barber and Brown [7.5] developed for their algorithm and was chosen for the results produced by the CORT algorithm in order to be compatible with the Sheffield data collection system. Hence the current density weighting:

$$\mathbf{S}' = \frac{\boldsymbol{l} - \mathbf{r}^2}{\boldsymbol{l}^2} \qquad \textbf{(7.8)}$$

where $\boldsymbol{l}$ and $\mathbf{r}$ are defined in Chapter three. This is combined into the backprojection operation.

7.3.2 Reconstruction Evaluation Criteria

To evaluate the reconstruction algorithm developed in Chapter six, a different set of parameters is required as the above parameters do not indicate the accuracy of the reconstruction algorithms. Most are qualitative, but a few methods have been used to indicate if convergence to a solution has been achieved. The simplest of these approaches is visual inspection, but this can be only a subjective measure of quality. An alternative approach is to plot profiles that are rows or columns of the digitised image matrix. A selected row or column, passing through the region of interest in an original phantom, is plotted using a common axis with corresponding rows or columns taken from the reconstructed images, as illustrated in Figures 7.19 and 7.20. Many researchers have adopted this technique [2.19][5.7].

The technique developed in this research aims to minimise the error between

the resistivity of the object under examination and the reconstructed resistivity. It is often useful for comparison purposes to have a single unit of measure for the closeness of reconstruction fit to the original (sometimes known as "goodness"). Several of these measures are available. These are [2.25]:

1) The residual of each iteration:

$$r^n = [\sum_{j=1}^{SN} [\frac{\delta V_j}{V_j} - A\lambda_j^n]^2]^{\frac{1}{2}} \qquad (7.9)$$

2) The average reconstructed density:

$$\bar{\rho}^n = \frac{1}{M} \sum_{i=1}^{M} \rho_i^n \qquad (7.10)$$

where ρ_i^n is the average resistivity of the image in the i^{th} pixel for the n^{th} iteration, and M is total number of pixels in the reconstructed image.

3) The variance:

$$\sigma^2 = \frac{1}{M} \sum_{i=1}^{M} (\rho_i^n - \bar{\rho}^n)^2 \qquad (7.11)$$

4) The distance or Q-value [2.21]:

$$Q = \frac{\sum_{j=1}^{K^2} (\rho_j^n - \rho_j^0)^2}{\sum_{j=1}^{K^2} (\rho_j^0 - \bar{\rho})^2} \qquad (7.12)$$

where K^2 is the number of pixels in the reconstruction, ρ^0 and ρ^n are the original and reconstructed image vectors respectively, and $\bar{\rho}$ is the mean value of the original image. This measures the deviation of the reconstruction from the test picture. Hence the lower the value of Q (Quality), the higher the image quality.

The use of Q for image evaluation cannot be considered as very reliable since large differences in only a few regions can give a large value of Q. In the EIT case, the accuracy of the modelled projection data is dependent on the number of sub-pixels

used to create it. If the number of pixels is reduced to match the reconstructed value, there is a greater possibility of error in the simulated projection. An illustration of Q is given in Figure 7.6. The optimum value for γ obtained from this method does not agree with the results presented in section 7.7. The latter uses the residue approach and is in good agreement with the reconstructions obtained from the model data. As Q was not considered as a reliable measure, the residual value eqn. (7.9) was also adopted to select desired parameters of image quality for this research. The residual value was adopted over the average and variance measures because it relies on the match between the measured boundary potentials and the calculated boundary potentials. If there is error in the modelling of the boundary potentials, this is not included in the measure, unlike the average and variance parameters.

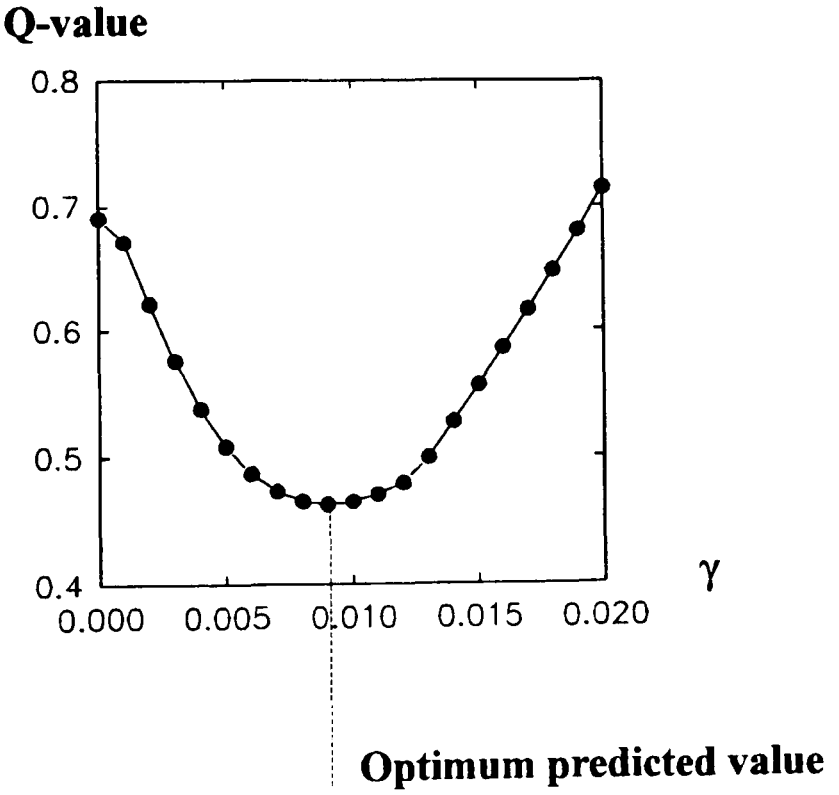

Figure 7.6 Graph of Q-value versus γ Divergent System.

It is normal practice to compare new reconstruction methods with those of convolution backprojection algorithms. In EIT system the main algorithm developed by Barber and Brown [1.17] is not easily reproduced, as part of the filter function is an

empirical function not given in the papers. Many authors describe this as a ramp function. [3.5]. Visual inspection of the Sheffield system's display, compared with the new approach, indicated that the new algorithm gave improved quality reconstructions.

7.4 Errors Produced by Noise

Noise limits the detection of the measured signal. Within the conductive region the smallest significant change that can be detected is that which yields a variation in the signal just exceeding the noise. This variation in signal is quantified here as the fractional change in potential compared with the actual potential value.

It is possible theoretically to relate the statistics of the noise in the collection system to the errors in the pseudo inverse of the associated system matrix [5.4]. This allows the noise artefact to be minimised in the final reconstructed image. If the value of the iteration parameter **n** is large for the pseudo inverse of the system matrix $\mathbf{M}^n$ (eqn. 5.32), then the pseudo inverse tends toward the true pseudo inverse i.e.:

$$\lim_{n \to \infty} \mathbf{A}\mathbf{M}^n \to \mathbf{I} \qquad (7.13)$$

$\mathbf{M}^n$ is used to denote the pseudo inverse of both parallel and divergent curvilinear systems in this case. The **3-D** presentation of the matrices for the parallel curvilinear pseudo inverse is shown in Figure 7.7. The figures show the change from the element dominance of $\mathbf{M}^n$, for small **n**, to the block diagonal dominance of the pseudo inverse $\mathbf{A}^+$.

a)

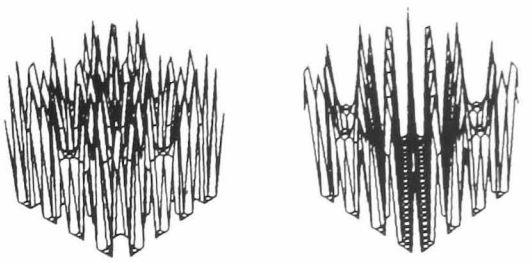

b) **n = 5**

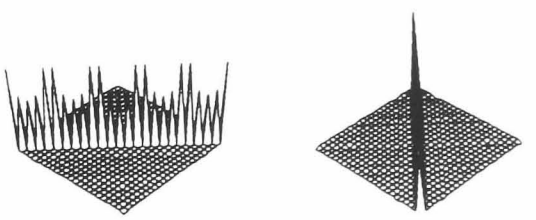

c) **n = 20**

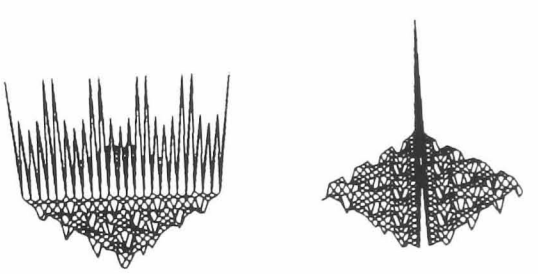

d) **n = 50**

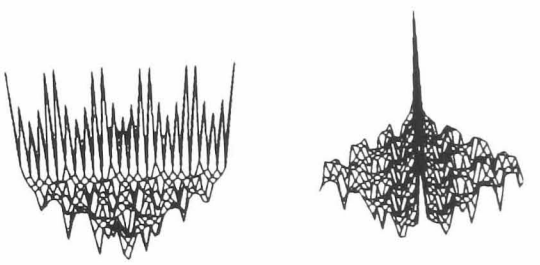

e) **n = 100**

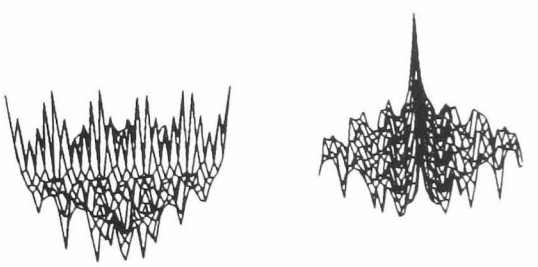

Figure 7.7 3-D plots of N = 5, S = 5, a) original system matrix, b) inverse at n = 5, c) n = 20, d) n = 50, e) n =100. Two views of each plot are given, one of which is rotated through 90°

If λ^n and $\hat{\lambda}^n$ denote the Lagrange multipliers estimated at the n^{th} iteration from the noisy and noiseless projection data respectively, then the variance of the error:

$$\varepsilon^n = (\lambda^n - \hat{\lambda}^n) \tag{7.14}$$

is obtained from equation (5.42) as:

$$\frac{1}{N}E(\varepsilon^T\varepsilon) = \frac{1}{N}E(\eta^T M^{n^T} M^n \eta) \tag{7.15}$$

where η denotes the additive noise process and **E()** denotes the mathematical expectation operator. Using the matrix theorem [7.6]:

$$\mathbf{x^T F x = tr[F\, x x^T]} \tag{7.16}$$

where **F** and **x** are **N** by **N**, and **N** by **1** matrices respectively, and **tr**. denotes the trace, for white noise, equation 7.16 becomes:

$$\frac{1}{N}E(\varepsilon^T\varepsilon) = \frac{1}{N}E(\mathrm{tr}M^{n^T} M^n \eta\eta^T) = \frac{\sigma_\eta^2}{N}\mathrm{tr}[M^{n^T} M^n] \tag{7.17}$$

since:

$$E(M^{n^T} M^n) = M^{n^T} M^n \tag{7.18}$$

and

$$E(\eta\eta^T) = \sigma_\eta^2 I \tag{7.19}$$

where σ_η^2 is the noise variance. The trace of the matrix is equal to the sum of its eigenvalues, hence:

$$\frac{1}{N}E(\varepsilon^T\varepsilon) = \sigma_\eta^2 \sum_i (q_i^n)^2 = \sigma_\varepsilon^2 \tag{7.20}$$

where q_i^n are the non zero eigenvalues of M^n.

As the iteration number increases, the estimate of $\hat{\lambda}^n$ approaches the true solution of the noiseless problem, and therefore the σ_ε^2 approaches the true mean square Lagrange multiplier error.

Goutis and Drossos [5.7] found that for large **n** the eigenvalues of $[\mathbf{M}^n]^{-1}$ are small, and correspondingly the eigenvalues of $\mathbf{M}^n$ become large and σ_ε^2 increases. Therefore if the iteration is too high the noise is amplified, but if a very low choice of **n** is used, then σ_ε^2 is a poor measure of the Lagrange multiplier error. Values of $\left\|\hat{\lambda}^n - \lambda_T\right\|$ where λ_T denotes the true solution of the noiseless problem are plotted against **n** and γ. These are presented in Figure 7.8 and 7.9 for the curvilinear and divergent curvilinear systems. The noiseless case converges to the exact solution for a low value of γ. The true noiseless solution assumes that the sample space used is relatively small. In the EIT system this is not true as the number of electrodes is limited. This leads to aliasing error that is always present in this low resolution system.

$\left\|\hat{\lambda}^n - \lambda_T\right\|$

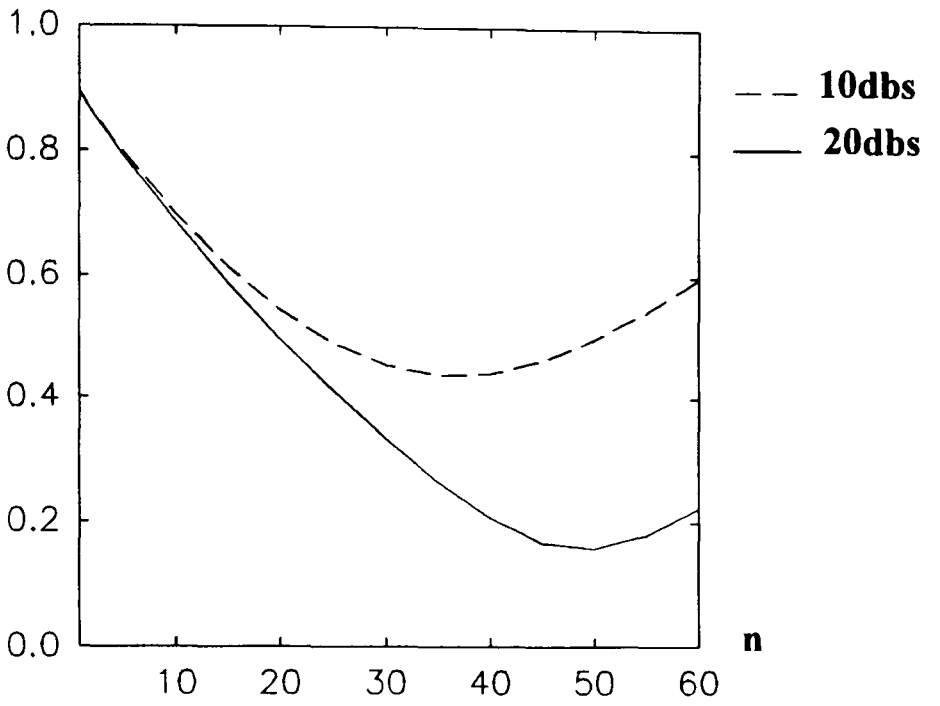

Figure 7.8 $\left\|\hat{\lambda}^n - \lambda_T\right\|$ **against n for parallel curvilinear system**

$\left\|\hat{\lambda}^n - \lambda_T\right\|$

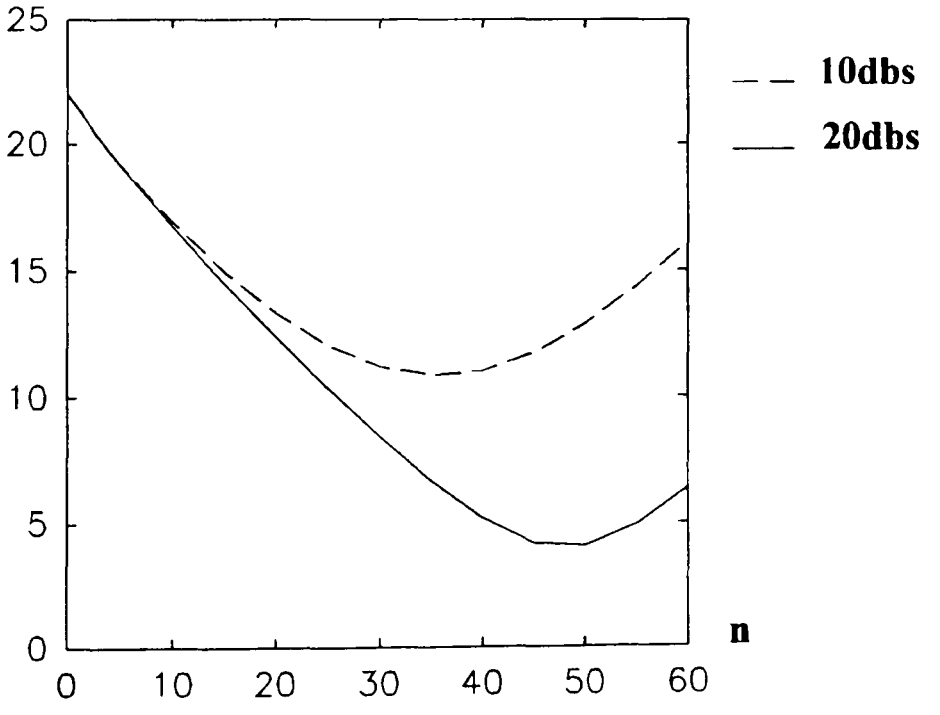

Figure 7.9 $\left\|\hat{\lambda}^n - \lambda_T\right\|$ **against n for divergent curvilinear system**

It was observed that for a low value of γ, the minimum of $\left\|\hat{\lambda}^n - \lambda_T\right\|$ occur at approximately the same iteration number at which the noise and error energies are matched. This was also proved by Goutis and Drossos [5.7] for fan beam geometries. To demonstrate this, the simulated boundary data were corrupted in separate tests with additive Gaussian noise. The signal-to-noise ratio (SNR) was calculated as:

$$\mathbf{SNR} = \mathbf{10.log_{10}}\left[\frac{\sum_{i=1}^{N}(V_i^0)^2}{\sum_{i=1}^{N}(n_i)^2}\right] \qquad \textbf{(7.21)}$$

The addition of Gaussian noise was used to demonstrate the robustness of the technique. The nature of the true noise is unknown and would require further research to consider effects such as temperature variations that cause deviation in the resistivity and the effect of the equipotential paths not following the defined transformation. The above could only be evaluated by clinical application of the algorithms.

7.5 Interpolation and Averaging

The images reconstructed in EIT are smooth reconstructions in the sense that the resistivity of the medium under investigation does not have large changes of resistivity from one region to the next. The range of values for the medium under investigation is given in table 7.1. With the collection data limited by the number of samples, the noise can be reduced by linear interpolation between adjacent Lagrange multiplier sub vectors. This produces smoother reconstructions as demonstrated by Drossos [5.7] on fan beam data.

Smooth reconstructions can also be produced by averaging a given set of noisy Lagrange multiplier vector estimates. If $\mathbf{x}$ denotes a noisy vector written as:

$$\mathbf{x} = \hat{\mathbf{x}} + \eta \qquad \textbf{(7.22)}$$

where $\hat{\mathbf{x}}$ is a noiseless vector, and η is a vector of zero mean white noise, and if $\hat{\mathbf{x}}_A$ denotes an average vector formed by averaging **K** different noisy vectors, defined by:

$$\hat{\mathbf{x}}_A = \frac{1}{\mathbf{K}} \sum_{i=0}^{K} \mathbf{x}_i \tag{7.23}$$

then since $\hat{\mathbf{x}}_A$ is a weighted sum of independent Gaussian random variables, the probability density $\mathbf{p}_{\hat{x}_A}(\hat{\mathbf{x}}_A)$ is also Gaussian [7.7]. Since $\mathbf{p}_{\hat{x}_A}(\hat{\mathbf{x}}_A)$ is also Gaussian, it is therefore completely characterised by the bias and the variance of the estimator. The expected value of $\hat{\mathbf{x}}_A$ is equal to the expected value of $\mathbf{x}_n$ and consequently the bias is equal to zero. To obtain the variance of the sample mean, [7.8] compute:

$$\mathbf{E}[\hat{\mathbf{x}}_A^2] = \frac{1}{\mathbf{K}^2} \sum_{i=0}^{N-1} \sum_{j=0}^{N-1} \mathbf{E}[\mathbf{x}_i \mathbf{x}_j] \tag{7.24}$$

hence:

$$\mathbf{E}[\hat{\mathbf{x}}_A^2] = \frac{1}{\mathbf{K}^2} [\sum_{i=0}^{N-1} \mathbf{E}[\mathbf{x}_i^2] + \sum_{i=0}^{N-1} \sum_{\substack{j=0 \\ j \neq i}}^{N-1} \mathbf{E}[\mathbf{x}_i]\mathbf{E}[\mathbf{x}_j]] \tag{7.25}$$

and

$$\mathbf{E}[\hat{\mathbf{x}}_A^2] = \frac{1}{\mathbf{K}} \mathbf{E}[\mathbf{x}_n^2] + \mathbf{x}_A^2 \frac{\mathbf{K}-1}{\mathbf{K}} \tag{7.26}$$

Thus:

$$\mathbf{var}[\hat{\mathbf{x}}_A] = \mathbf{E}[\hat{\mathbf{x}}_A^2] - \{\mathbf{E}[\hat{\mathbf{x}}_A]\}^2 = \frac{1}{\mathbf{K}} (\mathbf{E}[\mathbf{x}_n^2] - \mathbf{x}_A^2) \tag{7.27}$$

and

$$\sigma^2_{x_A(j)} = \frac{1}{K} \sigma^2_{\eta(j)} \tag{7.28}$$

where **E[.]** denotes the expected value. $\sigma^2_{x_A(j)}$ and $\sigma^2_{\eta(j)}$ are the variances of $\mathbf{x}_A$ and η at the $\mathbf{j}^{th}$ sample. Equation (7.28) indicates that as **K** increases, the variability of the $\mathbf{j}^{th}$ sample decreases, and $\mathbf{x}_A$ approaches the noiseless vector **x**.

This procedure has been successfully applied by Gonzalez [7.9], when

averaging a set of noisy images. Herman [1.26], has also reported that an average of successive noisy reconstruction estimates is a better approximation to the original image than the individual estimates.

Drossos [5.4] showed for fan beam geometry that if the $\mathbf{n^{th}}$ noisy Lagrange multiplier vector estimate λ^n is written as:

$$\lambda^n = \hat{\lambda}^n + \varepsilon^n \qquad \textbf{(7.29)}$$

where $\hat{\lambda}^n$ is the $\mathbf{n^{th}}$ estimate of the noiseless Lagrange multipliers vector, then the covariance matrices $\mathbf{R}_{\varepsilon^n}$, $\mathbf{R}_\eta$ of the error vector ε^n, and noise vector η, are related by:

$$\mathbf{R}_{\varepsilon^n} = \mathbf{M}^n \mathbf{R}_\eta \mathbf{M}^{n^T} \qquad \textbf{(7.30)}$$

For white noise $\mathbf{R}_\eta = \sigma_\eta^2 \mathbf{I}$, where σ_η^2 is the noise variance and the covariance matrix $\mathbf{R}_{\varepsilon^n}$ is diagonally dominant. Hence, the error vector samples are nearly uncorrelated. Based on the above, the following averaging procedure can be defined for $\mathbf{K}$ successive Lagrange multipliers vector estimates before and after the $\mathbf{n^{th}}$ iteration, where the variance of the projection error $\varepsilon_p = (\mathbf{p} - \hat{\mathbf{p}})$ equals approximately the variance of the additive noise. Hence the above averaging can be written as:

$$\lambda_A^{n,K} = \frac{1}{2K+1}(\lambda^{n-K} + .. + \lambda^{n-1} + \lambda^n + \lambda^{n+1} + .. + \lambda^{n+K}) \qquad \textbf{(7.31)}$$

$$\lambda_A^{n,K} = \frac{1}{2K+1}(\mathbf{M}^{n-K} + .. + \mathbf{M}^{n-1} + \mathbf{M}^n + \mathbf{M}^{n+1} + .. + \mathbf{M}^{n+K})\mathbf{p} \qquad \textbf{(7.32)}$$

Drossos [5.4] found that this procedure produced smoother reconstruction.

7.6 Estimating the Optimum Number of Iterations and Choice of Relaxation Factor

To compute the Lagrange multipliers, it is desirable to have a good estimate of the number of iterations required, since for noisy data, once the optimum number of iterations is passed, the quality of the image degrades for more iteration and hence greater computation time. All authors suggest that the choice should be in the range $\mathbf{0 < \gamma < 2}$ for the algorithms for other geometries to converge, although no proof of

the optimum has been given for the type of matrix used in this system. The ideal choice of the optimum number of iterations and the relaxation factor was obtained from the curves presented in Figures 7.10 and 7.11, in which $\|\mathbf{p}^0 - \hat{\mathbf{p}}^n\|$ the boundary error energy is plotted against **n** the number of iterations.

The data are presented in an inverted **3-D** form to demonstrate the optimum choice for relaxation parameter that occurs at the peak of the graph. The selected relaxation parameter value γ is then plotted in **2-D** to illustrate the convergence rate. To obtain a Gaussian distribution of the error in the pseudo inverse, a low value of γ with a large number of iterations is required. This empirical method was chosen because there is no documented analytical approach available in the literature.

Two algorithms have been developed for reconstructing resistivity images in this research; the direct method based on the Jacobi iterative technique and the recursive or successive relaxation method. Both approaches use similar values of γ and **n**.

The choice of **n** will depend upon the noise in the collection data. It was shown in section 7.4, that the statistics of the noise in the collection system could be related to the errors in the pseudo inverse of the associated system matrix. This assumes that the noise statistics are available from the collection system. For the modelled boundary data it was possible to control the noise source so that the statistics were known. This is not the case for data obtained using the Sheffield system. Noise due to the effect of lead capacitance is eliminated by using the difference data, but noise statistics due to other sources have yet to be fully investigated. This is beyond the scope of the research presented in this thesis. To select the required number of iterations for the data obtained from the Sheffield system, the true Lagrange multipliers λ_T were obtained by modelling a simple object (glass rod placed in the centre of a tank of saline solution). The error between λ_T and the Lagrange multipliers obtained from the Sheffield system was minimised to select a suitable value of **n**.

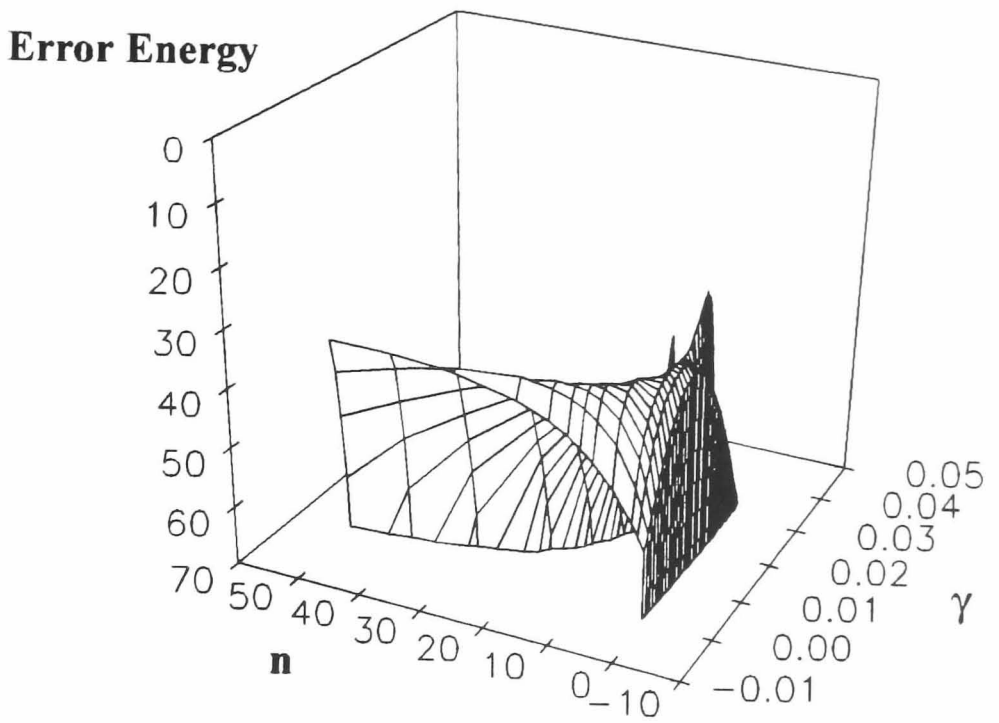

Figure 7.10(a) 3-D Plot of Error Energy, versus n the number of iterations, and γ , for Direct algorithm, Parallel orthogonal case.

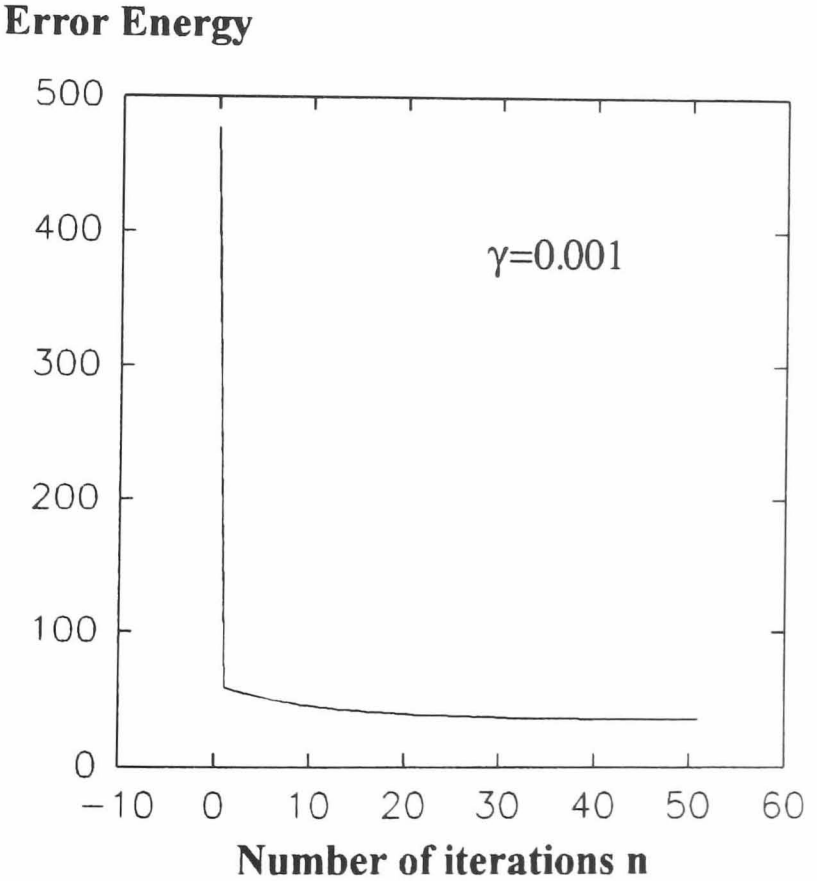

Figure 7.10(b) 2-D Plot of Error Energy, versus n the number of iterations for Direct algorithm, Parallel orthogonal case with optimum value of $\gamma = 0.001$, chosen from Figure 7.10(a).

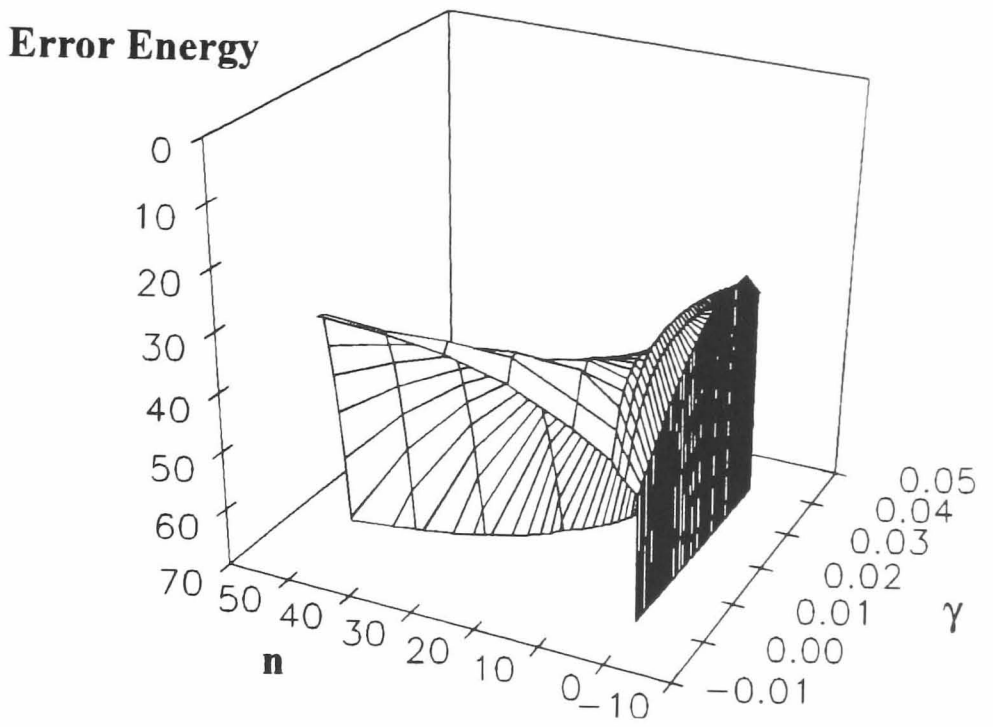

Figure 7.11(a) 3-D Plot of Error Energy, versus n the number of iterations, and γ, for Direct algorithm, Divergent orthogonal case.

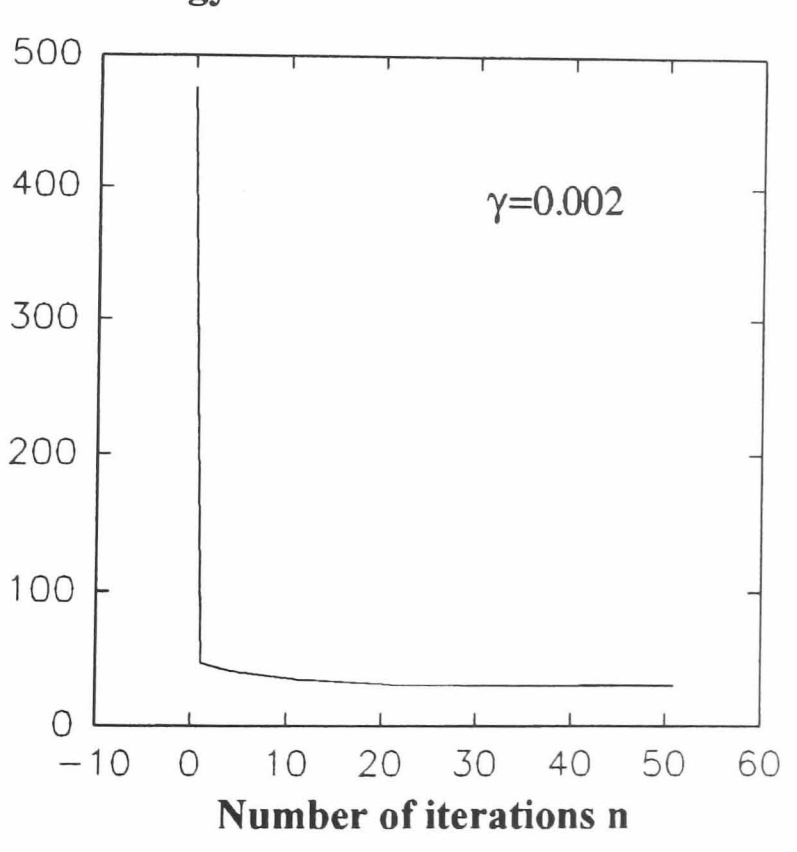

Figure 7.11(b) 2-D Plot of Error Energy, versus n the number of iterations for Direct algorithm, Divergent orthogonal case with optimum value of $\gamma = 0.002$, chosen from Figure 7.11(a).

From the plots obtained using modelled data, it is suggested that a relaxation parameter γ = **0.001**, with **n** = **50** (Figure 7.10) is appropriate for the parallel curvilinear system. This is illustrated in Figure 6.7(b) using modelled data of two elliptic objects shown in Figure 6.7(a). The divergent collection system was found to give the best results when γ = **0.002**, with **n** = **50** (Figure 7.11). This is illustrated in Figure 6.12 for the same test phantom as used for the parallel curvilinear system. This assumes that no noise is introduced into the collection data.

Figure 7.12 is example of a reconstruction for which variance of the error between the boundary data and the estimated boundary corresponding to the Lagrange multipliers used to obtain the reconstruction are approximately equal to the mean and variance of the added Gaussian noise. The error is matched for 20db (eqn. 7.21) of additive noise for parallel curvilinear geometry. The result demonstrates the best obtainable image in the presence of noise, even with limited collection data. This was repeated for the divergent geometry in Figure 7.14, and vector plots of a region of interest are also presented in Figures 7.15 and 7.16, to illustrate the effects of adding noise to the projection data.

It is possible to reduce the computation time in both the Jacobi and recursive algorithms by using a sub-optimal feasible solution SOFS [4.1]. The inverse of the associated system matrix converges to a reasonable solution after about five iterations, although this will not have the statistics of the system noise matched to those of the errors in the pseudo inverse. The distribution of the error will not be Gaussian, and this may reduce the distinguishability of some feature within the reconstructed resistivity as illustrated in Figure 7.13

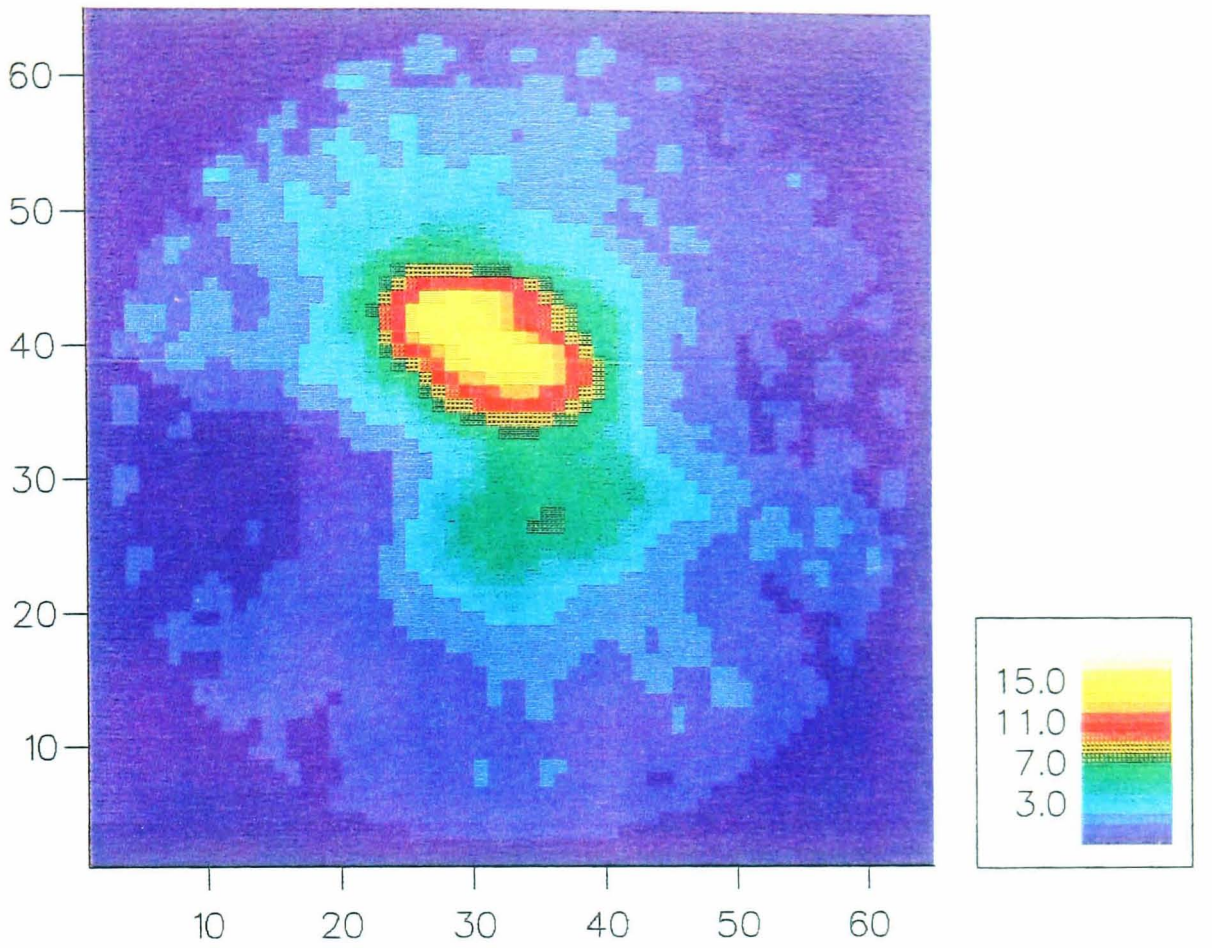

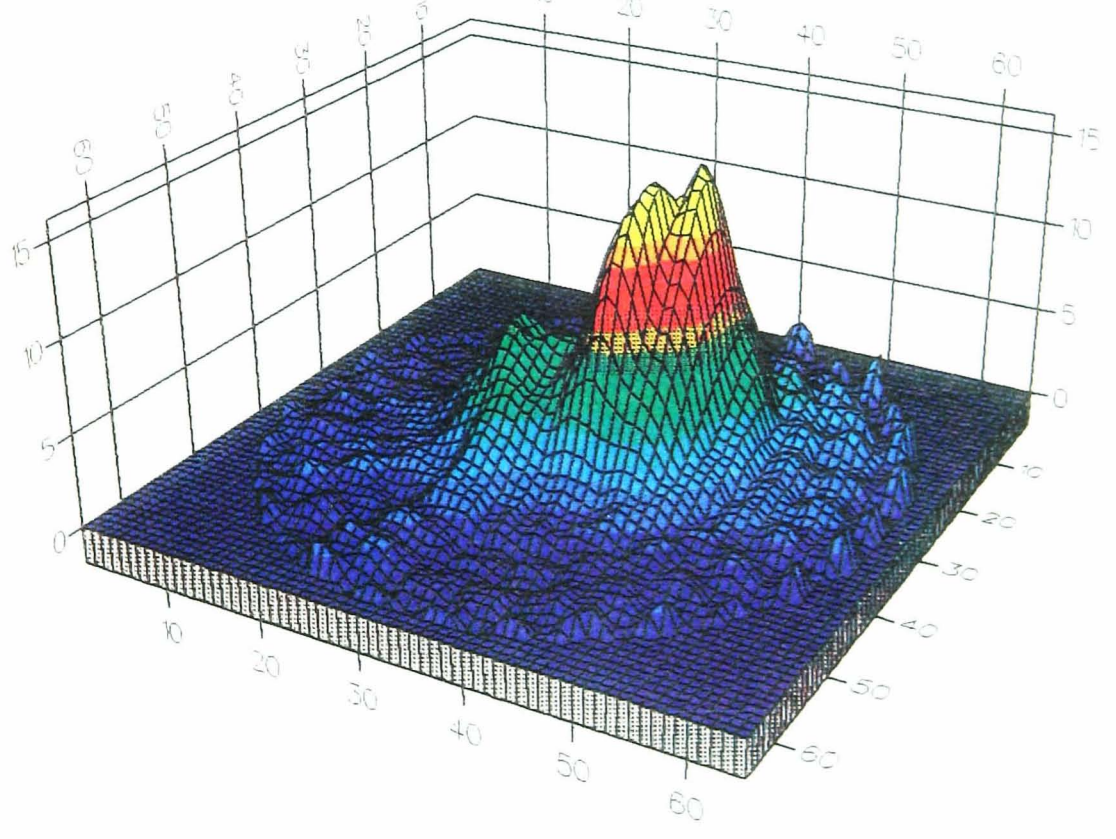

Figure 7.12 Reconstruction parallel curvilinear with 20db of additive noise, $\gamma = 0.001$ and n=50

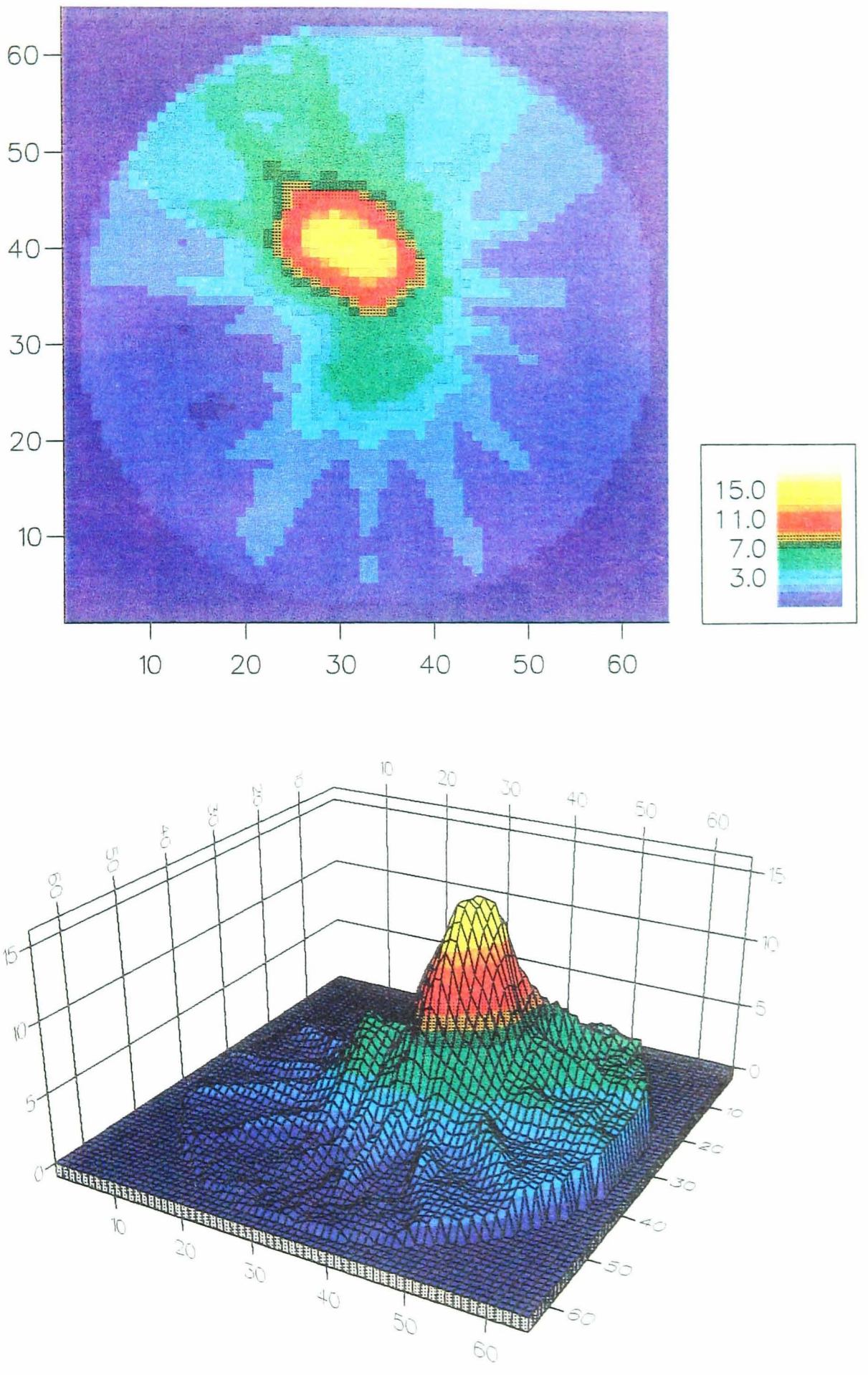

Figure 7.13 Reconstruction divergent curvilinear using a sub optimal solution, γ =0.006 and n=5

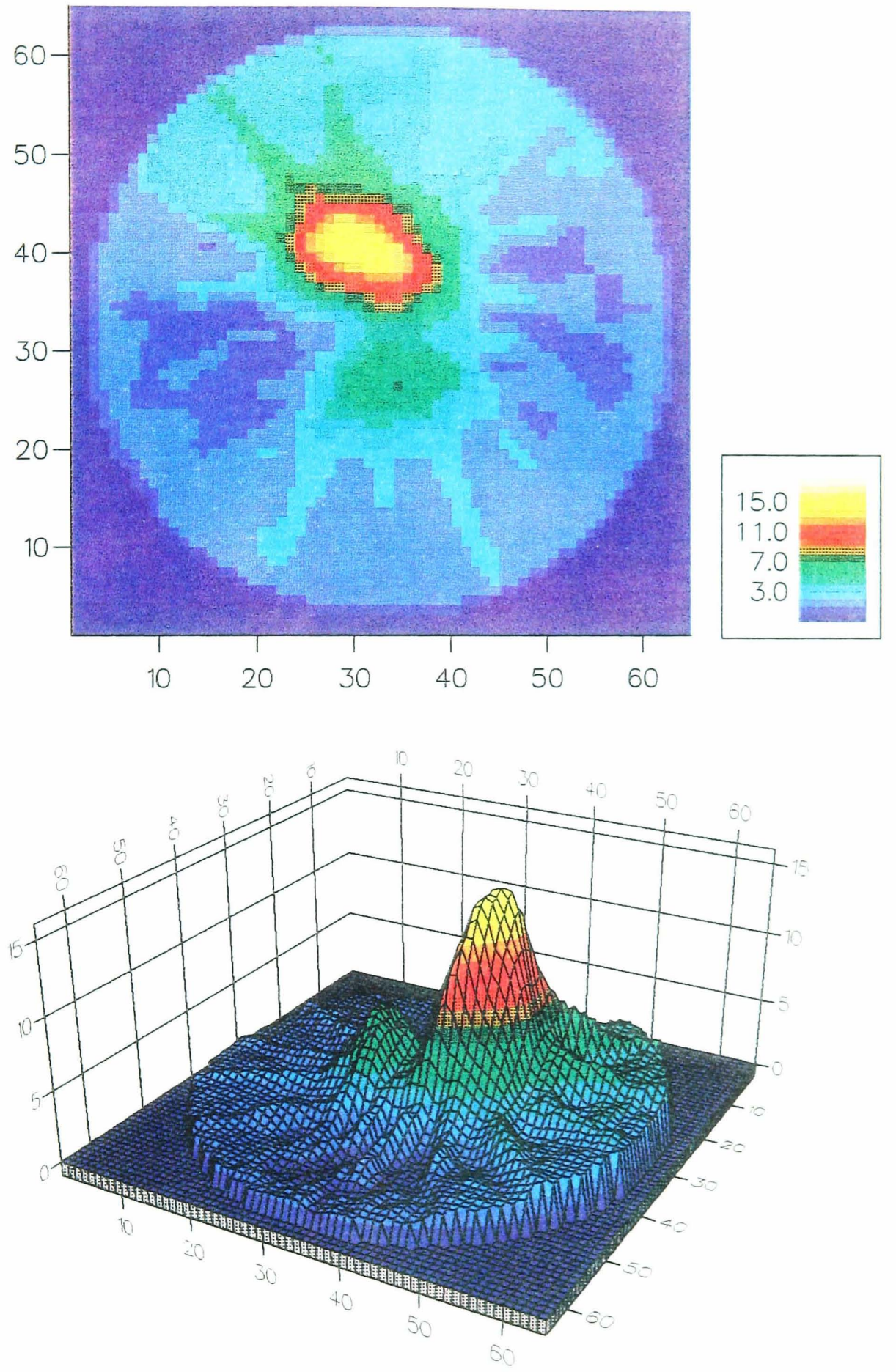

Figure 7.14 Reconstruction divergent curvilinear with 20db of additive noise optimised

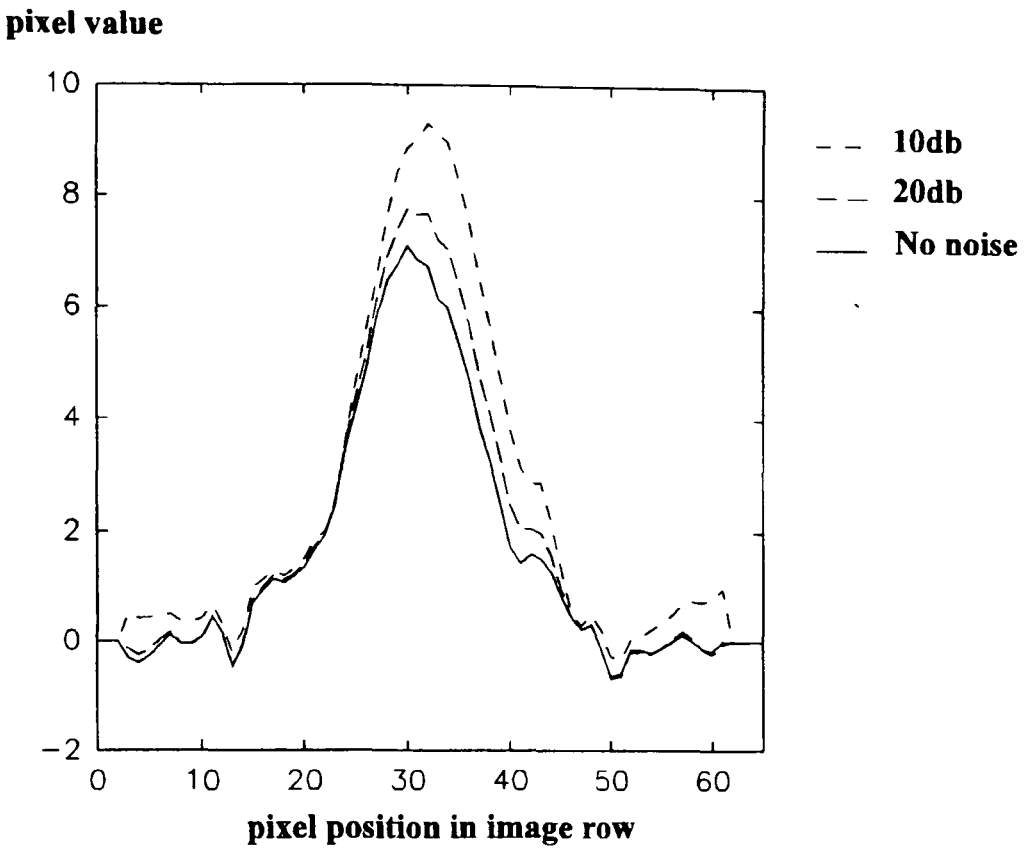

Figure 7.15 Plots of regions of interest vectors for parallel curvilinear images.

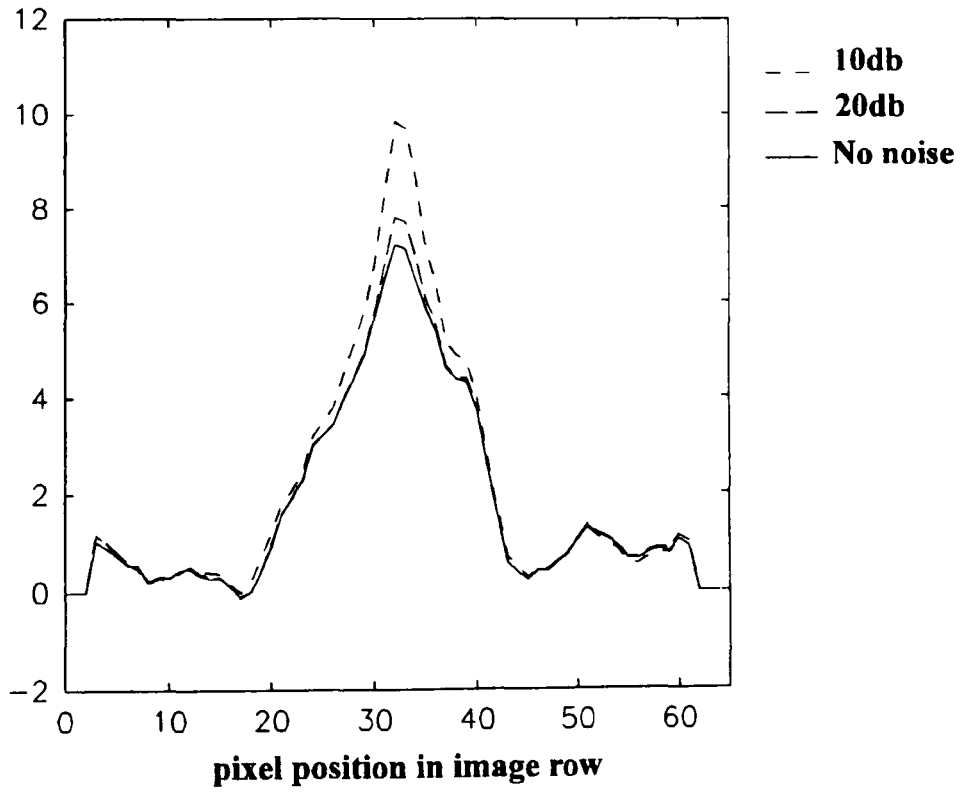

Figure 7.16 Plots of regions of interest vectors for divergent curvilinear images.

7.7 Speed and Storage

In the table presented at the end of Chapter five it was demonstrated that for X-ray tomography the speed of the direct algorithm approaches that of the convolution. As there is no equivalent convolution algorithm in EIT, and the filtered backprojection algorithm developed by Barber and Brown [7.5] is not fully detailed in the literature, an equivalent comparison is not possible. The computation time for all the algorithms is dominated by the backprojection operation, as this forms the main kernel of most algorithms. The main disadvantage with the CORT EIT algorithms is the storage requirement, although various procedures can be applied as detailed in Chapter five to reduce this requirement. The areas of equal elements in the submatrices cannot be exploited as for the parallel and fan beam cases to minimise the storage requirements in the same way. The submatrices generated by the EIT's equipotential paths do not have identifiable structures which can be exploited.

7.8 Sheffield System

The results presented in the next figures were reconstructed using data obtained from the Sheffield Mark I system [3.4]. This uses 16 electrodes to collect and inject the currents. Voltage measurements are not made either side of the current injection electrodes. This gives a total of 104 independent measurements. Using reciprocity [7.4], this was converted into 208 measurements to give a complete set of 16 projections with 13 samples per projection. To improve this, an endpoint interpolation scheme was used to extend the number of samples to 15 per projection. This gave a slight improvement in the reconstructed image for objects close to the electrodes. The limitation of only 13 samples is due to the problems of measuring the potential both sides of the current injection electrodes.

The EIT systems make use of the reciprocity theorem [7.4] to improve speed. This states that "the voltage measured by a pair of electrodes when current is injected through another pair, should be the same as the measured voltages when interchanging

the voltage measuring and current-injecting electrode pairs". This assumes the resistivity is homogeneous. In practice, these voltages do not coincide, and the mean reciprocity error is given as the square root of the sum of the squares of the differences between reciprocal values, divided by the number of value pairs.

The data obtained from the Sheffield system uses IEEE 754 standard floating point number format. This format was used to allow easy transport of the data files between different computers (PC's). Each potential reading is converted to the above format using a 12-bit ADC. As EIT images are formed from a change in the impedance distribution within a conducting region, two data frames are required; one before change in resistivity has occurred and one afterwards. The data frame collected before the change occurs is called the reference frame. The reconstructed image shows the spatial distribution of impedance change from this reference frame. Often one particular frame is chosen as the reference frame for the whole measurement. In general, the reference frame is not different from any other data frame and if a series of data frames is collected over a period of time, any one of the data frames could be chosen as the image reference.

The boundary values are produced from 104 independent boundary voltage measurements. For each boundary voltage $\mathbf{V_n}$, which has a value $\mathbf{V_{ref}}$ in the reference frame, the normalised resistivity changes are obtained from the normalised boundary changes, given by:

$$\mathbf{V_n'} = \frac{\mathbf{V_n} - \mathbf{V_{ref}}}{\mathbf{V_{ref}}} \qquad \textbf{(7.33)}$$

A tank of saline solution was used with a glass rod and a polyacrylamide gel, formed into a rod to demonstrate the new algorithm, with data obtained from the Sheffield collection system. The gel is sometimes known as 'solid water' and consists of 95% water, the conduction properties of which can be changed by addition of saline.

The Sheffield system can be configured to collect data only in the dipole mode,

therefore only the divergent curvilinear algorithm can be tested. One reconstruction of an image obtained using clinical data is presented in Figure 7.21. This illustrates the type of image that can be obtained using this method. All the images have been rescaled to use a linear scale range for convenience.

PAGE

NUMBERING

AS ORIGINAL

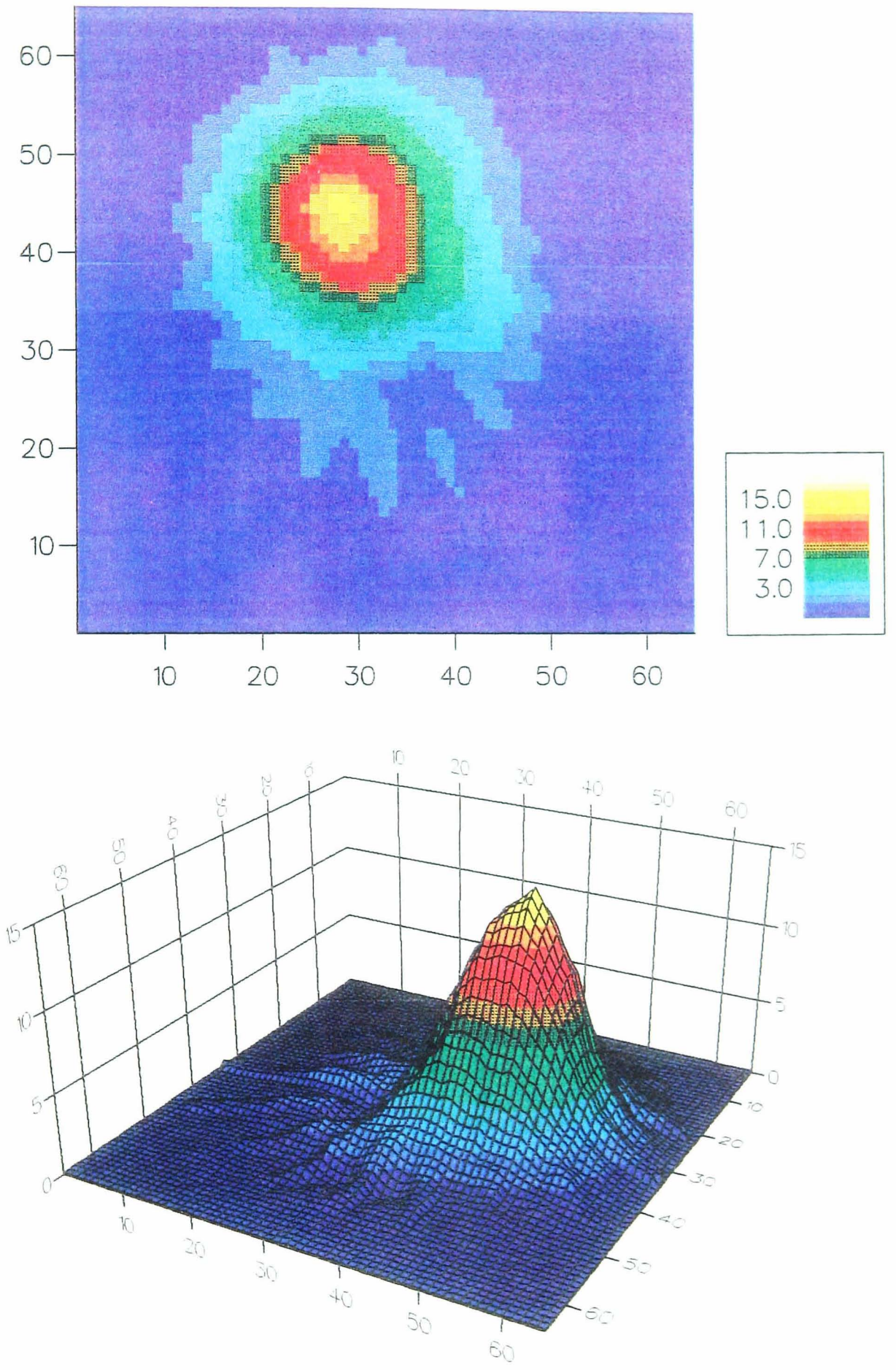

Figure 7.18 Reconstruction of Real Data From Sheffield System with glass rod of diameter 6.3mm at 16 mm from the centre of an 89mm diameter tank.

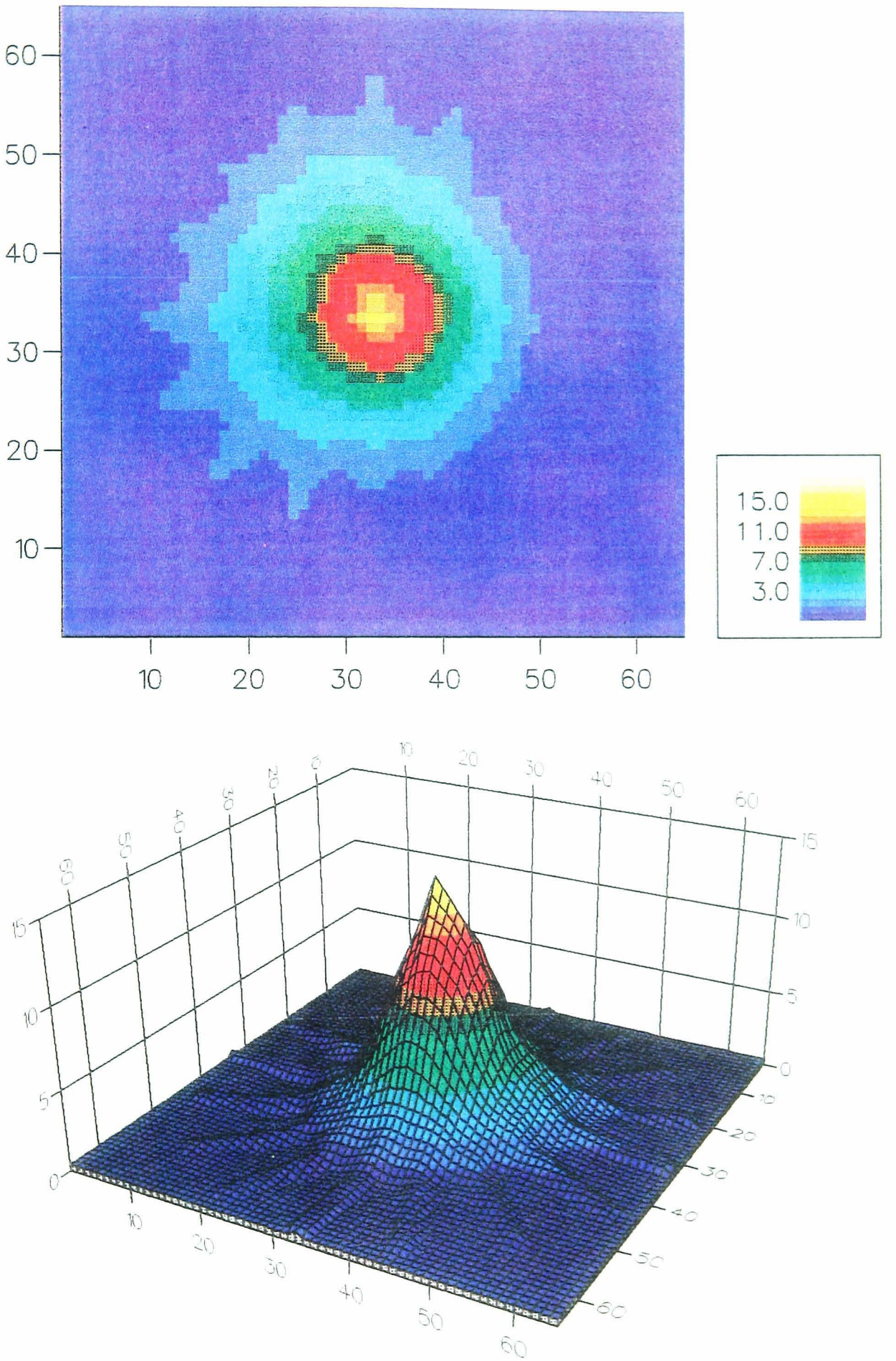

Figure 7.19 Reconstruction of Real Data From Sheffield System with polyacrylamide rod of 6.3mm at the centre of an 89mm diameter tank.

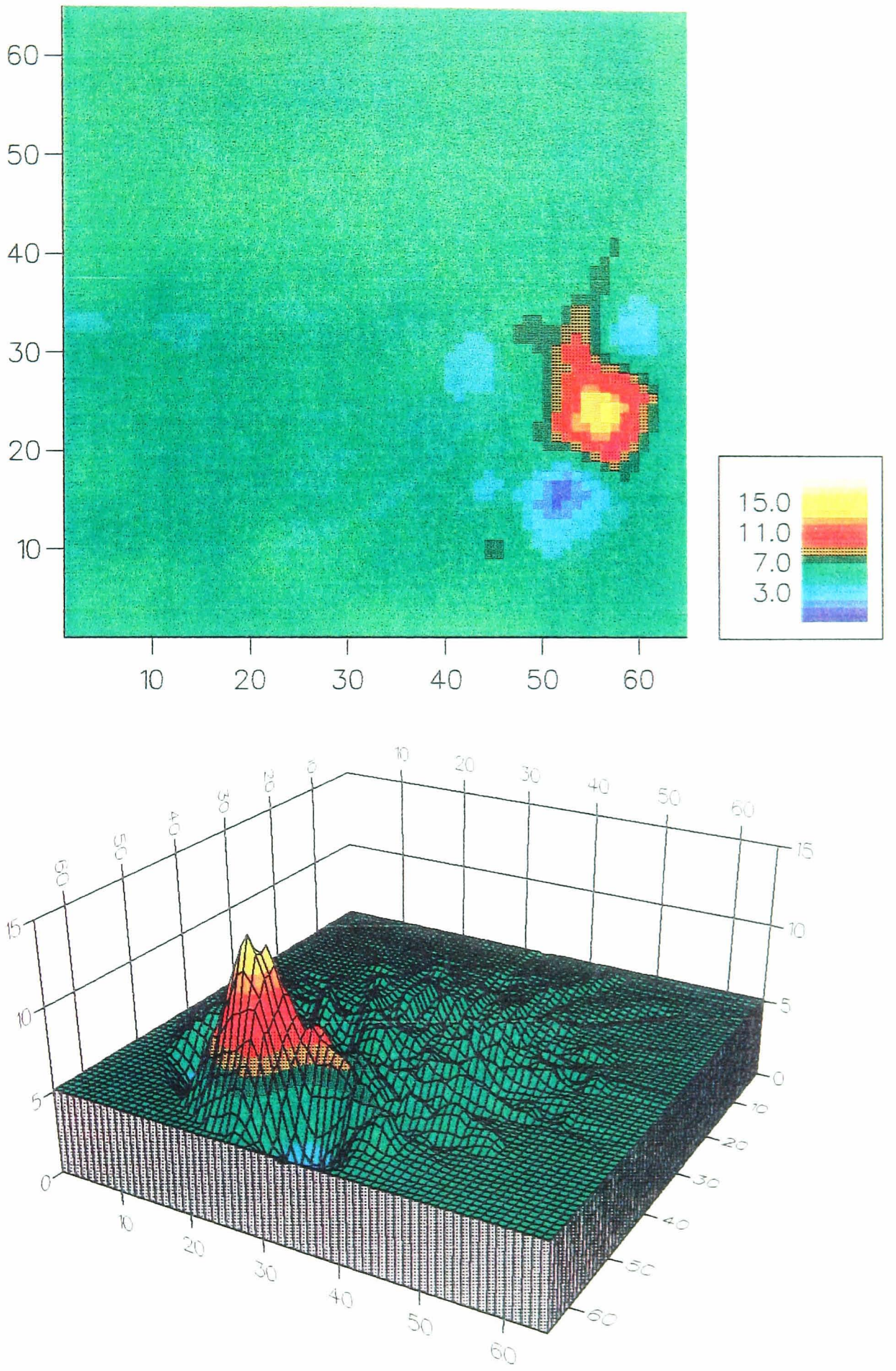

Figure 7.20 Reconstruction of Real Data From Sheffield System with polyacrylamide rod at side with diameter of 6.3mm and tank diameter of 89mm.

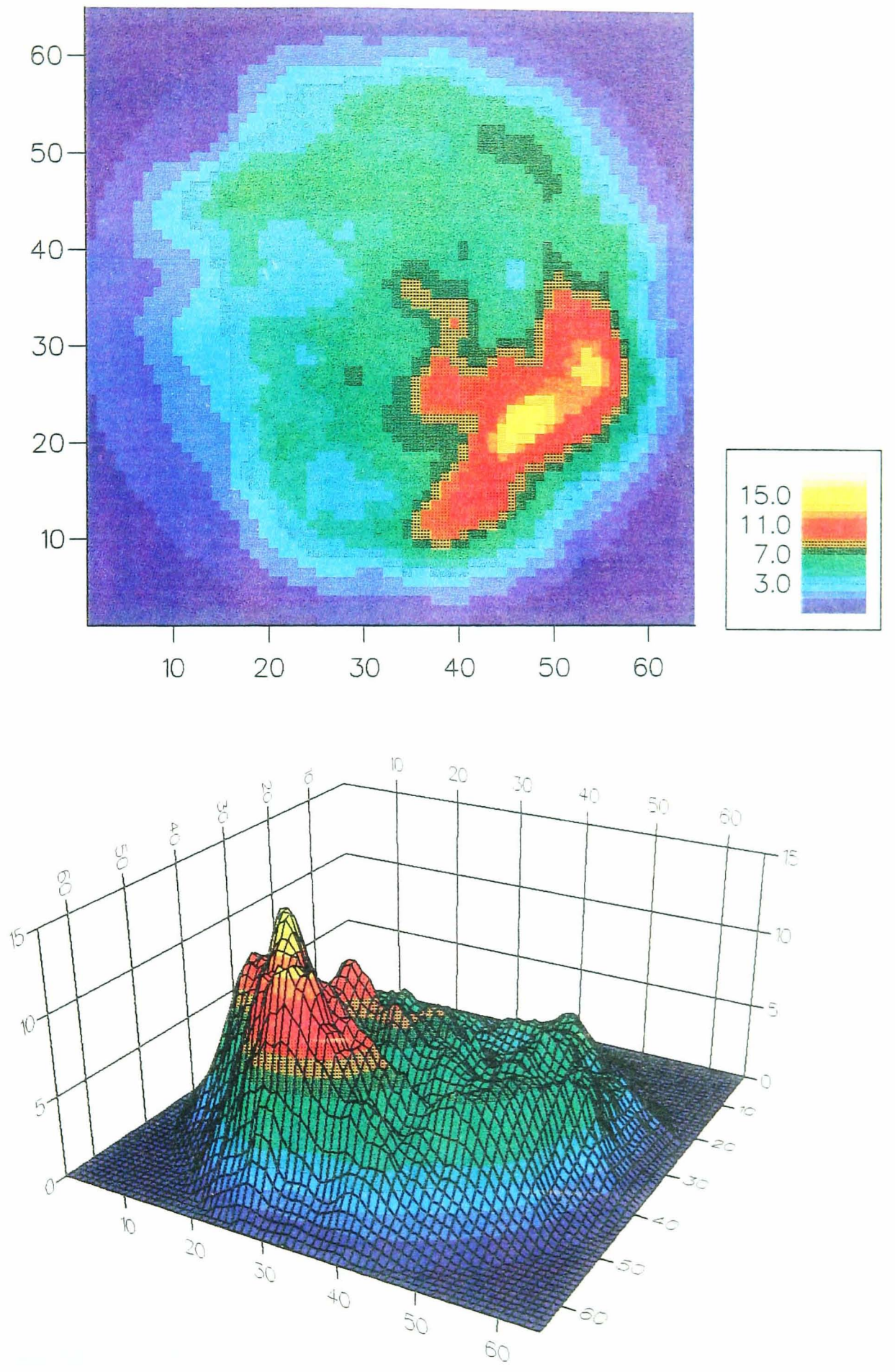

Figure 7.21 Example of reconstruction of clinical data obtained from the Sheffield system

7.9 Discussion

The main objectives of this Chapter are the evaluation of the new algorithms; with data produced using a mathematical phantom, and data obtained from the Sheffield Mark I system. Before the evaluation was presented, sets of parameters used to measure the performance of the algorithm were introduced, and a number of issues not considered in Chapter six were also addressed. These issues include the distribution of the current within the object to be reconstructed, which affects the attainable resolution and the accuracy of the final reconstructed image, and the choice of the number of iterations **n** and relaxation γ parameter used in the algorithm to maximise the quality of the reconstructed image.

It was found that the exact pseudo inverse results in a poor solution due to the effects of noise amplification [4.1]. However, Drossos [5.4] showed that if the iterations are allowed to continue, the error energy will increase due to system noise. The algorithms developed in this research can be adjusted such that the statistics of the noise are made to match the statistics of the error in the pseudo inverses of the associated system matrices. This is achieved in the iterative case by terminating when the error attains a sufficiently small energy. The criterion for termination in the iterative case takes the form of a noise matching constraint. Other approaches such as ART3 [7.10] for selection of the number of iterations where the equations are relaxed to improve convergence, were considered. In the ART3 case, the hyperplanes in the solution space which correspond to the images matching each projection are broadened to form hyperslabs [7.10], and the final solution must lie within the intersection of these hyperslabs. These modifications were found to give some improvement in image quality. However the resulting solutions are no longer optimal and the structure of the associated matrix is not maintained.

It was shown in section 7.4 that improved quality reconstructions could be obtained when the statistics of the noise are matched to the statistics of the error in the pseudo inverse of the associated system matrix. This was also demonstrated using the

modelled data for both types of EIT geometry. In the EIT environment the statistics of the noise still need to be determined. The difficulty in obtaining a model of the statistics was born out of the discussion on phantoms. These statistics can vary depending on the region of the body under examination, and can be obtained only from clinical data. The statistics of the stochastic model can also be influenced by a number of other sources: data collection noise, quantisation noise, aliasing error and the variations in the modelled geometry due to the equipotential lines not following the defined paths. The latter can be considered as additive noise in the associated system matrix. Errors, such as aliasing due to under-sampling, will be reduced as data collection methods improve. The errors due to the equipotential lines not following the defined transformation will also be minimised as the number of samples is increased. This is due to the dipole transform used to approximate the equipotential paths being closer to the true equipotential lines.

The number of samples used in this research is based on the number of electrodes used by the Sheffield data collection system. New systems have appeared with larger numbers of electrodes [7.11] which should improve the spatial resolution of the EIT system. The sampling problem is also related to the data collection method. The dipole method is favoured as the opposite electrode collection system gives only half the number of boundary measurements, limiting the spatial resolution.

As the EIT system has no suitable stochastic model, an estimate was made to select the value of the number of iterations **n** for the reconstruction of data obtained from the Sheffield data collection system. A set of boundary data was modelled from a mathematical phantom of a simple object, similar to a glass rod placed in the centre of a tank of saline solution. The modelled boundary data were used to create a set of true Lagrange multipliers from which the error between the Lagrange multipliers obtained from the saline tank and the true Lagrange multipliers was minimised to select **n**. This gave a reasonably good quality reconstruction. To find the exact value will require using the technique on clinical results so that statistical information can be used to set a

boundary. For example, a 95 per cent confidence region is usually chosen, whereas a 90 or 98 percent level may be more appropriate in some cases [4.1].

It may be appropriate in EIT to use an approach introduced in [4.1], in which fuzzy sets are used to quantify the uncertainty in the elements of the set, so that an element with a high membership function is considered more desirable than one that is low. Higher order statistics and multiple constraints appropriate for EIT can be incorporated into the model, but these could cause problems with excessive computation requirements.

If the CORT methodology is compared with other existing reconstruction algorithms, there are some similarities. The ART can be considered as an example of a constrained optimisation algorithm, in that it iteratively updates its estimates of the image by back projecting the errors between the measured projections and those corresponding to the current image estimate. This procedure converges to the image of minimum energy that matches the measured projections. The Newton-Raphson method described in Chapter three may also be considered as a constrained optimisation algorithm. Both approaches have a major drawback in that the associated system matrix structure is large, and does not contain useful structure to minimise the storage and computational requirements.

The CORT algorithms developed for X-ray and PET systems make use of areas of equal elements to produce reasonable reconstruction speeds. Typical X-ray systems have 300 projection measurements with 500 samples per measurement, giving associated system matrices of a greater order of magnitude than EIT. In EIT systems the samples are limited by the number of electrodes, and therefore the size of the associated matrices is much smaller. Also, the structures of the submatrices do not have areas of equal elements, a feature which was used in the X-ray and PET systems to minimise the memory requirements. This does not cause a problem in EIT with regard to speed of the reconstruction as the number of computational operations are reduced.

A summary of the advantages and disadvantages of the new approach to EIT reconstruction is given below. When relevant, they are compared with the Sheffield system.

Advantages:

a) Computational speed is comparable with the Sheffield system algorithm.

b) A valid image model is used in terms of the **N, 1-D** Lagrange multipliers that are computed from all the available potential measurements.

c) It matches the statistics of the Gaussian noise (variance and probability density function), to those of the potential measurement error.

d) Prior information about the structure of the image to be reconstructed or the noise statistic can be built into the algorithm.

e) Averaging and interpolation can be used to improve the reconstructions without any additional real-time computations.

f) Higher quality reconstructions than Barbar's and Brown's algorithm [7.5] are obtained from data with and without noise. This is particularly true in situations where the data set is limited.

Disadvantages:

a) A larger amount of computer memory is required than for to the Sheffield algorithm.

b) All the boundary profiles must be collected before reconstruction can begin.

8 SYSTEM DESIGN AND MODELLING

8.1 Introduction

In the preceding Chapters, the analysis has concentrated on the adaptation of the constrained optimisation technique for the EIT system. Computing efficiency was increased by improvement of the algorithm to minimise the number of operations required. Some parts of the procedure could not be improved by analytical means. One solution for obtaining a high performance from the reconstruction procedure is to employ a hardware implementation for the mathematical solutions. This Chapter concentrates on the development of hardware accelerators to perform specific functions within the reconstruction algorithm with the objective of obtaining real time reconstruction speeds. It is not the intention of this research to implement the solution in hardware, but to derive possible designs which could be used in feasibility studies for future development. Several approaches are investigated.

A key issue in any system design is to identify the bottlenecks in processing the data. Although a general purpose computing engine can be used to perform many of the computation functions required by image reconstruction, the parameters of the computational problem for reconstruction are fixed, that is, the resolution of the reconstructed image and the number of samples used for the projection data are both fixed before computation begins. To enhance performance, specific machines are required to perform parallel operations.

The processing engine to be described was evaluated by modelling it using a Verification Hardware Description Language (VHDL) system known as Verilog [8.1].

8.2 Design Methodology

There are several systematic methodologies suggested in [8.2][8.3][8.4][8.5], to find a definitive solution for parallel processing development. The most well known is Kung's [8.6] approach to the design of parallel systems. It was adopted in this research as it has yielded many examples of successful solutions. Kung's approach was formulated primarily for a systolic system, and although the solutions obtained in this research are not systolic, there are elements of similarity.

A systolic system [8.7] is a network of processors that rhythmically computes and passes data through the system. An important concept in systolic design is a high degree of regularity, with simple structures, suitable for implementation in Very Large Scale Integration (VLSI). A guide-line in this design is therefore to connect a large number of identical processing elements with a simple architecture which still maintains a certain degree of versatility. This versatility was required to obtain different versions of the proposed system for evaluation.

Two forms of mesh connection seemed particularly suitable for the design and are investigated in different versions; the linear in version one, and the orthogonally connected processor array in version two.

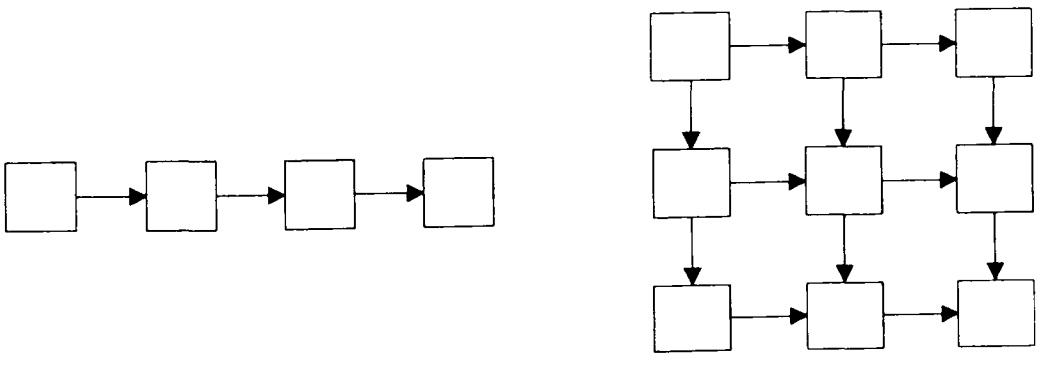

(a) Linear Connection **(b) Orthogonal Connection**

Figure 8.1 Two Mesh Connections for Data Transport

The Backprojection Engine (BPE) also makes use of the model of systolic

communication [8.8] in that each processor element (**PE**) of the array can operate on incoming data and move it, if necessary, to the output register without the need of storing the data in its local memory first. The arrays in the proposed systolic system developed in this research show that there is no need to send partial results from one **PE** to another.

8.2.1 Partitioning and Limitations

The simplest approach to mapping any numerical algorithm on to hardware is to assume that there is unlimited resource of hardware. This approach has been adopted in the analysis presented in this Chapter. Difficulties arise when problems of different sizes need to be mapped on to fixed dimensional arrays. It is assumed that in this system no partition scheme is required, as the final hardware solution would be implemented with a VLSI structure. Each **PE** is designed to be as simple as possible to minimise the gate count required for implementation.

Proposals do exist for similar solutions where Ipsen, Suad and Schultz [8.9] used systolic arrays for matrix inversion. They partitioned an any-size problem into sub-problems that operate with triangular sub-matrices. This reduces the dimensional requirements to the size of the available hardware. Any partitioning scheme brings an overhead of increased computational time.

A partitioning scheme proposed in the original development of the system [8.10] was to subdivide the image into sections. The data would be tagged with **x** and **y** bytes, identifying its final location in the final reconstructed image. A similar approach was taken by Lattard, Faure and Mazare (1990) [8.11] in which their massively parallel architecture for neural net emulation and image reconstruction uses a routing tag **dx** and **dy** to identify the pixel location. The approach that could be taken in this research is to partition the image into columns. If the resource is available, all the columns can be reconstructed simultaneously.

8.2.2 Top-down Mapping

Any array algorithm is a set of rules for solving a problem in a finite number of steps by several interconnected processors. It is design dependent on the machine characteristics and also on the interconnection strategies. Kung [8.6] states that the main aim for a given algorithm in algorithm-oriented array processor design is to systematically derive any array processor. To this end a simple notation has been adopted and is described in the next sections. The design method is formulated in three stages:

i) Generating the dependence graph. This defines the dependence of each node on its preceding input.

ii) Mapping the dependence graph on to a signal flow graph.

iii) Deriving an array structure from the signal flow graph.

From discussion in Chapter four, clearly the optimising algorithm offers the advantages of image quality and computational efficiency. Although the algorithm is efficient when implemented on a serial machine, the main bottleneck in performance is the technique of backprojection of Lagrange multipliers. The machine presented in this Chapter concentrates on the construction of the backprojection operator. Only the parallel data collection system is considered.

Two main assumptions are made for this implementation. First, the collection geometry is fixed, thus predetermining the size of **S** and **N**. Second, the size of the final reconstructed image is also fixed. These assumptions are not unreasonable as in most reconstruction system these parameters remain fixed. From Herman [2.19], the backprojection function can be defined for the Lagrange multipliers as:

$$\mathbf{B}_{\lambda}(\mathbf{r},\phi) = \int_{0}^{\pi} \lambda(\mathbf{r}\cos(\theta-\phi),\theta)\mathbf{d}\theta \qquad (8.1)$$

This integral is evaluated in two parts. The integral is first approximated using a Riemann sum as:

$$\Delta \sum_{m=0}^{N-1} \lambda(r\cos(m\Delta - \phi), m\Delta) \qquad (8.2)$$

This is followed by interpolation. In most CT systems, nearest neighbour or linear interpolation is used. Nearest neighbour is the most common because of its lower computation costs.

The equation for the Riemann sum, given above, is an approximation in terms of polar co-ordinates. Figure 8.2, illustrates the summation of values at a single point. Each λ sum intersects a single location on the polar map. The position of the single point is defined by **r** and θ.

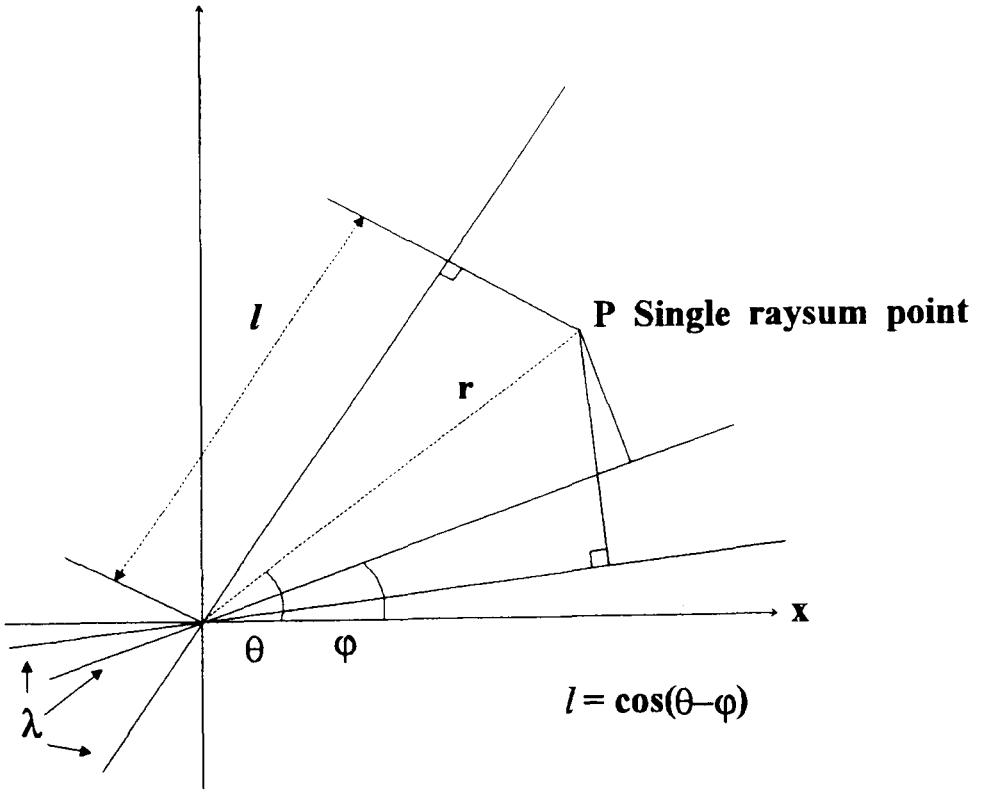

Figure 8.2 Polar Map

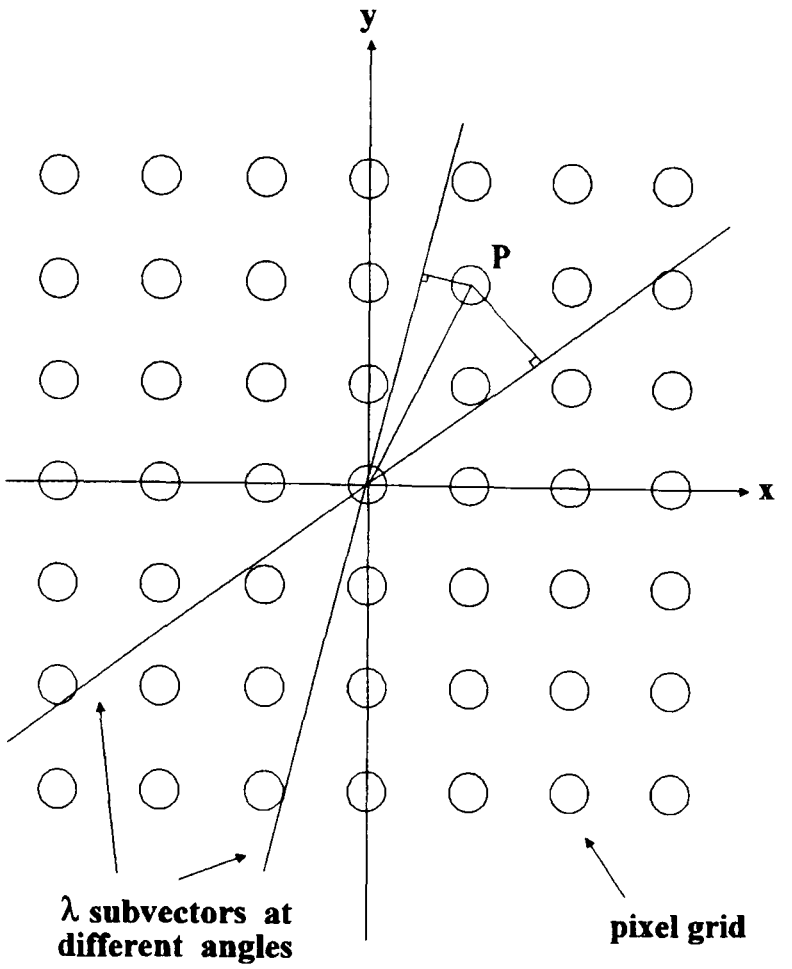

Figure 8.3 Polar Map superimposed on rectangular pixel grid.

The distance ***l*** defines the position of the Lagrange value that is added to this point in the co-ordinate space defined by the polar map. **P** in the polar space defines not only the λ sum intersection location, but also the location of each pixel in the rectangle space. If the Cartesian co-ordinate space is superimposed on to the polar space (Figure 8.3), the location of each pixel in the rectangular space, **r**, θ and therefore ***l***, can be predetermined.

This assumes that the λ sub-vector is continuous. As the sub-vector is sampled at discrete points, there is need for interpolation schemes to decide what percentage of the closest λ value will be assigned to the location in the rectangle space. The simplest approach is to use a nearest neighbour interpolation, where the nearest λ is assigned to the point in the rectangle space. Although this may not give the best reconstructions when data are limited, it does reduce the computation overheads required. Using this

interpolation scheme, the position of the Lagrange sub-vectors summed at point **P** can be defined by l. The latter is pre-computed before reconstruction, and is dependent only on the fixed geometry of the reconstruction data collection system and the final reconstructed image resolution. The l values can be stored as a set of address offsets in a host computer system. As the pixel resolution and the data collection system resolution remain constant, the address offsets do not change their values. Thus for a single pixel location, the following dependence graph can be constructed as illustrated in Figure 8.4.

8.2.3 Stage I: Dependence Graph Design

The dependence graph is a time independent graph which defines the dependence of an operation on the preceding operation. This is sometimes known as the index space. The dependence graph is relatively simple for this system as recursion can be eliminated. Using nearest neighbour interpolation requires only the defining of an address offset so that the values are added at the correct locations. The values l_1 to l_{N-1} are predefined.

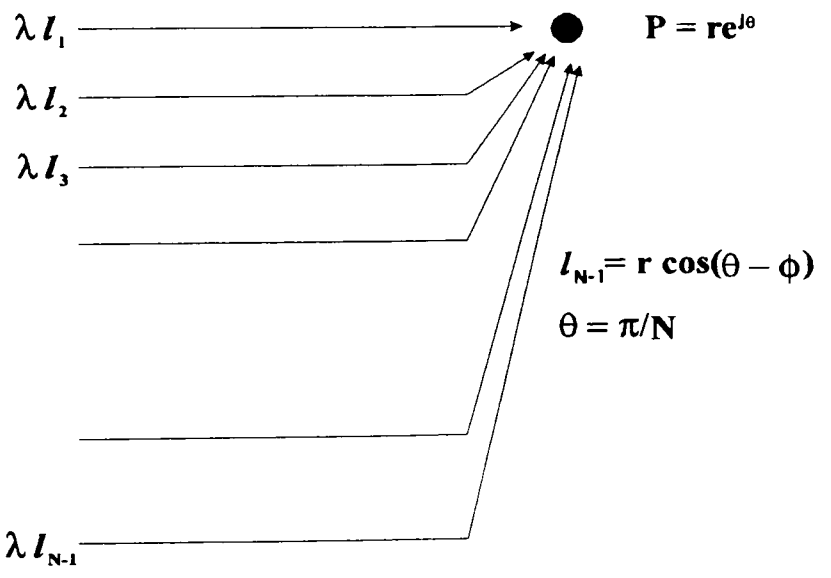

Figure 8.4 Dependence Graph for a single element

8.2.4 Stage II: The Signal Flow Graph Array Design

The Signal Flow Graph (SFG) consists of two basic elements. A node is denoted by a circle representing an arithmetic or logic function performed with zero delay, e.g., Multiply, ADD, OR, etc., and an edge denotes either a dependence relation or a delay [8.12]. To map the dependence graph on to the signal flow graph, a simple projection procedure is adopted which assigns to a **PE** the operations of all nodes along a line. Figure 8.5 shows the SFG for a single quadrant and the data ordering required for a 3 by 3 array with projections. Interpolation is left out at this point for clarity. Interpolation depends on the resolution of the reconstructed image and the data collection samples used. In this SFG the circle is used to denote an ADD operation only. The type of structure that emerges from the parallel algorithm shows the need to select data locations to assign to specific **PE**'s. This is performed by ordering the data into **N** blocks structured in serial streams. The ordering offsets are calculated once, then stored in a look-up table for future use. The offset is assigned to the Lagrange value by the host.

8.2.5 Stage III: Hardware Mapping

Mapping the SFG on to an array is performed by a one-to-one operation of transforming nodes into processors. Mapping is algorithm dependent and this limits the choice of approaches.

A simple approach was adopted by assigning one **PE** to each pixel in the final reconstructed image. However, difficulties arise when different sized systems need to be mapped on to fixed dimensional arrays. A partition scheme is required to adapt the array size. The argument for a single **PE** per pixel is based on the assumption that each **PE** is a simple VLSI structure would be implemented using Wafer Scale Integration (WSI) methods.

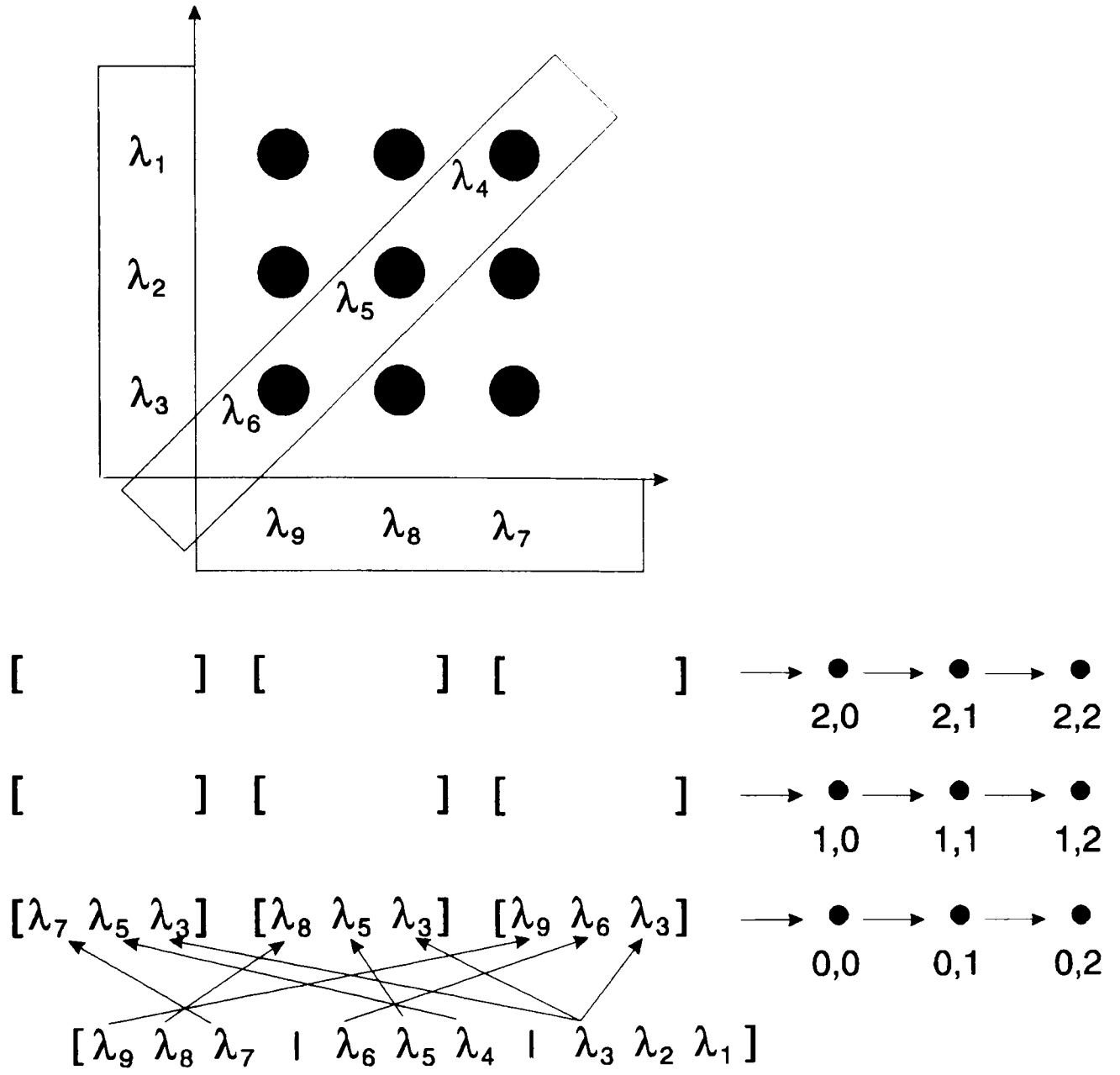

Projection at angle: 0, π/4 , π/2

Figure 8.5 Sort Path For Mapper

8.3 System Description

Several alternative approaches can be adopted in the construction of the computing engine that will subsequently be called the Back Projection Engine (BPE). Prototype systems based on bit-serial communication between **PE**'s are presented. The system architectures for the two systems are presented in Figure 8.12 and Figure 8.18 It is proposed that both systems comprise **S** by **S PE**'s, configured in a **2-D** orthogonal array. Each column of the array will depend on the size of the partitioning. The column can be subdivided to reduce the number of **PE**'s required. There are several common features between the different versions of the BPE. All the **PE**'s are evolved from a general Von Neumann processor architecture. The choice of a **PE** based on a simple Von Neumann machine allowed adaptation of the system in its development. A mixture of behavioural and gate level description is used in its evaluation. The main component parts for each **PE** are shown in the diagrams presented in Figures 8.11 and 8.17.

8.3.1 Mapper

The BPE performs its backprojection computation on a fixed set of data, the Lagrange multipliers. The assignment of a multiplier to a **PE** depends on the relation of the collection geometry to the size (in pixels) of the display. Since the system presented in this research uses one pixel to represent one **PE**, the same relationship holds true for the collection geometry and **PE**'s. Therefore, additional processing is necessary for the correct mapping of the Lagrange multipliers on the orthogonal PE array.

The main task of the mapper is ordering of data prior to input into the processor array. This must be performed as quickly as possible to take best advantage of the rest of the BPE. The assumption is made that the Lagrange multipliers have been computed and the data is stored so that the Mapper can obtain access to it in its original sampling order. It was shown in section 8.2.4 that a fixed set of data can be obtained from an investigation of the projection and display geometry. This gives all

the necessary information about how the Lagrange multipliers have to be mapped on to the **PE** array.

The data input for the BPE can be regarded as a wavefront of data bytes which is transported through the **PE** array synchronously, from column to column to the destination column of processors. A destination processor is invariably the first **PE** reached that is in accumulation mode. Since the data bytes carry no information about the destination, the assignment of the byte to the correct **PE** can be determined only by the order in which it is fed into the array. The sorting of the data is based on an algorithm known a Binsort [8.13]. The Mapper can be regarded as a hardware implementation of this algorithm. The amount of hardware resource needed for its implementation is quite large, but this is justified by the simulation results presented in section 8.6. The algorithm was chosen not only for its high efficiency, but also for its structural resemblance to the data transfer organisation between the Mapper and BPE.

The basic idea of the Binsort is that data are sorted by certain criteria. For each criterion a "bin" is available into which are put the data that fulfil the criterion. This criterion defines the destination of the Lagrange multipliers. In consequence, the "bins" must in some way represent the processor locations. This is done by assigning a (small) memory (the so called queue memory) to each processor. The control over the memories lies in the information stored in the location memory. It contains the vital information about the spread number and location address. A location memory word is used to distribute the data byte by controlling gates to the queue memories that correspond to the destination **PE**'s of the multipliers. These gates are connected to the memory write signals of the queue memories.

The phase in which this data sorting is carried out is called the collection phase. When the complete set of data is stored in the queue memories, a transition is made to the distribution phase. The data are then read out of the memories in a known order so that the multipliers will reach their destination **PE.**

An **n** bit distribution control signal is responsible for coupling the

corresponding memories of each **n** memory blocks on buses **1** to **n,** to load the output registers synchronously. The contents of the memories **11,21,..,n1** are read first before coupling **12,22,...,n2** until finally the contents of all memories have been read.

8.3.2 The Control Memories

The location memory stores the two-part information of spread values and location addresses in the following form. The word size corresponds to the size of the array (**n** by **n**), therefore the address of a **PE** is represented by the place of its assigned bit in this vector. $\mathbf{PE_{11}}$ is assigned to the LSB, $\mathbf{PE_{nn}}$ to the MSB. The bit index **k** in the memory word for a $\mathbf{PE_{ij}}$ is given by:

$$\mathbf{k = n(i-1)+j-1} \qquad \textbf{(8.3)}$$

with the index of the LSB **k = 0**, and the index of the MSB **k = (n x n) - 1**. For each Lagrange multiplier there is one memory word. The memory length is then equal to **N x S**, and the total memory size is given by **N x S x n x n** bits. The spread number is simply the number of set bits in one memory word. The control function of the memory is achieved by connecting it to a hold register which is enabled when a new byte has been received.

The organisation of the queue memory must obey the following requirements. The stored multipliers are **8**-bit words. Each queue memory must be capable of storing the value assigned to one of **N PE**'s. The memory size is thus determined to be **8 x N** bits. Both memories are addressed by the queue memory address counter, and the local memory address counter. The queue memory address counter will be counted up during the collection phase, and down during the distribution phase under control of **col_dis** signal.

8.3.3 Data Transmission

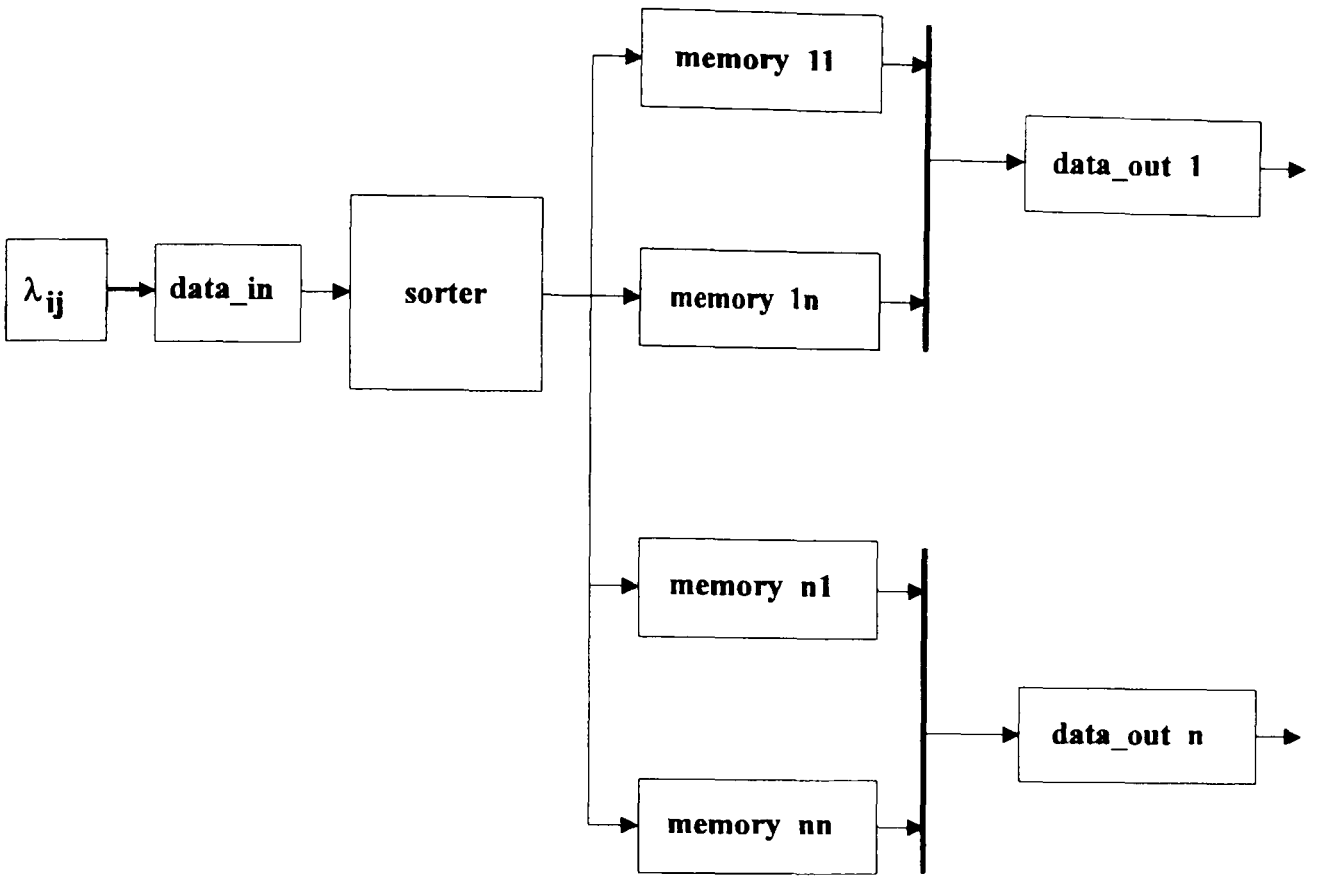

Figure 8. 6 Block Diagram of Mapper for Version One

While the queue memories are totally independent during the collection phase, there is an established order of reading their contents and forwarding it to the BPE during the distribution phase. This is derived from the fact that the data bytes are input in a column order. The Mapper must therefore have **n** outputs, each of which is connected to a row of processors in the BPE to input data synchronously for each row. It follows that the output of all **n** memories assigned to the **PE**'s of one row share one bus connection to the output register, as indicated in the block diagram of Figure 8.6

Due to the row synchronised mechanism, the controller has to send only **n** different read signals to the queue memories. The output registers were chosen to be 10-bit shift registers for serial data communication, to hold 8-bit data values, and the two protocol bits to signal the start of transmission. Figure 8.7 illustrates the communication links to the Host and the BPE.

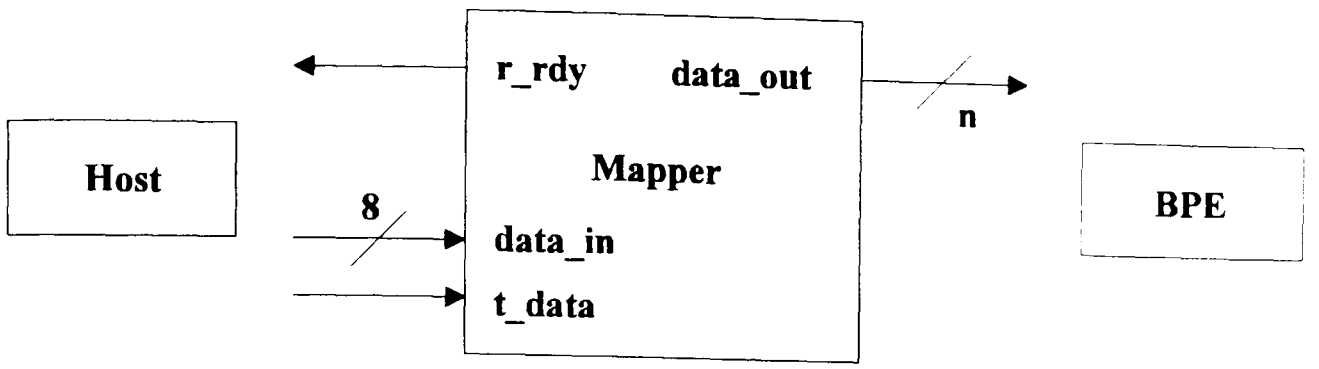

Figure 8.7 Communication Links of the Mapper Version One

The data bytes are simply loaded into the row output registers, beginning with the memory that is assigned to the first **PE** in the row, until the last word is read out of the $\mathbf{n}^{th}$ memory.

8.3.4 Mapper Version Two

Mapper two uses a completely different approach to its design. The data location is sent with the data byte itself, so there is no requirement for data sorting. This approach leads to reduction in the hardware resources necessary for its realisation.

Although there is no sort operation in this version of the Mapper, it relies on the same type of spread and location information. Since only one data byte can be input into the **PE** array at any time, the strategy of assigning one Lagrange multiplier to all its destination **PE**'s simultaneously must be abandoned. In this version it was decided to use the information separately in two memories. The spread memory contains only the spread value that is used to control the number of assignment operations that will be carried out for each Lagrange value. This operation is the attaching of the **PE** address to the data byte. The location memory contains the row and column address of the **PE**. The block diagram of Figure 8.8 illustrates the principle.

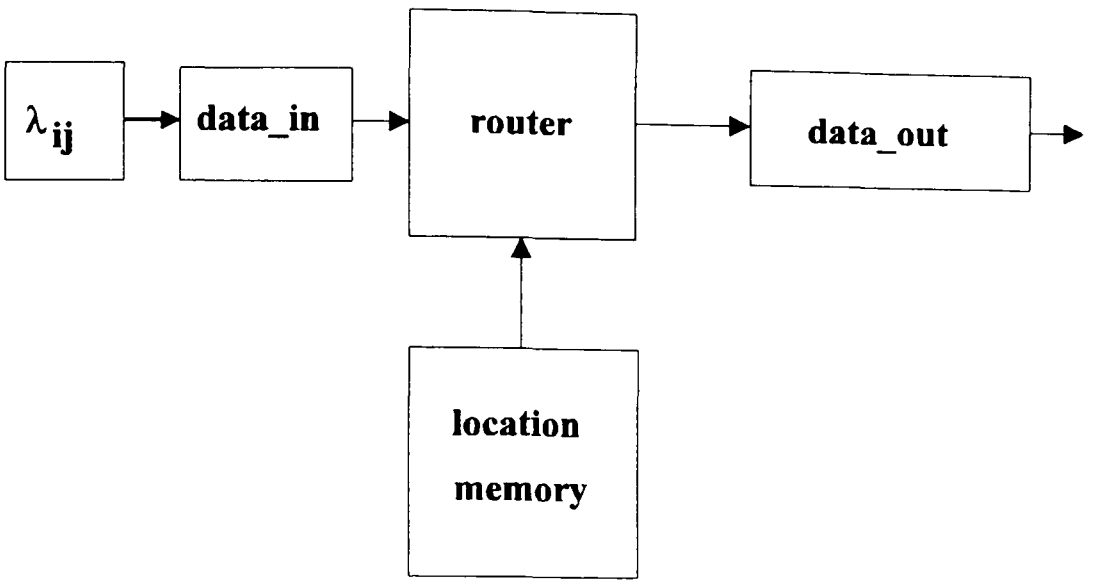

Figure 8.8 Block Diagram of Mapper Version Two

Incoming data bytes received from the Host are kept in an input register. This operation triggers the loading of a spread counter with the spread number in the spread memory. The counter is decremented by the controller after each assignment, indicating the completion of the current data byte distribution when reaching zero. The spread memory as well as the location memory are addressed by counters in the same manner as was described for version one.

In one distribution cycle, the data byte is loaded into the output register with the location address that is read from the location memory. Then the contents of the **data_out** register are shifted to the BPE. After this, the controller decides if another assignment is to be performed on the same data byte. In any case, the location memory counter will be incremented to read the next location address. After the completion of a distribution cycle, a new data byte is requested from the Host and the process starts again. This process is illustrated in Figure 8.9.

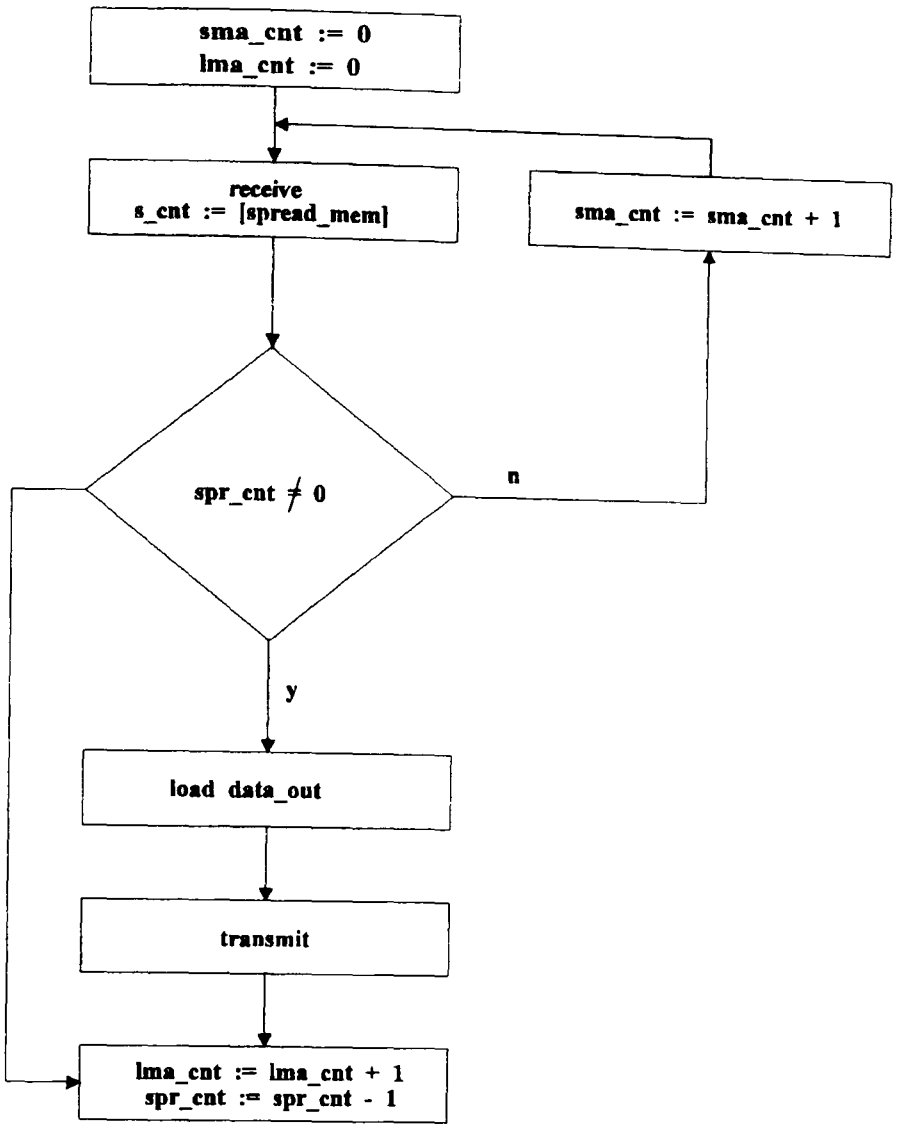

Figure 8.9 Flow Diagram of Mapper Function Version Two

8.3.4.1 Spread Memory

Since a single spread number always corresponds to a single Lagrange multiplier, the length of the memory is determined by the number of computed multipliers. The spread number itself has a value that can vary between **0** and **n x n**, (in the theoretical case of only one projection consisting of one sample). For the simulation a four-bit memory was used that allows a maximum spread of one multiplier to **15 PE's**, which should be sufficient for all relevant practical geometries. This assumption yields a memory size of **4 x N x S** bits.

8.3.4.2 Location Memory

The Location memory stores the address information for **N** values per **PE**, and for every **PE** in the array (**n x n**). The memory length must therefore be **N x n x n**. The word size is the address width of the **PE** location.

8.3.4.3 Data Transmission

The Mapper in this version is connected to only one of the BPE processors. It therefore has one outgoing data line. The transmission of data follows the same rules as for version one. The output register is a **26** bit shift register to store the data byte, the **PE** address, and the start sequence. The communication links are depicted in Figure 8.10.

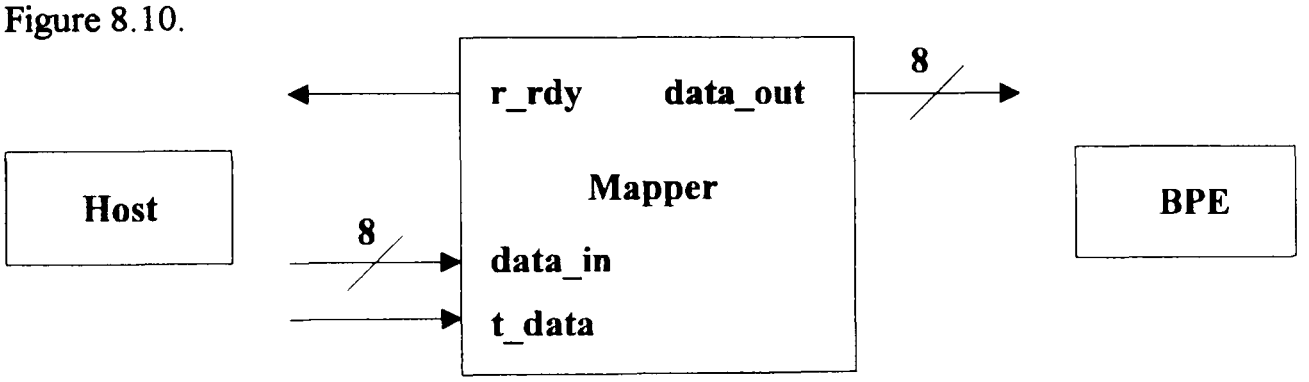

Figure 8.10 Communication Links of the Mapper Version Two

Both versions of the BPE are fed by a Mapper, or router, that sorts the incoming data according to a predetermined set of parameters.

8.4 System One

In system one, illustrated in Figure 8.12, an orthogonal grid of processors is connected in one plane only. The array can be stacked to form a **1-D** column of processors, but this increases the I/O requirements from the mapper. The **PE** in Figure 8.11 uses bit-serial communication for data. There is no need in this system to transmit address information, as the **PE**'s are in a fixed array configuration.

A design goal of this version of the BPE was to reduce the communication links between the processors. There are no handshake lines in this approach. Instead, two

bits are attached to the data byte to signal the start of a transmission.

The I/O manager is able to detect a falling edge at the data input, and starts the transfer of the data byte into the input register. Since the total number of transferred bits is known, there is no need for a stop bit. The data transmission is controlled by two signals, input ready and output ready, that are interchanged between the I/O manager and the decoder. The I/O manager has control over the input and output register. Since the clear and set signals are necessary only when using the parallel register, these signals are issued only to the output register.

When the I/O manager detects the falling edge of the startbit sequence, it initiates a transfer of the incoming data byte to the input register. When the transmission is complete, the input ready signal is given to the decoder. The decoder is responsible for deciding if the bus is free to transfer the data from the input register. A routine called '**through**' then handles the transfer, by enabling the buffer that couples the input register to the data bus. The I/O manager is informed via the output ready signal that the data byte is ready for output. The I/O manager takes control of the output register, loads it with the data byte from the bus and shifts it (with the start sequence) to the next processor.

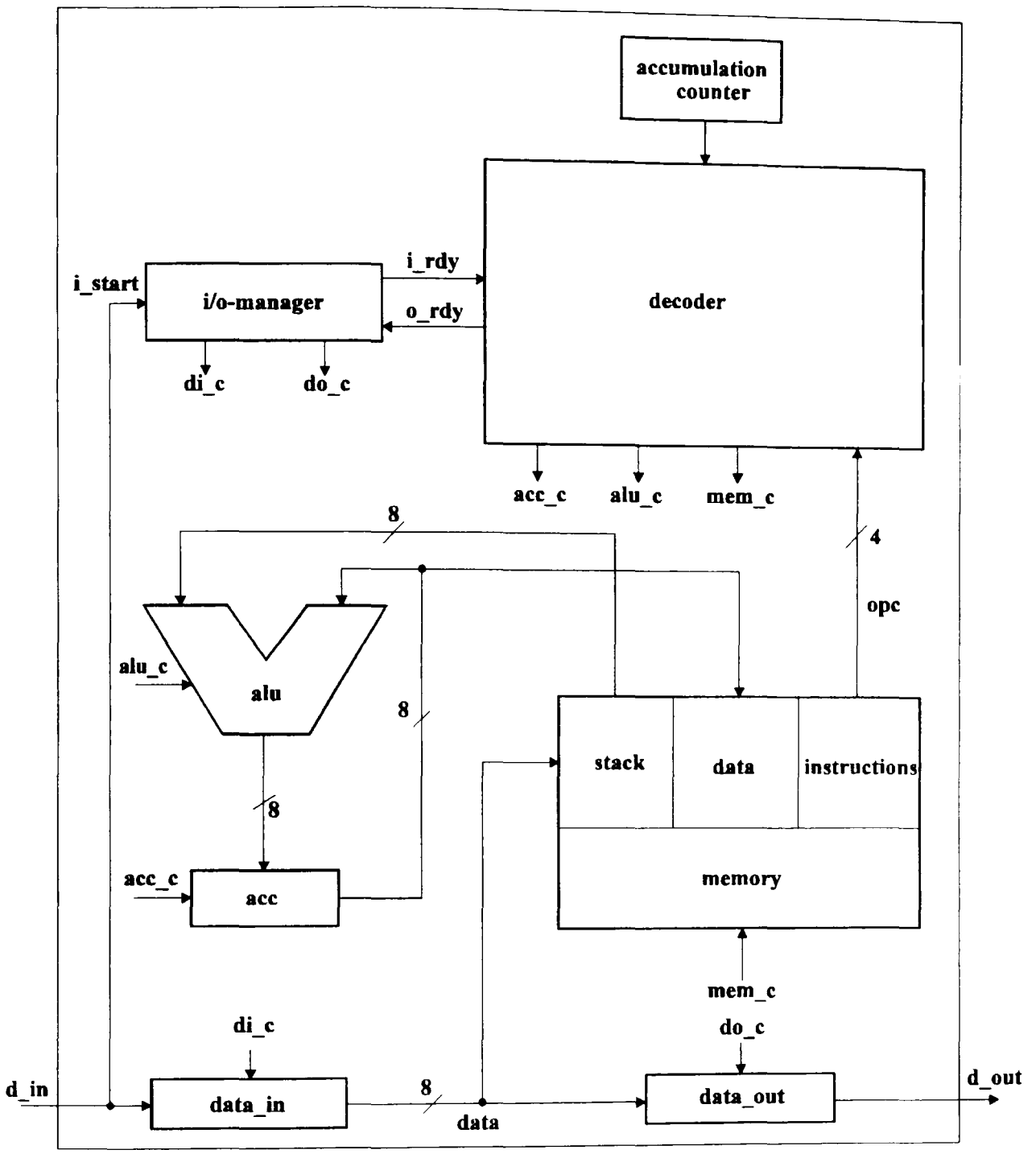

Figure 8.11 Processor Element (PE) for System One

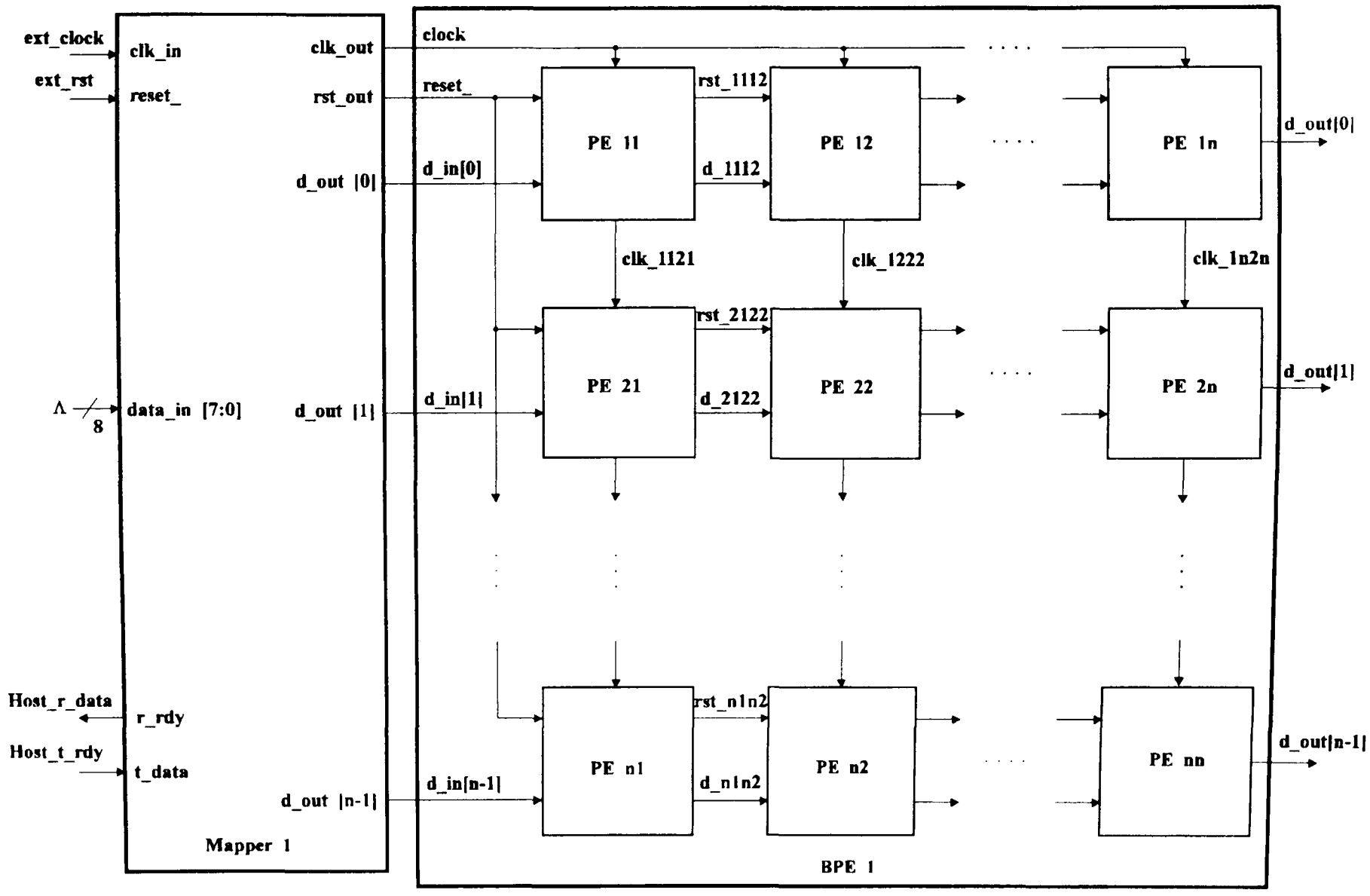

Figure 8.12 System One

The control routines introduce a timing constraint which effects the time that must elapse between the transmission of two data bytes. It is possible for the time between the input ready and the output ready signals to vary, depending on when in the fetch/execute cycle the input ready signal goes **HIGH.** The minimum time is given by $T_{io_{min}}$ = **1hct**(high clock time) when the bus is free, and the maximum of $T_{io_{max}}$ = **5hct** when a fetch or execute cycle has to be completed first. The I/O manager needs a fixed time of **12.5hct**, defining the minimum time between two output ready signals as T_{oo} = **13hct**. This gives the constraint on the interval between two input ready signals (as shown in Figure 8.13), as T_{ii} = **17hct**. Since the transfer of the byte itself needs **10hct,** the transmission interval has to be a minimum of 7 **hct**.

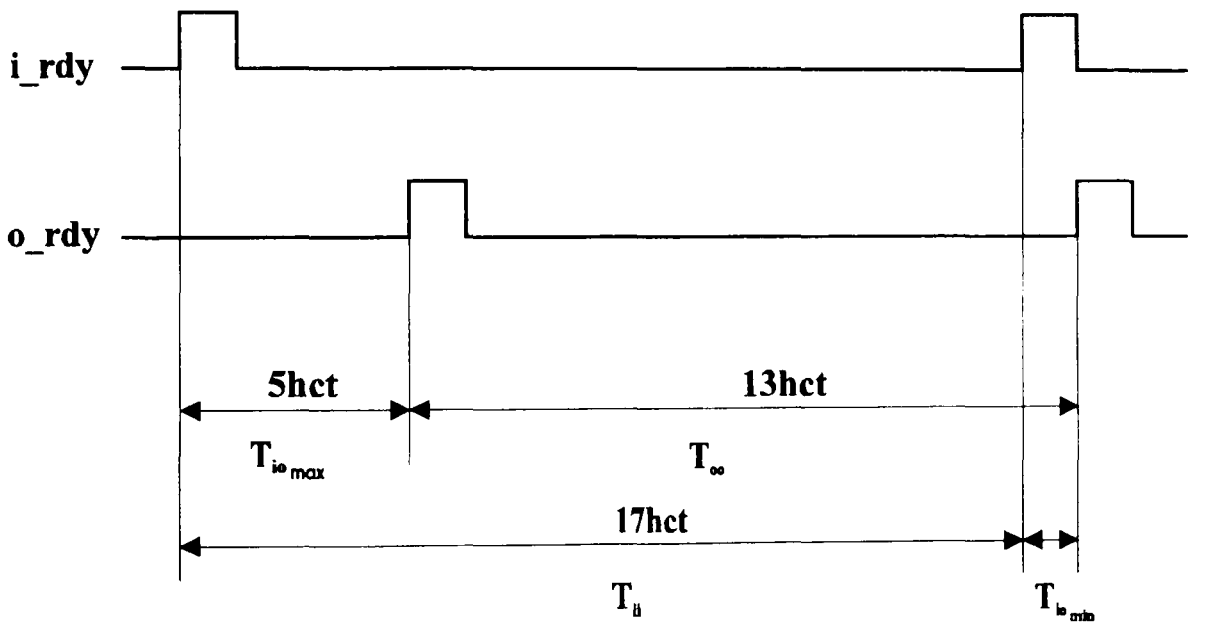

Figure 8.13 Data Transfer Timing

To obtain speed improvements in the processor design, the data processing is separated from the data transmission. The stored programme is executed only if actual data are there to be processed. The **PE** has two programmes loaded into it. The first is an accumulation programme that is automatically called by the decoder when a data byte is taken into the input register. The responsibility for correct data transfer is taken by the I/O manager programme. This controls the peripheral registers of the **PE** and

gives the necessary signals to the decoder. To reduce the connectivity in the array as much as possible, no connection is made from a **PE** back to the sending **PE**. Therefore there is no means of deciding if the receiving **PE** is ready for a new data byte. To overcome this problem, a stack is implemented (located in memory to save silicon area), where an incoming data byte is transferred. This is performed by the decoder immediately after it has received the input ready signal. This allows the process of data transmission to be detached from the data processing. The **accumulation mode** and the **bypass mode** can overlap. If the accumulation counter is not fully decremented and the stack is not empty, then the decoder will start the programme to sum the next data byte. When the accumulation counter reaches '**zero**', all incoming data are routed directly to the output register while the processor goes on with processing the data stack. To avoid a collision on the data bus, if two bytes are transmitted respectively but processed at the same time, the instruction cycle of the **PE** is interrupted at a suitable moment (at the end of a fetch or execute cycle), and the bus is freed for the data byte to be routed to the output register.

8.4.1 Instruction Set

A simple instruction set has been devised for the **PE** that allows suitable adaptability. This is presented in table 8.1.

Table 8.1 **Instruction Set for PE's**

Name	Operator	Operation
Programme Control Operations		
HALT	_	stop processor operation
SKIP	_	no operation
BREK	ma	stop fetch/execute cycle and set programme counter to ma
JUMP	ma	Unconditional jump to ma
Memory Operations		
LAC	ma	load accu with operand in memory at ma
STAC	ma	store accu in memory at ma
LDDO	ma	Load o/p register with operand in memory at ma
Arithmetic Operations		
SHIL	_	shift left accu contents by one bit
SHIR	_	shift right accu contents by one bit
ADDS	sa	add operand at sa to accu
ADDN	ma	add operand at ma to accu
SUBN	ma	subtract operand at ma from accu
MULN	ma	mult. accu by operand at ma
DIV	ma	Divide accu by operand at ma

ma = memory address

sa = stack address

8.4.2 Memory Organisation

The memory is organised as shown in Figure 8.14.

0 0 h...1 f h	Instructions
2 0 h..2 F h	Stack
3 0 h...f f h	Data

Figure 8.14 Memory Map Version One

Part of the memory is reserved for a stack to minimise the space required. To avoid unnecessarily complicated control mechanisms, the stack is organised as a LIFO (since it is of no concern in which order the data bytes are processed), with its own address space that accommodates a maximum of **16** words. It is possible to vary this space if the specification is changed.

8.5 System Two

In this version of the BPE, the addressing concept is changed to an approach similar to the method used in large transputer networks, termed worm-hole routing [16]. This was done to obtain some similarity with the transputer for comparison purposes. The data processing organisation is the same as version one.

The data distribution throughout the **PE** array in version one is arranged in columns. It is the responsibility of the mapping processor to route the data to the **PE**'s in the correct order, which demands sorting of the data prior to routing. One way of avoiding this sorting is to attach an address label to each data byte that will be compared with the **PE** address at the input. This will lead either to processing the data or to routing it to the next **PE**. This means a data byte can be transmitted from the Mapper to the BPE when it reaches the Mapper. The disadvantage is the additional

length of the data stream to be transmitted. The size of the BPE array would define the required additional address word size. If a maximum array size of **256** by **256** were assumed, the size of the additional address word is **16**-bits (**8**-bit row and **8**-bit column).

A new module called '**router**' was added in version two to deal with the necessary address operations . Instead of the decoder being informed of the advent of new data, the Router gets the input ready signal. The algorithm used to decide if the destination processor is reached is depicted in the flow diagram of Figure 8.15

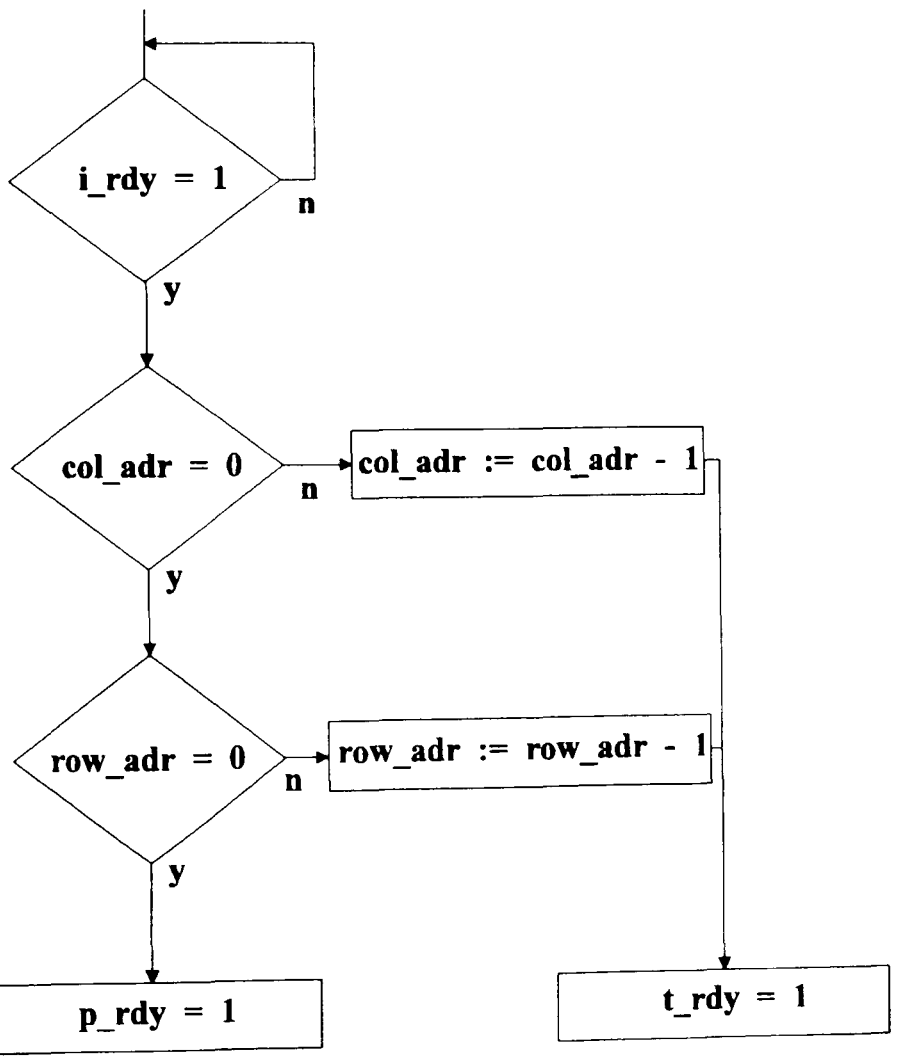

Figure 8.15 Flow Diagram of Data Routing for Version Two

To avoid having to label each processor with a different address, the method of Interval Labelling [8.17] is used. The address is compared with zero, and if that is not true, it will be decremented and routed to the next **PE.** This is done for the column

first, so the data will be routed horizontally to the right, until the destination column is found, then vertically down to the destination row.

8.5.1 Data Transmission

The routing through the array without prior sorting makes it necessary to interconnect the processors not only horizontally but also vertically. The data flow is thus oriented in two directions: to the right and down as shown in Figure 8.18. Data is input only to the array at **PE 11** in the upper left corner of the array to avoid further interconnections. The possibility of changing this approach is discussed in the last section of this chapter.

The same restrictions of data transmission interval time as for version one have to be taken into account. In this case the simulation showed that the time needed for processing a data byte (in accumulation mode) is small compared to the transmission time. Therefore the processor has already finished the instruction cycle before a new data byte comes in. This means the processor is always ready to transfer the byte without delay. The time $\mathbf{T_{io}}$ is therefore ensured to be **1hct.** The necessary interval between two data byte transmission, not including the data byte itself, can be reduced by **4hct**. This is illustrated in Figure 8.16

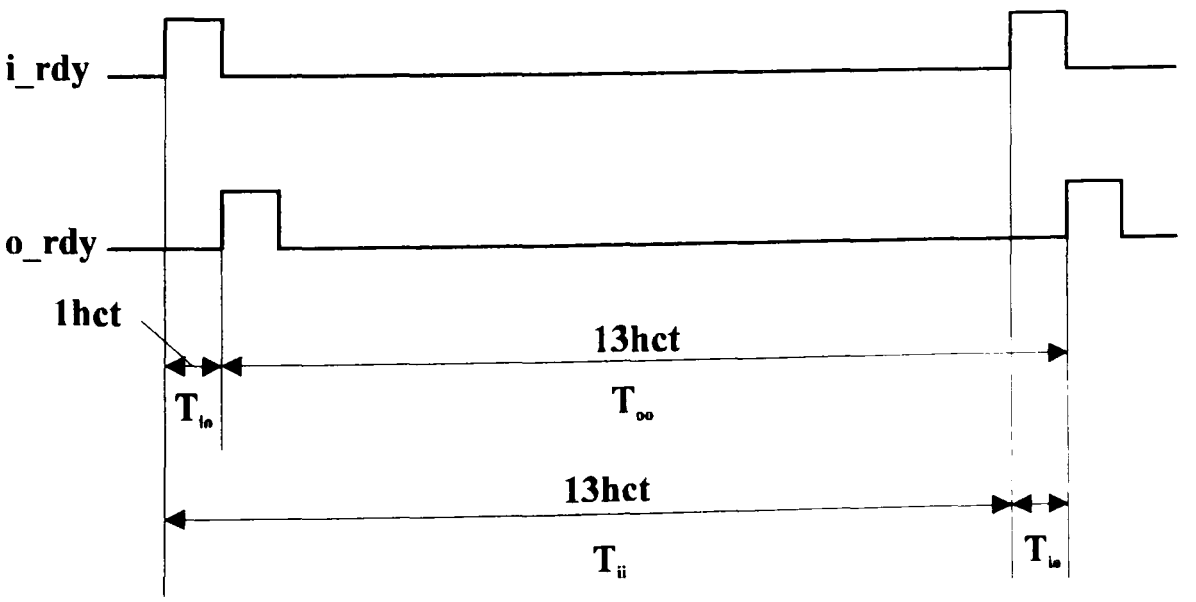

Figure 8.16 Data Transfer Timing Version Two

The **PE** and full system for version two are illustrated below in Figures 8.17 and 8.18 respectively.

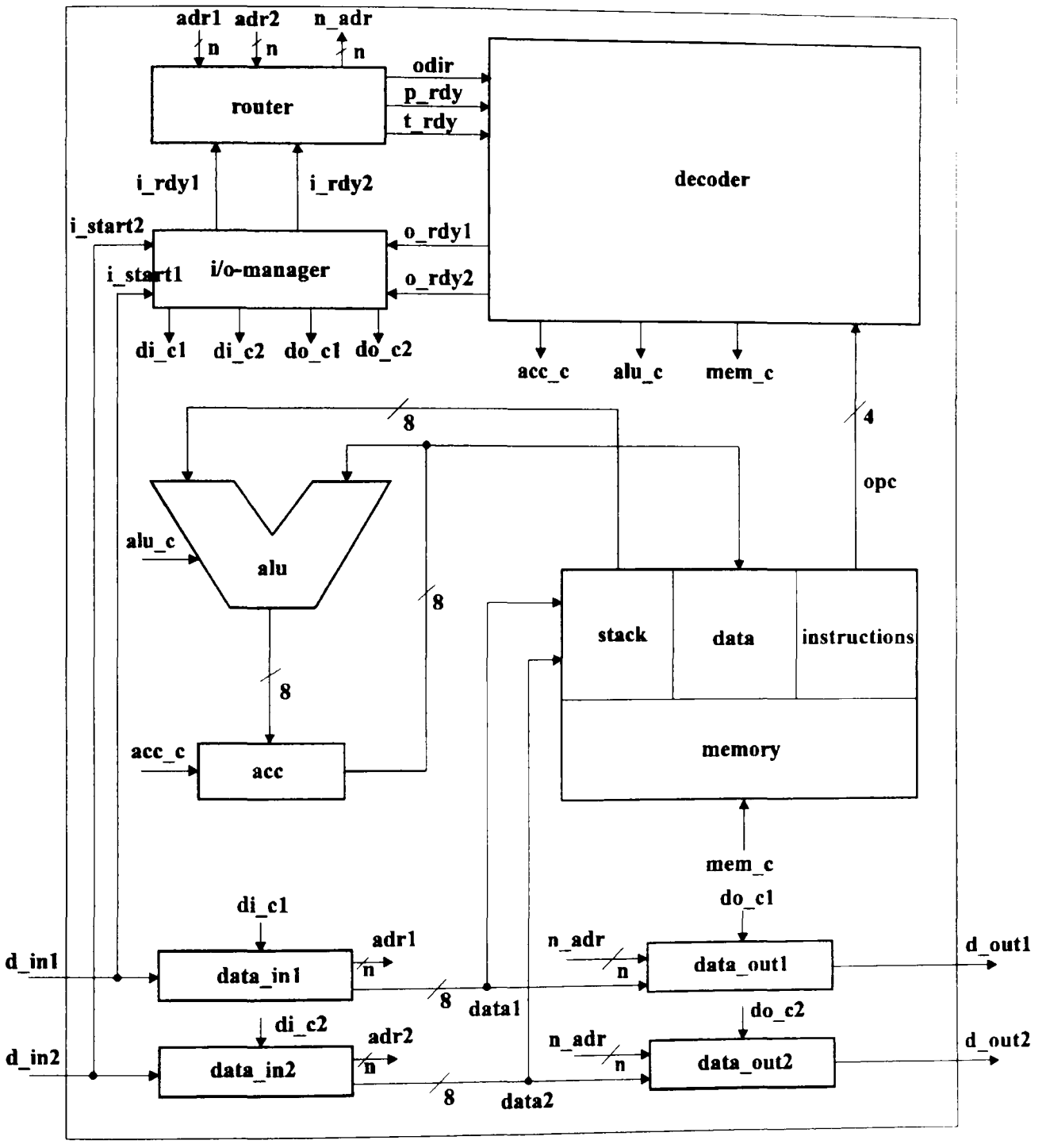

Figure 8.17 Processor Element Version Two

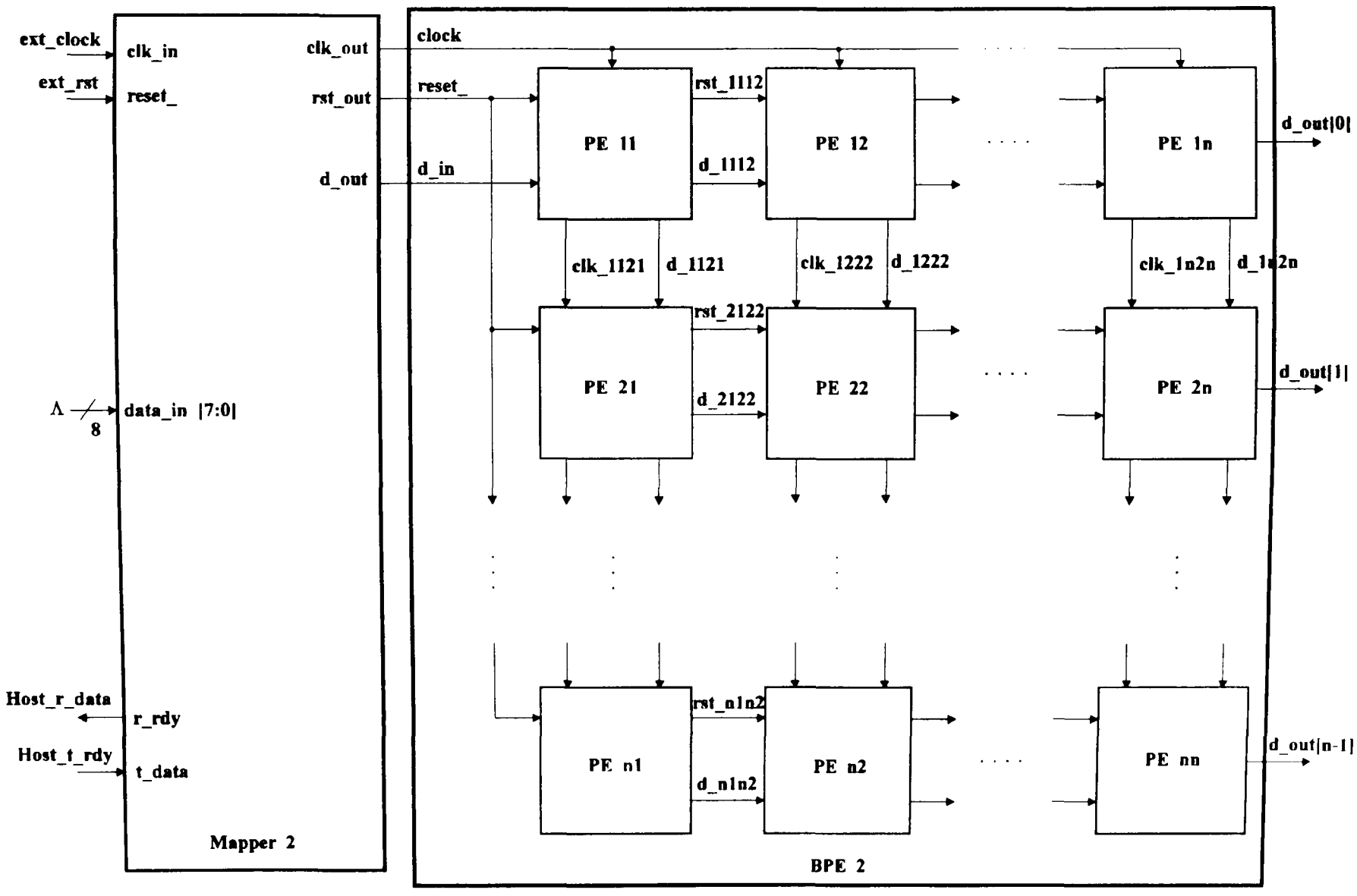

Figure 8.18 System Two

8.6 Results

The simulation results were obtained using a simulation tool called Verilog, which is part of the CADENCE [8.1] design framework for full custom VLSI design. Verilog is classed as a VHDL. It differs from the VHDL 1076 standards [8.17], but parsers are available to transform the code form the Verilog environment, to the VHDL 1076 environment.

The two versions of the BPE were compared by plotting the total cycle time required to compute the backprojection against the number of **PE**'s used. The results are tabulated below in tables 8.2, 8.3, 8.4 and plotted in Figures 8.19 and 8.20. These results indicate that as the number of **PE**'s is increased, version one has a clear advantage over version two in terms of the required number of cycles. As the BPE is technology independent, it is difficult to estimate comparisons between this approach and a standard stand-alone general-purpose processing engine. If a **30MHz** clock is assumed, the projected reconstruction time is approximately **40μs**. This compares to the same operation performed on a VAX11/780, which took over five minutes of CPU time for a **65** by **65** image.

Table 8.2 BPE Computation Cycles

	Computation Cycles	
Number of **PE**'s in array	Version 1	Version 2
1	178	164
4	275	614
9	372	1364
16	469	2414

Table 8.3 Mapper assignment Cycles

	Assignment Cycles	
Number of **PE**'s in array	Version 1	Version 2
1	479	160
4	479	640
9	479	1440
16	479	2560

Table 8.4 BPS Computation Cycles

	Computation Cycles	
Number of **PE**'s in array	Version 1	Version 2
1	657	164
4	754	663
9	851	1472
16	948	2619

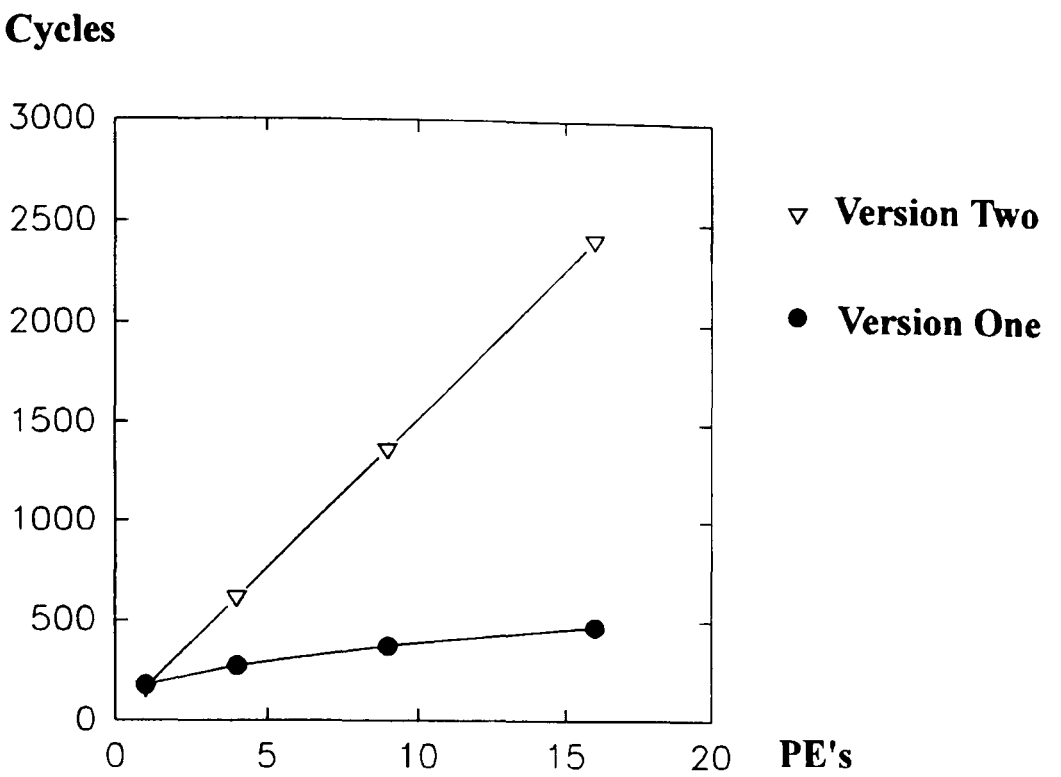

Figure 8.19 Plot of cycles against number of processors without Mapper

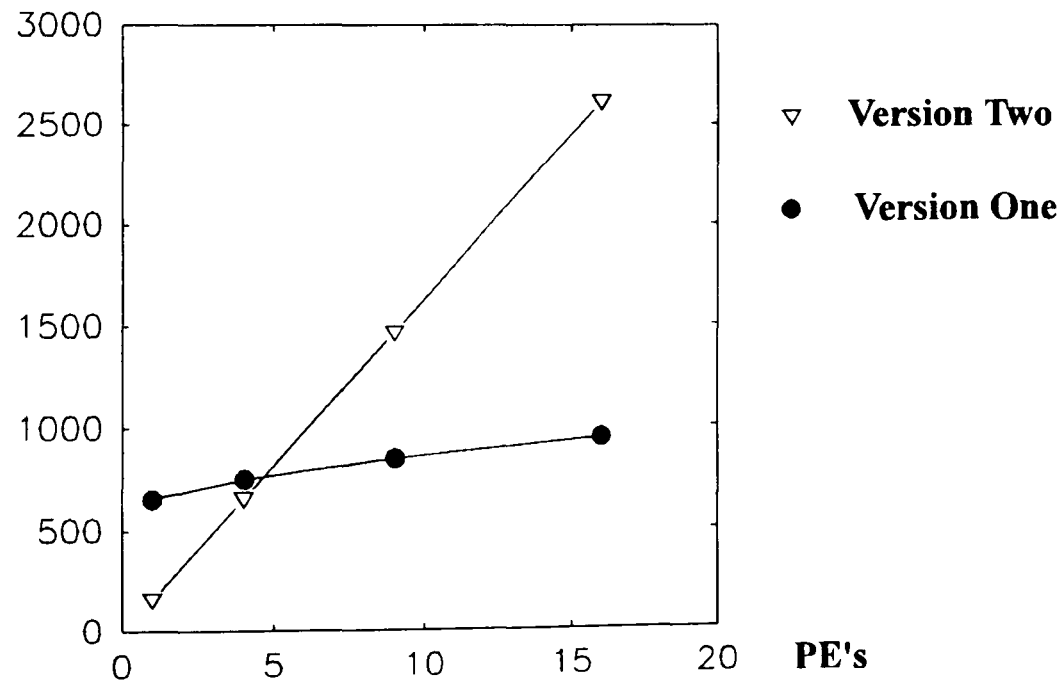

Figure 8.20 Plot of cycles against number of processors with Mapper

8.7 Discussion

The architectures proposed in this Chapter demonstrate the use of a novel hardware design to accelerate the reconstruction procedure. It can produce results at a faster throughput than those obtained by general purpose computing engines. The actual improvement will greatly depend on the partition scheme that is dictated by the available hardware, (the number of **PE**'s used in the array) A column partitioning scheme is suggested as the best candidate. This offers a balance between input connectivity and data through-put. The columns of **PE**'s that equate to column vectors of the reconstructed image could be divided into subvectors, and the image could be reconstructed in block rows.

The BPE was developed because general purpose machines based on SIMD architectures are not very suitable to this reconstruction problem. Two versions of the BPE were explored. The first models a novel approach to the architecture which is ideal for VLSI implementation, i.e., a regular repeatable structure is created which is ideal for mapping to silicon. The second uses an approach based on the data management structure of transputers. This model was produced to provide a comparison with the first version, and because the majority of systems that have been developed previously use transputers. The end goal of developing a special purpose device is to improve the performance in term of computation speed. This is particularly important for EIT application in which the main hardware platform use is a PC.

The comparison of the performance of this machine with other machines can only be estimated, because such information is hard to obtain. The limited imformation gives single figures of merit, with no indication to show if the performance change is linear when the size of the array or the resolution of the reconstructed image is changed.

At the University of Averio (UA), a machine with 4 units based on 6800's, reconstructs **128** by **128** images in about **30s** [8.14]. The University of Bristol (UB) developed an architecture based on a transputer network [8.15]. The processing time

required by one transputer T414 is about **10.0μs**, to handle a maximum of **5** by **5** pixels. If a **512** by **512** image is reconstructed, a processing time of **0.4s** is required. Also, for the **512** by **512** image, a **100** transputers would be required. The Massively Parallel Architecture (MPA) developed by Lattard, Faure and Mazare [8.11], uses a **32** by **32** cell array to obtain the same performance as the transputer based machine. A summary of the machines above is given in table 8.5.

Table 8.5 Summary of Machines

Machine	Total number of processors in array	Image size	Processing time
UA	**4**	**128 x 128**	**30.0s**
UB	**1**	**5 x 5**	**10.0μs**
UB	**100**	**512 x 512**	**0.4s**
MPA	**1024**	**512 x 512**	**0.4s**

The BPE is primarily designed for VLSI implementation and its speed will depend on the technology used to implement it. Direct comparison with the above machines is difficult, as the machines mainly use FBP algorithms that lend themselves to parallel implementation. The main advantage with the BPE is that the design approach allows for efficient VLSI implementation, and similar speeds can be obtained as with the Massively Parallel Architecture but with algorithms that are superior.

A machine developed by Goutis [8.16] suggested a MIMD architecture for a special purpose processor based on the successive relaxation algorithm The excessive computation is drastically reduced by exploiting the structure of the submatrices of the **G** matrix. The backprojection operations still dominate the total computation time in

this machine. This machine would have been useful for comparison with BPE, but no information has been produced that gives its performance.

The results for the two versions of the BPE show that version one is the preferred option. These results satisfy the basic objective of this part of the research. This was to develop a model of the system on which a feasibility study could be conducted to evaluate the possible advantages and disadvantages of these approaches towards the backprojection operation.

The two versions were modelled using a hardware description language known as Verilog [8.1]. The reasoning was that the waste of resources (in terms of material and finance) could be avoided and the flexibility of computer simulation allows for experimentation and enables the "development" of different versions. Since Verilog allows most ideas to be realised in a behavioural description, the work done here was not concerned with actual physical restrictions such as timing or space constraints, although the delay times encountered in electronic devices have been taken into account in a general way. The design assumes ideal elements but allows for parameter adjustment for realisation. Despite these restrictions, the design was concerned mainly with optimisation of computation speed and the reduction of array interconnectivity.

The results obtained from the modelling of the two systems lead to the following conclusions:

i) Advantages:

Version one uses a minimal number of operations to perform the backprojection operation. This will lead to a speed improvement regardless of the technology used.

Both versions are relatively easy to implement as VLSI devices and hence realise the advantages of speed and cost.

Version two has a similar structure to a transputer based system, which allows it to adapt to changes in configuration.

ii) Disadvantages:

Neither version is flexible to changes in hardware such as the resolution of the reconstructed image or the number of samples used.

Further research is required to adapt either system for the EIT geometries and to bring the system closer to an actual hardware implementation. This is beyond the scope of the work undertaken in this research.

9 CONCLUSIONS AND SUGGESTIONS FOR FURTHER WORK

9.1 Summary of the Research

The use of electrical impedance measurements to provide a **2-D** map of the distribution of resistivity within the human body has a great potential in medical diagnosis. There are several areas in clinical medicine and physiology where it has been suggested that the use of such a technique, known as electrical impedance tomography (EIT), could offer significant advantages over existing methods. In the majority of cases these have been supported by preliminary studies, but the application of the algorithms in clinical use have been demonstrated only in a small number of cases. There are two major areas that need to be addressed if EIT is to be fully exploited. First, there is a requirement to identify the link between physiological changes and resistivity and second, ways must be found to improve the quality of the reconstructed resistivity images. The first objective is outside the scope of this research, but a full review of the biomedical applications of EIT is given by Holder and Brown [9.1]. The second was the subject of this thesis and is summarised in this final Chapter.

Following the introduction of the research topic in Chapter one, the objectives of the research were defined with an indication of the scope of the investigation. A survey of methods for reconstructing images was presented next, in Chapters two and three. Chapter two concentrated on the methods applicable to X-ray systems, where a taxonomy of the approaches was developed. As EIT reconstruction problems tend to be considered separately from other methods, due to the nature of the data collection method, Chapter three reviews the EIT approaches and summarises both Forward and Inverse problems.

The conclusions drawn from these reviews suggest that the Constrained Optimisation Reconstruction Technique (CORT), which was successfully applied to

X-ray systems, could also offer solutions in EIT. The CORT method requires the selection of a cost criterion to produce a model. This cost criterion is not unique and a number of them were presented in Chapter four. It was found that optimisation of the image energy cost criterion resulted in a simple model, known as the backprojection model. This expresses the image in terms of the **1-D** Lagrange multipliers. This model is linear and its main kernel, which is backprojection, is also used by the convolution and ART methods. Chapter four introduces both the primal and dual approach to CORT, and derives the models that relate the Lagrange multiplier to the solution of the reconstructed image. Only the parallel X-ray geometry was investigated in this Chapter, so that the methodology could be fully explained. It was concluded that the backprojection model offers the most suitable approach for exploitation in EIT.

The algorithms for computer implementation of the backprojection model were presented in Chapter five. Variations of the model were also given for the divergent geometry, to demonstrate how different geometries affect the structure of the algorithm. An important criterion is that the algorithm must be able to produce reasonable reconstruction in the presence of noise and limited data. Not all the algorithms presented in Chapter five are suitable for EIT implementation with these requirements. The Jacobi method does satisfy the above requirements and hence was adopted for this research. This allowed the statistics of the noise to be matched with the statistics of the errors in the pseudo inverse of the associated system matrix.

A mathematical model for the EIT geometry was described in Chapter six. Two different geometries were presented; the opposite electrodes method which is termed the parallel curvilinear geometry and the dipole method defined as the divergent curvilinear geometry. The opposite method offered a more uniform current distribution, but has a limited number of samples per boundary measurement, whereas the dipole approach gives a non-linear current distribution with twice as many samples, thus allowing a higher spatial resolution. The Forward problem in both cases was solved by standard analytical methods and then applied to the CORT to produce specific models for each geometry. The requirement in both cases was to maintain the

structure of the associated system matrices in order to exploit the advantages of similar structures previously derived from the parallel and fan beam geometries in X-ray systems.

Novel approaches for evaluation of the associated system matrices have been described which allow theses matrices to be evaluated relatively simply.

In Chapter seven, the results of the application of the new algorithms were demonstrated with model boundary data. In the divergent curvilinear case, both modelled data and data obtained from the Sheffield Mark I system were used. The data obtained from the Sheffield system were obtained in two forms: the boundary profiles obtained from a phantom, consisting of a saline tank with glass and polyacrylimide rods, and second, clinical data.

The other issues considered in this Chapter were noise corruption of the data, the current distribution in the medium under examination, selection of the relation parameter and the optimal number of iterations.

A major advantage with the CORT's algorithms is that they can be adjusted so that statistics of the error in the pseudo inverse of the associated system matrix match the statistics of the noise within the data. This minimises the effects of noise amplification in the reconstructed image. If the noise is assumed to be Gaussian (which may not be the case in a real EIT system), the iteration can be terminated when the error between the true Lagrange multipliers and the Lagrange multipliers obtained at each iteration is a minimum. The number of iterations is chosen to be large to ensure that the distribution of the projection error is approximately Gaussian. This is achieved by ensuring the relaxation factor γ is as low as possible. The algorithm converges for $\mathbf{0 < \gamma < 2}$, where γ is the relaxation factor.

The CORT algorithms were found to be optimised with the modelled boundary data when the relaxation factor was chosen as **0.001** with **50** iterations for the opposite electrode method, and **0.002** with **50** iterations for the divergent system. The data obtained from the Sheffield Mark I system were found to give the best results when the relaxation factor was **0.002** with **10** iterations.

Chapter eight departed from the main theme of the EIT research to consider the possibilities of improving the performance of the reconstruction algorithm by means of hardware. The main bottleneck in the reconstruction procedure was identified as the backprojection operation. Using a hardware description language, a system was developed which could improve the performance of this main kernel. Only the parallel geometry was considered in this part of the research. A new system was proposed which can improve the processing of images using a simple interpolation scheme.

9.2 Review of the Research Objectives

It is of interest to reflect upon the original research objectives presented at the end of Chapter one, and assess how well the objectives have been met. The primary objective was to apply CORT to EIT. This objective has been achieved for two different data collection methods, and the primary results of both algorithms are presented in Chapter six. The issue of improving the quality of the reconstructed image without incurring excessive computation cost has also been addressed by maintaining the permuted block circulant structure of the associated system matrices.

The main objective has been achieved in a number of stages. First, the opposite electrode method, which is the simpler of the two geometries, was defined mathematically. A co-ordinate system known as Bipolar was used to solve the Forward problem. It was decided to deal only with the temporal image reconstruction problem in this research, as static image reconstruction has not been proved to be useful in clinical applications. A mathematical model was derived which relates the **1-D** Lagrange multipliers to the reconstructed image. The model is linear and has a very important physical interpretation, which is that the resistivity image can be produced by backprojecting the **1-D** Lagrange multiplier functions between the equipotential paths at different angles.

The next objective was to obtain a computationally efficient implementation of the new algorithms. It was found that the approximate inverses for the new geometries were permuted block circulant. This allows the matrices to be diagonalised using the

block FT matrix. A procedure was also given that allowed the pseudo inverse to be precomputed. Since the structure of the inverse was maintained, the stored requirements need be only one half of a block row. The only major computation requirement for estimating the Lagrange multipliers for backprojection is the multiplication by the block diagonal eigenvalues matrix.

A third objective was to maximise the quality of the reconstructed image which could be produced from this new approach. Chapter six presents the results of noise matching. Additive noise was applied to the normalised boundary profiles (projections), and the number of iterations **n** and the relaxation parameter γ were selected to give the optimum quality of the reconstructed image. This was repeated for the dipole method. In both cases, the new algorithms produced reasonably accurate reconstruction in the presence of noise, with less computation requirements than other methods such as Newton-Raphson and its variations.

It was found that the approximate inverse matrices corresponding to the Jacobi iterations are diagonally dominant, and become block diagonally dominant as the iterations parameter **n** increases. A relationship between the variance of the error between the noisy and noiseless Lagrange multipliers corresponding to the $\mathbf{n}^{th}$ iteration, and the variance of the measurement noise in terms of the eignvalues of the approximate inverse, holds true for the new geometries. This relationship indicated that, for large **n**, the eigenvalues of the approximate inverse become very large, and this results in an amplification of the noise.

The need to obtain an optimum reconstruction in the presence of noise is particularly important in EIT because the difficulty with the EIT system is the collection geometry. Although it is assumed to be a circle, it may be deformed to accommodate the object under examination. This modification of the geometry can be considered as another source of noise in the collection system and can be accommodated more readily by CORT than by transform based methods.

It is suggested that there are two main reasons for the greatly improved reconstruction accuracy when using the CORT, compared with the transform based methods adopted by Barber and Brown [1.17].

i) Each **1-D** function to be backprojected depends on all the boundary profiles and not on an independently derived function for a point spread function (psf).

ii) The constraints (boundary profiles) are satisfied within a limit determined solely by the statistics of the noise used.

Another objective of the research was to reconstruct images from data obtained from the Sheffield Mark I system. A test phantom was used, constructed of clear perspex and filled with a saline solution, having glass and polyacrylimide rods in the solution at fixed positions. The Sheffield system can measure only boundary data using the dipole method, therefore comparisons are not possible with the opposite collection method. The dipole collection method also introduces the problem of non-uniform current distribution which can cause problems in maintaining the structure of the associated system matrix. This is important to obtain the computation efficiency that the permuted block circulant matrix offers. The weighting for the current density was easily incorporated into the backprojection operation. There are a number of options for this weighting, depending on the desired results of the reconstruction. These can be good sensitivity, high accuracy, or a compromise between the two, when indicating small changes in resistivity.

The final objective was to investigate the development of hardware required to improve the computation speed of reconstruction. This was achieved for parallel X-ray data by proposing a parallel processing engine to handle the backprojection operation which is the main bottleneck in most reconstruction algorithms. The suggested processing engine was demonstrated using Verilog which is a hardware description language.

9.3 Summary of Advantages of new Approach

The main advantages of the new approach can be summarised as follows.

a) The structure of the associated matrix can be used to improve the performance of the algorithm, by reducing the computation time.

b) The evaluation of the associated system matrices is relatively simple, using the novel methods described in Chapter six.

c) The effects of the current sensitivity are incorporated during backprojection, allowing it to be optimised for sensitivity or accuracy, and for modification to match experimental data (Chapter six).

e) The effect of current density distribution is separated from the associated system matrix and this enables the structure of the matrix to be maintained (Chapter six).

f) The statistics of the noise within the data collection system can be matched to the statistics of the error in the pseudo inverse, which appears to improve the quality of the reconstruction (Section 7.4).

g) Prior information regarding regions of different sensitivity can be incorporated into the algorithm to give more accuracy in reconstruction. This is highly beneficial in brain imaging where the brain is surrounded by the skull, resulting in more accurate reconstruction of the brain functions (Chapter four).

h) The positions of features within the image are not distorted in contrast with other approaches. This is important in clinical use of the EIT system (Chapter seven).

i) The CORT method is less susceptible to electrode positioning.

9.4 Suggestions for Further Research

There is a need for a detailed comparison study of other algorithms using clinical data. This has a number of problems, as the data collection method varies between the FEM algorithm, and those associated with the Sheffield system. Also, the full details of other methods are not always given in the literature. For example, the

algorithm used by the Sheffield system is partly based on an empirical approach for deriving the filter function. Yorkey and Webster [9.2] give a limited comparison of the reconstruction algorithms, claiming that the N-R method has an improved performance compared with six other methods. Their results were validated only on modelled data, and not on clinical data. Also, their comparison has become dated and does not include new approaches.

Another useful area of investigation, which may lead to improving the computation speed of the algorithms, is the structure of the pseudo inverse. This contains a number of elements that are very small. To reduce the storage requirements, it would be worth investigating the effect of setting these elements to zero and observing if removing their contributions causes notable degradation to the reconstructed image.

The algorithms developed in this thesis mainly operate in the space domain. Durrani and Goutis [9.3] showed that, by implementing constrained optimisation techniques in the Fourier domain, it was possible to include more elaborate cost functions that lead to better reconstructions. Moreover, this allowed for the utilisation of the speed of the FFT. It is suggested that it would be useful to investigate these elaborate cost functions in EIT.

There are also non-medical areas for application of these techniques, eg. silicon tomography. There is a requirement during the processing stages of IC manufacture, to measure accurately parameters such as the semiconductor doping density or sheet resistivity. Boundary profiles could be obtained by measuring potentials on the periphery of the silicon wafer, which could be used to reconstruct a map of the resistivity of the sheet resistance.

Methods based on the backprojection between equipotentials are derived from an analysis of the 2-D problem, such as the approach taken in this research. It is suggested by Guardo *et al.* [9.4], that improvements could be obtained by considering the 3-D conductivity distribution. It would be useful to adapt the CORT method for 3-

D to enhance its accuracy. This would require the development of a 3-D scanning system to collect the boundary data.

The result presented in Figure 7.21 shows a reconstruction of the resistivity change in a brain. The algorithms developed so far have assumed that the complete domain to be reconstructed has similar resistivity, with small changes between regions. The brain is surrounded by the skull which has a higher order of resistivity than the soft tissue inside. Presently available systems cannot image through the skull. It is suggested by Holder [9.5] that the localisation of epileptic foci in ambulatory patients could be achieved using a ring of subdural electrodes. To eliminate the need for the subdural electrodes, the CORT algorithm could be adapted to include prior information in the associated system matrix, of different sensitivities in different regions. This would allow the small resistivity changes within the brain to be more accurately identified for the monitoring of cerebral ischaemia and for imaging of slow or rapid impedance changes during functional activity.

The research presented in this thesis provides a new development in the reconstruction of images for EIT. At present, these algorithms are being evaluated on brain images and require the combination of clinical evaluation with improvement to the algorithms based on the clinical results. This research would represent a major future advance in neuroscience technology.

Appendix A

Euler-Lagrange Method with higher order derivatives

[4.2 page 101, 4.3 page 94]

Suppose the functional $\mathbf{C(.)}$ be defined as:

$$\mathbf{I} = \iint_{\mathbf{D}} \mathbf{C}(\mathbf{x}, \mathbf{y}, f, f_{\mathbf{x}}, f_{\mathbf{y}})\mathbf{dxdy} \qquad \textbf{(A.1)}$$

where subscripts are employed to indicate partial differentiation, to avoid cumbersome notation. Hence:

$$f_{\mathbf{x}} = \frac{\partial f}{\partial \mathbf{x}} \qquad f_{\mathbf{xy}} = \frac{\partial^2 f}{\partial \mathbf{y} \partial \mathbf{x}} \quad \text{etc.}$$

Let $f(\mathbf{x}, \mathbf{y})$ be a **2-D** contiguously differential image that minimises $\mathbf{I}$. To effect the extremisation of A.1, a one-parameter family of comparison functions $\bar{f}(\mathbf{x}, \mathbf{y})$ is introduced:

$$\bar{f}(\mathbf{x}, \mathbf{y}) = f(\mathbf{x}, \mathbf{y}) + \varepsilon\eta(\mathbf{x}, \mathbf{y}) \qquad \textbf{(A.2)}$$

where $\eta(\mathbf{x}, \mathbf{y})$, is an arbitrary differentiable function for which:

$$\eta(\mathbf{x}, \mathbf{y}) = \mathbf{0} \quad \text{on} \quad \mathbf{s} \qquad \textbf{(A.3)}$$

where $\mathbf{s}$ is the boundary curve of $\mathbf{D}$ and ε is a small parameter of the family.

This can be expressed in words as:

Tentative solution = Exact solution + Variation of $f(\mathbf{x}, \mathbf{y})$

$\bar{f}(\mathbf{x}, \mathbf{y})$ $\quad$ $f(\mathbf{x}, \mathbf{y})$ $\quad$ $\varepsilon\eta(\mathbf{x}, \mathbf{y})$

Replacing $f(\mathbf{x}, \mathbf{y})$ by $\bar{f}(\mathbf{x}, \mathbf{y})$ in A.1 and expanding $\mathbf{I}$ by Taylor's theorem, then taking the first variation, an extremum for $\varepsilon = 0$ is obtained, hence:

$$\mathbf{I}'(\mathbf{0}) = \mathbf{0} \qquad \textbf{(A.4)}$$

where:

$$\mathbf{I(\varepsilon) = \iint_D C[x, y, \bar{f}, \bar{f}_x, \bar{f}_y - \sum_{k=1}^{N} \lambda_k(x_k)]dxdy} \qquad \textbf{(A.5)}$$

Using A.2 to compute

$$\frac{\partial \bar{f}}{\partial \varepsilon} = \eta, \qquad \frac{\partial \bar{f}_x}{\partial \varepsilon} = \eta_x, \qquad \frac{\partial \bar{f}_y}{\partial \varepsilon} = \eta_y$$

and differentiating A.5 with respect to ε gives:

$$\mathbf{I'(\varepsilon) = \iint_D [\frac{\partial C}{\partial \bar{f}} \eta + \frac{\partial C}{\partial \bar{f}_x} \eta_x + \frac{\partial C}{\partial \bar{f}_y} \eta_y - \sum_{k=1}^{N} \lambda_k(x_k)\eta]dxdy} \qquad \textbf{(A.6)}$$

Since, according to A.2, setting $\varepsilon = 0$ is equivalent to replacing $\bar{f}$ by f, then:

$$\mathbf{I'(0) = \iint_D [\frac{\partial C}{\partial \bar{f}} \eta + \frac{\partial C}{\partial \bar{f}_x} \eta_x + \frac{\partial C}{\partial \bar{f}_y} \eta_y - \sum_{k=1}^{N} \lambda_k(x_k)\eta]dxdy = 0} \qquad \textbf{(A.7)}$$

due to A.4. Applying Green's theorem (analogous to integration by parts), to the middle two terms of A.7:

$$\mathbf{0 = \iint_D \eta[\frac{\partial C}{\partial f} - \frac{\partial}{\partial x}\left(\frac{\partial C}{\partial f_x}\right) - \frac{\partial}{\partial y}\left(\frac{\partial C}{\partial f_y}\right)]dxdy + \int_s \eta[\frac{\partial C dy}{\partial f_x dz} - \frac{\partial C dx}{\partial f_y dz}]dz} \qquad \textbf{(A.8)}$$

$$\mathbf{0 = \iint_D \eta[\frac{\partial C}{\partial f} - \frac{\partial}{\partial x}\left(\frac{\partial C}{\partial f_x}\right) - \frac{\partial}{\partial y}\left(\frac{\partial C}{\partial f_y}\right)]dxdy} \qquad \textbf{(A.9)}$$

due to A.3. Hence:

$$\mathbf{I'(\varepsilon) = \iint_D \eta[\frac{\partial C}{\partial f} - \frac{\partial}{\partial x}\left(\frac{\partial C}{\partial f_x}\right) - \frac{\partial}{\partial y}\left(\frac{\partial C}{\partial f_y}\right) - \sum_{k=1}^{N} \lambda_k(x_k)]dxdy} \qquad \textbf{(A.10)}$$

and the extremising function $f = f(x, y)$ must satisfy:

$$\mathbf{\frac{\partial C}{\partial f} - \frac{\partial}{\partial x}\left(\frac{\partial C}{\partial f_x}\right) - \frac{\partial}{\partial y}\left(\frac{\partial C}{\partial f_y}\right) - \sum_{k=1}^{N} \lambda_k(x_k) = 0} \qquad \textbf{(A.11)}$$

Appendix B

The Primal-Dual Method

The duality theorems presented below can often be justified only for convex problems. Hence:

Consider the dual method for the convex problem:

$$\begin{aligned} &\textit{minimize } f(\mathbf{x}) \\ &\textit{subject to } \mathbf{G}(\mathbf{x}) \le \theta, \mathbf{x} \in \Omega \end{aligned} \tag{B.1}$$

Assuming that the constraint is regular, this problem is equivalent to:

$$\begin{aligned} &\max \; \textit{inf}\left\{ f(\mathbf{r}) + < \mathbf{G}(\mathbf{r}), \mathbf{z}^{\cdot} > \right\} \\ &\mathbf{z}^{\cdot} \ge \theta \; \mathbf{r} \in \Omega \end{aligned} \tag{B.2}$$

Or, defining the dual functional:

$$\begin{aligned} \phi(\mathbf{z}^{\cdot}) = \inf_{r \in \Omega} &\left\{ f(\mathbf{r}) + < \mathbf{G}(\mathbf{r}), \mathbf{z}^{\cdot} > \right\} \end{aligned} \tag{B.3}$$

the problem is equivalent to the dual problem:

$$\begin{aligned} &\textit{maximize } \phi(\mathbf{z}^{\cdot}) \\ &\textit{subject to } \mathbf{z}^{\cdot} \ge \theta \end{aligned} \tag{B.4}$$

The dual problem B.4 has only the constraints $\mathbf{z}^{\cdot} \ge \theta$. Hence, assuming that the gradient of ϕ is available, the dual problem can be solved in a routine fashion. (Note the primal problem B.1 has only equality constraints of the form $\mathbf{Ar} = \mathbf{b}$. The dual

problem B.4 will have no constraints). Once the dual problem is solved yielding an optimal $\mathbf{x}_0^*$, the primal problem can be solved by minimising the corresponding Lagrangian [4.5 p. 299].

Appendix C

Lagrange Multiplier Theorems of Constrained Optimisation

Theorem 1:[4.5, page 217]

Let $\mathbf{X}$ be a linear vector space, $\mathbf{Z}$ a normed space, Ω a convex subset of $\mathbf{X}$ and $\mathbf{P}$ the positive cone in $\mathbf{Z}$. Assume that $\mathbf{P}$ contains an interior point.

Let $\mathbf{h}$ be a real-valued convex functional on Ω, and $\mathbf{G}$ a convex mapping from Ω into $\mathbf{Z}$. Assume the existence of a point $\mathbf{x}_1 \in \Omega$ for which $\mathbf{G}(\mathbf{x}_1) < \theta$, (i.e., $\mathbf{G}(\mathbf{x}_1)$ is an interior point of $\mathbf{N} = -\mathbf{P}$, and $\mathbf{N} = -\mathbf{P}$ is called the negative cone in $\mathbf{X}$).

Let:

$$\mu_0 = \inf \mathbf{h}(\mathbf{x}) \quad \textit{subject to} \quad \mathbf{x} \in \Omega, \mathbf{G}(\mathbf{x}) \leq \theta \qquad \text{(C.1)}$$

assuming μ_0 is finite. Then there is an element $\mathbf{z}^0 \geq \theta \in \mathbf{Z}^*$ such that:

$$\mu_0 = \inf_{\mathbf{x} \in \Omega} \left\{ \mathbf{h}(\mathbf{x}) + < \mathbf{G}(\mathbf{x}), \mathbf{z}_0^* > \right\} \qquad \text{(C.2)}$$

Furthermore, if the infimum is achieved in C.1 by an $\mathbf{x}_0 \in \Omega$, $\mathbf{G}(\mathbf{x}_0) \leq \theta$, it is achieved by $\mathbf{x}_0$ in C.2 and

$$< \mathbf{G}(\mathbf{x}_0), \mathbf{x}_0^* >= 0 \qquad \text{(C.3)}$$

Proof: [4.5 page 218]

Theorem 2:[4.5 page 224]

Assume the same conditions as for Theorem 1. The Dual functional can be expressed as:

$$\phi(z^*) = \inf_{x \in \Omega}[h(f) + < G(f), z^* >] \tag{C.4}$$

where $\phi(z^*)$ is known as the dual Lagrangian. The solution to the primal problem, equation A.1 is:

$$\mu_0 = \inf_{\substack{G(f) \le \theta \\ x \in \Omega}} h(f) = \max_{z^* \ge \theta}\{\phi(z^*)\} \tag{C.5}$$

This equation is known as the dual solution.

Proof:[4.5 page 224]

Appendix D

Fan beam matrix elements

This proof, given by Drossos [5.7], shows that the $\mathbf{h}_{ki,nj}$ matrix elements depend on the angle ψ' between the dichotomies of the **nj** and **ki** strips only, as the angular width $\Delta\theta$ is taken to be constant. Consider the equation:

$$\mathbf{h}_{nj,ki} = \iint_{s} \frac{1}{\mathbf{r}_k \mathbf{r}_n} \mathbf{r}_k d\mathbf{r}_k d\theta_k \qquad \textbf{(D.1)}$$

where $\mathbf{r}_k$, θ_k, $\mathbf{r}_n$, l_1, l_2 and ϕ are shown in Figure D.1, and $\Delta\theta = \pi / S$.

$\mathbf{r}_k = \mathbf{O}_k\mathbf{A}$

$\mathbf{r}_n = \mathbf{O}_n\mathbf{A}$

$l_1 = \mathbf{O}_k\mathbf{B}$

$l_2 = \mathbf{O}_k\mathbf{C}$

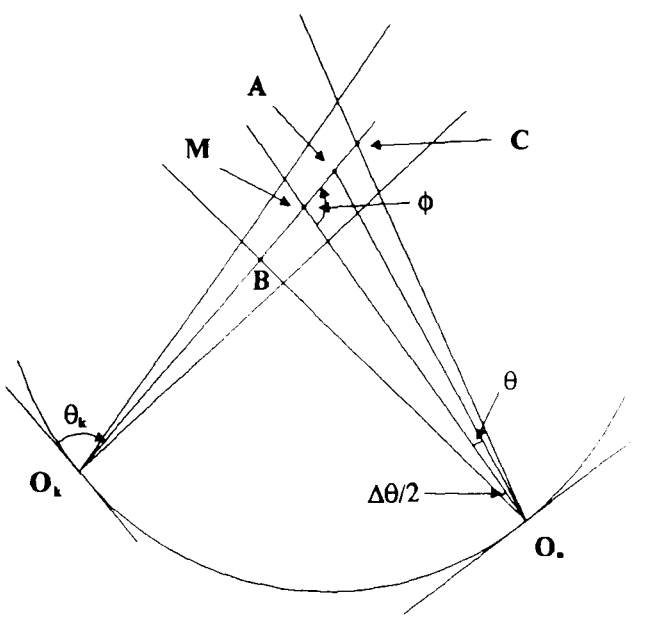

Figure D.1.

For the triangle $\mathbf{O}_n\mathbf{MA}$ in Figure D.1, the following relationship is deduced:

$$\frac{\mathbf{s}}{\sin\theta} = \frac{\mathbf{r}}{\sin\phi} = \frac{\mathbf{R}}{\sin(\phi+\theta)} \qquad \textbf{(D.2)}$$

where $\mathbf{s} = \mathbf{AM}$, $\mathbf{r} = \mathbf{O}_n\mathbf{A}$, and $\mathbf{R} = \mathbf{O}_n\mathbf{M}$.

Using equation (D.2), equation (D.1) can be expressed as:

$$\mathbf{h_{nj,kl}} = \int_{\psi'-\Delta\theta/2}^{\psi'+\Delta\theta/2}\int_{l_1}^{l_2}\frac{\mathbf{1}}{\mathbf{r_n}}\mathbf{dr_k}\mathbf{d\theta_k} = \int_{\psi'-\Delta\theta/2}^{\psi'+\Delta\theta/2}\left[\int_{-\Delta\theta/2}^{\Delta\theta/2}\frac{\mathbf{d\theta}}{\mathbf{\sin(\phi+\theta)}}\right]\mathbf{d\phi} \qquad \textbf{(D.3)}$$

Integrating with respect to θ gives:

$$\mathbf{h_{kl,nj}} = \int_{\psi'-\Delta\theta/2}^{\psi'+\Delta\theta/2}\mathbf{ln}\left|\frac{\mathbf{\tan\left(\frac{\phi}{2}+\frac{\Delta\theta}{4}\right)}}{\mathbf{\tan\left(\frac{\phi}{2}-\frac{\Delta\theta}{4}\right)}}\right|\mathbf{d\phi} \qquad \textbf{(D.4)}$$

which depends on ψ' only, as $\Delta\theta$ is taken to be constant.

Appendix E

Bipolar Co-ordinate system

Let $\mathbf{a}$ denote the point at which the current injection electrodes are placed on the boundary of the medium under investigation. The complex potential due to a source of strength $\mathbf{k}$ at $\mathbf{z=-a}$ is:

$$\mathbf{k\ln(z+a)} \qquad \textbf{(E.1)}$$

The complex potential due to a sink of strength $\mathbf{k}$ at $\mathbf{z=a}$ is:

$$\mathbf{-k\ln(z-a)} \qquad \textbf{(E.2)}$$

Then by superposition:

The complex potential due to source at $\mathbf{z=-a}$, and sink at $\mathbf{z=a}$, both of strength $\mathbf{k}$ is:

$$\mathbf{w(z)=k\ln(z+a)-k\ln(z-a)=k\ln\left(\frac{z+a}{z-a}\right)} \qquad \textbf{(E.3)}$$

Let:

$$\mathbf{z+a=r_1e^{j\theta_1}} \qquad \mathbf{z-a=r_2e^{j\theta_2}} \qquad \textbf{(E.4)}$$

Then:

$$\mathbf{w(z)=u+jv=k\ln\left(\frac{r_1e^{j\theta_1}}{r_2e^{j\theta_2}}\right)=k\ln\left(\frac{r_1}{r_2}\right)+jk(\theta_1-\theta_2)} \qquad \textbf{(E.5)}$$

Hence:

$$\mathbf{u=k\ln\left(\frac{r_1}{r_2}\right)} \qquad \mathbf{v=k(\theta_1-\theta_2)} \qquad \textbf{(E.6)}$$

Using:

$$\mathbf{r_1=\sqrt{(x+a)^2+y^2}}, \quad \mathbf{r_2=\sqrt{(x-a)^2+y^2}} \qquad \textbf{(E.7)}$$

and

$$\mathbf{\theta_1=\tan^{-1}\left(\frac{y}{x+a}\right)}, \quad \mathbf{\theta_2=\tan^{-1}\left(\frac{y}{x-a}\right)} \qquad \textbf{(E.8)}$$

the equipotential lines illustrated in figure E.1 are given by:

$$\frac{\sqrt{(x+a)^2+y^2}}{\sqrt{(x-a)^2+y^2}} = e^{\frac{\alpha}{k}} \qquad \textbf{(E.9)}$$

This can be written in the form:

$$[x - a\coth(\frac{\alpha}{k})]^2 + y^2 = a^2 \operatorname{csc} h^2(\frac{\alpha}{k}) \qquad \textbf{(E.10)}$$

which for different values of α are circles having centres at $a\coth(\frac{\alpha}{k})$, and radii equal to $a\left|\operatorname{csc} h(\frac{\alpha}{k})\right|$.

The current lines (streamlines) illustrated in figure E.1 are given by:

$$\tan^{-1}\left(\frac{y}{x+a}\right) - \tan^{-1}\left(\frac{y}{x-a}\right) = \frac{\beta}{k} \qquad \textbf{(E.11)}$$

or, taking the tangent of both sides and simplifying:

$$x^2 + [y + a\cot(\frac{\beta}{k})]^2 = a^2 \csc^2(\frac{\beta}{k}) \qquad \textbf{(E.12)}$$

which for different values of β are circles having centres at $-a\cot(\frac{\beta}{k})$, and radii $a\left|\csc(\frac{\beta}{k})\right|$. These circles pass through $(-a,0)$ and $(a,0)$.

If $k = 1$ and from **E.3:**

$$u + jv = \ln\frac{z+a}{z-a} \qquad \textbf{(E.13)}$$

hence:

$$e^{u+jv} = \frac{z+a}{z-a} = \frac{\frac{z}{a}+1}{\frac{z}{a}-1} \qquad \textbf{(E.14)}$$

therefore:

$$\frac{z}{a} = \frac{e^{u+jv}+1}{e^{u+jv}-1} = \frac{e^{(\frac{u+jv}{2})} + e^{-(\frac{u+jv}{2})}}{e^{(\frac{u+jv}{2})} - e^{-(\frac{u+jv}{2})}} \qquad \textbf{(E.15)}$$

and

$$\frac{z}{a} = \coth\frac{u + jv}{2} \tag{E.16}$$

by expansion and simplification:

$$\frac{z}{a} = \frac{\sinh u - j\sin v}{\cosh u - \cos v} \tag{E.17}$$

therefore:

$$x + iy = a\left[\frac{\sinh u - j\sin v}{\cosh n - \cos v}\right] \tag{E.18}$$

hence:

$$x = \frac{a\sinh u}{\cosh u - \cos v} \qquad y = -\frac{\sin v}{\cosh u - \cos v} \tag{E.19}$$

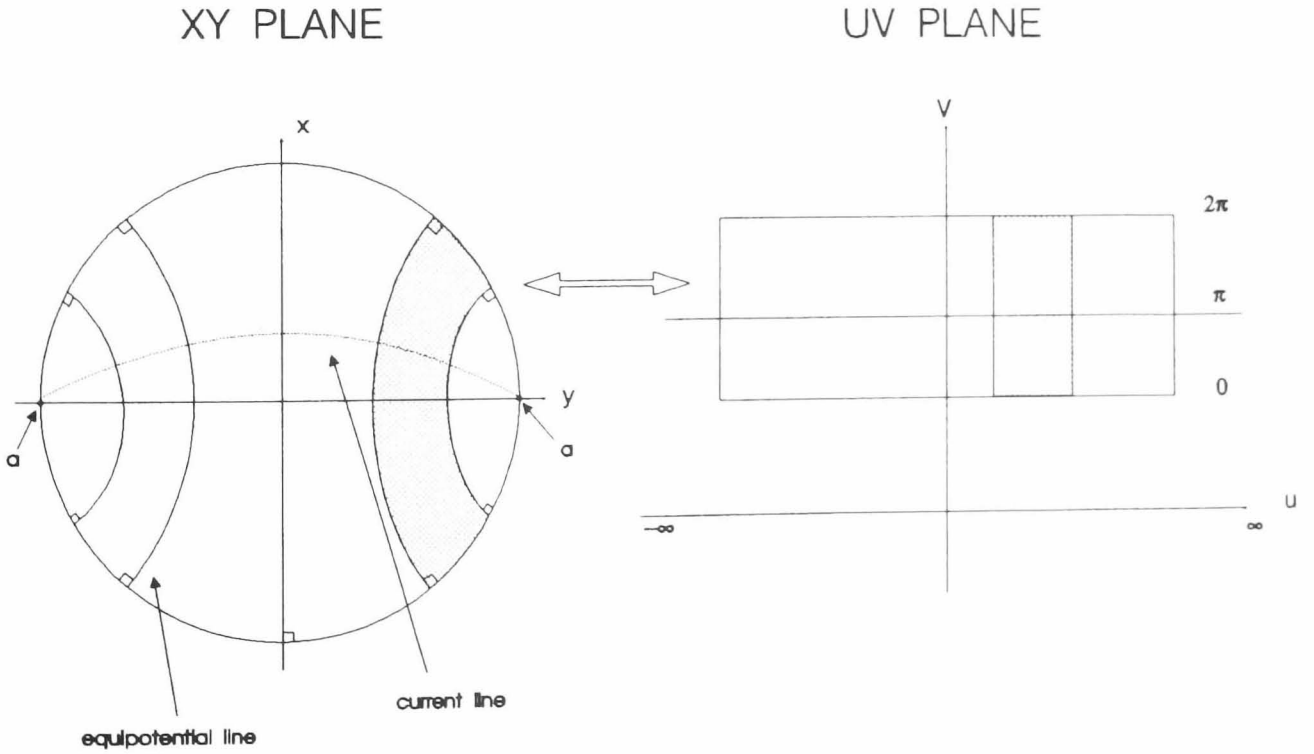

Figure E.1 Conformal Transformation

[E.1, page 248][E.2, page 140]

Appendix F

Dipole System

Assuming the distance between two adjacent electrodes is very small and is denoted by 2τ, and the current is injected at these electrodes, then from the conformal mapping transformation the complex potential is given by:

$$w(z) = u + jv = \frac{1}{x + jy} \tag{F.1}$$

Therefore:

$$u + jv = \frac{x - jy}{x^2 + y^2} \tag{F.2}$$

hence:

$$u = \frac{x}{x^2 + y^2} \qquad v = \frac{-y}{x^2 + y^2} \tag{F.3}$$

and

$$x = \frac{u}{u^2 + v^2} \qquad y = \frac{v}{u^2 + v^2} \tag{F.4}$$

Under this transformation, for:

$$u_i = const = \frac{1}{2\alpha_i} \tag{F.5}$$

$$x^2 + y^2 - 2\alpha_i x = 0 \tag{F.6}$$

where α_i denotes the radii of the circles in the x, y plane illustrated in Figure F.1.

Therefore:

$$(x - \alpha_i)^2 + y^2 = \alpha_i^2 \tag{F.7}$$

For:

$$v_j = const = \frac{1}{2\beta_j} \tag{F.8}$$

hence:

$$x^2 + y^2 + 2\beta_j y = 0 \qquad \textbf{(F.9)}$$

where β_j denotes the radii of the circles in the x, y plane illustrated in figure F.2.

Therefore:

$$x^2 + (y + \beta_j)^2 = \beta_j^2 \qquad \textbf{(F.10)}$$

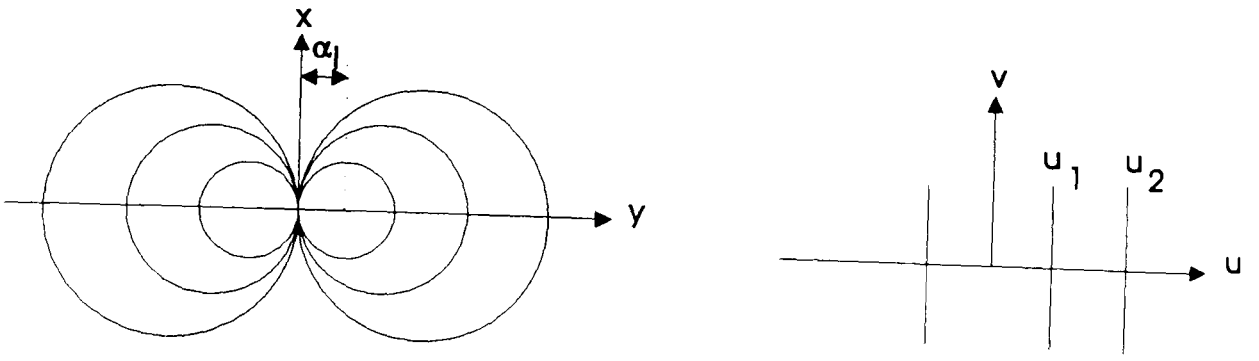

Figure F.1 Conformal transformation of equipotential lines

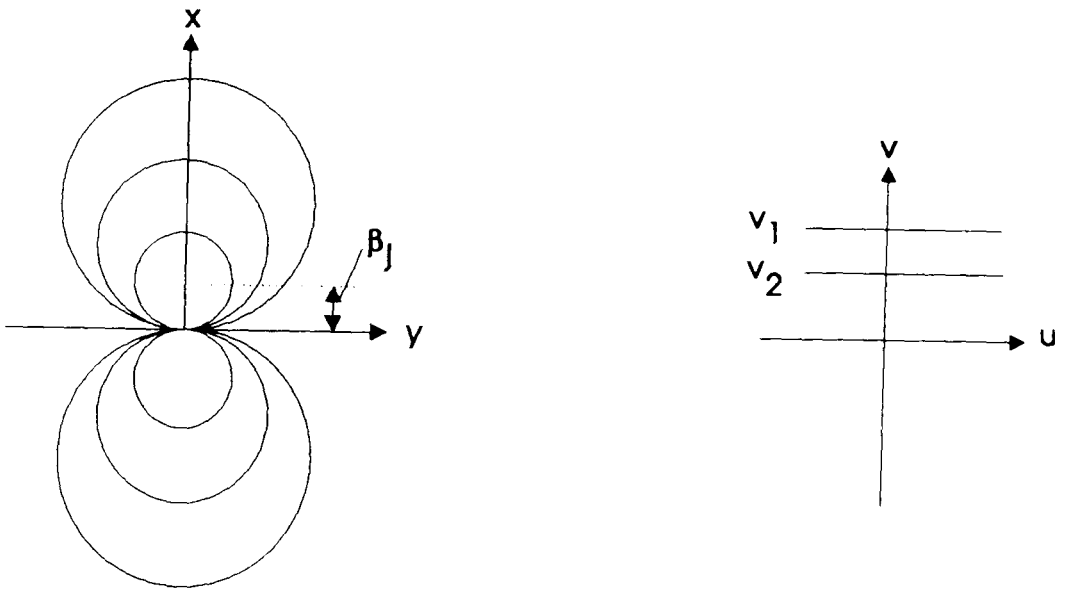

Figure F.2 Conformal transformation of current line

Note that this transformation, known as the dipole approach, approximates the current and equipotential paths. It can result in significant error close to the electrodes, when the gap between the drive electrodes 2τ is not sufficiently small [3.5, page 110].

Appendix G

Effective Resolution limits in EIT

Relationship between voltage and current density:[3.9][G.1]

Consider a circular region $\mathbf{R_b}$ having radius $\mathbf{r_b}$ and conductivity σ_b, illustrated in figure G1.

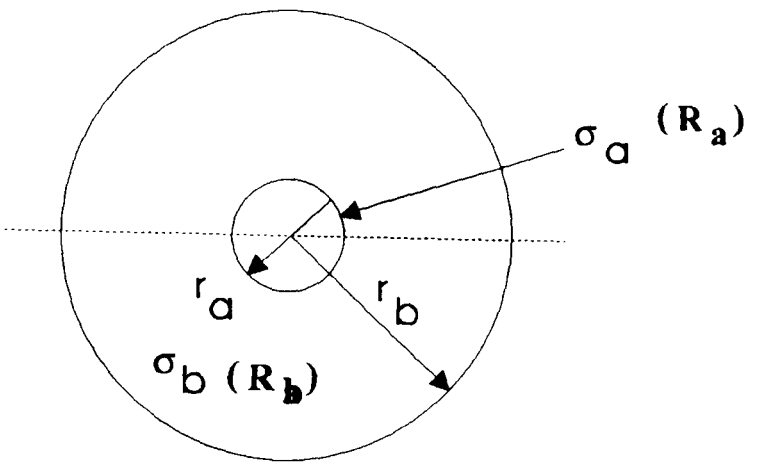

$$\alpha = \frac{\sigma_a}{\sigma_b}, \beta = (\frac{r_a}{r_b})^2$$

Figure G.1.

At the centre of $\mathbf{R_b}$ is a smaller circular region $\mathbf{R_a}$, of radius $\mathbf{r_a}$ and conductivity σ_a. The voltage **V** within $\mathbf{R_b}$ can be expressed in terms of polar co-ordinates $\mathbf{r},\theta$. Suppose a current density distribution $\mathbf{J}(\theta)$ is impressed upon the boundary at $\mathbf{r} = \mathbf{r_b}$. A voltage $\mathbf{V}(\theta)$ then appears on the boundary due to current flow through the region. This situation is simple enough for the voltage and current density distributions to be explicitly related. One approach to this is to express Laplace's Equation in polar co-

ordinates. The resulting partial differential equation may then be separated into two ordinary differential equations using separation of variables. The result is an expression relating the voltage $\mathbf{V}(\theta)$ and current density distribution $\mathbf{J}(\theta)$ to one another, and to the parameters that describe the conductive region. As a result of the use of polar co-ordinates, the eigenfunctions involved in the solution incorporate terms in $\cos\theta$ and $\sin\theta$.

Let $\mathbf{J}_n(\theta)$ be the optimal current density distribution impressed on the boundary, then the Fourier series of $\mathbf{J}_n(\theta)$ is given by:

$$\mathbf{J}_n(\theta) = \mathbf{A}_n \cos n\theta + \mathbf{B}_n \sin n\theta \qquad \textbf{(G.1)}$$

where **n=1** is the best injection current because it produces the maximal distinguishability. The distinguishability decreases as **n** increases. By solving Laplace's equation in polar co-ordinates using equation (G.1) as the Neumann boundary condition, the boundary voltage can be expressed as:

$$\mathbf{V}_n(\theta) = \mathbf{C}_n \cos n\theta + \mathbf{D}_n \sin n\theta \qquad \textbf{(G.2)}$$

where **n=1,2,..** etc.

Assuming that $\mathbf{B}_n = 0$ and expressing the relationship between $\mathbf{J}_n(\theta)$ and $\mathbf{V}_n(\theta)$ as:

$$\mathbf{z}_{nn} = \frac{\mathbf{V}_n}{\mathbf{J}_n} = \frac{\mathbf{C}_n}{\mathbf{A}_n} = -\frac{\mathbf{r}_b}{n\sigma_b}\frac{(1+\alpha)+(1-\alpha)\beta^n}{(1+\alpha)-(1-\alpha)\beta^n} \qquad \textbf{(G.3)}$$

where α and β are defined in Figure G.1, and $\mathbf{z}_{nn}$ is the driving point impedance, when $\alpha = 1$ (i.e. a homogenous object), the driving point impedance becomes:

$$\mathbf{z}_{nnh} = -\frac{\mathbf{r}_b}{n\sigma_b} \qquad \textbf{(G.4)}$$

and

$$\mathbf{V}_{nh} = \mathbf{z}_{nn}\mathbf{J}_n \qquad \textbf{(G.5)}$$

Two parameters can now be defined:

Visibility is defined as:

$$\mathbf{v_n = \frac{V_n - V_{nh}}{V_n + V_{nh}} = \frac{z_{nn} + z_{nnh}}{z_{nn} + z_{nnh}}} \qquad \textbf{(G.6)}$$

Substituting equation **G.3** and equation **G.4** into **G.6** gives:

$$\mathbf{v_n = \frac{(1-\alpha)\beta^n}{1+\alpha}} \qquad \textbf{(G.7)}$$

Sensitivity is defined as a fractional change in voltage for a fractional change in conductivity contrast. For cosine injected currents:

$$\mathbf{V_n(\theta) = A_n z_{nn} \cos n\theta} \qquad \textbf{(G.8)}$$

Differentiating the above equation with respect to α, and multiplying by $\alpha / \mathbf{V_n}(\theta)$ gives:

$$\mathbf{s_n = [\frac{\delta V}{V} / \frac{\delta \alpha}{\alpha}]_n = \frac{-4\alpha\beta^n}{(1+\alpha)^2 - (1-\alpha)^2\beta^n}} \qquad \textbf{(G.9)}$$

where $\mathbf{s_n}$ is the sensitivity, $\delta \mathbf{V} / \mathbf{V}$ is the fractional change in voltage or the maximal admissible noise, and $\delta\alpha / \alpha$ is the conductivity resolution.

The relationships developed so far are derived for a centrally placed circular region. These relationships may be modified so that they can be applied to off-centre circular regions. This is achieved by conformally mapping any off-centred region on to an equivalent central region, and then using the earlier relationships. This approach is valid because the solution to Laplace's equation remains invariant under conformal transformation.

Consider the conformal transformation illustrated in Figure G.2

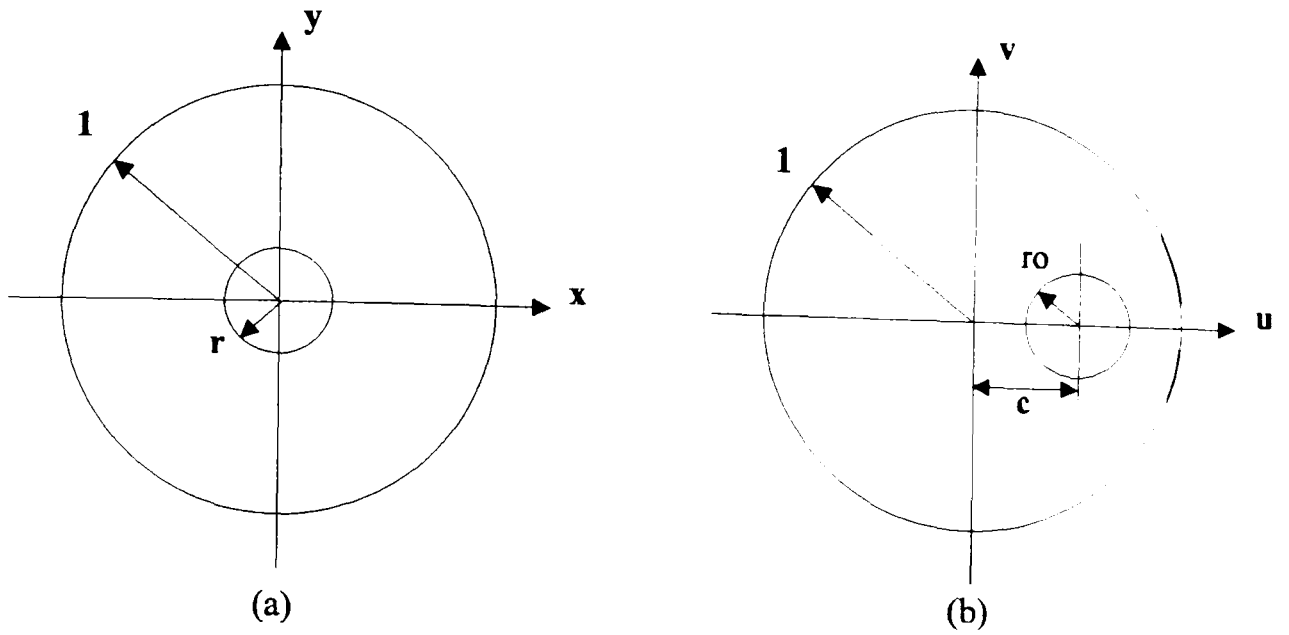

Figure G.2

Let $\mathbf{z = x + jy}$ and $\mathbf{w = u + jy}$ then:

$$\mathbf{z = (d - w)/(wd - 1)} \qquad \mathbf{w = (d + z)/(d - z)} \qquad \textbf{(G.10)}$$

and

$$\mathbf{r = [1 - c^2 + ro^2 - [(1 - c^2 + ro^2)^2 - 4ro^2]^{\frac{1}{2}}]/2ro} \qquad \textbf{(G.11)}$$

$$\mathbf{d = [1 + c^2 - ro^2 - [(1 + c^2 - ro^2)^2 - 4ro^2]^{\frac{1}{2}}]/2c} \qquad \textbf{(G.12)}$$

$$\mathbf{ro = \frac{r(1 - d^2)}{(1 - r^2 d^2)}} \qquad \textbf{(G.13)}$$

$$\mathbf{c = \frac{d(1 - r^2)}{(1 - r^2 d^2)}} \qquad \textbf{(G.14)}$$

This describes the manner in which the resolution varies throughout the conductive region, provided the accuracy, contrast and noise remain fixed. The improvement in resolution, as compared with that at the centre, may be expressed by the ratio **r/ro** as a function of position **c**. **r/ro** depends only on **c** for most values of **ro**. The relationship is given by:

$$\lim_{\mathbf{ro \to 0}} \mathbf{(r/ro)} = \mathbf{\frac{1}{(1 - c^2)}} \qquad \textbf{(G.15)}$$

which can be arrived at after expressing the square root in the expression for **r** in equation (G.11) as a binomial expansion.

REFERENCES

[1.1] Bracewell, R.N.: Image reconstruction in radio astronomy, in Herman G.T., Ed., Image reconstruction from projections, Berlin: Springer, pp. 81-104, 1979.

[1.2] Herman, G.T.: Image reconstruction from projections: The fundamentals of Computer Tomography, New York, Academic Press, 1980.

[1.3] Hounsfield, G.N.: Computing transverse axial scanning (tomography), I. Description of system, Brit. J. Radiol., Vol. 46, pp 1016-1022, 1973.

[1.4] Axel, L., Arger, P.H., and Zimmerman, R.A.: Applications of computerised tomography to diagnostic radiology, Proc. of IEEE, Vol. 71, No. 3, pp. 293-297, 1983.

[1.5] Budinger, T.F. and Gullberg, G.T.: Three-dimensional reconstruction in nuclear medicine emission imaging, IEEE. Trans., Nuclear Sci., Vol. NS-21, pp. 2-20, June 1974.

[1.6] Kouris, K., Ganett, E. S. and Herman, G.T.: Sampling Properties of Stationary and Half-Rotation Ring in Positron Emission Tomography. Journal of Computer Assisted Tomography. Vol. 5 No. 5, pp. 744-754, 1981.

[1.7] Jaszczak, R.J.: Tomographic Radiopharmeceutical Imaging. Proceedings of the IEEE, Vol. 76, No. 9, Sep. 1988.

[1.8] Cho, H.Z., Hilal, S.K., R.A: Experimental results of dichotomic sampling in circular ring positron emission tomograph, IEEE, Trans. Nucl. Sci., V. NS-20, pp. 1893-1898, 1983.

[1.9] Lauterbur, P.C.: Image information by induced local interactions: example employing nuclear magnetic resonance, Nature (London), Vol. 242, pp. 190-191, 1973.

[1.10] Cho, Z. H., Kim, H. S., Song, H. B. and Cumming, J.: Fourier transform nuclear magnetic resonance tomographic imaging, Proc. IEEE, vol. 70, pp. 1152-1173, Oct. 1982.

[1.11] Glover, G. and Sharp, J.C.: Reconstruction of ultrasound propagation speed distributions in soft tissue, IEEE Trans. Sonic Ultrason., Vol. SU-24, pp.229-234, July 1977.

[1.12] Greenleaf, J.F., Johnson, S.A., Lee, L.S., Herman, G.T. and Wood, E.H.: Algebraic reconstruction of spatial distributions of acoustic absorption within tissue from their two dimensional acoustic projections, Acoustical Holography, Vol. 5, P.S. Greene, Ed. N.Y.: Plenum Press, pp. 591-603, 1974.

[1.13] Kisslo, J., Von Ramm, O.T. and Thurstone, F.L.: Cardiac imaging using a phased linear array ultrasound system. II. Clinical technique and application, Circulation, Vol. 53, pp. 262-267, 1976.

[1.14] Glover, G., and Sharp, J.C.: Reconstruction of ultrasound propagation speed distributions in soft tissue, IEEE Trans. Sonic Ultrason., Vol. SU-24, pp. 229-234, July 1977.

[1.15] Schreiman, J.S., Gisvold, J.J., Greenleaf, J.F., and Bahn, R.C.: Ultrasound transmission computed tomography of the breast, Radiology, Vol. 150, pp. 523-530, Feb. 1984.

[1.16] Goodwin-Johansson, S.H., Subrahmanyan, R., Floyd, C.E., and Massound, H.Z.: Two-dimensional Impurity Profiling with Emission Computed Tomography Techniques, IEEE Transactions on Computer-aided design, Vol. 8, No. 4, April 1989.

[1.17] Bracewell, R.N.: Strip integration in radio astronomy, Aust. J. Phys., Vol. 9, pp. 198-217, 1956.

[1.18] Barber, D.C. and Brown, B.H.: Applied potential tomography, J. Phsys. E.: Sci. Instrum. Vol. 17. pp. 723-33. 1984.

[1.19] Plonsey, R. and Barr, R.: The four electrode technique applied to cardiac muscle. IEEE, Trans. Biomed. Eng. BME-29 pp.541-6, 1982.

[1.20] Radon, J.: Uber die bestimmung von funktionen durch ihre integralwerte langs gewisser mannigfaltigkeiten, Berichte Saechsische Academic der

Wissenschaften, Vol. 69, pp. 262-277, 1917.

[1.21] Wenner, F.: A Method of Measuring Earth Resistivity, Scientific Paper of the Bureau of Stands No. 258, Oct. 1915

[1.22] Klotz,: Refined versions employing coded apertures, 1974.

[1.23] Littelton, J.T.: Tomography: Physical Principle and Clinical Applications, The Williams and Wilkins. Co., Baltimore, 1976.

[1.24] Herman, G. T., Lent, A. and Rowland, S. W.: ART: Mathematics and Applications A report on the Mathematical Foundations and on the Applicability to Real Data of the Algebraic Reconstruction Techniques. J. theor. Biol. 42, 1-32, 1973.

[1.25] Lewitt, R.M.: Reconstruction algorithms: Transform methods, Proc. of IEEE, Vol. 71, No. 3, pp. 390-408, 1983.

[1.26] Ramachandran, G.N. and Lakshminaarayanan, A.V.: Three dimensional reconstruction from radiographs and electron micrographs; application of convolution instead of Fourier transforms. Proc. Nat. Acad. of Sci., Vol. 68, No. 9, pp. 2236-2240, 1971.

[1.27] Herman, G.T., Lakshminaraynan, A.V., and Rowland, S.W.: The reconstruction of objects from shadowgraphs with high contrasts Pattern Recognition, V.7, pp. 157-165, 1975.

[1.28] Herman, G.T. and Lent, A.: Iterative reconstruction algorithms, Comp. Biol. Med., V. 6, pp. 273-294, 1976.

[1.29] Durrani, T.S. and Goutis, C.E.: Optimisation techniques for digital image reconstruction from their projections, IEE. Proc. Pt. E, Comput. and Digital Tech., Vol. 127 No. 5, pp. 161-169, September 1980.

[1.30] Wood, S.L. and Morf, M.: A Fast Implementation of a Minimum Variance Estimator for Computerised Tomography Image Reconstruction. IEEE. Transactions on Biol. Eng. Vol. BME-28, No. 2, February 1981.

[1.31] O'Donnell. M.: Applications of VLSI Circuits to Medical imaging. Proceedings

of the IEEE, Vol. 76, No. 9, Sep. 1988.

[1.32] Arthur, F., Gmitro, V., Trep, G., and Gini, R.: Videographic Tomography-Part1: Reconstruction with Parallel-Beam Projection Data. IEEE. Transactions on Medical imaging. VOL. 9, NO. 4, December 1990.

[2.1] Kuhl, D.E. and Edwards, R.Q.: Image separation radioisotope scanning. Radiology, Vol. 80, pp. 653-662, 1963.

[2.2] Gordan, R. and Herman, G.T.: Three-dimensional reconstruction from projections: a review of algorithms. In " International Review of Cytology," Academic Press, N.Y. Vol. 38 pp. 111-151, 1974.

[2.3] Davis, P.J. and Rabinowitz, P.: Convolution algorithms for arbitrary projection angles. IEEE. Trans. Nucl. Sci. NS-26, pp. 2670-2673, 1979.

[2.4] Bracewell, R.N.: Strip integration in radio astronomy, Aust. J. Phys., Vol. 9, pp. 198-217, 1956.

[2.5] DeRosier, D.J. and Klug, A.: Nature, 217, 130, 1968.

[2.6] Crowther, R.A., DeRosier, D.J. and Klug, A.: The reconstruction of three dimensional structure form projections and its applications to electron microscopy. Proc. Roy. Soc. London, Vol. A317, pp. 319-340, 1970.

[2.7] Hamming , R.W.: Digital Filters. Englewood Cliffs, NJ: Prentice-Hall, 1977.

[2.8] Smith, P.R., Peters, T.M. and Bates, R.H.T.: Image reconstruction from finite numbers of projections, J. Phys. A: Math., Nucl. Gen, Vol. 6, pp. 361-382, 1973.

[2.9] Shepp, L.A. and Logan, B.F.: The Fourier reconstruction of a head section, IEEE. Trans. Nucl. Sci., vol. NS-21, pp. 21-43, 1974

[2.10] Kwoh, Y.S., Reed, I.S., and Truong, T.K.: A generalised $|\omega|$-filter for 3-D reconstruction, IEEE. Trans. on Nucl. Sci. Vol. NS-24, No. 5, pp. 1990-1998, 1977.

[2.11] Herman, G.T., Rowland, S.W., and Yau, M.N.: A comparative study of the use of linear and modified cubic spline interpolation for image reconstruction, IEEE

Trans. Nucl. Sci., Vol. NS-26, No. 2, pp. 2879-2894, 1979.

[2.12] Peters, T.M.: Algorithms for fast back and reprojection in computed Tomography, IEEE. Trans. Nucl. Sci., Vol. NS-28, No. 4, pp. 3641-3647, 1981.

[2.13] Rowland, S.W.: Computer implementation of image reconstruction formulas. Herman, G.T., Ed., Image reconstruction from projections, Berlin: Springer, pp. 9-78, 1979.

[2.14] Bracewell, R.N. and Riddle, A.C.: Inversion of fan-beam scans in radio astronomy, The Astrop. J.V. 150, pp. 427-434, 1967.

[2.15] Chesler, D.A. and Riederer, S.J.: Ripple suppression during reconstruction in transverse tomography. Phys. Med. Biol. Vol. 20, pp. 632-636, 1975.

[2.16] Gordon, R., Bender, R. and Herman, G.T.: Algebraic reconstruction techniques (ART) for three dimensional electron microscopy and x-ray photography, J. thero. Biol. Vol. 29, pp. 471-481, 1970.

[2.17] Hounfield, G.N.: A method of and apparatus for examination of a body by radiation such as x-ray or gamma radiation, Patent Specification 1283915, The Patent Office, 1972

[2.18] Kaczmarz, S.: Angenaherte auflosung von systemen linearer gleichungen, Bull. Acad. Pol. Sci. Lett. A, Vol. 6-8A, pp. 355-357, 1937.

[2.19] Herman, G.T.: Image reconstruction from projections: The fundamentals of Computerised Tomography, N.Y. , Academic Press, 1980.

[2.20] Kouris, K., Tuy, H. and Lent, A.: Reconstruction from projections, IEE. Trans. Med. Im., Vol. MI-1, pp. 161-167, 1982.

[2.21] Herman, T.G., Lent, A. and Rowland, S.W.: ART: Mathematics and Applications A report on the Mathematical Foundations and on the Applicability to Real Data of the Algebraic Reconstruction Techniques. J. theor. Biol. Vol. 42, pp. 1-32, 1973.

[2.22] Gordan, R.: A Tutorial on ART, IEEE. Trans. on Nucl. Sci., Vol. NS-21, June

1974.

[2.23] Gaader, N.T. and Herman, G.T.: Computer graphics and Image processing, 1, 97, 1972.

[2.24] Gilbert, P.: Iterative methods for the reconstruction of three-dimensional objects from projections. J. Theor. Biol. 36, pp.105-117, 1972.

[2.25] Lakshminarayanan, A.V. and Lent, A.: Methods of Least Squares and SIRT in Reconstruction, J. theor. Biol. Vol. 76, pp. 267-295, 1979.

[2.26] Goitein, P.F.C.: Iterative Lest Square Technique (ILST), J. theor. Biol. Vol. 36. pp. 105, 1972.

[2.27] Goutis, C.E., Leahy, R.M. and Drossos, S.: Reconstructions for limited view projection data, ICASSP. Boston, IEEE, 1983.

[2.28] Kwoh, Y.S., Reed, I.S. and Truong, T.K.: Backprojection speed improvement for 3-D reconstruction, IEEE. Trans. on Nucl. Sci. Vol. NS-24, No. 5, pp. 1999-2006, 1977

[2.29] Kelieff, G. and Durrani, T.S. Parallel algorithms for tomographic image reconstruction, 3rd int. conf. on image processing and its applications. IEE. Conf. Vol. 1072. pp. 178-181, 1989.

[2.30] Lakshiminarayanan, A.V.: Reconstruction from divergent ray data, Tech. rep. 92, Dept. Comp. Sci., SUNY, 1975.

[2.31] Herman, G.T., Lakshminarayanan, A.V. and Naparstek, A.: Reconstruction Tomography in diagnostic radiology and Nuclear medicine, MM. Ter-Pogossian, Ed., Un. Park press, pp. 105-117, 1977.

[2.32] Lewitt, R.M.: Reconstruction Algorithms: Transform Methods, PROC. IEEE. Vol. 71, No. 3, March 1983.

[2.33] Natterer, .F.: The mathematics of computerised tomography, Wiley. ISBN 0 471 909599, 1986.

[2.34] Kak, A.C. and Slaney, M.: Principles of computerised tomographic imaging, IEEE press, ISBN 0-87942-198-3, 1988.

[2.35] Webb, S.: The physics of medical imaging, pub. Adam Hilger. Medical Science Series. ISBN 0-85274-349-1, 1990.

[3.1] Yorkey, T.J.: Comparing reconstruction methods for electrical impedance tomography, PhD Thesis, Dept. of Electrical and Computer Eng., Univ. Wisconsin, Madision, WI 53706, 1986.

[3.2] Hua, P., Webster, J.G. and Tompkins, W.J.: Effect of the measurement method on noise handling and image quality of EIT imaging, Proc. Annu. Int. Conf. IEEE. Eng. in Medicine and Biology Society Vol. 9, pp. 1429-30, 1987.

[3.3] Brown, B.H and Seager, A.D.: Applied potential tomography: possible clinical applications, Clin. Phys. Physiol. Meas. Vol. 6, pp. 109-21, 1985.

[3.4] Brown, B.H. and Seager, A.D.: The Sheffield data collection system, Clin. Phys. Physiol. Meas. Vol. 8 Suppl. A. pp. 91-7, 1987.

[3.5] Webster, J.G.: Electrical Impedance Tomography, Pub. Adam Hilger, ISBN 0-85274-304-1, 1990.

[3.6] Tong, P. and Rossettos, J.N.: Finite Element Method: Basic Technique and Implementation, Cambridge, M.A: MIT Press, 1977.

[3.7] Smith, G.D.: Numerical Solution of Partial Differential Equations: Finite Difference Methods, Third Edition, Oxford Applied Mathematics and Computing Science Series. ISBN 0-19-859641-3, 1987.

[3.8] Barber, D.C. and Seager, A.D.: Fast reconstruction of resistive images, Clin. Phys. Phsiol. Meas. Vol. 8 Suppl. A. pp. 47-54, 1987.

[3.9] Seager, A.D., Barber, D.C. and Brown, B.H.: Theoretical limits to sensitivity and resolution in impedance imaging Clin. Phys. Physiol. Meas. Vol. 8 Suppl. A. pp. 13-31, 1987.

[3.10] Breckon, W.R. and Pidcock, M.K.: Mathematical aspects of impedance imaging. Clin. Phys. Phsiol. Meas. Vol. 8. Suppl. A. pp. 77-84, 1987.

[3.11] Kotre, C.J.: A sensitivity coefficient method for the reconstruction of electrical impedance tomograms. Clin. Phys. Physiol. Meas., Vol. 10, No. 3, pp. 275-

281, 1989.

[3.12] Kim Y, Webster, J.G. and Tompkins, W.J.: Electrical impedance imaging of the thorax, J. Microwave Power. Vol. 18. pp. 245-57, 1983.

[3.13] Yorkey, T.J., Webster, J.G. and Tompkins, W.J.: An improved perturbation technique for electrical impedance imaging with some criticisms, IEEE. Trans. Biomed. Eng. BME-34. pp. 898-901, 1987.

[3.14] Kim, Y. and Woo, H.W.: A prototype system and reconstruction algorithms for electrical impedance technique in medical body imaging, Clin. Phys. Physiol. Meas. Vol. 8 Suppl. A. pp. 63-70, 1987.

[3.15] Wexler, A., Fry,. B. and Neuman, M.R.: Impedance-computed tomography algorithm and system. Appl. Optics, Vol. 24. pp. 3985-92, 1985.

[3.16] Massara, R.E.: Optimisation methods in electronic circuit design, Pub. Longman Scientific Technical. pp. 19 ISBN 0-582-01497-2, 1991.

[3.17] Yorkey, T.J., Webster, J.G., and Tompkins, W.J.: Comparing reconstruction algorithms for electrical impedance tomography, IEEE. Trans. Biomed. Eng., Vol. BME-34, pp. 843-52, 1987.

[3.18] Hue, P., Woo, E. J, Webster, J. G., and Willis, T.J.: Iterative Reconstruction Methods Using Regularization and Optimal Current Patterns in Electrical Impedance Tomography. IEEE. Trans. on Medical Imaging, Vol. 10. No. 4, December 1991.

[3.19] Woo, E.J., Hua, P., Webster, J.G., and Tompkins, W.J.: A Robust Image Reconstruction Algorithm and its Parallel Implementation in Electrical Impedance Tomography, IEEE. Trans. on Medical Imaging, Vol. 12, No. 2, June 1993.

[4.1] Leahy, R.M., and Goutis, C.E.: An Optimal Technique for Constraint-Based Image Restoration and Reconstruction., IEEE TRANSACTIONS on Acoustics, Speech, and Signal Processing, Vol. ASSP-34, No. 6, December 1986.

[4.2] Akhiezer,N.I.: The Calculus of Variations. Blaisdell Pub.Co.N.Y., 1962.

[4.3] Weinstock, R.: Calculus of Variations, With Applications to Physics and Engineering. Dover Publications, Inc. N.Y., 1974.

[4.4] Luenberger, D.G.: Optimisation by vector space methods, N.Y., Wiley, 1st edition, 1969.

[4.5] Jaynes, E.T.: On the rationale of Maximum-Entropy methods, Proc. of IEEE, Vol. 70-, No. 9, pp. 939-952, 1982.

[4.6] Burg, J.P.: Maximum entropy spectral analysis, (thesis) Proc., 37th Meet. Soc. Exploration Geophysicists, Stanford, C.A., 1975.

[4.7] McClellan, J.H. and Lang, S.W.: Duality for multidimensional MEM spectral analysis. IEE PROC., Vol. 130, Pt. F, No. 3, April 1983

[4.8] Leahy, R.M., Goutis, C.E., and Drossos, S.N.: Tomographic and spectral estimation using noise statistics, IEEE. Int. Conf. Acoust., Speech, Signal Processing, ICASSP-84, San Diego, C.A. pp. 431-434, 1984.

[4.9] Minerbo, G.: A maximum entropy algorithm for reconstructing a source form projection data, Comp. Graph. Vol. 10. p. 48, 1979.

[4.10] Trussell, H.J.: Convergence criteria for iterative restoration methods, IEEE. Trans. Acoust., Speech, Signal Processing. Vol. 31, pp. 129-136, Feb. 1983

[5.1] Goutis, C.E.: Constraint optimisation algorithms for digital image reconstruction from projections, PhD. thesis, Southampton University, 1978.

[5.2] Hunt, B.R.: A Matrix Theory Proof of the Discrete Convolution Theorem, IEEE. Trans, on Audio and Electroacoutics. Vol. 4, Au-19, December 1971.

[5.3] Goutis, C.E. and Durrani, T.S.: Digital image reconstruction by circulant-like matrix algorithms, Proc. of IERE conf. on digital processing of signals in communications, No. 37 Loughborough, UK, pp. 285-292, 1977.

[5.4] Drossos, S.N.: Algorithms in Image Reconstruction form Projections, Ph.D. Thesis. University of Newcastle, 1984.

[5.6] Goutis, C.E., and Durrani, T.S.: Tomographic algorithms for general line

integrals, IEEE. Trans. Nuclear Science Oct., 1982.

[5.7] Goutis,.C.E., and Drossos, S.N.: Fast iterative algorithms for reconstruction from divergent-ray projections, IEE. Proceedings, Vol. 131, Pt. E, No. 3, May, 1984.

[5.8] Shim, Y.S., and Cho, Z.H.: SVD pseudo inversion image reconstruction, IEEE. Trans. Acoust. Sp. and Sig. Process., Vol. 4. ASSP-29, pp. 904-909, 1981.

[6.1] Kohn, R., and Vogelius, M.: Relaxation of a variational method for impedance computed tomography, Commum. Pure appl. Math. Vol. 42, pp. 1097-1112, 1987.

[6.2] Kohn, R.V., and McKenney, A.: Numerical implementation of a variational method for electrical impedance tomography, Inverse Problems Vol. 6, pp. 389-414, 1990.

[7.1] Griffiths, H.:Cardiff Resistor-mesh Phantom for EIT, EC Workshop on Phantoms for Electrical Impedance Tomography, November 1990.

[7.2] Sakamoto, K., Yorkey, T.J. and Webster, J. G.: Some physical results from an impedance camera, Clin. Physiol. Meas. Vol. 8 A. pp. 71-76, 1987.

[7.3] Holder, D.S.: Performance of the "Sheffield" electrical impedance tomography system with respect to imaging brain function in the adult head. Proceedings of European concerted action in process tomography (ECAPT) conference, Manchester, 1992.

[7.4] Rosell, J., Riu, P. and Pallas-Areny, R.: A parallel data acquisition system for electrical impedance tomography. Proc. Annu. Conf. IEEE. Engineering in Medicine and Biology Society Vol. 11. pp. 459-460, 1989.

[7.5] Barbar, D.C., and Brown, B.H.: Recent developments in applied potential tomography Information Processing in Medical Imaging, ed. S. Bacharach (Dordrecht: Martinus Nijhoff) pp. 446-62, 1986.

[7.6] Bellman, R.: Introduction to matrix analysis, Second edition, Tata McGraw-

Hill, 1979.

[7.7] Davenport, W.B.: Probability and Random Processes, McGraw-Hill Book Company, New York, 1970.

[7.8] Oppenheim, A.V., and Schafer, R.W.: Digital Signal Processing, Prentice-Hall, ISBN 0-13-214635-5, 1975.

[7.9] Gonzalez, R.C, and Wintz, P.: Digital image processing, Addison-Wesley Pub. Co., Inc, Lodon, 1977.

[7.10] Censo, Y.: Finite series expansion reconstruction methods, Procc. IEEE, Vol. 71, No. 3, pp. 409-419, 1980.

[7.11] Hua, P., Woo, J.E., Webster, J.G., and Tompkins. W.J.: Using Compound Electrodes in Electrical Impedance Tomography. IEEE. Trans. on Biomedical. Eng., Vol. 40, No. 1, January 1993.

[7.12] Eyuboglu, B.M., Brown, B.H., and Barber, D.C.: Limitations to SV Determination from APT Images, Proc. of the 11th. annual int. conf. of the IEEE. Engineering in medicine and biol. Soc. Vol. 11 part 2, pp. 442-443, 1989.

[7.13] Isaacson, D.: Distinguishability of conductivities by electric current computered tomography, IEEE. Trans. Med. Imag., Vol. M1-5, pp. 91-95, 1986.

[7.14] Cheney, M., and Isaacson, D.: Distinguishability in Impedance Imaging, IEEE. Trans. on Bio. Eng., Vol. 39, No. 8, August 1992.

[7.15] Holder, D.: Clinical and physiological applications of Electrical Impedance Tomography, UCl Press Ltd. ISBN: 1-85728-164-0 HB, 1993.

[8.1] Verilog-XL Reference Manual, 1990.

[8.2] Li, G.J., and Wach, B.W.: The design of optimal systolic arrays, IEEE transactions on computers, Vol. C3A, No 1, Jan. 1985.

[8.3] Kuojuey, R. Liu. and Yao, K.: A systematic approach to bit recursive systolic array design. International conference on systolic arrays, Proceedings, May. 1988.

[8.4] Moldovan, D: On the design of algorithms for VLSI systolic arrays, Proceedings of the IEEE, Vol. 77 No 1, Jan. 1983.

[8.5] Valero-Garci'a, M., Navarro, J.J., LLaberi'a J.M., and Valero M.: Implementation of systolic algorithms using pipelined functional units, Proceedings, Application specific array processors. IEEE. Computer Society Press, ISBN 0-8186-9089-5, pp. 272-283, 1990

[8.6] Kung, S. Y.: VLSI Array Processors. International Conference on Systolic arrays, University of Oxford, July 1986.

[8.7] Kung, H.T., and Leiserson, C.E.: Systolic Arrays (for VLSI). Sparse Matrix Symposium, Society for Industrial and Applied Mathematics, pp. 256-282, 1978.

[8.8] Kung, H.T.: Systolic communication. In Proceedings - International Conference on Systolic Arrays, pp. 695-703, 1988.

[8.9] Ipsen, I.C.F., Suad, Y., and Schultz, M.H.: Complexity of Dense Linear System Solution on a Multiprocessor Ring, Research report 3.49 Dept. of computer Science, Yale University, 1984.

[8.10] Bayford, R.: A bit-serial Systolic Backprojection engine, In Multiprocessor computer architectures, Edited by Fountain, T.J. and Shute, M.J. pub North-Holland, ISBN: 0 444 882154, pp. 185-202, 1990.

[8.11] Lattard, D., Faure, B., and Mazare, G.: Massively parallel architecture: Application to neural net emulation and image reconstruction, Proceedings, Application specific array processors. IEEE. Computer Society Press, ISBN 0-8186-9089-5, pp.214-225, 1990

[8.12] Kuojuey, R. L., and Yao, K.: A systematic approach to bit recursive systolic array design. International conference on systolic arrays, Proceedings, May, 1988.

[8.13] Aho, A.V., Hopcroft, J.E., and Ullman, J.D.: Data structures and algorithms. Addison-Wesley, 1987.

[8.14] Borges, A.R., and Ferrari de Almeida A.M.B.: A Multiprocessor Architecture for Image Reconstruction in CT, Ed. Allison-Wesley, Parallel Processing for Computer Vision and Display, 1989.

[8.15] Kingsford, N., Dagless, E.L., Belchmber, R.M., Betteridge, D., Lilley, T. and Roberts, J.D.: Image reconstruction using the Transputer, IEEE Proceedings, Vol. 133, Pt. E. No. 3, pp. 139-144, 1986.

[8.16] Goutis, C.E.: Special purpose processor for block circulant matrices with elliptical structures. Newcastle University report,1985.

[8.17] IEEE Standard VHDL Language Reference Manual. IEEE, Std. 1076, New York, 1988.

[9.1] Holder, D.S. and Brown, B.H.: Biomedical application of EIT a critical review, In 'Clinical and physiological applications of electrical impedance tomography', ed. Holder, D.S. UCL press: London, 1993.

[9.2] Yorkey, T.J., and Webster, J.G.: A comparison of impedance tomographic reconstruction algorithms, Clin. Phys. Physiol. Meas., Vol. 8, Suppl. A, pp. 55-62, 1987.

[9.3] Goutis, C.E., and Durrani, T.S.: Digital image reconstruction by circulant-like matrix algorithms, Proc. of IERE Conf. on Digital processing of signals in communications, Loughbourough UK. Vol. 37 pp. 285-295, 1977.

[9.4] Guardo, R., Boulay, C., Murrat, B., and Bertrand, M.: An Experimental Study in Electrical Impedance Tomography Using Backprojection Reconstruction, IEEE, Trans. on Biomedical Eng. Vol. 38, No. 7, July 1991.

[9.5] Holder, D.S.: Electrical Impedance Tomography (EIT) of Brain Function, Human Sciences Press, Inc. Vol. 5, No. 2, 1992.

[D.1] Spiegel, M.R.: Schaum's outline series, Theory and Problems of Complex Variables, Schaum's outline series. McGraw-Hill, pp. 248, 1974.

[D.2] Spiegel, M.R.: Schaum's outline series, Theory and Problems of Vector Analysis, Schaum's outline series. McGraw-Hill, pp. 140, 1974.

[F.1] Gisser, D.G., Isaacson, D., and Newell, J.C.: Current topics in impedance imaging, Clin. Phys. Physiol. Meas., 1987, Vol. 8, Suppl. A, pp. 39-46, 1987.